OFFICE OF CIVILIAN RADIOACTIVE WASTE MANAGEMENT
MODEL COVER SHEET

1. QA: QA

Page: 1 of: 111

Complete Only Applicable Items

2. Type of Mathematical Model

[X] Process Model [ ] Abstraction Model [ ] System Model

Describe Intended Use of Model:

Conceptual model for ventilation and its numerical applications and validation

Technical Contact/Department:
EBS

3. Title:
Ventilation Model

4. DI (including Rev. No. and Change No., if applicable):
ANL-EBS-MD-000030 REV 01

5. Total Attachments:
~~11~~ vc 10/29/02 12

6. Attachment Numbers - No. of Pages in Each:
I - 5, II - 4, III - 3, IV - 3, V - 2, VI - 2, VII - 2, VIII - 2, IX - 2, X-2, XI-22, XII - 22

	Printed Name	Signature	Date
7. Originator	Veraun Chipman		10/14/2002
8. CSO	Bruce Kirstein		10/15/02
9. Checker	Jim Kam		10/15/02
10. QER	Ken McFall		10/15/02
11. Responsible Manager/ Lead	Veraun Chipman		~~10/14/2002~~ vc 11-1.02 10/15/02
12. Responsible Manager	Dan Thomas		10/15/2002

13. Remarks:

OFFICE OF CIVILIAN RADIOACTIVE WASTE MANAGEMENT
MODEL REVISION RECORD

2. Model Title:

Ventilation Model

3. DI (including Rev. No. and Change No., if applicable):

ANL-EBS-MD-000030 REV 01

4. Revision/Change No.	5. Description of Revision/Change
00	Initial issue
01	Initial issue

CONTENTS

Page

FIGURES

Page

TABLES

Page

1. PURPOSE

The purpose of the Ventilation Model is to simulate the heat transfer processes in and around waste emplacement drifts during periods of forced ventilation. The model evaluates the effects of emplacement drift ventilation on the thermal conditions in the emplacement drifts and surrounding rock mass, and calculates the heat removal by ventilation as a measure of the viability of ventilation to delay the onset of peak repository temperature and reduce its magnitude. The heat removal by ventilation is temporally and spatially dependent, and is expressed as the fraction of heat carried away by the ventilation air compared to the fraction of heat produced by radionuclide decay. One minus the heat removal is called the wall heat fraction, or the remaining amount of heat that is transferred via conduction to the surrounding rock mass. Downstream models, such as the *Multiscale Thermohydrologic Model* (BSC 2001), use the wall heat fractions as outputted from the Ventilation Model to initialize their post-closure analyses.

The Ventilation Model report was initially developed to analyze the effects of preclosure continuous ventilation in the Engineered Barrier System (EBS) emplacement drifts, and to provide heat removal data to support EBS design. Revision 00 of the Ventilation Model included documentation of the modeling results from the ANSYS-based heat transfer model. The purposes of Revision 01 of the Ventilation Model are:

1. To validate the conceptual model for preclosure ventilation of emplacement drifts and verify its numerical application in accordance with new procedural requirements as outlined in AP-SIII-10Q, *Models* (Section 7.0).
2. To satisfy technical issues posed in KTI agreement RDTME 3.14 (Reamer and Williams 2001a). Specifically to demonstrate, with respect to the ANSYS ventilation model, the adequacy of the discretization (Section 6.2.3.1), and the downstream applicability of the model results (i.e. wall heat fractions) to initialize post-closure thermal models (Section 6.6).
3. To satisfy the remainder of KTI agreement TEF 2.07 (Reamer and Williams 2001b). Specifically to provide the results of post-test ANSYS modeling of the Atlas Facility forced convection tests (Section 7.1.2). This portion of the model report also serves as a validation exercise per AP-SIII.10Q, *Models*, for the ANSYS ventilation model.
4. To further satisfy KTI agreements RDTME 3.01 and 3.14 (Reamer and Williams 2001a) by providing the source documentation referred to in the KTI Letter Report, *Effect of Forced Ventilation on Thermal-Hydrologic Conditions in the Engineered Barrier System and Near Field Environment* (Williams 2002). Specifically to provide the results of the MULTIFLUX model which simulates the coupled processes of heat and mass transfer in and around waste emplacement drifts during periods of forced ventilation. This portion of the model report is presented as an Alternative Conceptual Model with a numerical application, and also provides corroborative results used for model validation purposes (Section 6.3 and 6.4).

The scope of developing, validating, and implementing the Ventilation Model is described in the *Technical Work Plan for Engineered Barrier System Department Modeling and Testing FY 02 Work Activities* (BSC 2002). No deviations from the EBS TWP were made.

The scope of the model documentation includes:

1. A description of the conceptual and numerical model for the heat transfer mechanisms in ventilated emplacement drifts and in the surrounding host rock.
2. A description of an alternative conceptual model and its numerical application, which couples the heat transfer mechanisms with mass transfer in and around the ventilated emplacement drifts.
3. A discussion of the applicability of the wall heat fraction to initialize downstream post-closure thermal models.
4. Documentation of the model validation approach.

The primary limitation of the Ventilation Model Report is that it does not attempt to predict repository performance during the preclosure period. Rather, the intended purpose of the report is to validate a conceptual model for preclosure ventilation that may be exercised in subsequent and future analyses. Therefore, the use of the results presented herein is limited to the validation and verification processes.

2. QUALITY ASSURANCE

The technical work in this model report is a part of the EBS Modeling and Testing tasks listed in the EBS TWP (BSC 2002), and classifies the activities to prepare, complete, and issue the Ventilation Model as Quality Affecting. Therefore, this document is subject to the requirements of the *Quality Assurance Requirements and Description* (QARD) document (DOE 2000). A Technical Change Request (T2001-0172) was approved in accordance with AP-3.4Q, *Level 3 Change Control.* The repository subsurface ventilation system has been classified as Conventional Quality from *Classification of the MGR Subsurface Ventilation System* (CRWMS M&O 1999a). The governing procedure for preparation of this model report is OCRWM procedure AP-SIII.10Q, *Models.*

Qualified and accepted input data and references have been identified. All electronic data used during the preparation of this Model Report were obtained from the Technical Data Management System as appropriate. Electronic data were controlled and managed in accordance with AP-SV.1Q, *Control of the Electronic Management of Information.* Unqualified data used in this report are tracked in accordance with AP-3.15Q, *Managing Technical Product Inputs.* Computer software and model usage is discussed in Section 3 of this document.

3. USE OF SOFTWARE

Computer software was used in the preparation of this Model Report. Table 3-1 lists the software used as well as the software tracking numbers (where appropriate), CPU(s), operating systems, and physical location where the software was installed. All software listed in Table 3-1 was obtained from Software Configuration Management, was appropriate for the applications used, and was used within the range of validation in accordance with AP-SI.1Q, *Software Management*. Use of software has been documented in accordance with AP-SI.1Q.

Table 3-1. Software

Code	Software Tracking Number	CPU	Physical Location	Operating System
ANSYS V5.6.2	10145_5.6.2-00 10145_5.6.2-01	SGI Octane, M&O #114441 Sun Microsystems UltraSPARC, M&O #117683	Las Vegas, NV	IRIX 6.5 Solaris 2.7
MULTIFLUX 2.2 (10/29/01)	Unqualified Software 10485-2.2 (10/29/01)-00	Sun Microsystems Ultra 2, vent.ymp.gov, M&O #114616 Sun Microsystems Ultra 2, dryheat.ymp.gov, M&O #117147	Las Vegas, NV	Solaris 5.7
MATLAB V5.3	Exempt	Sun Microsystems Ultra 2, vent.ymp.gov, M&O #114616 Sun Microsystems Ultra 2, dryheat.ymp.gov, M&O #117147	Las Vegas, NV	Solaris 5.7
NUFT V3.0s	10088-3.0s-01	Sun Microsystems Ultra 2, vent.ymp.gov, M&O #114616 Sun Microsystems Ultra 2, dryheat.ymp.gov, M&O #117147	Las Vegas, NV	Solaris 5.7
RADPRO v3.22	10204-3.22-00	Sun Microsystems Ulta 2, hydro.ymp.gov, M&O #115488	Las Vegas, NV	Solaris 5.6.1
Mathcad 2001 Professional	Exempt	Dell Pentium Workstation, M&O #151635	Las Vegas, NV	Windows 2000
Microsoft Excel 97	Exempt	Various YMP M&O Computers	Las Vegas, NV	Windows 95, Windows 2000

3.1 ANSYS V5.6.2

ANSYS v5.6.2 is a commercially available computer program and is classified as qualified software (per AP-SI.1Q, *Software Management*). ANSYS v5.6.2 was used to implement the ventilation conceptual model in one of two alternate numerical model calculations. ANSYS v5.6.2 is a general purpose finite element analysis (FEA) code, and is used in many disciplines of engineering that deal with topics including structural, geotechnical, mechanical, thermal, and fluids. ANSYS was used to numerically implement the ventilation conceptual model. Two ANSYS numerical models for ventilation are presented herein, ANSYS-Coarse and ANSYS-Refined.

3.2 MULTIFLUX V2.2 (10/29/01)

MULTIFLUX v2.2 (10/29/01) was developed at the University of Nevada, Reno under cooperative agreement with the DOE for the express purpose of numerically modeling the coupled heat and mass transfer within and around ventilated emplacement drifts. MULTIFLUX v2.2 (10/29/01) is unqualified software. Two alternate numerical MULTIFLUX models were developed for this Model Report. The first, MULTIFLUX-Con, is a heat transfer only model similar to the ANSYS models and is used for corroborative purposes. The second, MULTIFLUX-Full, is presented as an Alternative Conceptual Model and simulates the effects of water and water vapor phase change and transport on the ventilated emplacement drift.

3.3 MATLAB V5.3

The MATLAB v5.3 software is required by MULTIFLUX v2.2 (10/29/01) since parts of MULTIFLUX software package were written using the MATLAB programming language. The MATLAB v5.3 software is an exempt software product in accordance with AP-SI.1Q.

3.4 NUFT V3.0s

NUFT v3.0s (Non-isothermal Unsaturated Flow and Transport model) is classified as qualified software (per AP-SI.1Q, *Software Management*), and simulates multi-phase, multi-component non-isothermal flow and transport in porous media. As a part of the MULTIFLUX software, the NUFT v3.0s software package is used to simulate the heat and mass transport at the drift wall-to-host rock interface and in the fractured porous media surrounding the emplacement drift.

3.5 RADPRO V3.22

RADPRO V3.22 is classified as qualified software (per AP-SI.1Q, *Software Management*), and is used to generate input files for NUFT V3.0s to simulate radiative heat transfer within the drift. For this Model Report, RADPRO V3.22 is used to generate input files as part of the in-drift submodel validation exercises of Section 7.

3.6 Mathcad 2001 Professional

Mathcad 2001 Professional is a commercially available software package. The Mathcad software provides a technical computing environment centered on real mathematical expressions and notation. For this Model Report, the Mathcad software was used to solve an analytical expression as part of the host rock submodel validation exercises of Section 7. The Mathcad software is an exempt software product in accordance with AP-SI.1Q. The formulas used, as well as their inputs and outputs, are documented in Attachment XI.

3.7 Microsoft Excel 97

Microsoft Excel 97 is a commercially available spreadsheet software package. Excel 97 is used in conjunction with the ANSYS v5.6.2 software to numerically implement the ventilation

conceptual model. It is also used to make plots of data and perform computations using standard functions such as cell addition, subtraction, multiplication, and division. The Excel 97 software is an exempt software product in accordance with AP-SI.1Q. Only standard functions and formulas are used. They are documented in Attachments I, II, III, V, VI, X, and DTNs MO0210MWDTVE30.018, MO0210MWDTEM30.019, MO0209MWDANS30.017, MO0210MWDVEN30.005. Sections 4 and 5 list the inputs to the formulas, and Section 6 and 7 present the output.

4. INPUTS

This section describes data, parameters, and criteria used to develop and validate the Ventilation Model. All data and parameters in this model report are used solely as inputs in the development of the numerical applications of either the ventilation conceptual model or the ventilation alternative conceptual model. No design analysis or parameters were generated based on the inputs. Therefore, the use of any unqualified data as inputs is justified. The input data presented in this section are designated in accordance with AP-3.15Q.

4.1 DATA AND PARAMETERS FOR THE VENTILATION MODELS

This section describes the data and parameters, and their sources, used to develop, numerically apply, and validate the ventilation conceptual and alternative conceptual models.

4.1.1 Emplacement Drift Location within the Repository Footprint

Northing 233760 and easting 170750 (CRWMS M&O 1999b) was chosen as a representative location within the repository footprint for the emplacement drift inlet of the ventilation model. This location is considered representative in terms of its distance from an edge of the footprint, geology and infiltration rate. It is from this location that the stratigraphic unit thicknesses and material and thermal properties were taken (Sections 4.1.2 through 4.1.3). Because the MULTFILUX model uses NUFT as part of its ventilation simulations, certain stratagraphic material, hydrologic, and thermal properties are required beyond those needed for the ANSYS ventilation models. As such, the NUFT LDTH chimney location l4c4 (northing 233808, easting 170501) of the MSTH Model (BSC 2001) was used to obtain these additional properties (Section 4.1.4).

4.1.2 Stratigraphic Unit Comparisons

The stratigraphic units associated with northing 233760 and easting 170750 (ANSYS) and chimney l4c4 (NUFT) are characterized using different names. Therefore, the ANSYS stratagraphic units were directly compared to the NUFT units using the properties of thermal conductivity (wet and dry), density, and heat capacity (Attachment XII). By the comparison, equivalent ANSYS units of the NUFT l4c4 location were identified. For example, l4c4 unit tsw35 compares directly to Tptpll (ANSYS) based on values for thermal conductivity, etc. Table 4-1 shows the stratigraphic unit comparisons made from Tables 4-2 and 4-5.

Table 4-1. Equivalency between the ANSYS-Based and NUFT l4c4 Stratigraphic Units

l4c4 Units	Equivalent ANSYS Units
Tcw11	Tpcrv
Tcw12	Tpcpln
Tcw13	Tpcpv2
ptn21	Tpcpv1
ptn22	Tpbt4
ptn23	Tpy
ptn24	Tpbt3
ptn25	Tpp
ptn26	Tpbt2
Tsw31	Tptrv3, 2, 1
Tsw32	Tptrn
Tsw33	Tptrl, Tptpul
Tsw34	Tptpmn
Tsw35	Tptpll
Tsw36	Tptpln
Tsw37	Tptpln
Tsw38	Tptpv3, 2
Tsw39	Tptpv1
ch1z	Tpbt1
ch1v	Tpbt1
ch2v	Tac5, 4, 3
ch3v	Tac5, 4, 3
ch4v	Tac5, 4, 3
ch5v	Tac5, 4, 3
ch2z	Tac2, 1
ch3z	Tac2, 1
ch4z	Tac2, 1
ch5z	Tac2, 1
ch6	Tacbt

4.1.3 Thickness, Density, Thermal Conductivity, and Specific Heat of the ANSYS Stratigraphic Units

The thicknesses of the ANSYS stratigraphic units (northing 233760, easting 170750), rock grain density, thermal conductivity, and specific heat used in the ANSYS model are listed in Table 4-2. These are average values at this location within the repository emplacement area (DTN: SN0003T0571897.013 and summarized by CRWMS 1999b). Note that DTN: SN0003T0571897.013 is unqualified and has been superseded by DTN: SN0011T0571897.014. Because this report is intended to use numerical examples to compare models for corroboration and validation purposes, use of the data as provided in DTN: SN0003T0571897.013 is considered adequate. Also note that there is no accounting in the ANSYS-based models for porosity. Therefore, the grain density shown in Table 4-2 represented the bulk density in the ANSYS-based models.

In order to determine the thickness of Tpcrv down to Tpcpv3, the following calculation is necessary. The average elevations of the surface and the top of Tpcpv2 are 1421.28 m and 1306.98 m (CRWMS M&O 1999b) respectively. Therefore, the thickness of the overburden above Tpcpv2 is 114.3 m (surface elevation - Tpcpv2 elevation).

In addition, the average elevation of the repository horizon (drift bottom) is 1072.3 m (DTN: SN0003T0571897.013). Therefore, the depth to the spring line of the emplacement drift is calculated to be 346.23 m (surface elevation - repository horizon elevation - half the drift diameter).

The thickness of the units from Tpcpv2 (including Tpcpv2) down to Tacbt is 492.27 m as calculated from the unit thickness data of Table 4-2. Therefore, the total thickness for all the stratagraphic units shown in Table 4-2 is 606.57 m (overburden above Tpcpv2 + thickness of Tpcpv2 down to Tacbt). The thickness from the emplacement drift spring line to the bottom of the Tacbt unit is 260.34 m (total thickness - depth from the ground surface to the drift spring line).

This information is used in constructing the ANSYS ventilation models and the NUFT portions of the MULTFLUX ventilation models of Section 6.

Table 4-2. Thermal Modeling Parameters by Stratigraphic Unit

T/M Unit	USGS Unit		ISM 3.0	Thickness	Grain Density	Thermal Conductivity		Specific Heat		
				(m)	(kg/m^3)	T<100°C (wet)	T>100°C (dry)	T<95°C	95°C<T<114°C	T>114°C
						(W/m·K)		(J/kg·K)		
TCw	Tpcrv		No Data	No Data	2550	2.00	1.60	823	3879	823
	Tpcrn		No Data	No Data	2550	2.00	1.60	823	3879	823
	Tpcrl		No Data	No Data	No Data	No Data	No Data	No Data	No Data	No Data
	Tpcpul		No Data	No Data	2520	1.67	1.23	882	4352	882
	Tpcpmn		No Data	No Data	2510	1.94	1.53	837	4010	837
	Tpcpll		No Data	No Data	2510	1.76	1.02	847	4019	847
	Tpcpln		No Data	No Data	2510	1.88	1.28	837	4010	837
	Tpcplnc		No Data	No Data	No Data	No Data	No Data	No Data	No Data	No Data
PTn	Tpcpv	3	Tcpv3	0.0	2470	0.98	0.54	857	4570	857
		2	Tcpv2	5.49						
	Tpcpv1		Tcpv1	4.69	2380	1.07	0.50	1037	6048	1037
	Tpbt4		Tcbt4	0.53	2340	0.5	0.35	1077	21976	1077
	Tpy		Yucca	7.05	2400	0.97	0.44	849	16172	849
	Tpbt3		Tcbt3_dc	4.58	2370	1.02	0.46	1016	20669	1016
	Tpp		Pah	14.09	2260	0.82	0.35	1330	25560	1330
	Tpbt2		Tpbt2	9.69	2370	0.67	0.23	1224	23878	1224
	Tptrv3		Tptrv3	4.58	2510	1.00	0.37	834	5137	834
	Tptrv2		Tptrv2	0.53						
TSw1	Tptrv1		Tptrv1	1.06						
	Tptrn		Tptrn	46.85	2550	1.62	1.06	866	5629	866
	Tptrl		Tptrl	8.98	2510	1.58	0.89	882	5693	882
	Tptpul		Tptpul	77.68	2510	1.80	0.71	883	5694	883
TSw2	Tptpmn		Tptpmn	29.94	2530	2.33	1.56	948	4568	948
	Tptpll		Tptpll	106.21	2540	2.02	1.20	900	4663	900
	Tptpln		Tptpln	47.73	2560	1.84	1.42	865	4523	865
TSw3	Tptpv3		Tptpv3	20.61	2360	2.08	1.69	984	1958	984
CHn1	Tptpv2		Tptpv2	2.99						
	Tptpv1		Tptpv1	11.27						
	Tpbt1		Tpbt1	3.35	2310	1.31	0.7	1057	21076	1057
	Tac5	Tac(v)	Calico	84.37	2240	1.17	0.58	1201	23863	1201
	Tac4									
	Tac3									
	Tac2	Tac(z)			2350	1.2	0.61	1154	22086	1154
	Tac1									
CHn2	Tacbt				2440	1.35	0.73	1174	13561	1174

DTN: SN0003T0571897.013

4.1.4 Hydrologic and Thermal Properties of NUFT l4c4 Stratigraphic Units

Each NUFT l4c4 stratigraphic unit has two sets of properties, one for its matrix and another for its fractures. The matrix properties are permeability, porosity, Van Genuchten α parameter, Van Genuchten β parameter, residual saturation, and satiated saturation. The fracture parameters include the six categories used for the matrix of the rock (although the values for the fractures are different) and 3 additional parameters: active fracture parameter, fracture frequency, and fracture to matrix area. The thermal properties include grain density, grain specific heat, wet thermal conductivity, and dry thermal conductivity.

The matrix properties, fracture properties, and thermal properties corresponding to the base case infiltration flux are given in the file 1d-driftscale_basecase.xls (DTN: LB990861233129.001). The base case matrix properties are reproduced in Table 4-3. The base case fracture properties are reproduced in Table 4-4. Thermal properties are reproduced in Table 4-5. The tortuosity factor is 0.7 (BSC 2001).

As noted earlier in Section 4.1.3, the ANSYS models treat the grain density as the bulk density (i.e. no accounting is taken of the porosity of the specific geologic unit). However, NUFT internally calculates the bulk density of the medium given the grain density and the porosity. In addition, the grain density is apportioned by the method described in Section 5.13 to account for the dual permeability active fracture method. Therefore, a one-to-one comparison between the ANSYS-based and MULTIFLUX/NUFT-based models is achieved by first apportioning grain density between the matrix and the fracture, and then using the porosity to calculate a bulk density equal to that used in the ANSYS-based model. Note the results of this calculation are grain densities, which are used in the MULTIFLUX/NUFT model, that are not the same as those listed in Table 4-5. The opposite approach is more correct (i.e. calculating a bulk grain density for the ANSYS models rather than using grain density in Table 4-2). However, since the purpose is simply to compare the results of the different numerical models, the approach is sufficient. The following equations were derived to calculate ANSYS equivalent bulk densities for use in the MULTIFLUX/NUFT models:

$$\rho_{m-equivalent} = \frac{\rho_{grain} \cdot (1 - \phi_f)}{1 - \phi_m} \qquad \text{Eq. 4-1}$$

$$\rho_{f-equivalent} = \frac{\rho_{grain} \cdot \phi_f}{1 - \phi_f} \qquad \text{Eq. 4-2}$$

where

$\rho_{m\text{-}equivalent}$ = equivalent matrix density (kg/m^3)
$\rho_{f\text{-}equivalent}$ = equivalent fracture density (kg/m^3)
ρ_{grain} = grain density (kg/m^3)
ϕ_m = matrix porosity (dimensionless)

ϕ_f = fracture porosity (dimensionless)

Table 4-3. Matrix Properties of Stratigraphic Units

Unit	Permeability (m^2)	Porosity (Fraction)	Van Genuchten α (Pa^{-1})	Van Genuchten m (λ)	Residual Saturation (Fraction)	Satiated Saturation (Fraction)
tcw11	3.86E-15	0.253	4.00E-05	0.47	0.07	1
tcw12	2.74E-19	0.082	1.81E-05	0.241	0.19	1
tcw13	9.23E-17	0.203	3.44E-06	0.398	0.31	1
ptn21	9.90E-13	0.387	1.01E-05	0.176	0.23	1
ptn22	2.65E-12	0.439	1.60E-04	0.326	0.16	1
ptn23	1.23E-13	0.254	5.58E-06	0.397	0.08	1
ptn24	7.86E-14	0.411	1.53E-04	0.225	0.14	1
ptn25	7.00E-14	0.499	5.27E-05	0.323	0.06	1
ptn26	2.21E-13	0.492	2.49E-04	0.285	0.05	1
tsw31	6.32E-17	0.053	3.61E-05	0.303	0.22	1
tsw32	5.83E-16	0.157	3.61E-05	0.333	0.07	1
tsw33	3.08E-17	0.154	2.13E-05	0.298	0.12	1
tsw34	4.07E-18	0.11	3.86E-06	0.291	0.19	1
tsw35	3.04E-17	0.131	6.44E-06	0.236	0.12	1
tsw36	5.71E-18	0.112	3.55E-06	0.38	0.18	1
tsw37	4.49E-18	0.094	5.33E-06	0.425	0.25	1
tsw38	4.53E-18	0.037	6.94E-06	0.324	0.44	1
tsw39	5.46E-17	0.173	2.29E-05	0.38	0.29	1
ch1z	1.96E-19	0.288	2.68E-07	0.316	0.33	1
ch1v	9.90E-13	0.273	1.43E-05	0.35	0.03	1
ch2v	9.27E-14	0.345	5.13E-05	0.299	0.07	1
ch3v	9.27E-14	0.345	5.13E-05	0.299	0.07	1
ch4v	9.27E-14	0.345	5.13E-05	0.299	0.07	1
ch5v	9.27E-14	0.345	5.13E-05	0.299	0.07	1
ch2z	6.07E-18	0.331	3.47E-06	0.244	0.28	1
ch3z	6.07E-18	0.331	3.47E-06	0.244	0.28	1
ch4z	6.07E-18	0.331	3.47E-06	0.244	0.28	1
ch5z	6.07E-18	0.331	3.47E-06	0.244	0.28	1
ch6	4.23E-19	0.266	3.38E-07	0.51	0.37	1
pp4	4.28E-18	0.325	1.51E-07	0.676	0.28	1
pp3	2.56E-14	0.303	2.60E-05	0.363	0.1	1
pp2	1.57E-16	0.263	2.67E-06	0.369	0.18	1
pp1	6.40E-17	0.28	1.14E-06	0.409	0.3	1
bf3	2.34E-14	0.115	4.48E-06	0.481	0.11	1
bf2	2.51E-17	0.259	1.54E-07	0.569	0.18	1

DTN: LB990861233129.001

Table 4-4. Fracture Properties of Stratigraphic Units

Unit	Permeability	Porosity	Van Genuchten α	Van Genuchten m (λ)	Residual Saturation	Satiated Saturation	Active Fracture Parameter	Frequency	Fracture to matrix area
	(m2)		(Pa-1)		(Fraction)	(Fraction)		(1/m)	(m2/m3)
tcw11	2.41E-12	0.028	3.15E-03	0.627	0.01	1	0.30	0.92	1.56
tcw12	1.00E-10	0.02	2.13E-03	0.613	0.01	1	0.30	1.91	13.39
tcw13	5.42E-12	0.015	1.26E-03	0.607	0.01	1	0.30	2.79	3.77
ptn21	1.86E-12	0.011	1.68E-03	0.58	0.01	1	0.09	0.67	1.00
ptn22	2.00E-11	0.012	7.68E-04	0.58	0.01	1	0.09	0.46	1.41
ptn23	2.60E-13	0.0025	9.23E-04	0.61	0.01	1	0.09	0.57	1.75
ptn24	4.67E-13	0.012	3.37E-03	0.623	0.01	1	0.09	0.46	0.34
ptn25	7.03E-13	0.0062	6.33E-04	0.644	0.01	1	0.09	0.52	1.09
ptn26	4.44E-13	0.0036	2.79E-04	0.552	0.01	1	0.09	0.97	3.56
tsw31	3.21E-11	0.0055	2.49E-04	0.566	0.01	1	0.06	2.17	3.86
tsw32	1.26E-12	0.0095	1.27E-03	0.608	0.01	1	0.41	1.12	3.21
tsw33	5.50E-13	0.0066	1.46E-03	0.608	0.01	1	0.41	0.81	4.44
tsw34	2.76E-13	0.01	5.16E-04	0.608	0.01	1	0.41	4.32	13.54
tsw35	1.29E-12	0.011	7.39E-04	0.611	0.01	1	0.41	3.16	9.68
tsw36	9.91E-13	0.015	7.84E-04	0.61	0.01	1	0.41	4.02	12.31
tsw37	9.91E-13	0.015	7.84E-04	0.61	0.01	1	0.41	4.02	12.31
tsw38	5.92E-13	0.012	4.87E-04	0.612	0.01	1	0.41	4.36	13.34
tsw39	4.57E-13	0.0046	9.63E-04	0.634	0.01	1	0.41	0.96	2.95
ch1z	3.40E-13	0.00017	1.43E-03	0.631	0.01	1	0.10	0.04	0.11
ch1v	1.84E-12	0.00069	1.09E-03	0.624	0.01	1	0.13	0.10	0.30
ch2v	2.89E-13	0.00089	5.18E-04	0.628	0.01	1	0.13	0.14	0.43
ch3v	2.89E-13	0.00089	5.18E-04	0.628	0.01	1	0.13	0.14	0.43
ch4v	2.89E-13	0.00089	5.18E-04	0.628	0.01	1	0.13	0.14	0.43
ch5v	2.89E-13	0.00089	5.18E-04	0.628	0.01	1	0.13	0.14	0.43
ch2z	3.12E-14	0.00043	4.88E-04	0.598	0.01	1	0.10	0.14	0.43
ch3z	3.12E-14	0.00043	4.88E-04	0.598	0.01	1	0.10	0.14	0.43
ch4z	3.12E-14	0.00043	4.88E-04	0.598	0.01	1	0.10	0.14	0.43
ch5z	3.12E-14	0.00043	4.88E-04	0.598	0.01	1	0.10	0.14	0.43
ch6	1.67E-14	0.00017	7.49E-04	0.604	0.01	1	0.10	0.04	0.11
pp4	3.84E-14	0.00043	5.72E-04	0.627	0.01	1	0.10	0.14	0.43
pp3	7.60E-12	0.0011	8.73E-04	0.655	0.01	1	0.46	0.20	0.61
pp2	1.38E-13	0.0011	1.21E-03	0.606	0.01	1	0.46	0.20	0.61
pp1	1.12E-13	0.00043	5.33E-04	0.622	0.01	1	0.10	0.14	0.43
bf3	4.08E-13	0.0011	9.95E-04	0.624	0.01	1	0.46	0.20	0.61
bf2	1.30E-14	0.00043	5.42E-04	0.608	0.01	1	0.10	0.14	0.43

DTN: LB990861233129.001

Table 4-5. Thermal Properties of Stratigraphic Units

Model Layer	Rock Grain Density	Rock Grain Specific	Dry Conductivity	Wet Conductivity
	Kg/m3	Heat (J/Kg K)	W/m K	W/m K
tcw11	2550	823	1.6	2
tcw12	2510	851	1.24	1.81
tcw13	2470	857	0.54	0.98
ptn21	2380	1040	0.5	1.07
ptn22	2340	1080	0.35	0.5
ptn23	2400	849	0.44	0.97
ptn24	2370	1020	0.46	1.02
ptn25	2260	1330	0.35	0.82
ptn26	2370	1220	0.23	0.67
tsw31	2510	834	0.37	1
tsw32	2550	866	1.06	1.62
tsw33	2510	882	0.79	1.68
tsw34	2530	948	1.56	2.33
tsw35	2540	900	1.2	2.02
tsw36	2560	865	1.42	1.84
tsw37	2560	865	1.42	1.84
tsw38	2360	984	1.69	2.08
tsw39	2360	984	1.69	2.08
ch1z	2310	1060	0.7	1.31
ch1v	2310	1060	0.7	1.31
ch2v	2240	1200	0.58	1.17
ch3v	2240	1200	0.58	1.17
ch4v	2240	1200	0.58	1.17
ch5v	2240	1200	0.58	1.17
ch2z	2350	1150	0.61	1.2
ch3z	2350	1150	0.61	1.2
ch4z	2350	1150	0.61	1.2
ch5z	2350	1150	0.61	1.2
ch6	2440	1170	0.73	1.35
pp4	2410	577	0.62	1.21
pp3	2580	841	0.66	1.26
pp2	2580	841	0.66	1.26
pp1	2470	635	0.72	1.33
bf3	2570	763	1.41	1.83
bf2	2410	633	0.74	1.36

DTN: LB990861233129.001

The inputs listed in Tables 4-3 and 4-4 are used in the MULTIFULX-Full model. The thermal inputs listed in Table 4-5 are used for all ANSYS and MULTIFLUX calculations of Section 6 as well as the submodel verification exercises of Section 6.5.

4.1.5 Infiltration Flux

The infiltration flux for the preclosure ventilation period at the repository location identified by chimney l4c4 is 10.13 mm/yr (DTN: GS000308311221.005, modern day, mean infiltration value). This input is used in the MULTIFLUX-Full model.

4.1.6 Atmospheric Pressure

At the average elevation of the repository horizon, 1072.3m (Section 4.1.3), the barometric pressure is 89,060 Pa (Hartman 1982). This input is used for all ANSYS and MULTIFLUX calculations of Section 6 as well as the submodel verification exercises of Section 6.5.

4.1.7 Stefan-Boltzmann Constant

The Stefan-Boltzmann constant for radiative heat transfer calculations is 5.669×10^{-8} $W/m^2 \cdot K^4$ (Icropera and DeWitt 1996). This input is used throughout for all radiative heat transfer calculations of Section 6 as well as the submodel verification exercises involving radiation of Section 6.5.

4.1.8 Waste Package Thermal Properties

The thermal properties for the waste package outer shell are listed in Table 4-6. These values are for Alloy 22 material based on *Thermal Calculation of the Waste Package with Backfill* (CRWMS M&O 1999c). This input is used for all ANSYS and MULTIFLUX calculations of Section 6 as well as the submodel verification exercises of Section 6.5.

Table 4-6. Thermal Properties for Waste Package

Parameter	Value
Density (kg/m^3)	8690
Thermal Conductivity (W/m·K)	12.52[a]
Specific Heat (J/kg·K)	435.25[b]
Emissivity	0.87

Note: [a] Averaged value over the temperature range of 48 to 300°C.
[b] Averaged value over the temperature range of 52 to 300°C.

4.1.9 Emplacement Drift Spacing

The emplacement drift spacing is 81 meters centerline to centerline from the *Emplacement Drift System Description Document* (CRWMS M&O 2000b). This information is used for establishing adiabatic boundary conditions for all ANSYS and MULTIFLUX calculations of Section 6 as well as the submodel verification exercises of Section 6.5.

4.1.10 Waste Package Spacing

The waste packages are spaced 10 cm apart from the *Emplacement Drift System Description Document* (CRWMS M&O 2000b). This input is used for all ANSYS and MULTIFLUX calculations of Section 6.

4.1.11 Emplacement Drift Diameter

The diameter of the waste emplacement drifts is 5.5 m from the *Emplacement Drift System Description Document* (CRWMS M&O 2000b). This input is used for all ANSYS and

MULTIFLUX calculations of Section 6 as well as the submodel verification exercises of Section 6.5.

4.1.12 Ventilation Air Properties

The properties of the ventilation air are listed in Table 4-7. The values of density, dynamic viscosity, thermal conductivity, and specific heat are based on an intake air temperature of 25°C (Section 5.8) and an atmospheric pressure of 89,060 Pa (Section 4.1.6). The other properties listed in Table 4-7 are derived using the following equations.

$$\upsilon = \frac{\mu}{\rho} \qquad \text{Eq. 4-3}$$

$$\alpha = \frac{k}{\rho c_p} \qquad \text{Eq. 4-4}$$

$$Pr = \frac{\upsilon}{\alpha} \qquad \text{Eq. 4.5}$$

where

υ = kinematic viscosity (m^2/s)
μ = dynamic viscosity (kg/m·s)
ρ = density (kg/m^3)
α = thermal diffusivity (m^2/s)
k = thermal conductivity (W/m·K)
c_p = specific heat (J/kg·K)
Pr = Prandtl number (dimensionless)

The air properties and parameters in Table 4-7 are held constant throughout the length of the emplacement drifts during the entire ventilation period. This information is used for all ANSYS and MULTIFLUX calculations of Section 6.

Table 4-7. Property Values for Ventilation Air

Parameter	Value	Source
Density, ρ (kg/m^3)	1.0561	CRWMS M&O 1998a
Dynamic Viscosity, υ (kg/m·s)	1.8371×10^{-5}	Holman 1997, linear interpolation
Thermal Conductivity, k (W/m·K)	0.0261	Holman 1997, linear interpolation
Specific Heat, c_p (J/kg·K)	1005.7	Holman 1997, linear interpolation
Kinematic Viscosity, μ (m^2/s)	1.7395×10^{-5}	Eq. 4-3 (Daugherty et al. 1965)
Thermal Diffusivity, α (m^2/s)	2.4573×10^{-5}	Eq. 4-4 (Incropera and DeWitt 1996)
Prandtl Number, Pr (dimensionless)	0.7079	Eq. 4.5 (Incropera and DeWitt 1996)

4.1.13 Thermal Conductivity of Air at the Ground Surface Model Boundary

The thermal conductivity of air at 16°C (ground surface) is 0.0254 W/m·K (Holman 1997). This input is used in Section 6 to determine the thermal gradient from the ground surface to the water table for all the ventilation models.

4.1.14 Waste Package Lengths, Diameters, Quantities, Sequence, Spacings, and Initial Heat Generation Rates

The lengths, diameters, quantities, and initial heat generation rates for the waste packages are listed in Table 4-8, and are based on *Enhanced Design Alternative (EDA) II Repository Estimated Waste Package Types and Quantities* (CRWMS M&O 1999d). This information is used in Attachment I and II to compute a repository average heat decay curve for the ANSYS and MULTIFLUX models of Section 6. The waste packages are placed end-to-end with a 0.1 m spacing in the following sequence (CRWMS M&O 2000b): The waste package segment shown below is mirrored down the entire length of the drift:

½ DHLW, 44 BWR, 21 PWR, DHLW, 21 PWR, 44 BWR, 21 PWR, ½ DSNF

where

DHLW = DOE high level waste package
BWR = boiling water reactor waste package
PWR = pressurized water reactor waste package
DSNF = defense spend nuclear fuel waste package

Table 4-8. Number and Initial Heat Generation Rates for Average CSNF and DHLW Waste Packages

Waste Package Type		Length of Waste Packages (m)	Diameter of Waste Packages (m)	Number of Waste Packages	Initial Heat Generation Rate (kW/package)
21-PWR	Absorber Plates	5.305	1.564	4,279	11.3337
	Control Rode	5.305	1.564	87	2.3709
12-PWR	Long	5.791	1.250	158	9.5402
44-BWR	Absorber Plates	5.275	1.594	2,889	7.1346
24-BWR	Thick Plates	5.245	1.238	6	0.4910
5-DHLW	Short	3.73	2.030	1,249	4.0580
5-DHLW	Long	5.357	2.030	414	5.8280[a]
Navy (DSNF)	Combined	5.888	1.869	285	7.1350[b]
DOE/Other		5.57	No Data	598	0.7930

Note: [a] Estimated value by assuming that the initial heat generation rates for 5-DHLWs, short and long, are linearly proportional to their lengths (4.058kW×5.357m/3.73m=5.828kW)
[b] Averaged value equal to that of 44-BWR

4.1.15 Waste Package Thermal Decay

The decay characteristics of the commercial spent nuclear fuel (CSNF) waste packages are listed in Table 4-9 (CRWMS M&O 1999d). These values are used in Attachment II to calculate a repository average thermal decay curve that is used in the all the numerical ventilation models of Section 6.

Table 4-9. Time-dependent Heat Generation Rates for Average CSNF Waste Packages

Time (years)	21-PWR Absorber Plates (kW/package)	21-PWR Control Rods (kW/package)	12-PWR Long (kW/package)	44-BWR Absorber Plates (kW/package)	24-BWR Thick Absorber Plates (kW/package)
0.01	11.3337	2.3709	9.5402	7.1346	0.4910
1	10.9954	2.3285	9.2722	6.9146	0.4829
5	9.9653	2.1785	8.4286	6.2682	0.4445
10	8.9956	2.0095	7.5901	5.6536	0.4030
15	8.1887	1.8547	6.8815	5.1467	0.3689
20	7.5138	1.7241	6.3149	4.7102	0.3341
25	6.9115	1.6038	5.8009	4.3098	0.3065
30	6.3792	1.4942	5.3407	3.9701	0.2806
40	5.4984	1.3106	4.5868	3.3915	0.2369
50	4.7912	1.1649	3.9792	2.9326	0.2033
60	4.2229	1.0443	3.5026	2.5621	0.1754
70	3.7685	0.9479	3.1031	2.2625	0.1536
80	3.3915	0.8698	2.7908	2.0227	0.1361
90	3.0866	0.8070	2.5304	1.8264	0.1222
100	2.8314	0.7545	2.3024	1.6685	0.1111
150	2.0790	0.5983	1.6766	1.1977	0.0799
200	1.7291	0.5244	1.3818	0.9878	0.0684
250	1.5128	0.4796	1.2029	0.8725	0.0622
300	1.3654	0.4452	1.0804	0.7889	0.0583

4.2 DATA AND PARAMETERS FOR THE POST-TEST ANSYS-BASED MODEL OF THE VENTILATION TEST PHASE 1

This section describes the data and parameters, and their sources, used to develop, numerically apply, and validate the post-test ANSYS-based model of the Ventilation Test Phase 1.

4.2.1 Physical and Thermal Properties for Simulated Waste Package

The physical and thermal properties used in the calculation for the simulated waste package and heating rod are listed in Table 4-10. These values are for carbon steel material. The values of density, thermal conductivity, and specific heat are the averages over a temperature range of 20°C to 50°C measured for the corresponding parameters (Stroe 2001). The emissivity value is obtained based on the *Heat Transfer* for sheet steel (Holman 1997).

According to the *Conceptual Arrangement Simulated Emplacement Ventilation Test* (CRWMS M&O 2000c), the designed diameter of the waste package pipe is 0.4064 m (16 in).

Table 4-10. Physical and Thermal Properties for Simulated Waste Package

Parameter	Value
Density (kg/m^3)	7840[a]
Thermal Conductivity (W/m·K)	38.37[a]
Specific Heat (J/kg·K)	410.98[a]
Emissivity	0.8[b]

Note: [a] Stroe 2001, p.3. Averaged over a temperature range of 20 to 50°C.
[b] Holman 1997, Table A-10, p. 651 for sheet steel.

4.2.2 Physical and Thermal Properties for Concrete Pipe

The physical and thermal properties for the concrete pipe used in the calculation are listed in Table 4-11. The values of density, thermal conductivity, and specific heat are the averages over a temperature range of 20°C to 50°C measured for the corresponding parameters (Stroe 2001).

The designed inner and outer diameters of the concrete pipe are 1.3716 m (54 in.) and 1.651 m (65 in.), respectively (CRWMS M&O 2000c).

Table 4-11. Physical and Thermal Properties for Concrete Pipe

Parameter	Value
Density (kg/m^3)	2280[a]
Thermal Conductivity (W/m·K)	2.75[a]
Specific Heat (J/kg·K)	1016.16[a]
Emissivity	0.93[b]

Note: [a] Stroe 2001, p.3. Averaged over a temperature range of 20 to 50°C.
[b] Incropera and DeWitt 1996, Table A.11.

4.2.3 Physical and Thermal Properties for Insulating Material

The physical and thermal properties for the insulating material (fiber glass) used in the calculation are listed in Table 4-12. The density and thermal conductivity are obtained from the *Standard Fiber Glass Duct Wrap* provided by the manufacturer (CertainTeed 1996). The other thermal property values are obtained based on the *Heat Transfer* (Holman 1997) and the *Fundamentals of Heat and Mass Transfer* (Incropera and DeWitt 1996). The designed thickness of the insulation is 0.0508 m (2 in.) (CRWMS M&O 2000c).

Table 4-12. Physical and Thermal Properties for Insulating Material

Parameter	Value
Density (kg/m^3)	12[a]
Thermal Conductivity (W/m·K)	0.04[a]
Specific Heat (J/kg·K)	700[b]
Emissivity	0.96[c]

Note: [a] CertainTeed 1996.
[b] Holman 1997, Table A-3.
[c] Incropera and DeWitt 1996, Table A.11, selected from a range of 0.93 to 0.96 for asbestos sheet.

4.2.4 Physical and Thermal Properties for Invert Material

The physical and thermal properties for the invert material (fine crushed tuff) used in the calculation are listed in Table 4-13. The density, thermal conductivity, and specific heat values based on the *Thermal and Physical Properties of Granular Materials* (CRWMS M&O 2000d). The emissivity is obtained based on the *Fundamentals of Heat and Mass Transfer* (Incropera and DeWitt 1996).

Table 4-13. Physical and Thermal Properties for Invert Material

Parameter	Value
Density (kg/m^3)	2530[a]
Thermal Conductivity (W/m·K)	0.14[b]
Specific Heat (J/kg·K)	363[b]
Emissivity	0.93[c]

Note: [a] CRWMS M&O 2000d, Table 4, mean value for fine crushed tuff.
[b] CRWMS M&O 2000d, Table 6, mean value for fine crushed tuff.
[c] Incropera and DeWitt 1996, Table A.11, selected from a range of 0.93 to 0.96 for red brick.

4.2.4 Ventilation Test Flow Rates, Heat Loads, and Measured Data

The various cases of the Phase 1 Ventilation Test, and ventilation flow rates and heat loads used for the Post-Test ANSYS model are listed in Table 4-14 and were obtained from the *Development Plan for Ventilation Test* (CRWMS 2000g). The measured data from the test were used for input parameters and boundary conditions, as well for comparison to the ANSYS model results (Section 7.1.2)

Table 4-14. Ventilation Phase 1 Test Matrix

Test No.	Case No.	Nominal Flow (m^3/s)	Nominal Power (kW/m)
1	4	1	0.18
2	5	0.5	0.18
3	1	1	0.36
4	5	2	0.36
5	3	0.5	0.36
6	6	3	0.36

4.3 CRITERIA

No design criteria were used in the model report. The model setup and inputs used in this report were numerical examples for model validation purposes only. No design analysis was performed in this document.

4.4 CODES AND STANDARDS

Not used.

5. ASSUMPTIONS

All assumptions in this model report are used solely as numerical examples for comparisons of outputs from models for model corroboration or validation purposes only. Each assumption treated as model input is appropriately used. No design analysis or parameters were generated based on the assumptions. Therefore, the assumptions listed in this section do not require confirmation.

5.1 REPRESENTATIVE REPOSITORY LOCATION

Northing 170,750 and easting 233,760 were chosen as a representative repository location in terms of distance from an edge, geology and infiltration rate. It is from this location that the hydrologic and thermal properties for the stratigraphic units (Section 4.1.4) are taken.

5.2 REPRESENTATIVE WASTE PACKAGE DIAMETER

For the purposes of this Model Report, it is assumed that all waste packages have the same diameter. The diameter used in all calculations is that of the 21-PWR waste packages, or 1.564 m (Table 4-8). This assumption is based on the waste stream, where the greatest quantity of waste packages is comprised of 21-PWRs. This information is used throughout Sections 6 and 7.

5.3 WASTE PACKAGE MASS

The masses of individual waste packages were calculated using the waste package outer shell density of 8690 kg/m^3 (Section 4.1.8), a waste package diameter of 1.564 m (Section 5.2), and the waste package lengths from Table 4.8 (Section 4.1.14). For example, the mass of a 21-PWR is calculated as: (8690 kg/m^3)×(5.305 m)×(π/4×(1.564 m)^2) = 88,566 kg. The masses of other waste packages are calculated in the same way and are listed below:

Table 5-1. Waste Package Mass

WP Type	Mass (kg)
21-PWR	88566
44-BWR	88065
HLW	62272
DSNF	98299

This information is used as input for the MULTIFLUX models. To accommodate the MULTIFLUX axial discretization scheme, the mass of each WP is inputted as two identical half-waste packages.

5.4 THE DRIFT WALL LINER FOR THE MULTIFLUX MODEL

The MULTIFLUX code was developed with the capability of specifying a drift-wall-liner for ground support material as input. Since no liner material is considered in this report, the inputs for wall liner are specified to be the same as those of the host rock at the repository horizon. Because the liner and rock are simulated as the same material, the thickness of the liner can be arbitrary. Hence, a thickness of 0.01m is used in the MULTIFLUX models. The liner is

assumed to be transparent to moisture transport in MULTIFLUX, however, an "artificial" moisture resistance, Rv, is assigned to the liner proportional to its thickness. This Rv resistance, as well as the partial vapor pressure drop, dp, across the Rv are both used in the balancing iteration of the MULTFLUX numerical process. Upon convergence of the iteration, the dp pressure drop becomes close to zero irrespective of the "artificial" value of Rv. The value of Rv, which is modified by a user defined multiplier, rgvf, does not affect the moisture balance or the partial vapor pressure distribution. However, if the Rv is too small due to a minute liner thickness, the iteration convergence may become too slow. The user-defined multiplier of rgvf = 50 was found to be a reasonable value for the current liner thickness based on observing the run-time convergence speed and maximum numbers of the moisture transport iteration cycles. This information is used to prepare the MULTIFLUX input files.

5.5 CONCENTRIC WASTE PACKAGE EMPLACEMENT WITHIN THE DRIFT

For the ANSYS and MULTIFLUX models, the waste packages are suspended in the center of the emplacement drift. This is a limitation of the MULTIFLUX V2.2 software code. For comparison purposes, the ANSYS models also used a concentrically located package. As such, no invert or ground support systems are present to participate in the heat and mass transfer processes. Ground support systems would tend to facilitate additional heat removal from the waste package, via conduction through the supports to the host rock. Although conservative in nature, the impact of this assumption on the output of the Ventilation Model (i.e. wall heat fractions) is considered minimal. This assumption is used throughout the document.

5.6 EMPLACEMENT DRIFT LENGTH

For the preclosure ventilation calculations, the drift length from the air inlet of emplacement drift to the central exhaust main is assumed to be 600 m. The basis for this assumption comes from *Subsurface Facility System Description Document* (CRWMS M&O 2000a) where the maximum emplacement drift split is specified to be 600 m, and any emplacement length in excess of 600 m will be assumed to be unusable space. This information is used throughout the document.

5.7 PRECLOSURE VENTILATION RATE

The preclosure ventilation calculations were performed using an airflow rate of 15 m^3/s based on the assumption that at that rate, at least 70% of the heat generated by the waste packages can be removed. The 70% removal guidance comes from *Subsurface Ventilation System Description Document* (CRWMS M&O 2000e). This ventilation flow rate is used throughout the document.

5.8 AIRFLOW TEMPERATURE AT THE DRIFT ENTRANCE

The temperature of the intake airflow at the emplacement drift inlet is assumed to be 25°C based on *Repository Subsurface Waste Emplacement and Thermal Management Strategy* (CRWMS 1998a). This temperature is also assumed constant during the entire preclosure ventilation period. This assumption is used throughout the document.

5.9 ROCK PROPERTIES FOR OVERBURDEN ABOVE Tpcpv2 UNIT

As shown in Table 4-2, the rock properties for the overburden above the Tpcpv2 unit are incomplete. This is due to the lack of thickness data for individual units within the overburden. The rock properties for the each unit within the overburden are assumed to the same as those of Tpcpv2 because of proximity.

5.10 RELATIVE HUMIDITY AND VAPOR PRESSURE OF AIR AT THE DRIFT ENTRANCE

The relative humidity of the ventilation air for the ANSYS and MULTIFLUX-Con models is zero. This is limitation of the ANSYS software codes. The relative humidity of the ventilation air at the drift inlet is assumed to be 30% for the MULTIFLUX-Full model based on the *Overall Development and Emplacement Ventilation Systems* (CRWMS M&O 1997) which reports values between 20 to 40%.

The vapor pressure at a given RH and intake air temperature can be calculated by multiplying the RH by the saturation vapor pressure (Hartman 1982):

$$P_v = \phi \cdot 0.6105 e^{\left(\frac{17.27 \cdot T}{237.3+T}\right)} \qquad \text{Eq. 5-1}$$

where

P_v = vapor pressure (kPa)
ϕ = relative humidity (dimensionless)
T = temperature (°C)

Based on the assumption of 30% relative humidity for the intake ventilation air, and an inlet air temperature of 25° C, the saturation vapor pressure is calculated from Equation 5-1 to be 3.16662 kPa and the vapor pressure to be 0.950 kPa.

5.11 HEAT OUTPUT FOR DHLW AND NAVY FUEL

The heat output data for the Naval and DHLW packages are not available. Therefore, the initial heat output of the Naval package is assumed to be the same as that of 44BWR, 7.1346 kW (Table 4-8). The heat decay curves for the Naval and DHLW packages are assumed to be the same as the CSNF. The rationale for this assumption is that the Naval and DHLW packages comprise a small portion of the total waste-stream such that uncertainties in this assumption will have no significant impact on the overall lineal heat load calculated in Attachment I.

5.12 HOST ROCK EMISSIVITY

An emissivity of 0.9 for the Tptpll unit where the majority of emplacement drifts will be located was used based on *Fundamentals of Heat and Mass Transfer* (Incropera and DeWitt 1996).

5.13 THERMAL CONDUCTIVITY AND DENSITY FOR THE ACTIVE FRACTURE MODEL

As indicated in Section 4.1.2, the NUFT Active Fracture Method requires apportioning of certain material, hydrologic, and thermal properties listed in Table 4-2. Certain properties, such as grain density and thermal conductivity, are apportioned as follows:

fracture property = total property x (fracture porosity)
matrix property = total property x (1 - fracture porosity)

For example, the ANSYS unit Tptpll is equivalent to the NUFT l4c4 unit Tsw35. From Table 4-2, the wet thermal conductivity of Tptpll is 2.02 W/m·K. From Table 4-4, the fracture porosity is 0.011. It follows then that the thermal conductivity for the Tptpll or Tsw35 fracture continuum is 0.0222 W/m·K, and the for the matrix continuum 1.998 W/m·K. The same process is repeated for apportioning the grain density.

The rationale for this is that there is no commonly accepted approach to apportioning fracture and matrix conductivity and density. However, it is important to note that the total value of conductivity and the total value of density are conserved. Therefore, the total conductive heat flow is the same as a single continuum with the same total value of thermal conductivity. Similarly, during the transient (heat-up) period, the correct mass density of the rock mass is honored. This assumption has no impact on the model.

5.14 WASTE PACKAGE INITIAL SURFACE TEMPRATURE

The initial temperature on the waste package surface at the time of emplacement is assumed to be 70°C. This assumption is based on the average of the initial temperatures of the waste package surfaces as calculated from *Multiple WP Emplacement Thermal Response -Suite 1* (CRWMS M&O 1998b).

6. MODEL DISCUSSION

During the preclosure period, the rate of heat generation by the waste package in the emplacement drifts is at its peak. Ventilation of the drifts can remove a portion of the thermal energy generated during the preclosure period by spent fuel as well as the moisture mobilized from the surrounding rock mass. The net effect of emplacement drift ventilation is to delay the onset of the peak waste package and drift wall temperatures as well as to decrease their magnitude.

The thermal energy removed by ventilation must be determined by analyzing, at the least, thermal radiation, thermal convection, and thermal conduction which occur simultaneously in the drift and the surrounding rock mass. The following sections provide:

1. An explanation of the conceptual model of the heat transfer mechanisms for ventilated emplacement drifts.
2. A discussion of the numerical application of the conceptual model using the ANSYS and MULTIFLUX software codes, and presentation of the results in terms of temperatures and ventilation heat removal rates.
3. A presentation of an alternative conceptual model which considers the coupled effects of water phase change, mass transport, and heat transfer on the effectiveness of ventilation to remove heat from waste emplacement drifts.
4. A comparison of the numerical model results and energy balance closures that provide verification that these numerical techniques are applied properly to the conceptual model.
5. Further model verification using comparative submodels, and where applicable analytical solutions, which isolate the coupled heat transfer processes into individual phenomena.
6. A discussion of the applicability of the wall heat fraction (1 - heat removal) as computed by the numerical ventilation models to initialize downstream post-closure thermal-hydrologic models.

6.1 CONCEPTUAL MODEL FOR IN-DRIFT VENTILATION

When air is directed into an emplacement drift, thermal energy released from the waste packages is transferred to the in-drift and host rock surroundings. The heat transfer processes vary with time and with axial position (i.e. the distance down the length of the drift from the airflow entrance point).

6.1.1 Heat Transfer Processes

The heat transfer processes for ventilation of emplacement drifts are outlined below and shown in Figure 6-1. Figure 6-1 also includes other heat and mass transfer processes that will be outlined later in Section 6.3 when the alternate conceptual model for ventilation is presented.

1. Thermal radiation transfers heat from the surface of the waste package to the drift wall. The rate at which the heat is transferred can be calculated using the Stefan-Boltzmann Law for gray surface radiation exchange at any time during the preclosure period, using

the waste package surface and drift wall temperatures. This calculation also requires knowledge of the geometry and emissivities of the waste package and drift wall surfaces.

2. Convection transfers heat from the surface of the waste package to the airflow, due to the temperature differences between the surface and the moving air. The heat flow rate can be calculated using Newton's Cooling Law at any time during the preclosure period, using the bulk temperature of the airflow and the temperature of the waste package surface. This calculation also requires knowledge of the convective heat transfer coefficients that implicitly describe the effects of the airflow, the drift geometry, and surface properties on the heat transfer rates.

3. Convection transfers heat from the drift wall surface directly to the airflow, due to the temperature differences between the wall surface and the moving air, similar to process (2). The sum of the two convective heat transfer rates determines the rate of energy addition to the moving air, and can be used to calculate the axial rate of air temperature increase. This calculation also requires knowledge of the convective heat transfer coefficients that implicitly describe the effects of the airflow, the drift geometry, and surface properties on the heat transfer rates. Axially along the drift, the convection heat transfer (processes 2 and 3) can be combined with the air mass flow rate and its specific heat, to calculate the axial change of air temperature.

4. Conduction transfers heat within the rock mass due to changes in drift wall temperature. The heat flow rate into the rock can be determined using Fourier's Conduction Law at any time during the preclosure period, using the temperature gradient in the rock mass. This calculation requires knowledge of the thermal conductivity, saturation, density, and heat capacity of the rock (which may vary spatially).

The heat transfer rates for the processes described above can be related by considering the overall conservation of thermal energy except during the early transient response when the waste package temperature is rapidly changing. The following summarizes the coupled components of the thermal energy conservation during quasi-steady-state conditions when energy storage is relatively constant:

- The sum of the radiative heat transfer rate from the waste package to the drift wall (process 1 from above), and the convective heat transfer rate from the waste package into the airflow (process 2), must equal to the total rate of heat released from the waste package.

- The sum of the convective heat transfer rates from the waste package and drift wall into the airflow (processes 2 and 3), and the conductive heat transfer rate into the rock (process 4), must also be equal to the total rate of heat released from the waste package.

- The sum of the convective heat transfer rates from the drift wall into the airflow (process 3), and the conductive heat transfer rate into the rock (process 4), must be equal to the rate of radiant heat released from the waste.

Five additional processes have not been explicitly included in the conceptual model. The first includes the mass transport of water and water vapor and the coupled latent and sensible heat transfer associated with the phase change and movement of water. However, these latent heat effects and near-field host rock mass transport processes can be approximated using boiling point temperature dependent values for the thermal conductivity and specific heat of the rock. This can account for vaporization of pore water and dryout in an approximate sense, but cannot accurately track changes of saturation and evolution of properties. In most cases, the temperatures needed to change these properties are not reached during the preclosure period. These processes are presented in greater detail in Section 6.3.

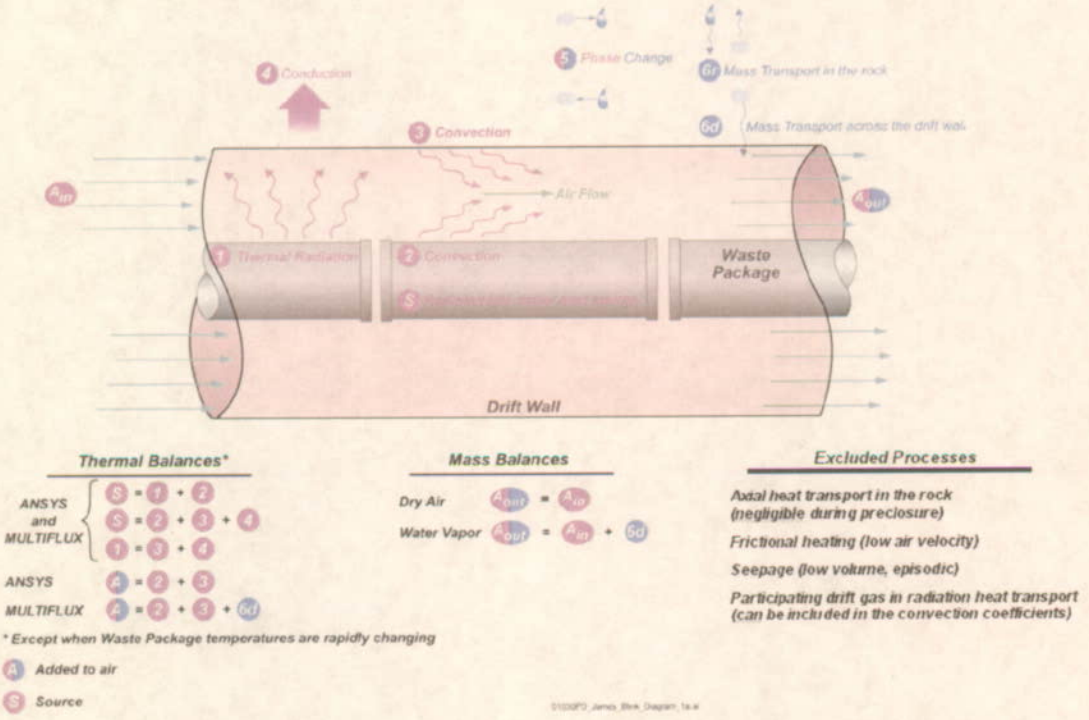

Figure 6-1. Conceptual Model for Heat and Mass Transfer Within and Around an Emplacement Drift

The second process excluded from the conceptual model is the axial transport of heat and mass within the rock domain. This process is assumed to have negligible influence on the ventilation heat removal ratio during the duration of the ventilation period. This is due to the small thermal diffusivity of rock (~1×10^{-7} m^2/s) and the large (hundreds of meters) scale of the repository footprint. The axial heat transport process is captured in the MSTH model that calculates preclosure and postclosure in-drift and rock temperatures and moisture contents for use in the TSPA. The MSTH model uses the ventilation heat removal ratio calculated by the Ventilation Model as input.

The third process not included in the ventilation conceptual model is the frictional heating of the air and engineered components due to the moving air. This process is assumed to be negligible (compared to the waste package heat source) due to the low flow velocities.

The fourth process not included in the ventilation conceptual model is episodic flow of liquid water into the drift air (due to heterogeneities in the host rock and episodic infiltration). It is assumed that the total heat added to the airflow by vaporizing such seeps is small compared to the heat from radionuclide decay. It should be noted that the conceptual model does account for vaporization of liquid water within the host rock and movement of the vapor into the drift, but that process adds only the sensible heat due to the temperature difference between the entering water vapor and the airflow.

Finally, the fifth process not included in the ventilation conceptual model is the participation of the drift gas in the radiation process. Water vapor is an effective absorber of infrared radiation, and the effect of its absorption and re-radiation of thermal energy is currently being evaluated.

6.1.2 Basis Heat Transfer Equations for the Ventilation Model

The following three equations represent energy balances for processes 1, 2 and 3 as outlined above in Section 6.1.1 and Figure 6-1:

$$Q_{wp} = \pi L \cdot \left[d_{wp} h_{rad} (T_{wp}^4 - T_{dw}^4) + d_{wp} h_{wp-air} (T_{wp} - T_{air-bulk}) \right] \quad \text{Eq. 6-1}$$

$$Q_{dw} = \pi L \cdot \left[d_{wp} h_{rad} (T_{wp}^4 - T_{dw}^4) - d_{dw} h_{dw-air} (T_{dw} - T_{air-bulk}) \right] \quad \text{Eq. 6-2}$$

$$(\dot{m} c_p)_{air} (T_{air-out} - T_{air-in}) = \pi L \cdot \left[d_{wp} h_{wp-air} (T_{wp} - T_{air-bulk}) + d_{dw} h_{dw-air} (T_{dw} - T_{air-bulk}) \right] \quad \text{Eq. 6-3}$$

where

Q_{wp} = heat generated by the waste package (W)
Q_{dw} = heat conducted into the rock (W)
T_{wp} = waste package surface temperature (K)
T_{dw} = drift wall temperature (K)
$T_{air\text{-}bulk} = (T_{air\text{-}in} + T_{air\text{-}out})/2$
$T_{air\text{-}in}$ = ventilation air temperature at the drift segment inlet (K)
$T_{air\text{-}out}$ = ventilation air temperature at the drift segment outlet (K)
$h_{wp\text{-}air}$ = waste package surface convection heat transfer coefficient ($W/m^2 \cdot K$)
$h_{dw\text{-}air}$ = drift wall convection heat transfer coefficient ($W/m^2 \cdot K$)
h_{rad} = radiation heat transfer coefficient ($W/m^2 \cdot K^4$)
L = drift segment length (m)
d_{wp} = waste package diameter (m)
d_{dw} = drift diameter (m)
$\dot{m}$ = ventilation mass flow rate (kg/s)
c_p = specific heat of air ($J/kg \cdot K$)

For the purposes of this model report, the convection heat transfer coefficients are calculated using the Dittus-Boelter correlation for fully developed turbulent flow in smooth tubes (Incropera and DeWitt 1996, Hartman 1982). Other appropriate correlations may also be used. Separate heat transfer coefficients may be used for the convective heat transfer from the inner surface (i.e. waste package) to the air, and for the outer surface (i.e. drift wall) to the air. This model report uses the same convection heat transfer coefficient for both surfaces.

$$Nu = \frac{h_{DB} \cdot D}{k} = 0.023 \cdot Re^{0.8} \cdot Pr^{0.4}$$

Eq. 6-4

or

$$h_{DB} = 0.023 \cdot \left(\frac{k \cdot Re^{0.8} \cdot Pr^{0.4}}{d_{dw} - d_{wp}} \right)$$

Eq. 6-4a

$$Re = \frac{\rho D V}{\mu} = \left(\frac{d_{dw} - d_{wp}}{A_{net}} \right) \cdot \left(\frac{\dot{m}}{\mu} \right)$$

Eq. 6-5

where

Nu = Nusselt Number (dimensionless)
D = length (m) = d_{dw} - d_{wp}
k = thermal conductivity (W/m·K)
h_{DB} = Dittus-Boelter convection heat transfer coefficient (W/m^2·K) = $h_{wp\text{-}air}$ = $h_{dw\text{-}air}$
Pr = Prandtl Number (dimensionless)
Re = Reynolds Number (dimensionless)
ρ = density (kg/m^3)
V = ventilation airflow velocity (m/s) = Q/A_{net}
Q = volumetric ventilation airflow (m^3/s) = $\dot{m}/\rho$
A_{net} = net cross-sectional available for airflow (m^2)
μ = dynamic viscosity of air (kg/m·s)

The radiation heat transfer coefficient is calculated from an analytical solution for concentric cylinders (Incropera and DeWitt 1996):

$$h_{rad} \equiv \frac{\sigma A_{wp}}{\frac{1}{\varepsilon_{wp}} + \left(\frac{1 - \varepsilon_{dw}}{\varepsilon_{dw}} \right) \cdot \frac{d_{wp}}{d_{dw}}}$$

Eq. 6-6

where

σ = Stefan-Boltzmann constant ($W/m^2 \cdot K^4$)
ε_{wp} = waste package surface emissivity
ε_{dw} = drift wall surface emissivity

6.2 NUMERICAL APPLICATION OF THE CONCEPTUAL MODEL

Two different numerical applications of the conceptual model described above for in-drift ventilation heat transfer are performed using the software codes ANSYS and MULTIFLUX. The results of each numerical application are compared later in Section 6.2.3. Each code has complementary strengths and limitations. An additional ANSYS numerical model with a different axial discretization along the length of the drift was also used. The purpose of this model was to evaluate the numerical sensitivity of the results to the discretization of the model domain in the axial direction. The first ANSYS model, named ANSYS-Coarse, divided the drift into 6 equal segments of 100 meters. The second ANSYS model, named ANSYS-Refined, divided the drift into 24 equal segments of 25 meters.

The MULTIFLUX model is an adaptation of the code's capabilities. Named MULTIFLUX-Con, it simulates only the sensible heat transfer, allowing a direct comparison to the ANSYS numerical model. Table 6-1 summarizes the models developed for numerical application of the ventilation conceptual model, and also includes the numerical application of the alternative conceptual model presented later in Section 6.3. Table 6-2 summarizes the major inputs, parameters, and boundary conditions for the numerical models.

Table 6-1. Ventilation Numerical Models and the Mechanisms of Heat Transfer Simulated

Numerical model Name	Sensible Heat Transfer	Latent Heat Transfer
ANSYS-Coarse	Calculated	Approximated
ANSYS-Refined	Calculated	Approximated
MULTIFLUX-Con	Calculated	Approximated
MULTIFLUX-Full	Calculated	Calculated

Table 6-2. Comparison of the ANSYS and MULTIFLUX Numerical Model Set-Ups and Input Parameters

Numerical model Setup/Inputs	ANSYS-Coarse	ANSYS-Refined	MULTIFLUX-Con	MULTIFLUX-Full
Boundary Conditions	$T_{surface}$ = 18.7°C $T_{water\ table}$ = 32.4°C $T_{mid\text{-}pillar}$ = adiabatic No Infiltration			$T_{surface}$ = 18.7°C $T_{water\ table}$ = 32.4°C $T_{mid\text{-}pillar}$ = adiabatic Infiltration = 10.13 mm/yr
Initial Heat Loading	1.5477 kW/m		1.5477 kW/m (Applied smoothly to waste packages, compensating for the unheated 0.1 m gaps between waste packages)	
Decay Function	Average for all CSNF Waste packages			
Convective Heat Transfer Coefficient on both the WP and Drift Wall (Attachment III)	1.89 $W/m^2 \cdot K$			
Mass Transfer Coefficient	NA		0	0.0012 kg/s
Ventilation Period	300 years			
Thermal Conductivity at the repository horizon (tsw-35)	Temperature Dependent: 2.02 W/m·K (<100°C) 1.20 W/m·K (≥100.1°C)			Saturation Dependent: 2.02 W/m·K (100%) 1.20 W/m·K (0%)
Specific Heat near the repository horizon (tsw-35)	Temperature Dependent: 900 J/kg·K (<95°C or ≥114.1°C) 4663 J/kg·K (≥95.1°C and <114°C)			900 J/kg·K (rock, water has separate properties)
Pillar Size	81-m (Drift Spacing)*		40.5-m (1/2 Drift Spacing)	
Drift Diameter	5.5 m			
Waste Package Diameter	1.564 m			
Inlet Air Relative Humidity	0%			30%
Inlet Air Temperature	25°C			
Initial Drift Wall Temperature	25°C			
Initial WP Temperature	70°C			
Emissivity	Gray Body to Gray Body 0.87 for Waste package 0.90 for Drift Wall		Equivalent Gray Body to Black Body 0.847 for Waste package 1.00 for Drift Wall	
Axial Discretization	100 m	25 m	3 Subdrifts with 5 Cells, 5 Cells, and 7 Cells, respectively; 21 Axial Locations per Cell (14 half-packages and 7 gaps)	

* The ANSYS numerical models spanned from mid-pillar to mid-pillar to eliminate small (~1%) errors in radiation view factors near reflecting boundaries.

6.2.1 ANSYS Methodology

The ANSYS numerical model integrates the results of a heat transfer calculation using a two-dimensional cross-section through the drift with a one-dimensional calculation of the forced convection through an axial segment of the drift. This process assumes that the convective heat fluxes from the waste package and drift wall to the air are constant within the drift segment. This constant heat flux assumption is equivalent to assuming that the air temperature increases linearly within the segment, and that the drift wall and waste package temperatures also increase linearly at the same rate. Such an assumption is much closer to reality than an assumption of

constant temperature within the segment and then a step change at the end. The departure from reality of the assumption of constant flux is slow along the drift, and is due to the increase of radiation heat transfer and conduction of heat into the host rock as the temperature increases. To test the validity of the assumption, the ANSYS numerical model was run with 100-m (ANSYS-Coarse) and 25-m (ANSYS-Refined) long segments.

Figures 6-2 and 6-3 illustrate the geometry and the main components of the ANSYS numerical models. In this method, a ventilated emplacement drift is treated as a series of finite drift segments. For each time step, a two-dimensional calculation of heat transfer between the waste package, drift wall, drift air, and the heat transfer into the host rock is done at the entrance to the first drift segment using the inlet air temperature as a heat sink. The resulting convective heat fluxes (at the waste package and drift wall surfaces) are assumed to be constant along the segment, allowing a one-dimensional calculation of the air temperature increase within the segment, using the air flow rate. The air temperatures at the end of the drift segment, at both the beginning and end of the time step, are then used in the next two-dimensional calculation, which occurs at the beginning of the next drift segment. The process is repeated along the entire drift split (from the air entry at the perimeter drift to the air exit into the exhaust main at the mid-length point of the drift), alternating between two-dimensional ANSYS calculations and one-dimensional air heating calculations using Microsoft Excel. At each time and ANSYS location, the heat fluxes are also used to calculate the ventilation heat removal rate.

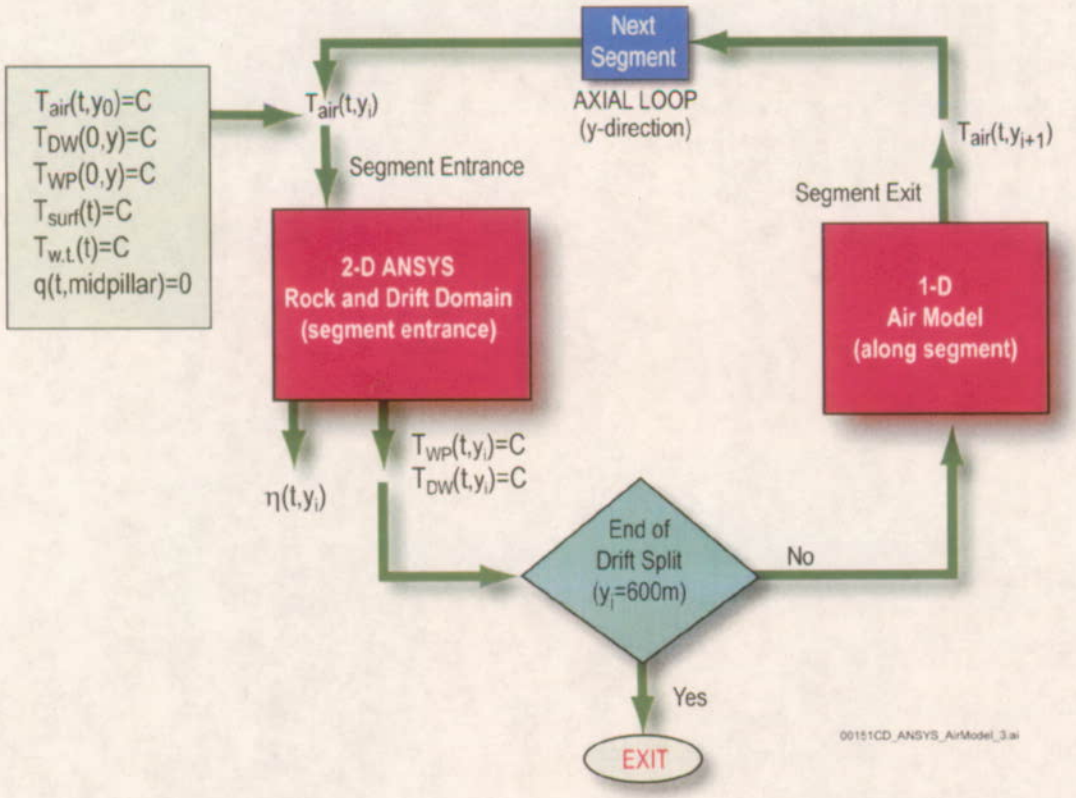

Figure 6-2. Flowchart Depicting the ANSYS Methodology for Calculating Heat Flow in and around a Ventilated Emplacement Drift

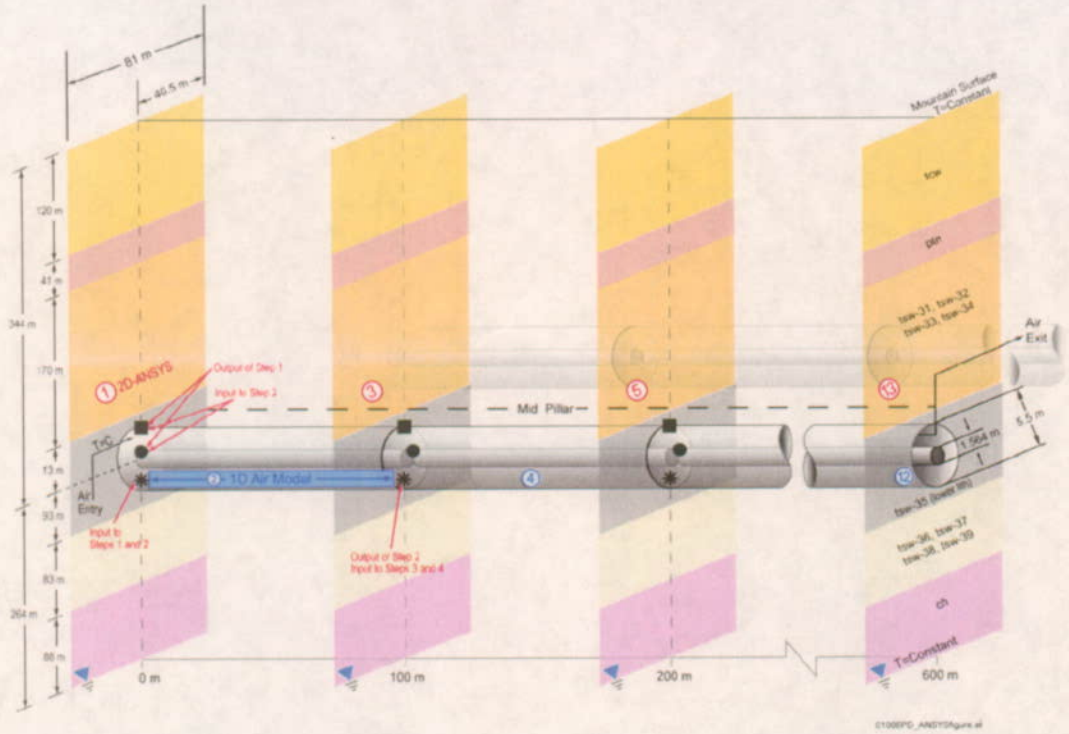

Figure 6-3. Schematic of the ANSYS Methodology for Calculating Heat Flow in and around a Ventilated Emplacement Drift

6.2.1.1 ANSYS Operational Details

The ANSYS process starts with defining a number of time-steps to represent the entire ventilation time period of interest. The total number of time intervals, and the length of each time-step can be selected according to the degree of calculational accuracy demanded and considerations of the expected computational time. The length of each timestep may be set differently to accommodate the variations of the thermal decay rate of the waste during different time periods. Generally, during the initial stages when the waste decays rapidly, short time steps can be arranged to provide detail during the more rapidly changing portion of the ventilation history. In the later stages of heat transfer, the thermal decay curves become relatively flat; thus longer time-steps can be used to reduce computational efforts.

In this approach, the entire drift is considered as a series of connected drift segments with some length. The total number of drift segments is related to segment length. It is desirable to choose a relatively short drift length for individual drift segments, to the extent practicable, so that the convective heat fluxes within a segment can be reasonably represented by a constant. The values of drift length may be set differently to accommodate the variations in rate of air temperature increase as the air flows through the drift.

Calculations are performed sequentially for each time-step through the ventilation period. At the entry to each drift segment two-dimensional thermal analysis is performed with ANSYS for the

sequence of time steps. Each time step uses the waste package thermal power, initial rock and waste package temperatures from the end of the previous time step, and the air temperature from the exit of the previous segment. The air temperature and waste thermal power are linearly interpolated in time during the time step, if ANSYS uses sub-time-steps to obtain numerical stability.

For each segment, applying the determined waste package and drift wall temperatures at the start and end of each time step, together with the air temperature at the same times, convective heat transfer rates at the segment entrance are calculated using Newton's Cooling Law. The obtained convective heat removal rate and the known airflow rate are used to determine the increase in internal thermal energy of the air, and the temperature of the airflow exiting the segment (at the start and end of each time step). The exit temperature history of the air is used in the ANSYS calculation at the entry of the next segment. This process is repeated to the end of the drift split, where a final ANSYS calculation determines the temperatures and ventilation heat removal ratio at that location.

6.2.2 MULTIFLUX-Con Methodology

The structure of the MULTIFLUX-Con numerical model is presented as two flow charts and a schematic in Figures 6-4 through 6-6. For the first subdrift, MULTIFLUX runs a series of two-dimensional rock domain conduction only calculations, using NUFT V3.0s with initial-guesses for the drift wall temperature history. As in the ANSYS numerical model in Section 6.2.1, the initial drift wall temperature is user-specified. Also similar to the ANSYS numerical models, the waste packages are located concentrically in the drift, and there is no invert present. All dimensions are the same as for the ANSYS numerical model, or as close as possible given the meshing constraints of the finite difference method associated with the NUFT runs. Very thin elements were used at the waste package and drift wall surfaces to assure that the temperatures obtained from the centers of these elements represented as closely as possible the temperature at the surface. A sensitivity study on the grid showed that the thickness of these elements did not impact the results.

The Numerical Transport Code Functionalization solver (NTCF) module of MULTIFLUX runs NUFT and assembles the results into a matrix. This matrix relates the perimeter-averaged drift wall temperature (a state parameter) to the drift wall heat flux (which can be thought of as a function of the near-field rock temperature gradient). The matrix includes 20 time periods by 20 combinations of the fluxes and temperatures. The diagonal of the matrix is the best estimate of the time evolution of the fluxes and temperatures at the subdrift mid-length, termed the "central values". For each time step (matrix row), the multiple combinations of state variables and fluxes represent potential situations at a given location in the drift, and the "best-fit" situation may be different (different columns) at each axial location.

Also for each time step, the computational fluid dynamics solver (CFD) module of MULTIFLUX calculates the in-drift convection and radiation heat transfer due to radioactively decaying waste in the eight waste packages. As in the ANSYS numerical model (Section 6.2.1), the initial (in time) waste package and drift wall temperatures, and the entering air temperature (invariant in time) are user-specified. At each of the 21 axial locations in the cell (one at each waste package half and one

at each gap), the CFD-calculated heat fluxes are compared to those of the matrix entries corresponding to the initial-guess (central value) temperature. The comparison and subsequent steps are controlled by the Direct Iteration and Successive Approximating Coupling solver (DISAC) of MULTIFLUX. If convergence is not satisfactory at each of the 21 axial locations, the temperature boundary condition at each axial location are updated using the NTCF matrices and the local heat fluxes from the previous iteration. Then, the CFD calculation is repeated to obtain improved local fluxes. When all 21 axial locations in the cell have converged, the time step is incremented, and the process repeated.

When the entire time history of the eight-waste-package cell is converged, the CFD process is repeated (under DISAC control) for the next cell, using the final values for the previous cell as the initial-guess temperatures, and using the same NTCF matrices. When the entire time history is complete for all the cells in the first subdrift, the matrix central values are compared to the histories at the mid-length location in the central cell in the subdrift. If the converged histories are not acceptably close to the matrix central values, those histories are used as new initial guesses, new NUFT calculations are used to construct new NTCF matrices, and the entire CFD-DISAC process is repeated for the entire subdrift, cell by cell and time step by time step.

When the first subdrift time histories have all converged, with the subdrift center histories being close to the matrix central values, MULTIFLUX moves to the second subdrift and repeats the process, using the first subdrift central location histories as initial guesses for the NUFT-NTCF process. When the second subdrift histories have all converged, the process is repeated for the third subdrift.

6.2.2.1 MULTIFLUX Operational Details

MULTIFLUX divides the drift split into three subdrifts (entry, middle, and exit regions) as shown in Figure 6-5. Each subdrift includes multiple cells (five, five, and seven cells, in the three subdrifts, respectively). Each cell includes a user-specified series of eight waste packages (two half and six full) separated by gaps. Each cell is identical to the previous cell (waste packages 1-8, 1-8, etc.) rather than reflecting (waste packages 1-8, 8-1, 1-8, etc.). The waste package dimensions and thermal power histories can be user-specified to represent the variability of the waste stream, or they can be smoothed to provide a nearly constant axial power variation which approaches the two-dimensional ANSYS method described in Section 6.2.1. However, the current version of MULTIFLUX used for these runs does not allow for a heat input to be assigned to the gaps present between waste packages. Therefore, each waste package is assigned a portion of the heat load associated with the gap, in addition to its linear loading. The difference in heat loading between the MULTIFLUX and ANSYS ventilation numerical models may generate local differences in the results. Nonetheless, since the ANSYS and MULTIFLUX ventilation numerical models have the same total energy per unit length generated throughout the entire emplacement drift, the axially averaged differences in the end results are expected to be small.

While the ANSYS ventilation numerical models use a gray body to gray body methodology to simulate radiation heat transfer, MULTFILUX uses gray body to black body. As discussed later in Section 6.5.1.1, a simple equation can be used to convert the two gray body emissivities to an

effective emissivity of a gray body radiating to a black body. The effective emissivity produces the same rate of heat transfer as the more complex gray body to gray body calculation.

The MULTIFLUX-Con numerical model is designed to simulate only sensible heat transfer during the 300-year preclosure ventilation period. This is accomplished by assigning zero initial liquid water saturation, zero permeability, and zero infiltration to the surrounding host rock matrix. Additionally, the saturation-dependent thermal properties (i.e. thermal conductivity and specific heat) of the host rock units are converted to ANSYS like temperature dependent thermal properties. In other words, the thermal conductivity changes in a step-wise manner from the wet to the dry value at 100°C. The latent heat of the matrix pore water is incorporated into the specific heat of the rock.

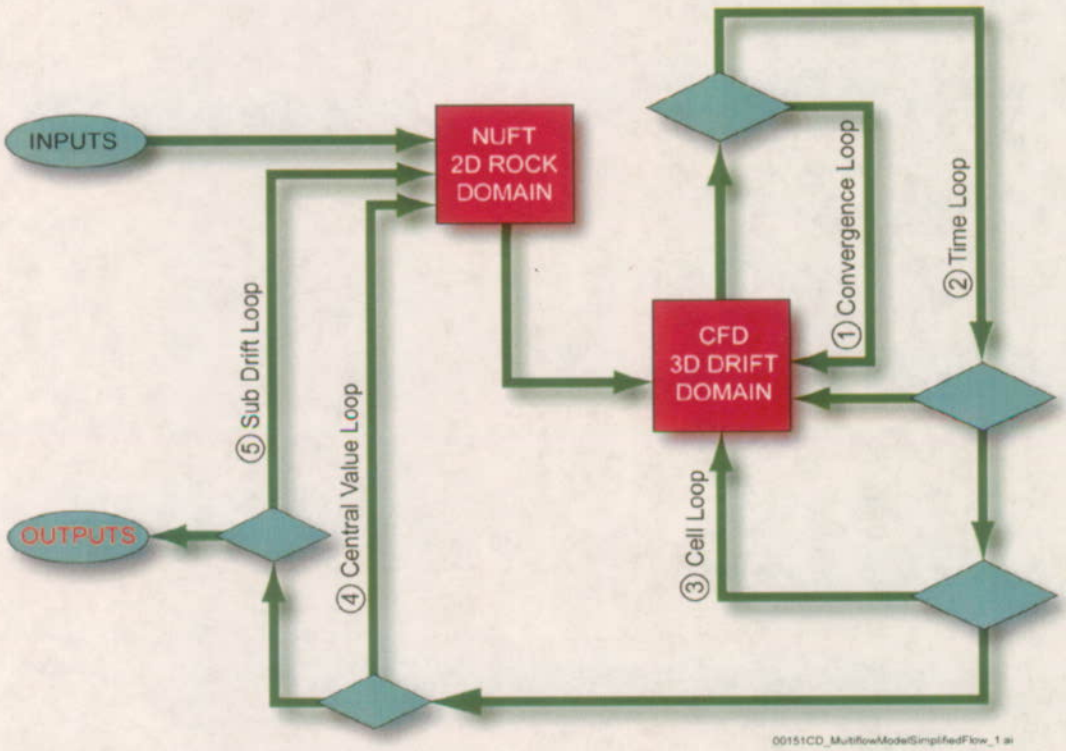

Figure 6-4. Simplified Flowchart Depicting the MULTIFLUX Methodology for Calculating Heat Flow in and around a Ventilated Emplacement Drift

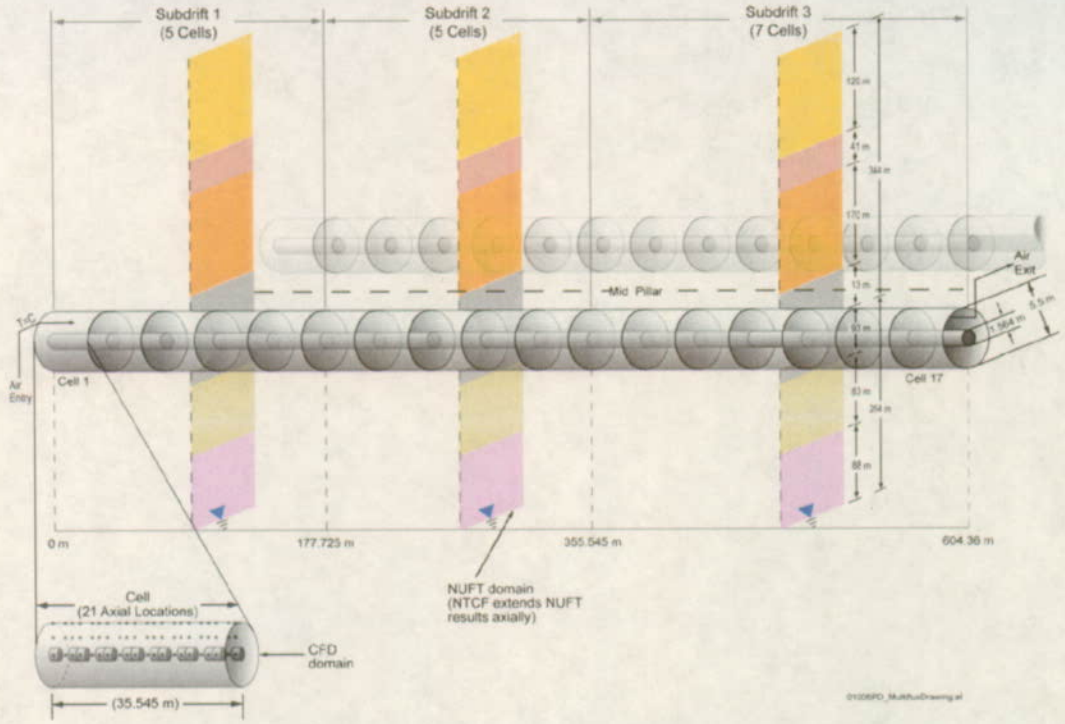

Figure 6-5. Schematic of the MULTIFLUX Methodology for Calculating Heat Flow in and around a Ventilated Emplacement Drift

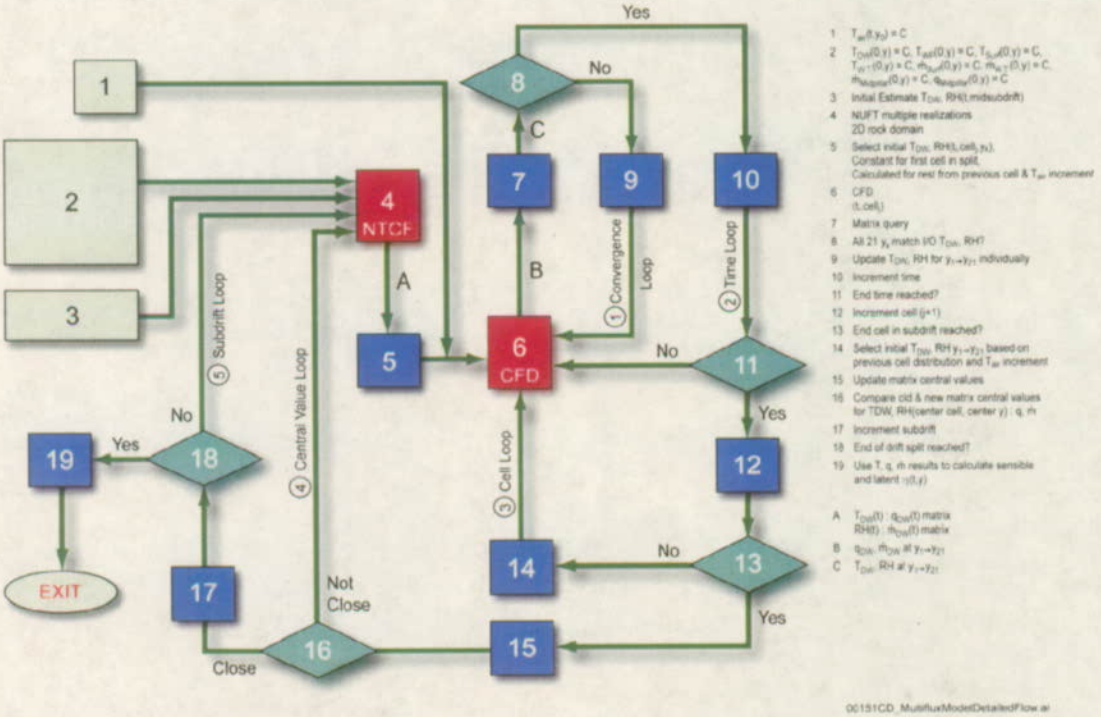

Figure 6-6. Flowchart Depicting the MULTIFLUX Methodology for Calculating Heat Flow in and around a Ventilated Emplacement Drift

6.2.3 Results

The results for the ANSYS-Coarse, ANSYS-Refined, and MULTIFLUX-Con models are presented in terms of temporally and spatially varying temperatures and heat removal rates. In addition, energy balances are presented for each numerical model. A comparison between the ANSYS-Coarse and ANSYS-Refined models quantifies the impact of the axial discretization along the drift length and serves as a model verification exercise. A comparison between the ANSYS and the MULTIFLUX-Con results provides added model verification in that two different numerical methodologies are applied to simulate the ventilation conceptual model.

6.2.3.1 The Effects of Axial Discretization (ANSYS-Coarse versus ANSYS-Refined)

The general trends of waste package, drift wall, and drift air temperatures as a function of time and axial drift length for the ANSYS-Refined numerical model are shown in Figure 6-7. The waste package and drift wall temperatures are perimeter-averaged results, while the in-drift air temperatures are bulk averaged. The following general observations with respect to waste package, drift wall, and drift air temperatures for each of the ANSYS numerical models can be made:

- With respect to time, temperatures peak early (between 2 to 5 years) and afterwards decline in an exponential fashion similar to the heat input decay curves

- With respect to location along the length of the drift, temperatures increase linearly, with the maximum temperatures occurring at the end of the 600-m long drift

Figures 6-8 and 6-9 not only reinforce these two general observations about temperatures, but also quantify the temperature differences between the ANSYS-Coarse and ANSYS-Refined numerical models. Table 6-3 summarizes the temperature results.

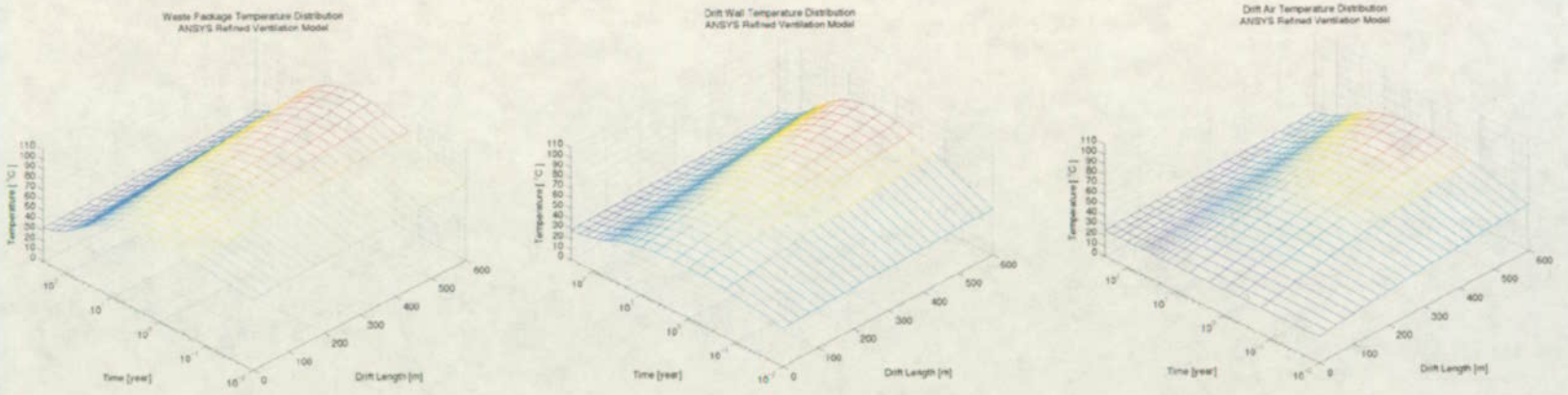

Figure 6-7. Waste Package, Drift Wall, and Drift Air Temperatures as a Function of Time and Drift Length for the ANSYS-Refined Ventilation Numerical Models (DTN MO0210MWDTVE30.018)

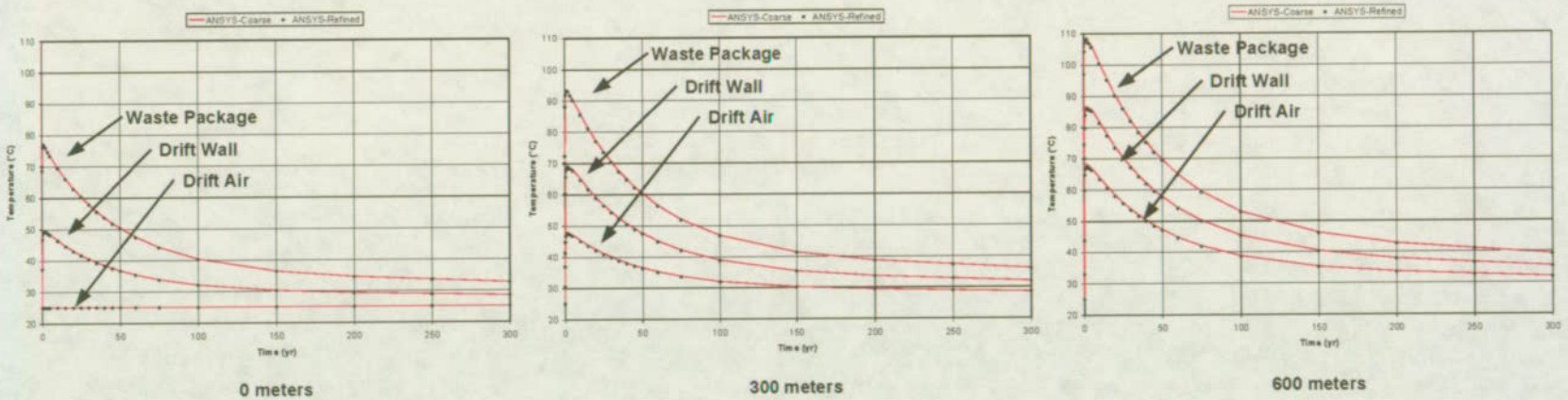

Figure 6-8. Plots of Waste Package, Drift Wall, and Drift Air Temperatures as a Function of Time at 0, 300, and 600 Meters from the Drift Entrance for the ANSYS-Coarse and ANSYS-Refined Ventilation Numerical Models (DTNs MO0210MWDTVE30.018 and MO0210MWDTEM30.019)

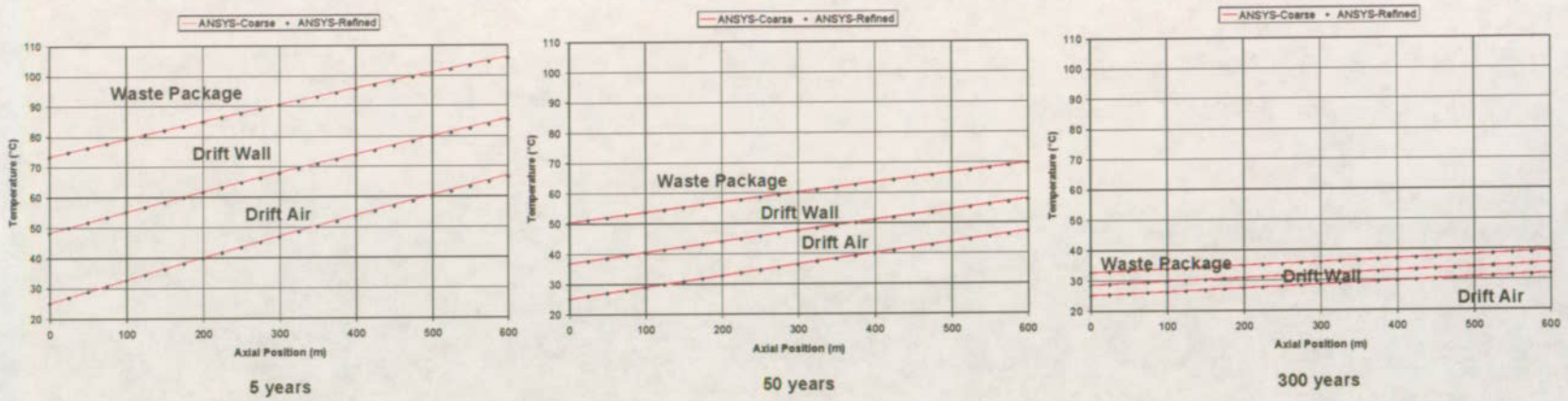

Figure 6-9. Plots of Waste Package, Drift Wall, and Drift Air Temperatures as a Function of Drift Length at 5, 50, and 300 Years from the Time of Waste Emplacement for the ANSYS-Coarse and ANSYS-Refined Ventilation Numerical Models (DTNs MO0210MWDTVE30.018 and MO0210MWDTEM30.019)

Table 6-3. Summary of Waste Package, Drift Wall, and Drift Air Temperatures for the ANSYS-Coarse and ANSYS-Refined Numerical Models

		Drift Entrance (0 m)			Drift Middle (300 m)			Drift Exit (600 m)		
		Temperature (°C)								
		Waste Package	Drift Wall	Drift Air	Waste Package	Drift Wall	Drift Air	Waste Package	Drift Wall	Drift Air
ANSYS-Coarse	5 years	73.4	48.2	25.0	90.5	67.9	47.0	106.1	85.6	66.8
ANSYS-Refined		73.4	48.2	25.0	90.2	67.7	46.7	105.7	85.2	66.3
ANSYS-Coarse	50 years	50.2	36.6	25.0	60.2	47.5	36.4	69.7	57.7	47.2
ANSYS-Refined		50.2	36.6	25.0	60.1	47.4	36.3	69.5	57.6	47.0
ANSYS-Coarse	300 years	32.5	28.4	25.0	35.8	31.8	28.4	39.1	35.2	31.8
ANSYS-Refined		32.5	28.4	25.0	35.8	31.8	28.4	39.1	35.2	31.8

The ANSYS-Coarse peak waste package, drift wall, and drift air temperatures occur at about 2 years and are, respectively 108.2, 84.7, and 67.0°C at 600 meters from the drift entrance. The ANSYS-Refined peak temperatures at the same time and drift location are 107.8, 84.2, and 66.4°C or about 0.4 to 0.6°C lower than the ANSYS-Coarse results. This trend for the two ANSYS numerical models is persistent throughout the entire set of temperature results as functions of both time and drift location.

Table 6-4 compares the sum of the heat fluxes from the waste package and drift wall to the air, within one 100-m segment, from direct calculation in ANSYS-Refined and interpolated between end members of the ANSYS-Coarse segment. The segment and time shown in the table have heat fluxes near the maximum.

Table 6-4. Linearity of Heat Flux into the Air (W/m) within one ANSYS-Coarse Segment (Between 100 and 200 m, at 5 years After Emplacement)

Numerical Model	100 m	125 m	150 m	175 m	200 m
ANSYS-Refined	1166.6	1156.7	1146.8	1137.1	1127.7
ANSYS-Coarse – end members	1166.0	-	-	-	1126.7
ANSYS-Coarse – interpolated values	-	1156.2	1146.3	1136.5	-
(Refined – Interpolated) / Refined	0.05%	0.05%	0.04%	0.05%	0.09%

The flux variation along the segment is about 3%. This small variation leads to changes in the heat fluxes that are about two orders of magnitude smaller. The fractional difference between the interpolated and calculated values is as small as the differences between the models at the common points (100 m and 200 m). These results, and temperature results presented earlier, support the assumption of nearly constant heat flux within the segment. These results also reinforce the hypothesis that the methodology of these ANSYS numerical models is generally insensitive to the number and length of sub-sections in the axial direction.

6.2.3.2 Temperature Comparisons for the ANSYS and MULTIFLUX-Con Models

The same general trends of temperature variation with time and distance from the drift entrance, as noted in Section 6.2.3.1 for the ANSYS numerical models, is observed for the MULTIFLUX-Con numerical model. Figure 6-10 shows the MULTIFLUX-Con raw temperature data. The raw data is fit using an element-length-weighted, least-square methodology (Attachment VII). The scattering of the raw waste package and drift wall temperatures is due to three causes. First, the waste package heat input is interrupted at the small gaps between waste packages, leading to less heat transport to the corresponding drift wall segments and lower drift wall temperatures in those locations. Second, there is a reduced set of radiation heat transfer connections in the vicinity of cell boundaries in the MULTIFLUX methodology since elements within one computational (eight waste package) cell cannot radiate to elements in the adjacent cell. This should lead to lower drift wall temperatures near the cell boundaries. Third, there is a potential coding error in setting up the radiation connections. This could explain the increase in waste package temperature and decrease in drift wall temperature near the end of each cell, and the opposite trends at the beginning of the following cells. Because the flow rate of the air tends to smooth these types of non-uniformities as the air mixes, the raw air temperature data vary smoothly with axial position.

Figures 6-11 shows the MULTIFLUX-Con and ANSYS-Refined temperature results as a function of time for locations near the drift entrance, drift middle, and drift exit. Figure 6-12 shows results as function of distance from the drift entrance for times around the maximum, median, and minimum temperatures. Table 6-5 summarizes the temperature results.

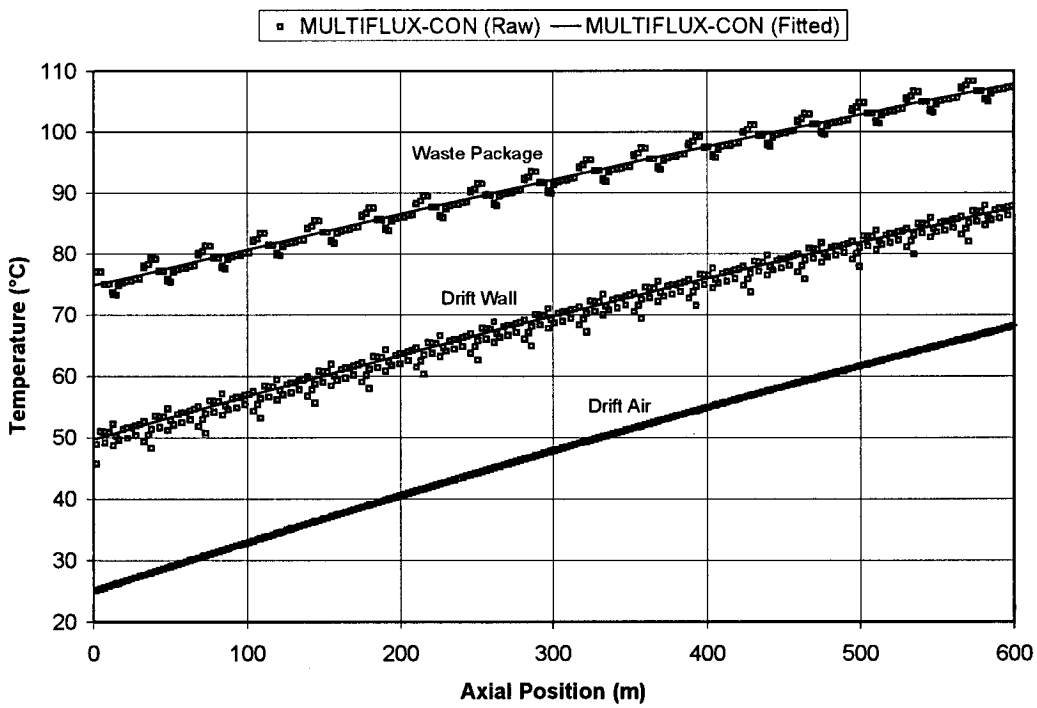

Figure 6-10. Raw and Fitted Waste Package, Drift Wall, and Drift Air Temperature Data for MULTIFLUX-Con as a Length from the Drift Entrance at 3.5 years (DTN MO0209MWDMUL30.002)

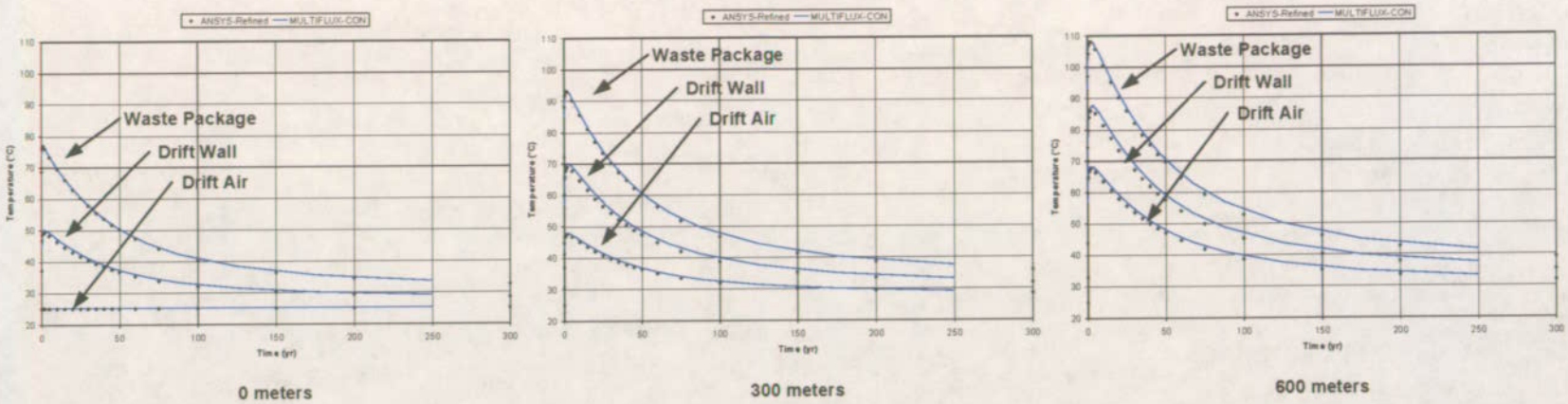

Figure 6-11. Plots of Waste Package, Drift Wall, and Drift Air Temperatures as a Function of Time at 0, 300, and 600 meters from the Drift Entrance for the ANSYS-Refined and MULTIFLUX-Con Ventilation Numerical Models (DTNs MO0210MWDTVE30.018 and MO0209MWDMUL30.002)

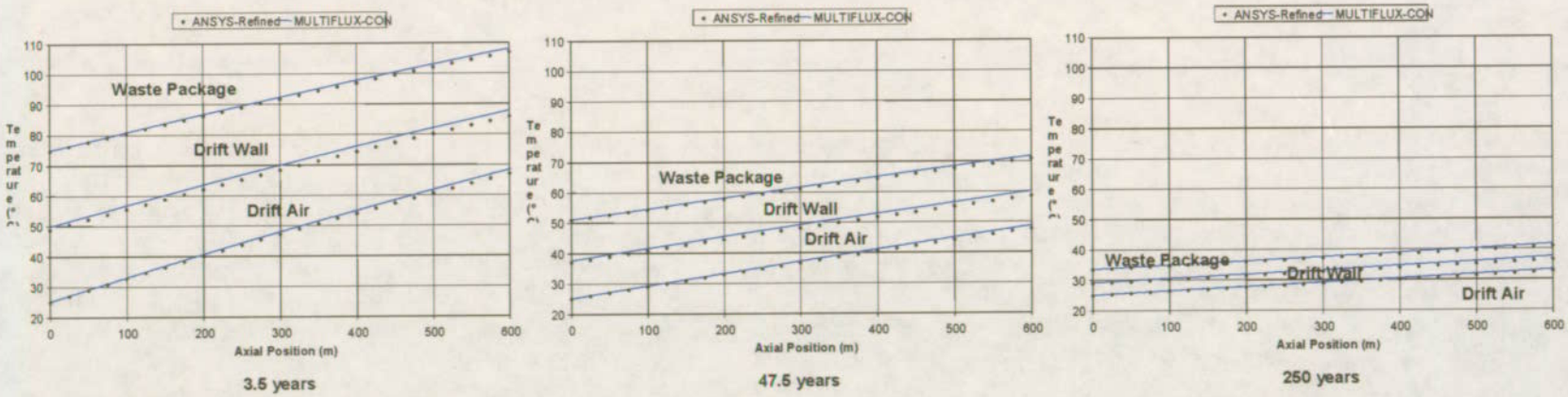

Figure 6-12. Plots of Waste Package, Drift Wall, and Drift Air Temperatures as a Function of Drift Length at 3.5, 47.5, and 250 Years from the Time of Waste Emplacement for the ANSYS-Refined and MULTIFLUX-Con Ventilation Numerical Models (DTNs MO0210MWDTVE30.018 and MO0209MWDMUL30.002)

Table 6-5. Summary of Waste Package, Drift Wall, and Drift Air Temperatures for the ANSYS-Refined, MULTIFLUX-Con, and DriftFlow Numerical Models

		Drift Entrance (0 m)			Drift Middle (300 m)			Drift Exit (600 m)		
		Temperature (°C)								
		Waste Package	Drift Wall	Drift Air	Waste Package	Drift Wall	Drift Air	Waste Package	Drift Wall	Drift Air
ANSYS-Refined	**3.5 years**	74.8	48.7	25.0	91.6	68.3	47.3	107.8	85.6	66.9
MULTIFLUX-Con		74.8	49.7	25.0	90.5	69.8	47.8	105.7	87.6	68.4
ANSYS-Refined	**47.5 years**	51.0	37.0	25.0	61.1	48.1	36.6	70.8	58.5	47.7
MULTIFLUX-Con		51.0	37.5	25.0	61.5	49.1	37.0	71.6	60.0	48.7
ANSYS-Refined	**250 years**	33.5	28.9	25.0	37.2	32.4	28.4	40.8	36.4	31.8
MULTIFLUX-Con		33.5	29.1	25.0	37.4	33.1	29.0	41.5	37.3	33.2

The temperature distributions for all the numerical models are within 2°C at all locations and times for each respective component (waste package, drift wall, and air). The MULTIFLUX-Con temperatures at all three components are generally higher than the corresponding ANSYS values. Such a situation would be expected if the heat transfer from the drift wall into the rock were slightly less effective in the MULTIFLUX-Con model. The conduction only submodel used for verification, described in Section 6.5.2.1, shows similar results after about 30 years.

6.2.3.3 Heat Flux Comparisons for the ANSYS and MULTIFLUX-Con Models

Although the ANSYS-Refined and MULTIFLUX-Con *temperatures* are similar for the waste package, drift wall and bulk air, the heat fluxes between these components are based on the *temperature differences* between them. These temperature differences are within 1°C for any time and location from the drift entrance. Small variations between the numerical models for temperatures (or temperature differences between components) can lead to larger differences between heat fluxes and ventilation heat removal ratio. Figure 6-13 shows the energy fluxes for the ANSYS-Refined and MULTIFLUX-Con numerical models using the nomenclature introduced in Figure 6-1 that describes the conceptual model (Section 6.1). The MULTIFLUX heat fluxes are shown as average values within a time period and axial region (computational cell), since the MULTFLUX results represent time periods (rather than individual times), and since an axial computational cell of eight waste packages is the smallest repeating unit of axial discretization. The ANSYS fluxes are interpolated at the same times and locations using a linear function between times and locations. Two time periods and axial regions are shown in Figure 6-13. The first time period and location (250 yr, 18 m) corresponds to the highest heat removal ratio, and the second (3.5 yr, 586 m) corresponds to the highest temperatures and lowest heat removal ratio after the five-year point. At very early times, efficiencies are lower since the drift wall is not initially warm enough to contribute to air heating.

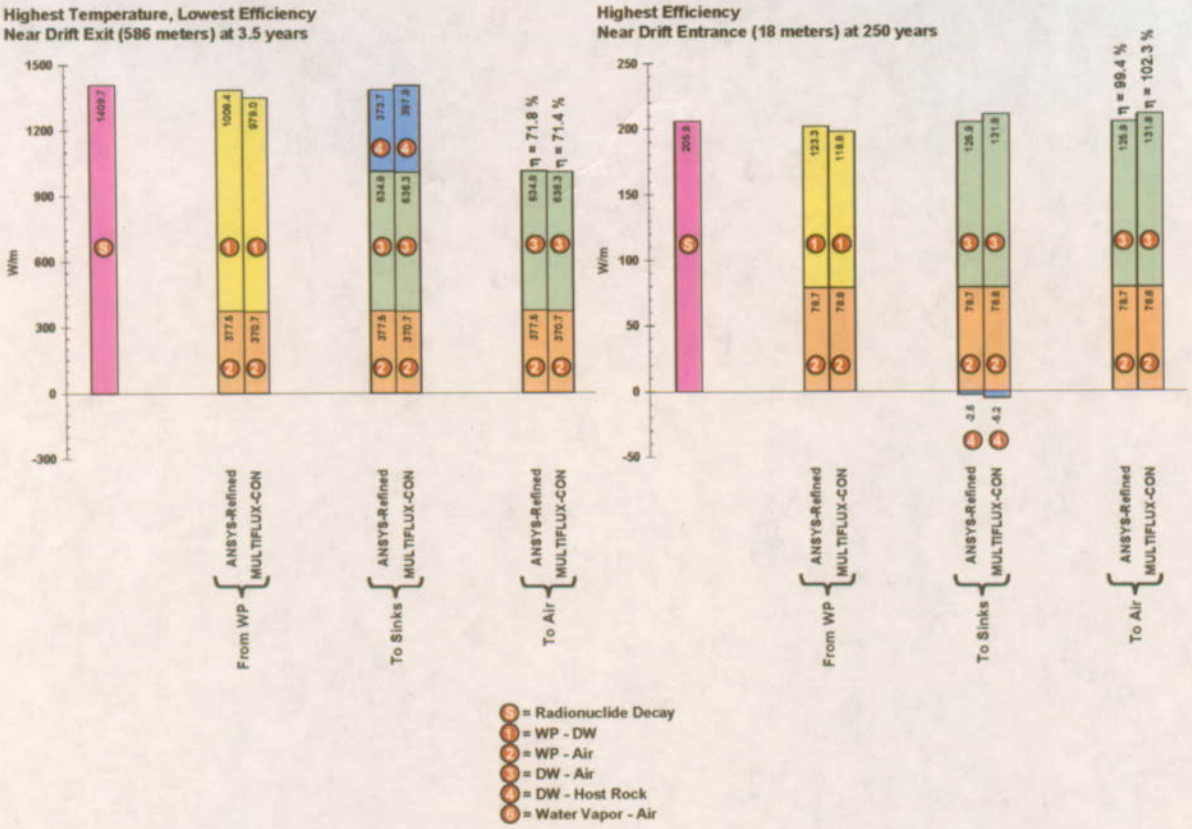

Figure 6-13. Heat Flux Distribution for the ANSYS-Refined and MULTIFLUX-Con Ventilation Numerical models at the Time and Location of the Highest Temperatures (left chart) and Ventilation Heat Removal Ratio (right chart)

The convection and radiation heat fluxes in Figure 6-13 are calculated directly from the differences between the waste package, drift wall, and drift air temperatures. The radionuclide decay power history provided to the numerical models is used directly in the heat flux calculations. Fluxes into the rock are obtained by subtraction for the ANSYS-Refined numerical model since the local values are not provided directly from the numerical model. The energy balance at the waste package is off by about 2% for the ANSYS numerical model.

For MULTIFLUX, the heat flux into the rock is the fundamental coupling parameter calculated as the interface between the rock and drift domains, and that flux is used directly in the energy balance presented in Figure 6-13. The convection heat fluxes can be accurately calculated from a two-dimensional formula consistent with the MULTIFLUX internal calculation. These values are adequate to construct energy balance checks for the overall heat sinks and for the air. To obtain an energy balance check at the waste package, the radiation heat flux is required, and a two-dimensional formula was used. However, the MULTIFLUX internal calculation is three-dimensional, and thus the energy check at the waste package in Figure 6-13 should be considered approximate. It is clear that MULTIFLUX internally calculates a proper radiation heat transfer flux, because the successful energy balance at the sinks depends on the radiation term within the numerical model.

Overall heat flow to the heat sinks balances in the ANSYS-Refined numerical model due to the constrained approach to obtain the local heat flux into the rock. The MULTIFLUX heat sinks balance is a direct calculation from the fluxes and temperatures provided by the software. Although the waste package temperature is higher than the drift wall temperature, the larger drift wall surface area results in more convective heat flow from the drift wall to the air than from the waste package to the air. For the highest temperature situation (3.5 years, 586 m) and the highest efficiency situation (250 year, 18 m), the separation of heat flows into the two heat sinks (air and rock) from the two engineered surfaces (waste package and drift wall) agrees for the two numerical models. For the highest efficiency situation, MULTIFLUX-Con calculates more heat being convected to the air than is released by radionuclide decay. This situation arises because at this late time, the ventilation air has begun to draw heat back out of the rock. This heat was stored at earlier times when the overall heat source was too strong to be removed by the airflow. The consequent temperature profile in the rock must increase to a peak at some location within the near-field and then decrease with additional distance from the drift. Inspection of the trend in the ANSYS results shows that a similar situation would occur with some additional ventilation duration, since the heat flux into the wall is less than 0.25% of the heat source at 250 yr near the drift entrance.

6.2.3.4 Heat Removal Comparisons for the ANSYS and MULTFLUX-Con Models

The ventilation heat removal ratio is the result of the total heat flow into the air divided by the total heat input to the system. For the highest temperature situation (3.5 yr, 586 m), the resulting ventilation efficiency is 71.8 and 71.4%, for the ANSYS-Refined and MULTIFLUX-Con numerical models, respectively. These results agree within 0.4%. This is the lowest efficiency calculated at any location or time after the temperature peak. In the highest efficiency situation (250 yr, 18 m), the MULTIFLUX-Con temperatures (air, waste package, and drift wall) are all higher, and more importantly, the temperature differences between components (WP to air, DW to air, and WP to DW) are essentially identical for the two numerical models. This results in efficiencies of 99.4 and 102.3% for ANSYS-Refined and MULTIFLUX-Con, respectively. These results agree within 3%. A ventilation efficiency greater than 100% simply means that the temperature or conduction heat transfer gradient has reversed in the host rock. In other words, some amount of heat which was conducted away from the drift wall and stored in the host rock during earlier times, has been conducted back to the drift wall during later times where it sinks back into the ventilation air.

The overall efficiency for the two models is shown in Table 6-6. Overall efficiency is defined as the total heat removed from the entire drift during the forced ventilation period, divided by the total heat added to the drift by radionuclide decay during the same period. The ANSYS-Refined and MULTIFLUX-Con numerical model results agree within 1.5% for overall efficiency.

Table 6-6. Overall Ventilation Heat Removal Ratio Calculated by ANSYS-Refined and MULTIFLUX-Con, for the 600-m Drift Split (for 50 and 300 yr Ventilation Durations)

Numerical Model	50 yr Ventilation Duration	300 yr Ventilation Duration
ANSYS-Refined	85.0%	94.6%
MULTIFLUX-Con	86.3%	94.0%

6.3 ALTERNATIVE CONCEPTUAL MODEL FOR IN-DRIFT VENTILATION

The alternative conceptual model for in-drift ventilation includes the addition of water and water vapor transport in the host rock, across the drift wall, and into the ventilation airstream. Water and water vapor mass transport is directly coupled to the heat transfer processes described in the conceptual model for in-drift ventilation. The impacts of the mass transport, in terms of latent heat transfer, temperature, heat removal rates, and near-field host rock dryout are evaluated using the MULTIFLUX software code.

6.3.1 Alternative Conceptual Model Heat and Mass Transfer Processes

The coupled heat and mass transfer processes for the alternative conceptual model for in-drift ventilation are the same as those for the conceptual model described in Section 6.1.1 and Figure 6-1 with the addition of two other processes:

5. Water phase change (evaporation and condensation) occurs within the host rock as the temperature and vapor pressure change. The rate of phase change can be calculated at any time during the preclosure period using the temperature and partial pressure of the water vapor within the rock. This calculation also requires knowledge of the porosity and saturation of the host rock, and is coupled to the mass transfer described in process 6.

6. Water (liquid and vapor phases) mass transfer occurs within the near-field host rock and the in-drift air. Water vapor moves within the host rock to cooler regions where it condenses, as described in process 5. It also enters the in-drift airflow at the drift wall, causing a change in relative humidity, and can potentially condense in cooler regions of the ventilation system, such as the exhaust main drift and exhaust shafts.

These mechanisms of heat and mass transfer involve both sensible and latent heat exchanges. Sensible heat is the energy associated with increasing temperature of a material, whereas the latent heat is the energy associated with vaporizing water. Application of the of the potential latent heat exchange in a ventilated emplacement drift requires a description of the water and water vapor movement within the surrounding rock mass during ventilation.

The heat transfer rates for processes 5 and 6 can be related to processes 1 through 4 by again considering the overall conservation of thermal energy except during the early transient response when the waste package temperature is rapidly changing. The following is an addition to the thermal energy conservation described in Section 6.1.1:

- The sum of the convective heat transfer rates from the waste package and the drift wall into the airflow (processes 2 and 3), and the heat of the water vapor transported back across the drift wall (process 6) equal the total heat added to the ventilation air.

Additionally, the mass transfer rates for processes 1 through 6 can be related by considering the overall conservation of mass during the ventilation period. The following summarizes the coupled components of the mass balance:

- The sum of the mass of the ventilation air into the drift and the water vapor that moves across the drift wall from the surrounding host rock, equals the mass of the air exiting the drift.

6.3.2 Theoretical Basis for Heat and Mass Transfer Processes

In addition to the equations presented in Section 6.1.2 for radiation, convection, and conduction heat transfer, the following equations take into account the mass transfer processes and their additions to the overall heat transfer.

An analog to the convective heat transfer is used to determine the mass transfer at the drift wall (Danko et al. 1988, Eq. 41):

$$Q_{m-dw} = \pi L \cdot \left[d_{dw} h_{m-dw} \left(\frac{P_{dw} - P_{air}}{P} \right) \right] \quad \text{Eq. 6-7}$$

where

$Q_{m\text{-}dw}$ = mass flux at the drift wall (kg/s)
$h_{m\text{-}dw}$ = mass transfer coefficient (kg/s·m^2)
P_{dw} = partial vapor pressure at the drift wall (Pa)
P_{air} = partial vapor pressure of the air (Pa)
P = total vapor pressure (Pa)

The mass transfer coefficient is defined as (Danko et al. 1988, Eq. 43):

$$h_{m-dw} = h_{dw-air} \cdot Le \quad \text{Eq. 6-8}$$

$$Le = \frac{Sc}{Pr} \quad \text{Eq. 6-9}$$

$$Sc = \frac{\upsilon}{D_{AB}} \quad \text{Eq. 6-10}$$

$$Pr = \frac{\upsilon}{\alpha} \quad \text{Eq. 6-11}$$

where

Le = Lewis number (dimensionless)
Sc = Schmidt number (dimensionless)
Pr = Prandtl number (dimensionless)
υ = kinematic viscosity (m^2/s)
D_{AB} = binary mass diffusion coefficient (m^2/s)
α = thermal diffusivity (m^2/s)

A detailed explanation of the heat and mass transfer equations for the host rock, as modeled by NUFT, can be found in the *NUFT V3.0s User's Manual* (CRWMS M&O 2000f), *Reference Manual for the NUFT Flow and Transport Code* (Nitao 1998) and *Documentation of the Thermal Energy Balance Equation used in the USNT Module of the NUFT Flow and Transport Code* (Nitao 2000).

6.4 NUMERICAL APPLICATION OF THE ALTERNATIVE CONCEPTUAL MODEL

The computer software MULTIFLUX V.2.0 is used to implement the alternative conceptual model, MULTIFLUX-Full, where sensible and latent heat exchange associated with ventilating emplacement drifts is involved.

6.4.1 MULTIFLUX-Full Methodology

The MULTIFLUX-Full methodology is essentially that same as the MULTIFLUX-Con presented earlier in Section 6.2.2 and can also be described using the flow charts and schematic in Figures 6-4 through 6-6. Similar to the MULTIFLUX-Con, a series of two-dimensional rock domain calculations using the NUFT V3.0s software are performed for the first subdrift with initial-guesses for not only the drift wall temperature, but also its pressure/humidity history. The NUFT submodel, as run by the NTCF solver for MULTIFLUX-Full, utilizes the active fracture method with the dual permeability model (AFM-DKM) to represent the coupled fracture and matrix continua of the rock domain.

The NTCF solver of the MULTIFLUX-Full model runs NUFT and assembles the results into two matrices, rather than the single matrix for MULTIFLUX-Con. The common matrix relates the drift wall temperature to the drift wall heat flux. The additional matrix relates the air pressure and humidity to the mass flux of water vapor crossing the drift wall. The DISAC solver is now required to converge the results of the CFD-calculated heat and mass fluxes to those of the NTCF matrix entries relating heat flux to temperature and mass flux to partial vapor pressure.

6.4.1.1 MULTIFLUX-Full Operational Details

The MULTIFLUX-Full numerical model calculates both heat and mass transfer in the rock domain. The thermal conductivity is a continuous function of saturation, varying linearly between the wet and dry values. The vapor pressure is a function of temperature; therefore, as temperature increases, the appropriate amount of matrix water is vaporized (absorbing the latent heat), and the mobilized vapor moves under the influence of gravity (i.e., buoyancy). The vapor

can condense at cooler locations, releasing the latent heat, and the condensate water can move under both capillary and gravity forces. The AFM-DKM model used in NUFT calculates the exchange of fluids between the matrix and fracture continua, including consideration of the fraction of the contact area that is wetted.

Thus, MULTIFLUX-Full simulates both latent and sensible heat transfer during the 300-year preclosure ventilation period. Because it includes latent heat, vapor mobility, and the drift mass-sink, the MULTIFLUX-Full ventilation numerical model is capable of simulating the competing effects of latent heat removal with near-field host rock dryout. The latent heat removal caused by pore water vaporization and entrance into the ventilation air stream at the drift wall tends to reduce temperatures within both the rock and the drift. At the same time, water vapor leaving the host rock to enter the ventilation air stream causes the host rock to dry, which in turn causes the saturation dependent thermal conductivity to decrease. The reduced thermal conductivity increases the temperature gradient within the dry portion of the rock, changing drift wall and in-drift temperatures in the opposite sense of the latent heat cooling. Determining which phenomenon dominates the drift wall temperature change requires detailed calculations using MULTIFLUX-Full.

The MULTIFLUX-Full numerical model is initialized by allowing the rock units to thermally and hydrologically equilibrate to a temperature gradient from the atmosphere to the water table, and an infiltration flux. The rock units are also assigned linear, saturation-dependent values of thermal conductivity and specific heat. Other operational details and input parameters are the same as outlined for the MULTIFLUX-Con model in Section 6.2.2.1.

6.4.2 Results

A comparison between the MULTIFLUX-Con and MULTIFLUX-Full numerical models addresses the validation of the conceptual model by assessing the impacts of water and water vapor mass transport on ventilated drifts. MULTIFLUX-Full incorporates every component of the conceptual model for heat (sensible and latent) and mass transfer in and around a ventilated emplacement drift (processes 1 through 6 of Section 6.1.1 and 6.3.1). The following sections describe the similarities and differences in temperature, heat flux, heat removal ratio, near-field rock dryout, and relative humidity of the ventilated air between the MULTIFLUX-Full and MULTIFLUX-Con numerical models.

6.4.2.1 Temperature Comparisons for the MULTFLUX-Full and MULTIFLUX-Con Models

MULTIFLUX-Full exhibits the same temperature trends as the ANSYS and MULTIFLUX-Con numerical models. Figures 6-14 shows the MULTIFLUX-Full and MULTIFLUX-Con temperature results as a function of time for locations near the drift entrance, drift middle, and drift exit. Figure 6-15 shows results as function of distance from the drift entrance for times around the maximum, median, and minimum temperatures. Table 6-7 summarizes the temperature results.

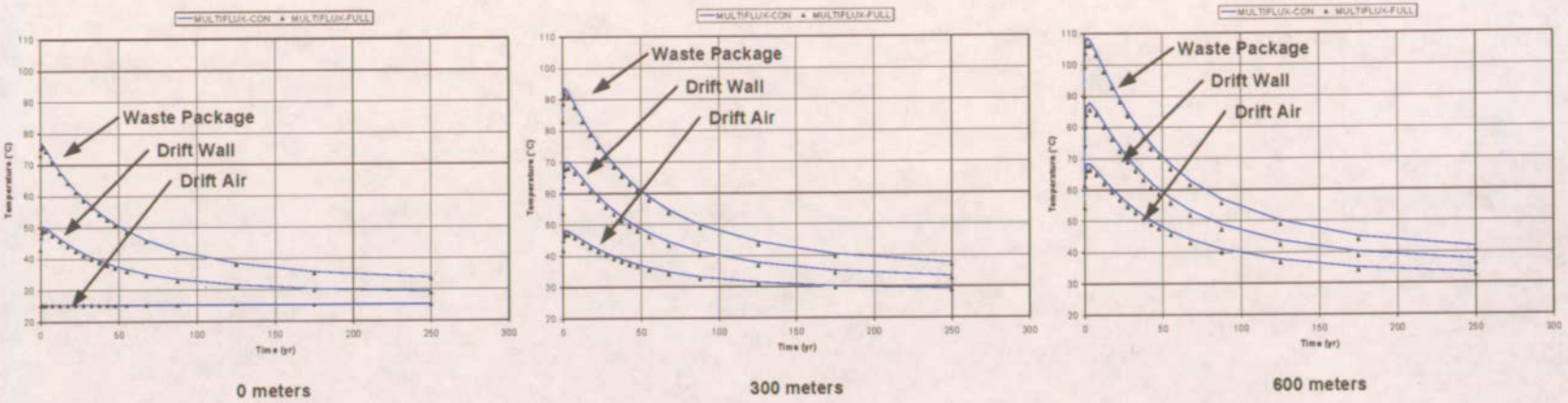

Figure 6-14. Plots of Waste Package, Drift Wall, and Drift Air Temperatures as a Function of Time at 0, 300, and 600 Meters from the Drift Entrance for the MULTIFLUX-Con and MULTIFLUX-Full Ventilation Numerical Models (DTN MO0209MWDMUL30.002)

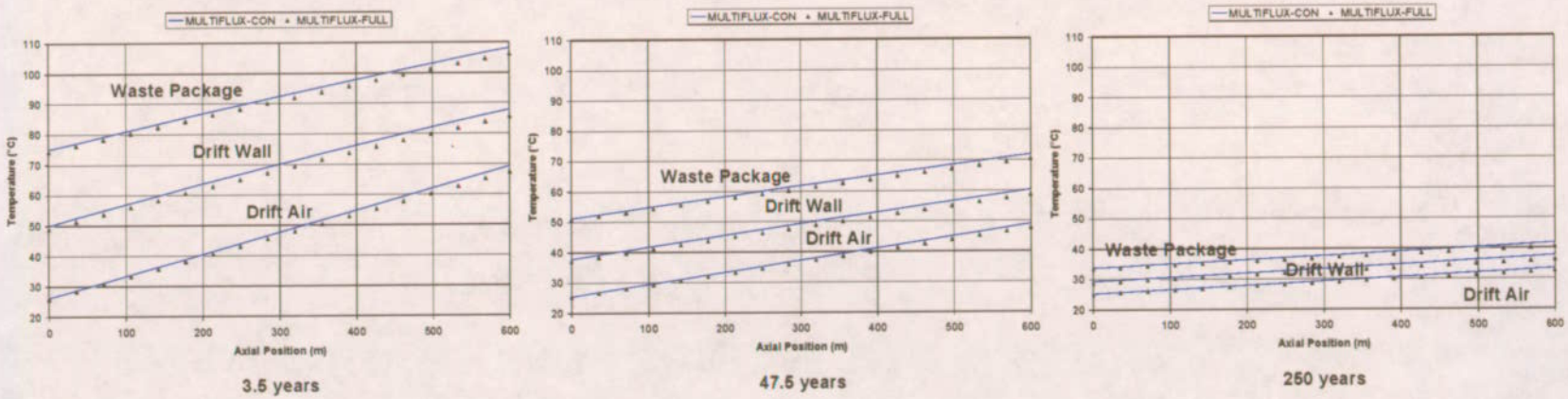

Figure 6-15. Plots of Waste Package, Drift Wall, and Drift Air Temperatures as a Function of Drift Length at 3.5, 47.5, and 250 Years from the Time of Waste Emplacement for the MULTIFLUX-Con and MULTIFLUX-Full Ventilation Numerical Models (DTN MO0209MWDMUL30.002)

Table 6-7. Summary of Waste Package, Drift Wall, and Drift Air Temperatures for the MULTIFLUX-Con and MULTIFLUX-Full Numerical Models

		Drift Entrance (0 m)			Drift Middle (300 m)			Drift Exit (600 m)		
		Temperature (°C)								
		Waste Package	Drift Wall	Drift Air	Waste Package	Drift Wall	Drift Air	Waste Package	Drift Wall	Drift Air
MULTFLUX-Con	3.5 years	74.8	49.7	25.0	90.5	69.8	47.7	105.7	87.6	68.4
MULTIFLUX-Full		74.2	48.8	25.0	90.8	68.0	46.8	106.0	85.4	66.7
MULTFLUX-Con	47.5 years	51.0	37.5	25.0	61.5	49.1	37.0	71.6	60.0	48.7
MULTIFLUX-Full		50.7	37.0	25.0	60.6	48.0	36.5	70.3	58.5	47.6
MULTFLUX-Con	250 years	33.5	29.1	25.0	37.4	33.1	29.0	41.5	37.3	33.2
MULTIFLUX-Full		33.3	28.8	25.0	36.9	32.5	28.7	40.5	36.2	32.5

The MULTIFLUX-Full raw data is fit in the same as the MULTIFLUX-Con and is documented in Attachment VIII. The temperature distributions for the two numerical models are within 2°C at all locations from the drift entrance and for all times. The MULTIFLUX-Full temperatures at all three components (drift wall, waste package, and air) are generally lower than the corresponding MULTIFLUX-Con values. Such a situation would be expected if the heat transfer within the rock domain were more effective in the MULTIFLUX-Full model. Several physical processes are simulated in the MULTIFLUX-Full numerical model that affect the rock domain heat and mass transfer, and hence affect the temperature distribution.

- Evaporation of pore water (which occurs at all temperatures, with increasing rate at higher temperatures) changes the thermal conductivity and heat capacity of the host rock. In turn the lower thermal conductivity of drier rock results in a steeper temperature gradient and higher drift wall temperature. The degree of dryout around the drift can be quantified by post-MULTIFLUX NUFT runs using the drift wall histories as boundary conditions. The results of these calculations are discussed later in Section 6.4.2.4.
- The evaporation and condensation of water creates local heat sinks and sources in host the rock.. These local sources and sinks change local temperature gradients and distributions and, hence, heat flows leading to local storage of energy at different rates than the MULTIFLUX-Con numerical model. Evaporation near the drift wall and condensation farther from the drift wall result in a flatter temperature gradient, but more effective heat transfer. These effects result in lower drift wall temperature.
- The movement of mobilized water vapor and liquid (condensate) carry sensible heat as they travel around the system. MULTIFLUX-Full calculates the water vapor that moves into the drift. Post-MULTIFLUX calculations demonstrate that the cooling of this vapor from the drift wall temperature to the airflow temperature does not add a significant amount of heat flux to the airflow, or significantly change the ventilation heat removal ratio. These results are discussed in Section 6.4.2.3.

6.4.2.2 Heat Flux Comparisons for the MULTFLUX-Full and MULTIFLUX-Con Models

The *temperature differences* between the waste package, drift wall, and air are similar for the two numerical models. Figure 6-16 shows the energy fluxes, similarly to what was done previously for ANSYS-Refined, for the two MULTIFLUX numerical models at two times and locations, using the nomenclature introduced in Figure 6-1 that describes the conceptual model (Section 6.1), and the times and locations selected in Section 6.4.2.1. The convection and radiation heat fluxes in Figure 6-16 are calculated as discussed in Section 6.2.3.3. The energy balance at the waste package is similar for each numerical model, with the two-dimensional hand calculation of radiation heat transfer from the temperatures under-predicting the actual three-dimensional radiation heat flux from the numerical model. The separation of the waste package thermal output into radiation and convection agrees for the two numerical models.

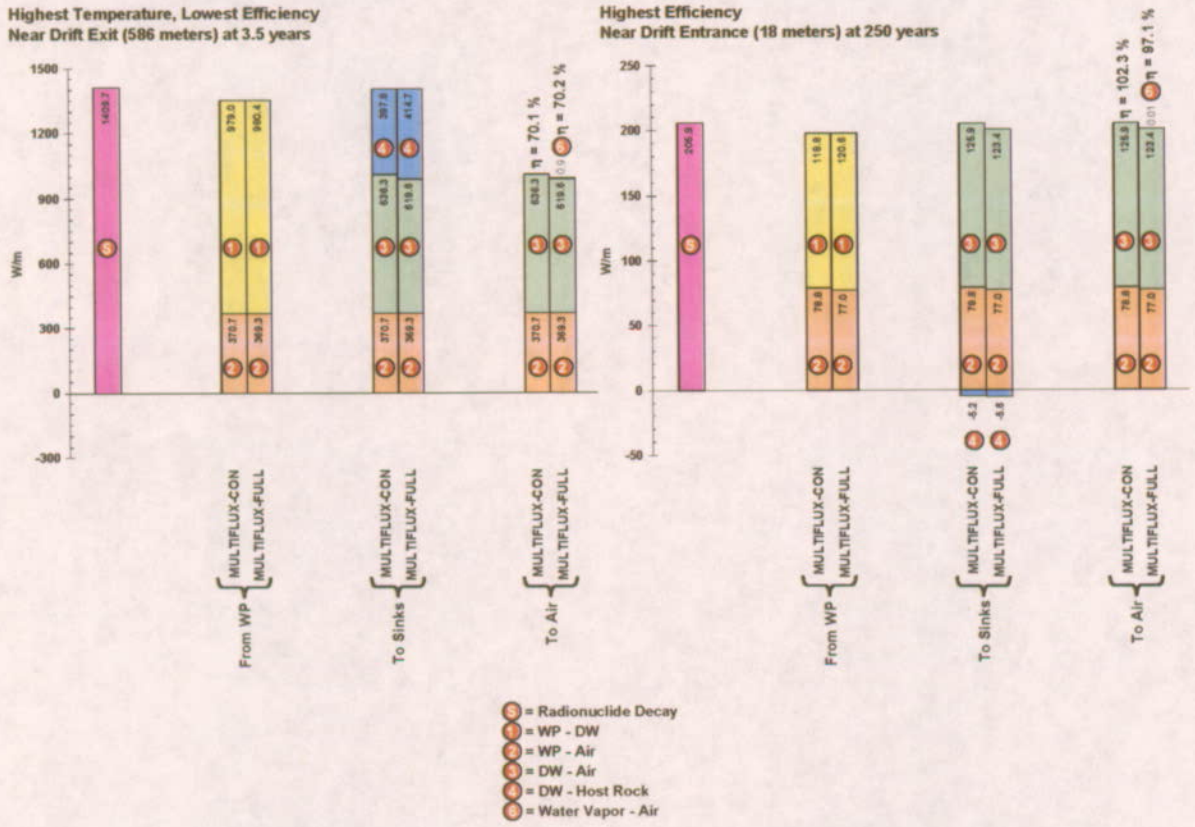

Figure 6-16. Heat Flux Distribution for the MULTIFLUX-Con and MULTIFLUX-Full Ventilation Numerical models at the Time and Location of the Highest Temperatures (left chart) and Ventilation Heat Removal Ratio (right chart)

The MULTIFLUX heat sinks balance is a calculation from temperatures and fluxes provided by the software. For the highest temperature situation (3.5 yr, 586 m), the two numerical models produce similar, but not identical, separation of heat flows into the two heat sinks (air and rock) from the two engineered surfaces (waste package and drift wall). For the highest efficiency

situation (250 yr, 18 m), only the MULTIFLUX-Con numerical model calculates more heat being convected to the air than is released by radionuclide decay. However, the MULTIFLUX-Full is very near that situation, with less than 3% of the waste package thermal power being conducted into the rock. This trend to higher ventilation efficiency is weaker for the MULTIFLUX-Full numerical model, consistent with the slightly lower drift wall temperature histories in that model and, hence, the slightly flatter in-rock temperature gradients.

6.4.2.3 Heat Removal Comparisons for the MULTFLUX-Full and MULTIFLUX-Con Models

The heat flow into the air heat sink also agrees for the two models in the highest temperature situation (3.5 yr, 586 m), with a consequent ventilation heat removal ratio of 70.1 and 70.2%, for the MULTIFLUX-Con and MULTIFLUX-Full numerical models, respectively. This is the lowest efficiency calculated at any location or time after the temperature peak. In the highest efficiency situation (250 yr, 18 m), the MULTIFLUX-Full temperatures (air, waste package, and drift wall) are all lower than for MULTIFLUX-Con. More importantly, the temperature differences controlling convection (WP-air, DW-air) are lower for MULTIFLUX-Full, and the temperature difference controlling radiation (WP-DW) is higher for MULTIFLUX-Full. This results in a smaller fraction of the energy being used to heat air.

The overall heat removal ratio for the two numerical models is shown in Table 6-8. The overall heat removal ratio is the total heat removed from the entire drift during the ventilation duration, divided by the total heat added to the drift by radionuclide decay during the same time period. The MULTIFLUX-Full overall efficiency is ~2% less than the conduction-only numerical model for a 50-yr ventilation duration, and about 4% less for a 300-yr ventilation duration. These lower efficiencies are consistent with the lower temperatures in the MULTIFLUX-Full results. The vaporization of pore water (at temperatures below the boiling point) followed by condensation at locations farther from the drift forms a heat pipe that reduces the in-rock temperature gradient while transferring heat through the rock domain more effectively than simple conduction. The more effective heat transfer in the rock reduces ventilation efficiency. Equivalently, the lower temperatures reduce the temperature differences that drive convection, reducing ventilation efficiency for a given heat source.

Table 6-8. Overall ventilation heat removal ratio calculated by MULTIFLUX-Con and MULTIFLUX-Full, for the 600 meter drift split (for 50 and 300 yr ventilation durations)

Numerical Model	50 yr Ventilation Duration	300 yr Ventilation Duration
MULTIFLUX-Full	84.3%	90.1%
MULTIFLUX-Con	86.3%	94.0%

6.4.2.4 The Effects of Latent Heat and Near-Field Dryout in the Host Rock for the MULTIFLUX-Full Model

Of the four ventilation numerical models, MULTIFLUX-Full was the only model to simulate the competing effects of latent heat removal and near-field dryout of the host rock. The effect of latent heat removal caused by an increase in the host rock and in-drift air water vapor content due to the vaporization of matrix pore water tend to lower temperatures with time and length

down the drift. However, as the liquid water present in the near-field host rock is vaporized, the thermal conductivity of the rock decreases. The effect of reducing the rock thermal conductivity tends to raise near-field rock temperature gradient, and hence temperatures, with time and length down the drift. As evident in the overall slightly lower temperature differences between the hot surfaces and the air for the MULTIFLUX-Full numerical model as compared to MULTIFLUX-Con, the latent heat removal effect on temperature is slightly stronger than the rock dryout effect.

Figures 6-17 and 6-18 illustrate the change in liquid saturation of the near field host rock at three different times for three different locations along the length of the drift. The locations represent the midpoints of the third, eighth, and fourteenth computational cells at which the DISAC module of MULTIFLUX balanced the direct NUFT and CFD results (or approximately 88, 265, and 479-meters from the drift entrance). At other locations, the DISAC balance is done with interpolated matrix values. In general, the near-field host rock above the springline of the drift remains at or near its ambient condition throughout the entire pre-closure period for at least the first 265-meters from the drift entrance. This indicates that, for some distance from the drift entrance (at least the first 265-meters), the temperature and ventilation effects that dry the near-field host rock above the springline of the drift are balanced with the ability of the matrix to rewet due to capillary effects and gravity drainage.

The host rock below the drift shows a tendency to dry with both time and length from the drift entrance, before any significant dryout occurs above the springline. This preferential dryout below the drift is attributed to temperature and ventilation effects overcoming the influx of recharge due to capillary effects within the drift shadow. Significant host rock dryout caused by heat and ventilation occur in all radial directions from the drift wall by the fourteenth chimney, or 479-meters from the drift entrance. The maximum change in saturation from about 97% down to 22% occurs around the 50-year mark. After 50 years, the host rock began to re-wet, which coincides with a decrease in the slopes of the drift wall temperature curves.

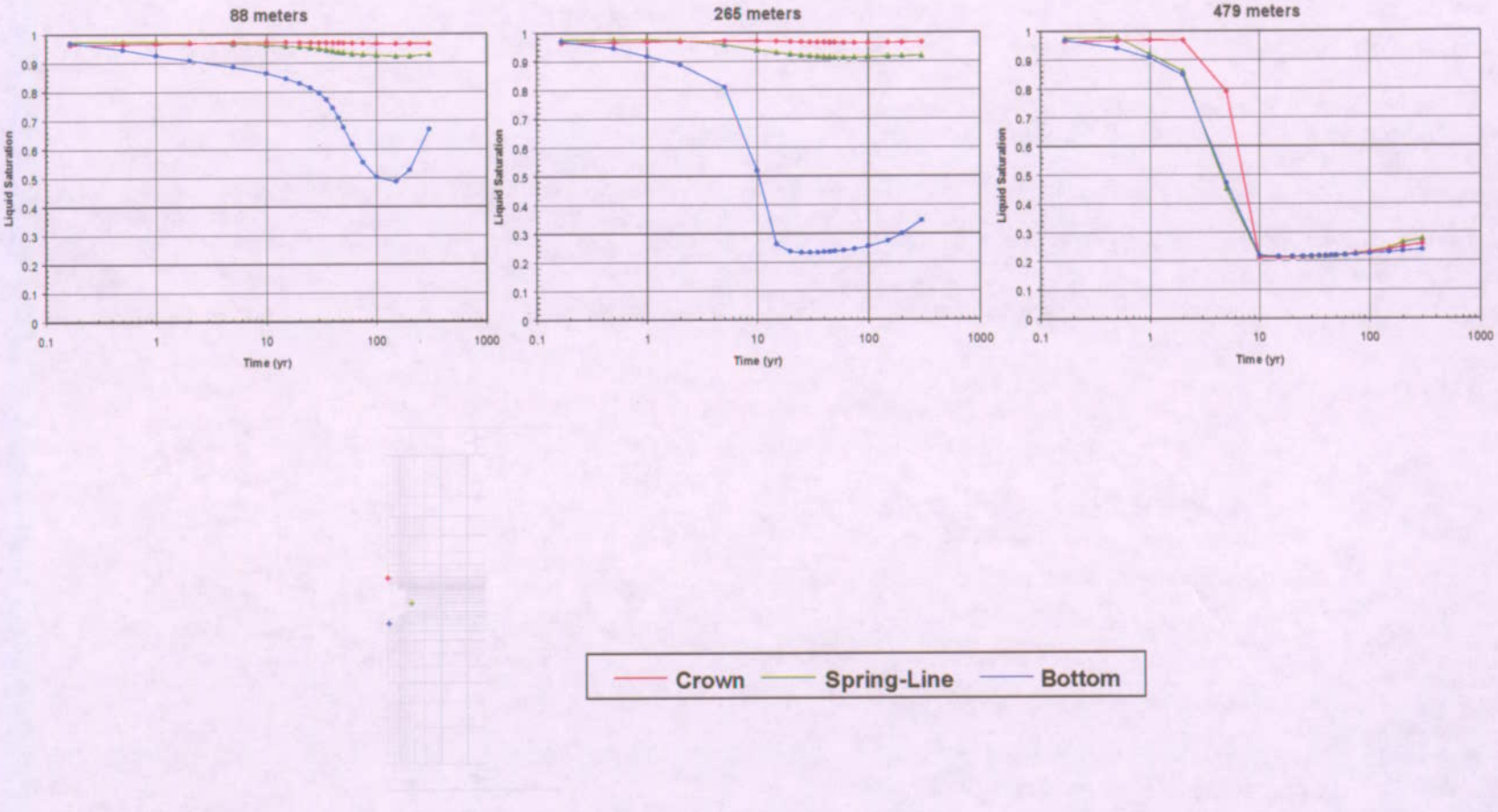

Figure 6-17. Plots of Matrix Liquid Saturation at 88, 265, and 479 meters for the MULTIFLUX-Full Ventilation Numerical Model (DTN MO0209MWDMUL30.002)

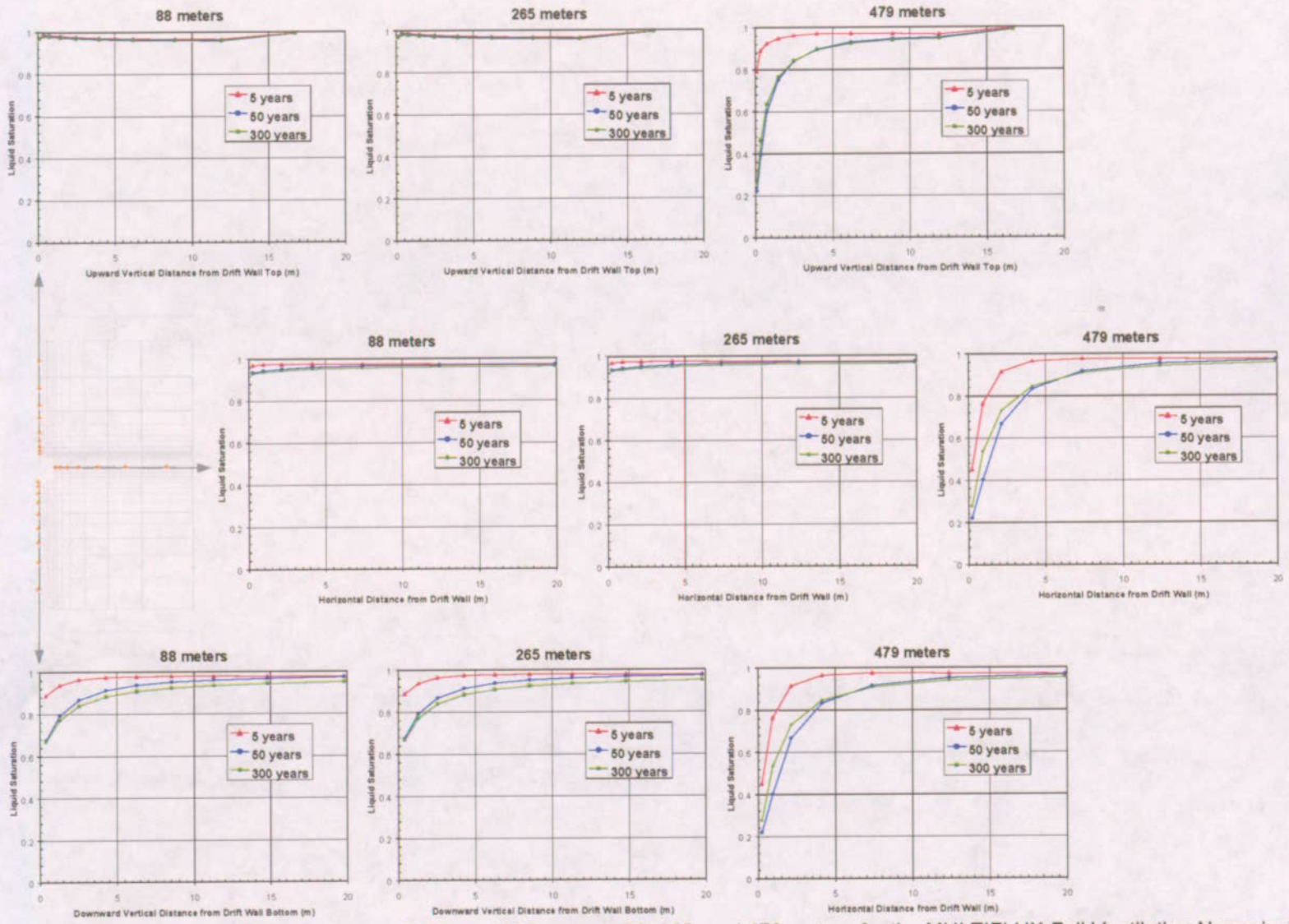

Figure 6-18. Matrix Liquid Saturation at 5, 50, and 300 years at 88, 265, and 479 meters for the MULTIFLUX-Full Ventilation Numerical Model (DTN MO0209MWDMUL30.002)

For the fourteenth chimney at its deepest radial location from the drift wall, the drying front caused by heat and ventilation reaches about 6 meters upwards and about 12 meters horizontally along the drift springline. The extent of the dryout front downward was greater than 12 meters, but this represented the combined effects of heat, ventilation, and drift shadow. In all, the dryout caused by heat and ventilation affects a significant volume of the near-field host rock.

6.4.2.5 In-Drift Relative Humidity for the MULTIFLUX-Full Model

The change in temperature of the drift air as it transits the drift split, and the water vapor added to the air from the host rock, change the relative humidity. Table 6-9 shows the relative humidity at its initial condition at the drift entrance, and at the drift exit for times when the temperature is near its maximum, median, and minimum values temperature.

Table 6-9. Relative Humidity at the Drift Split Entrance and Exit for MULTIFLUX-Full

Numerical Model	Drift Entrance	Drift Exit at 3.5 yr (time near peak temperature)	Drift Exit at 47.5 yr	Drift Exit at 250 yr
MULTIFLUX-Full Temperature	25°C	66.7°C	47.6°C	32.5°C
MULTIFLUX-Full (including water vapor transported across the drift wall)	30.0%	4.3%	9.6%	20.2%

6.5 VERIFICATION OF THE NUMERICAL MODELS

Sections 6.2.3 and 6.4.2 present a detailed verification process where the results of the ANSYS-Coarse, ANSYS-Refined, MULTIFLUX-Con, and MULTIFLUX-Full models are compared to each other. Besides these comparisons, various other model verification approaches were taken to assure that the numerical application of the ventilation conceptual model conserved both energy and mass. These verification approaches are outlined in Table 6-10, in addition to those presented in earlier sections. The approaches that use submodel comparisons are intended to separate the coupled heat and mass transfer mechanisms into individual components in which a single phenomenon of heat or mass transfer mechanism can be investigated. The results of these submodels are compared to each other, and where applicable, to analytical or text book solutions.

Table 6-10. Verification Methods

Numerical Application Requiring Verification	Description	Verification Method	Section
In-drift radiation heat transfer	Two-dimensional steady-state radiation heat transfer between concentric horizontal cylinders	Submodel comparison using ANSYS, MULTIFLUX, NUFT/RADPRO-rectangular mesh, NUFT/RADPRO-cylindrical mesh, Analytical solution	6.5.1.1
In-drift convection heat transfer	Two-dimensional steady-state forced convection heat transfer between concentric horizontal cylinders	Submodel comparison using ANSYS, NUFT-rectangular mesh, NUFT-cylindrical mesh, Analytical solution	6.5.1.2
Host rock conduction	Two-dimensional (cylindrical) temperature dependent thermal conductivity heat conduction, with saturation- dependent thermal conductivity	Submodel comparison using ANSYS, NUFT, Analytical Solution by Carslaw and Jaeger	6.5.2.1
	One-dimensional heat conduction caused by a 1°C step change at a boundary, with saturation- dependent thermal conductivity	Submodel comparison using NUFT-AFM/DKM, Analytical Solution by Carslaw and Jaeger	6.5.2.2
	One-dimensional conduction, back-calculating saturation-dependent thermal conductivity from the heat flux	Submodel comparison using NUFT	6.5.2.3
Ventilation Model (i.e. coupled in-drift and host rock heat transfer)	Discretization of the drift along its length	Model comparison using ANSYS-Coarse, ANSYS-Refined	6.2.3.1
	ANSYS Methodology versus the MULTIFLUX Methodology	Model comparison using ANSYS-Refined, MULTIFLUX-Con	6.2.3.2 through 6.2.3.4
	Assessing the effects of water and water vapor on the coupled heat and mass transfer processes	Model comparison using MULTIFLUX-Con, MULTIFLUX-Full	6.4.2.1 through 6.4.2.4

6.5.1 In-Drift Domain

Verification exercises involving in-drift radiation and convection heat transfer were investigated. The first group of submodels focuses on the two-dimensional (or radial) radiation heat transfer between the in-drift waste package and the drift wall. The second set or submodels is a duplication of the first, but uses forced convection heat transfer instead of radiation.

6.5.1.1 Submodels for Two Dimensional Radiation Heat Transfer between the Waste Package and Drift Wall

The submodels used to validate two-dimensional radiation heat transfer between the waste package and drift wall use a modified ANSYS simulation, a MULTIFLUX (CFD only) simulation, two different NUFT simulations, and an evaluation of an analytical solution. Each

submodel was run to steady state (using a constant heat source and constant drift wall temperature), at which time the waste package temperatures were compared.

The ANSYS and MULTIFLUX (CFD only) submodels used the same cylindrical mesh geometry and inputs as those used in the ventilation numerical models documented in Section 4 and 6.2, with the exception that a constant heat source of 1 kW/m was applied to the waste package rather than the exponential heat decay for repository models. The temperature of the drift wall was held constant at 25°C, and there was no forced ventilation. These problem specifications eliminate both heat transfer by conduction into the rock, and convection into the air, to isolate the radiation heat transfer mechanism.

Cylindrical and rectangular meshes were used for the two NUFT submodels. Similar to the ANSYS case, the drift wall was assigned a constant temperature of 25°C and the waste package was a constant source with a heat flux of 1 kW/m. RADPRO was run to determine the appropriate view factors for the NUFT model.

ANSYS uses a gray body to gray body model to simulate radiation heat transfer. Since NUFT and MULTIFLUX simulate gray body to black body radiation, the emissivities had to be adjusted to produce equal radiation heat transfer to the ANSYS numerical model that calculates gray body to gray body radiation. The equation for gray to gray body radiation heat transfer for infinite concentric cylinders where the view factor is one is as follows (Incropera and DeWitt 1996):

$$q_{12} = \frac{\sigma A_1 \left(T_1^4 - T_2^4\right)}{\frac{1}{\varepsilon_1} + \frac{1-\varepsilon_2}{\varepsilon_2}\left(\frac{r_1}{r_2}\right)}$$

Eq. 6-12

where

q_{12} = radiative heat transfer per unit length from the inner cylinder (1) to the outer (2) (W/m)
σ = Stefan-Boltzmann constant 5.670×10^{-8} W/m^2·K^4
A_1 = surface area per unit length of the inner cylinder (m^2/m)
T_1 = surface temperature of the inner cylinder (K)
T_2 = surface temperature of the outer cylinder (K)
ε_1 = surface emissivity of the inner cylinder
ε_2 = surface emissivity of the outer cylinder
r_1 = radius of the inner cylinder (m)
r_2 = radius of the outer cylinder (m)

The equation for gray to black body radiation heat transfer for the same case of infinite concentric cylinders is as follows (Incropera and DeWitt 1996):

$$q_{12} = \varepsilon_{eff}\sigma A_1\left(T_1^4 - T_2^4\right)$$

Eq. 6-13

where

q_{12} = radiative heat transfer from the inner cylinder (1) to the outer (2) (W)
ε_{eff} = effective emissivity of the gray body (subscript 1) when radiating to another gray body that is represented by a black body in the equation
σ = Stefan-Boltzmann constant 5.670×10^{-8} W/m^2·K^4
A_1 = surface area of the inner cylinder (m^2)
T_1 = surface temperature of the inner cylinder (K)
T_2 = surface temperature of the outer cylinder (K)

The equivalent gray to black body emissivity for the gray to gray body case is found by equating Equations 6-12 and 6-13 and solving for ε_{eff}:

$$\varepsilon_{eff} = \frac{1}{\frac{1}{\varepsilon_1} + \frac{1-\varepsilon_2}{\varepsilon_2}\left(\frac{r_1}{r_2}\right)}$$

Eq. 6-14

Using emissivities of 0.87 for the waste package and 0.90 for the drift wall in the ANSYS numerical model, the equivalent gray body to black body emissivity for NUFT and MULTIFLUX was calculated to be 0.847 using Equation 6-14.

The steady state waste package temperature was also evaluated analytically using Equation 6-12 for radiation heat transfer between concentric cylinders.

Table 6-11 summarizes the results. It should be noted that the temperatures for the ANSYS and MULTIFLUX (CFD) submodels are taken at the surface of the elements representing the waste package. NUFT uses a finite difference scheme, so the temperatures are obtained at the center of an element. No significant difference temperature gradient was found from the cell center to the edge because the elements are relatively small and each has a relatively high thermal conductivity. Each submodel was similar to the analytical solution. The NUFT cylindrical submodel matched the analytical solution perfectly. The ~1°C under prediction of the waste package temperature for the NUFT rectangular submodel was likely due to the slight errors in computing view factors of stair-step elements. The difference between the ANSYS and analytical solution was due to numerical error associated with the time stepping. The MULTIFLUX submodel produced the largest under prediction of waste package temperature, but was within ~8% of the analytic solution (when expressed as the error divided by the temperature difference between the drift wall and waste package). This difference could be due to the alternating fine (10 cm) and coarse (~2.5 m) axial zoning due to the gaps and waste packages, which could have led to errors in view factors.

Table 6-11. Waste package Temperatures for the Two Dimensional Radiation-Only Submodel

Method	$T_{waste\ package}$ at Steady State (°C)	$T_{model} - T_{analytical}$ (°C)
In-Drift Radiation Only Model (1 kW/m heat load, 0.847 effective emissivity)		
Analytical	58.8	Na
ANSYS	57.7	-1.1
NUFT – Rectangular	57.9	-0.9
NUFT- Cylindrical	58.8	0.0
MULTIFLUX (CFD)	56.2	-2.6

6.5.1.2 Submodels for Two Dimensional Forced Convection for the In-Drift Air Space

This submodel calculates two-dimensional forced convection heat transfer between concentrically located cylinders. The geometry and air flow rate are the same as those used in the full ANSYS and MULTIFLUX numerical models presented in Section 6.2 and 6.5.1.1. Each submodel includes a constant 1 kW/m waste package and a constant drift wall temperature of 25°C. Each submodel simulated a two-dimensional cross-section at the entrance of the drift where the in-drift air temperature was fixed at 25°C. Radiation was inactivated in each of these submodels.

For the ANSYS submodel, a convective heat transfer coefficient of 1.89 $W/m^2 \cdot K$ was used. The ANSYS gridding includes curved surfaces that closely approximates the geometry used for the analytical solutions.

For the two NUFT submodels, the convective heat transfer coefficient was converted to an equivalent thermal conductivity for the in-drift air, which is modeled as a porous medium with high permeability, using the following formula:

$$k_{th} = h \cdot dr \qquad \text{Eq. 6-15}$$

where

k_{th} = air boundary layer equivalent thermal conductivity ($W/m \cdot K$)
h = convective heat transfer coefficient ($W/m^2 \cdot K$)
dr = air boundary layer element thickness (m)

The NUFT-cylindrical gridding is also similar to the ANSYS and analytic geometry. The NUFT-rectangular gridding uses a Cartesian (stair-step) approximation of the curved surfaces of the cylindrical components. The perimeter of the stair-stepped waste package (computed by summing the exposed lengths of the outmost waste package elements) was equal to the perimeter of the circular ANSYS waste package and drift wall. Thus, the waste package and drift wall surface areas per unit length for each model were equal. This submodel was run in recognition that the MSTH model (BSC 2001) uses rectangular gridding (because cylindrical meshes in NUFT must be oriented parallel to the gravity vector for coupled heat and mass transport calculations). Also, because other effects within the remainder of the host rock domain do not

complicate this submodel, its results provide insights into evaluating the rock domain submodels described in Section 6.5.2.

Each of the submodel steady state waste package temperatures was compared to the result of the analytical solution, and is reported in Table 6-12. Newton's Law of Cooling for convection as applied to horizontal concentric cylinders is (Incropera and DeWitt, 1996):

$$q_{12} = hA_1(T_1 - T_2)$$

Eq. 6-16

where:

q_{12} = convection heat transfer from the inner cylinder (1) to the outer (2) (W)
h = convective heat transfer coefficient (W/m^2·K)
A_1 = surface area of the inner cylinder (m^2)
T_1 = surface temperature of the inner cylinder (K)
T_2 = surface temperature of the outer cylinder (K)

Table 6-12. Waste Package Temperatures for the Two-Dimensional Convection-Only Submodel

Method	$T_{waste\ package}$ at Steady State (°C)	$T_{model} - T_{analytical}$ (°C)
In-Drift Convection Only Model (1 kW/m heat load, 1.89 W/m^2 K convective heat transfer coefficient)		
Analytical	113.2	NA
ANSYS	113.0	-0.2
NUFT - rectangular	115.9	2.7
NUFT - cylindrical	113.4	0.2

Agreement between the analytical, ANSYS, and NUFT cylindrical model results is around 3%. The NUFT rectangular submodel result is only within 10% of the analytical solution. These results indicate that cylindrical meshing around the curved surfaces of the waste package and drift wall is more desirable than the stair-stepping approach. Note that for MULTIFLUX, the only stair-step approximations of curved surfaces are in the rock domain.

6.5.2 Host Rock Domain

Three validation submodels involving the near-field host rock conduction heat transfer were investigated. The first conduction-only submodel investigates the temperature response of the near-field host rock using a concentric cylinder arrangement similar to that used in the ventilation models. The second submodel calculates one-dimensional conduction using saturation-dependent thermal conductivity. The heat flow is initiated by a 1°C step change at one end of a finite domain. The third conduction submodel uses a similar setup as the first; however, in this case the thermal conductivity of the near-field host rock was back calculated from the heat flux. The intent of this submodel is to verify the way in which NUFT determines the rock thermal conductivity based on matrix liquid saturation.

6.5.2.1 Two Dimensional Conduction in the Host Rock Region Bounded Internally by a Cylindrical Drift

The first submodel calculates two-dimensional conduction in the host rock using a heat flux boundary condition at the drift wall. This submodel used ANSYS, NUFT, and an analytical solution by Carslaw and Jaeger to compute the host rock temperature evolution at a location some distance from the drift wall.

The ANSYS and NUFT simulations again used the geometries and meshes discussed for the previous submodels. Above and below the repository horizon, the elements representing the lithostratigraphic units were modified to represent a homogeneous media with matrix and fracture material and thermal properties of tsw-35. This facilitated a comparison to an analytical solution. The primary state variables (temperature, pressure, and liquid saturation) were fixed for the top and bottom boundaries to represent the atmosphere and the water table. Also, adiabatic (no heat flow) and no-mass-flow boundaries were implemented at the lateral edges of the domain (40.5 m from the cylinder axis). Because conduction was the only method of heat transfer being investigated for this submodel, the elements representing the waste package and open drift were modified to act as a single heat source. A constant heat source of 0.2 kW/m was distributed among these elements resulting in a constant heat flux into the host rock. This value of heat flux was chosen to produce repository-like drift wall temperatures. The thermal conductivity of the rock was held constant at the value representing 100% liquid saturation, and the permeability was set to zero, which ensured that the saturation did not change during NUFT the calculation.

MATHCAD was used to evaluate an analytical solution for conduction (Carslaw and Jaeger 1956) for the transient temperature response as a function of location from a constant heat source applied to the surface of an infinite domain bounded internally by a circular cylinder. Because the analytical solution represents an infinite domain, it is only suitable for comparison to the ANSYS and NUFT simulations at early times, before the simulations are influenced by the finite boundaries.

The results for the ANSYS and NUFT simulations, and for the analytical solution are shown in Table 6-13 and Figure 6-19. The plot shows the transient temperature response at a point 6 meters horizontally from the center of the drift (3.25 meters from the 5.5-m-diameter drift wall). For very early times (less than 1 year), the drift wall temperature change is small, and the grids may be too coarse to capture the detailed temperature fields. This early-time issue is more severe for the NUFT-rectangular grid since the heat flow during this early time will be significantly influenced by the stair-step boundary condition. For times between 5 and 10 years, the agreement between the numerical models and the analytic solution is within 1°C, and the two numerical models have identical results. Both the temperature and percentage accuracies increase as the number of grid elements involved in the heat flow increases (effectively increasing resolution). At 30 and 50 years, the numerical simulations become progressively warmer than the analytic solution. Due to the small rock thermal diffusivity ($\sim 1 \times 10^{-7}$ m^2/s), and the large size of the rock pillars (40.5 m to the mid-pillar), the numerical solutions are expected to be progressively warmer than the analytic solution after several decades. After that time, the

insulating effect of the adiabatic lateral boundaries affects the numerical solution, while the analytic solution does not include these boundaries.

The agreement (during the applicable time period) between the analytical and numerical solutions provides insight into the full model calculations in Section 6.4. That is, differences between the conduction-only MULTIFLUX-Con numerical model and the MULTIFLUX-Full model can be attributed to the effects of phase change and mass transport.

Table 6-13. Host Rock Conduction Verification

Host Rock Conduction Only Model (0.2 kW/m heat flux at the drift wall, homogenious with tsw-35 properties, T_0 = 27.3°C, k = 0 to preclude mass transport)					
Method	T_{DW} (°C)				
	1 yr	**5 yr**	**10 yr**	**30 yr**	**50 yr**
Analytical	34.8	44.6	50.0	57.7	61.6
ANSYS	35.6	45.6	50.5	59.4	65.0
NUFT-Rectangular	37.3	45.6	50.5	59.8	65.6
	$T_{DW(model)} - T_{DW(analytical)}$ (°C)				
ANSYS	0.8	1.0	0.5	1.7	3.4
NUFT-Rectangular	2.5	1.0	0.5	2.1	4.0
	$(T_{DW(model)} - T_{DW(analytical)}) / (T_{DW(analytical)} - T_{0(model)})$				
ANSYS	11%	5.8%	2.2%	5.6%	9.9%
NUFT-Rectangular	33%	5.8%	2.2%	6.9%	12%

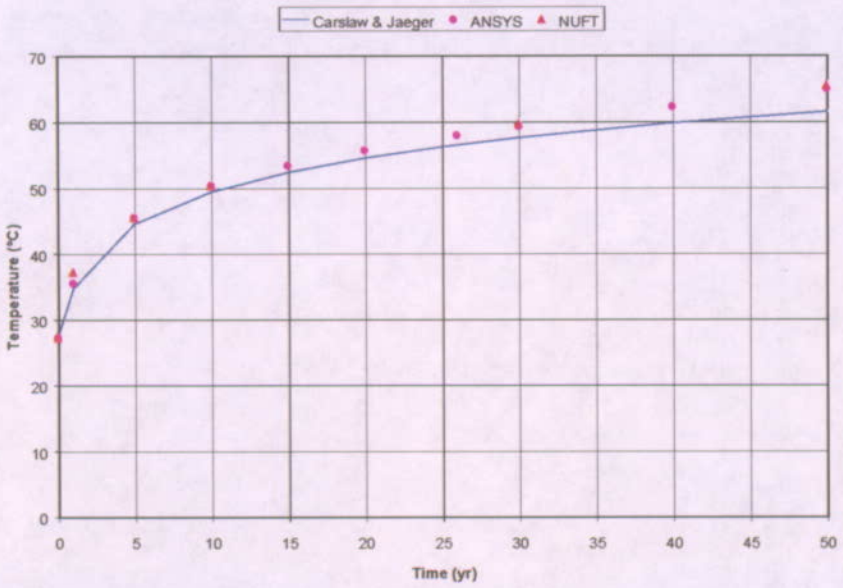

Figure 6-19. Analytical, ANSYS, and NUFT Conduction-Only Transient Temperature Responses of a Homogeneous Porous Medium with Material and Thermal Properties of tsw-35 Rock (DTN MO0209MWDMOD30.003)

6.5.2.2 One Dimensional Saturation Dependent Conduction Submodel

In this submodel, a 40-meter long, one-dimensional mesh was used to calculate saturation-dependent thermal conduction. A temperature gradient was imposed on the submodel by assigning an arbitrary initial temperature of 20°C, and imposing a 21°C temperature at one end at time zero, while holding the other end at 20°C. NUFT was used to simulate the heat transfer using rock properties of tsw-35. An arbitrary liquid saturation of 50% was assigned to the matrix and permeability was set to zero to inhibit mass transfer. A solution to one-dimensional transient heat conduction by Carslaw and Jaeger (Carslaw and Jaeger 1959) was evaluated for comparison to the NUFT results. The response of temperature as a function of distance from the heated end, at four sequential times is shown in Figure 6-20. The transient response of temperature showed good agreement with the analytical solution.

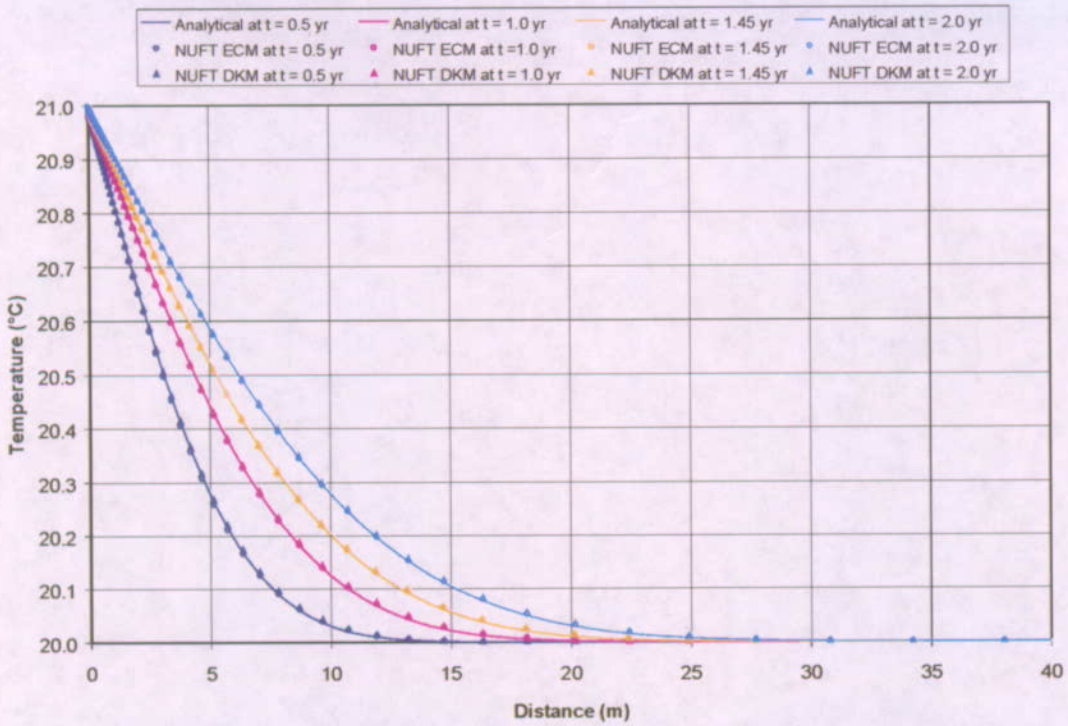

Figure 6-20. Transient Temperature Response for the NUFT Saturation Dependent Thermal Conduction Submodel as Compared to the Analytical Solution by Carslaw and Jaeger (DTN MO0209MWDMOD30.003)

6.5.2.3 Back-Calculation of Thermal Conductivity Submodel

This submodel demonstrates that NUFT properly calculates the thermal conductivity as a function of the liquid phase matrix saturation using the wet and dry conductivity values. It used the same one-dimensional mesh and boundary conditions as the submodel described in Section 6.5.2.1. The permeability of the rock unit was artificially set to zero to eliminate any fluid phase transport, which also forced the fluid phase saturation to remain constant. The submodel was run to steady state, and the heat fluxes were output for imposed values of liquid matrix saturation of 10, 25, 50, 75, and 100%. The effective rock thermal conductivity was computed from Fourier's Conduction Law (Incropera and DeWitt 1996):

$$q = k_{th} \frac{dT}{dl}$$

Eq. 6-17

For a homogeneous one-dimensional domain in steady state, with two imposed end temperatures, the temperature gradient is a constant that can be calculated from the boundary conditions:

$$q = k_{th} \frac{(T_1 - T_2)}{L}$$

Eq. 6-18

This equation can be rearranged to obtain the thermal conductivity:

$$k_{th} = \frac{qL}{T_1 - T_2}$$

Eq. 6-19

where:

k_{th} = thermal conductivity (W/m·K)
q = steady state heat flux (W/m^2)
l = axial distance from the zero location (m)
L = length (m)
T_1 = temperature at l = 0 m (K)
T_2 = temperature at l = L m (K)

The results, plotted in Figure 6-21, match a straight line which represents a linear interpolation between arbitrarily chosen values for dry and wet thermal conductivity.

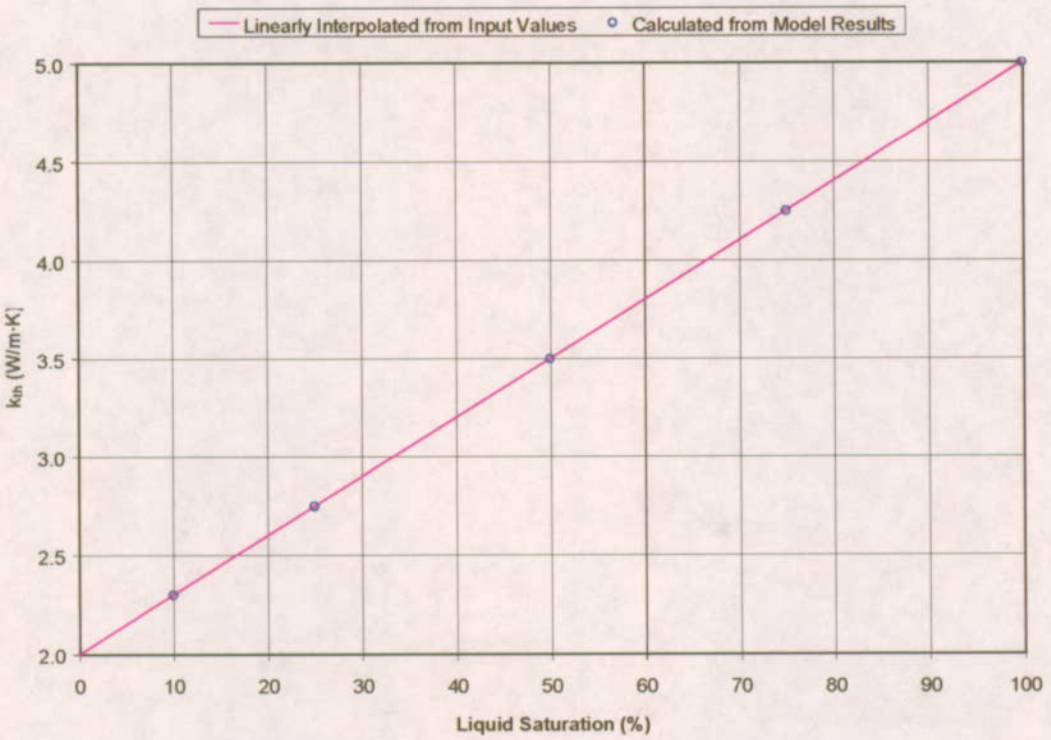

Figure 6-21. Back-Calculation of Thermal Conductivity for a Porous Media at Various Levels of Saturation Compared to a Linear Interpolation Between the Dry and Wet Values for Thermal Conductivity (DTN MO0209MWDMOD30.003)

6.6 APPLICABILITY OF WALL HEAT FRACTION TO DOWNSTREAM MODELS

The wall heat fraction is defined as one minus the ratio of heat removed by the ventilation to the heat generated by the waste package. The wall heat fraction can be expressed as a single value by integrating over both the duration of the pre-closure period and the length of the drift. It may also be applied as a function of time and drift length. Downstream models that do not explicitly model the ventilation period may implement the wall heat fraction in one of two ways during their preclosure runs to initialize their postclosure runs.

The first way is to introduce the heat flux adjusted by the wall heat fraction directly to the drift wall. Typically, a downstream model that uses the wall heat fraction in this manner does not model the in-drift components. Since the definition of the wall heat fraction is the amount of waste package heat delivered to the drift wall during the ventilation period, this method is the most straightforward. In this case, the only heat transfer mechanism being simulated is the conduction from the drift wall out to the host rock. Because the solution of the heat conduction equation is linear in nature with constant temperature heat sinks at the upper and lower boundaries of the domain, a unique solution for the temperature of the drift wall exists. Therefore, this method will result in both the same heat flux at the drift wall and the same drift wall temperature history as that predicted by the ventilation model from which the wall heat fraction was derived.

The second way the wall heat fraction may be used involves downstream models that include the in-drift components in their domains. These models typically reduce the waste package heat generation rate by the wall heat fraction and apply this new heat flux directly to the waste package rather than the drift wall. This type of application relies on both radiation and conduction heat transfer to deliver the right amount of heat to the drift wall, and replicate the drift wall temperature history as predicted by the upstream ventilation model. This approach is less straightforward than the first and requires further discussion as to its feasibility.

6.6.1 Theoretical Use of the Wall Heat Fraction at the Waste Package

Consider the case where the waste package heat output reduced the wall heat fraction, as calculated by a ventilation model, is used as a substitute for the preclosure convection to represent the preclosure heat removal by ventilation. An energy balance for the ventilation model is:

$$Q_{wp} = Q_{conv-wp} + Q_{rad} \qquad \text{Eq. 6-20}$$

where

$$Q_{conv-wp} = A \cdot \left(T_{wp} - T_{air}\right) \qquad \text{Eq. 6-21}$$

$$Q_{rad} = C \cdot \left(T_{wp}^4 - T_{dw}^4\right)$$

Eq. 6-22

The fraction of heat removed by the ventilation (i.e. by convection) is:

$$\eta = \frac{Q_{conv-wp} + Q_{conv-dw}}{Q_{wp}}$$

Eq. 6-23

where

$$Q_{conv-dw} = B \cdot \left(T_{dw} - T_{air}\right)$$

Eq. 6-24

The constants A, B, and C are defined as:

$$A = d_{wp} \cdot h_{wp-air}$$

Eq. 6-25

$$B = d_{dw} \cdot h_{dw-air}$$

Eq. 6-26

$$C = d_{wp} \cdot h_{rad}$$

Eq. 6-27

Substituting equations 6-21 and 6-22 into 6-20 yields:

$$Q_{wp} = A \cdot \left(T_{wp} - T_{air}\right) + C\left(T_{wp}^4 - T_{dw}^4\right)$$

Eq. 6-28

Substituting equations 6-21, 6-22, and 6-24 into 6-23 yields:

$$\eta = \left[\frac{\left[A \cdot \left(T_{wp} - T_{air}\right) + B \cdot \left(T_{dw} - T_{air}\right)\right]}{\left[A \cdot \left(T_{wp} - T_{air}\right) + C \cdot \left(T_{wp}^4 - T_{dw}^4\right)\right]}\right]$$

Eq. 6-29

For the downstream model, the waste package heat output is multiplied by the wall heat fraction to account for the heat removed during the preclosure ventilation period. Equation 6-30 represents the fraction of heat delivered to the drift wall:

$$Q'_{dw} \equiv Q_{wp} \cdot (1 - \eta)$$

Eq. 6-30

Substituting equations 6-28 and 6-29 into 6-30 yields:

$$Q'_{dw} = \left[A \cdot \left(T_{wp} - T_{air}\right) + C \cdot \left(T_{wp}^4 - T_{dw}^4\right)\right] \cdot \left[1 - \frac{\left[A \cdot \left(T_{wp} - T_{air}\right) + B \cdot \left(T_{dw} - T_{air}\right)\right]}{\left[A \cdot \left(T_{wp} - T_{air}\right) + C \cdot \left(T_{wp}^4 - T_{dw}^4\right)\right]}\right]$$

Eq. 6-31

An energy balance for the downstream model considered in this case (i.e. where the wall heat fraction is used as substitute for the heat transfer via convection) is:

$$Q'_{dw} = Q'_{rad}$$

Eq. 6-32

where

$$Q'_{rad} = C \cdot \left(T'^4_{wp} - T'^4_{dw}\right)$$

Eq. 6-33

where

T'_{wp} = waste package temperature of the downstream model (K)

T'_{dw} = drift wall temperature of the downstream model (K)

Substituting equations 6-31 and 6-33 into 6-32 and simplifying yields:

$$\left(T'^4_{wp} - T'^4_{dw}\right) = \left(T_{wp}^4 - T_{dw}^4\right) - \frac{B}{C} \cdot \left(T_{dw} - T_{air}\right)$$

Eq. 6-34

If $T'_{wp} = T_{wp}$ and $T'_{dw} = T_{dw}$ are to be true, then the term $\frac{B}{C} \cdot \left(T_{dw} - T_{air}\right)$ must be zero. For this to be true either the coefficient B must be zero, and/or the terms T_{dw} and T_{air} must be equal. The implication for either of these conditions is that there is no convective heat transfer between the drift wall and the drift air, which of course is not true. Therefore, a downstream application in which the wall heat fraction is used as a substitute for the convective heat transfer to simulate the preclosure heat removal by ventilation cannot accurately represent both the preclosure waste package and drift wall temperatures as calculated by the ventilation model.

However, if the use of the wall heat fraction in the downstream is model is to simply initialize the drift wall temperature such that $T'_{dw} = T_{dw}$, then T'_{wp} can be numerically forced to be:

$$T'_{wp} = \sqrt[4]{\left(T_{wp}^4 - T_{dw}^4\right) - \frac{B}{C}\cdot\left(T_{dw} - T_{air}\right) + T'^4_{dw}}$$

Eq. 6-35

6.6.2 Numerical Example Using the Wall Heat Fraction

Two numerical examples that apply the theoretical use of the wall heat fraction as described in Section 6.6.1 are presented below. Beforehand, it should be noted that the use of a single integrated value for the wall heat fraction, as compared to its use as a function of time and drift length, misrepresents the actual amount of energy that was transferred to the drift wall during the preclosure ventilation period.

6.6.2.1 Using the Single Integrated Value of Wall Heat Fraction

Using the single integrated value for the wall heat fraction from the ANSYS-Refined model, the total energy to the system over the 300-year preclosure period and 600 meter long drift becomes:

$$Q_{total} = \left(\int_{t=0}^{t=300\,yr} Q_{wp}\left(1 - \eta_{integrated}\right)dt\right)(600m)$$

Eq. 6-36

where

Q_{total} = total energy (J)
Q_{wp} = waste package lineal heat decay (kW/m)
$\eta_{integrated}$ = integrated heat removal fraction (dimensionless)

Using the lineal heat decay calculated for the ANSYS-Refined ventilation model in Attachment II, and the integrated heat removal of 94.6% reported in Table 6-6 for the ANSYS-Refined model, the total energy to the system over 300 years and 600 meters is 1.26×10^{14} J.

6.6.2.2 Using the Wall Heat Fraction as Function of Time and Drift Length

Conversely, if the heat removal fractions calculated as function of both time and drift length are used in place of the single integrated value, Eq. 6-36 becomes:

$$Q_{total} = \int_{L=0}^{L=600m}\left(\int_{t=0}^{t=300\,yr} Q_{wp}\left(1 - \eta(t,L)\right)dt\right)dL$$

Eq. 6-37

where

$\eta(t,L)$ = heat removal fraction at some time, t, and some drift location, L, (dimensionless)

Using the same lineal heat decay, and the heat removal fraction as function of time and drift length for the ANSYS-Refined model, the total energy to the system over 300 years and 600 meters is 2.12×10^{14} J, or almost 60% more energy than using the single integrated value for the wall heat fraction.

6.6.2.3 Numerical Example of Using the Wall Heat Fraction as Function of Time and Drift Length

A numerical example of the theoretical use of the wall heat fraction as described above in Section 6.6.1 is presented below. The example uses the wall heat fraction as function of time and drift length, as calculated by the ANSYS-Refined ventilation model, to reduce the waste package heat generation rate in a radiation and conduction only based ANSYS model. The results are depicted in Figures 6-22.

This examples illustrates the conclusion reached in Section 6.6.1 that it is numerically impossible to use the wall heat fraction as substitute for the heat removed by convection and predict the same waste package and drift wall temperatures as those from which the wall heat fraction came. This example also illustrates the numerical difficulty in solving the non-linear radiation heat transfer. Because the radiation involves the difference in temperatures to the fourth power, a unique solution depends upon the energy balance between the other heat transfer mechanisms. However, the constant temperatures imposed at the ground surface and the water table are far enough away from the repository horizon that they act as semi-infinite boundaries, leaving the numerical solution somewhat unbounded. The results of this example clearly illustrates this, as the temperatures of the waste package and drift wall for the model that used the wall heat fraction are different than the original temperatures.

6.6.2.4 Numerical Example of Using T'_{wp} as Function of Time and Drift Length Calculated From Equation 6-35

This example used equation 6-35 to constrain the waste package temperature over time and drift length. The derivation of equation 6-35 takes into account the reduction of the waste package power by the wall heat fraction (equation 6-30), however in this case a temperature boundary condition is assigned to the waste package surface rather than inputting the adjusted heat flux. The energy radiated to the drift wall is the same as in the example presented in Section 6.6.2.3. However for this application, the numerical solver is able to calculate the right temperature history of the drift wall as shown in Figure 6-23.

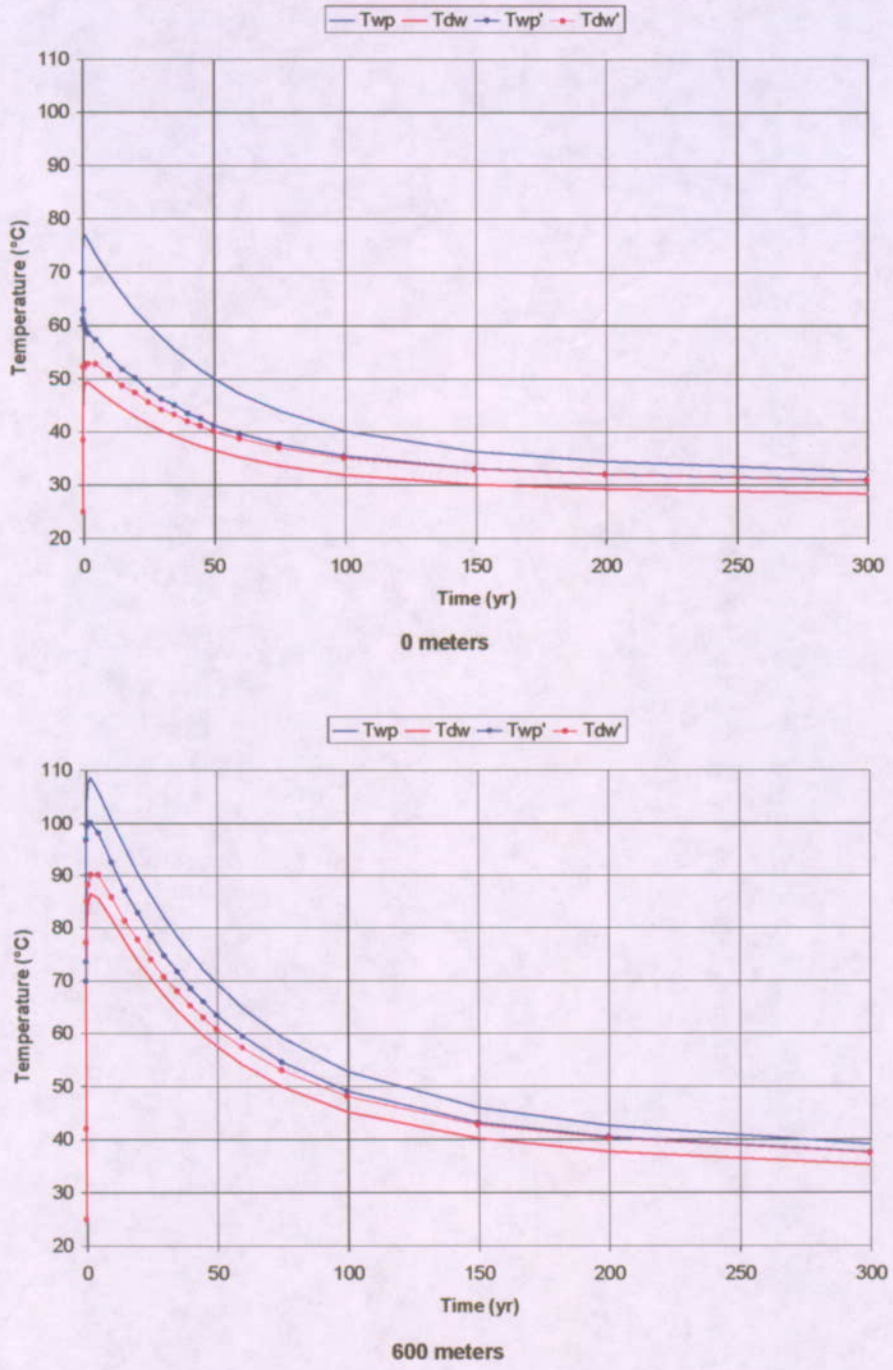

Figure 6-22. Application of the Wall Heat Fraction as a Function of Time and Drift Length to Reduce the Waste Package Heat Decay, Adjusted Heat Load Applied at the Waste Package Surface with Temperature Results Shown for the Drift Entrance and Exit (DTN: MO0210MWDVEN30.005)

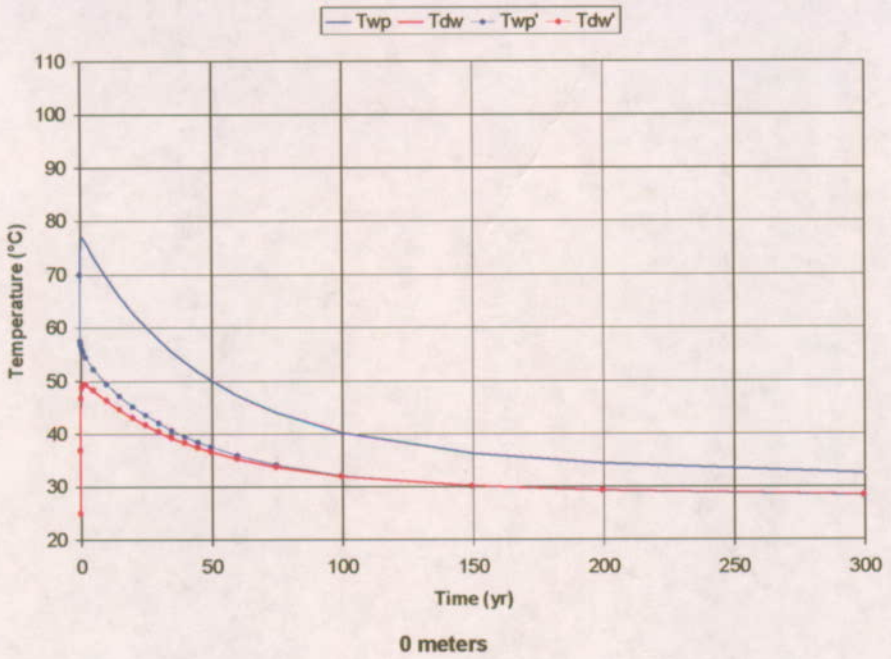

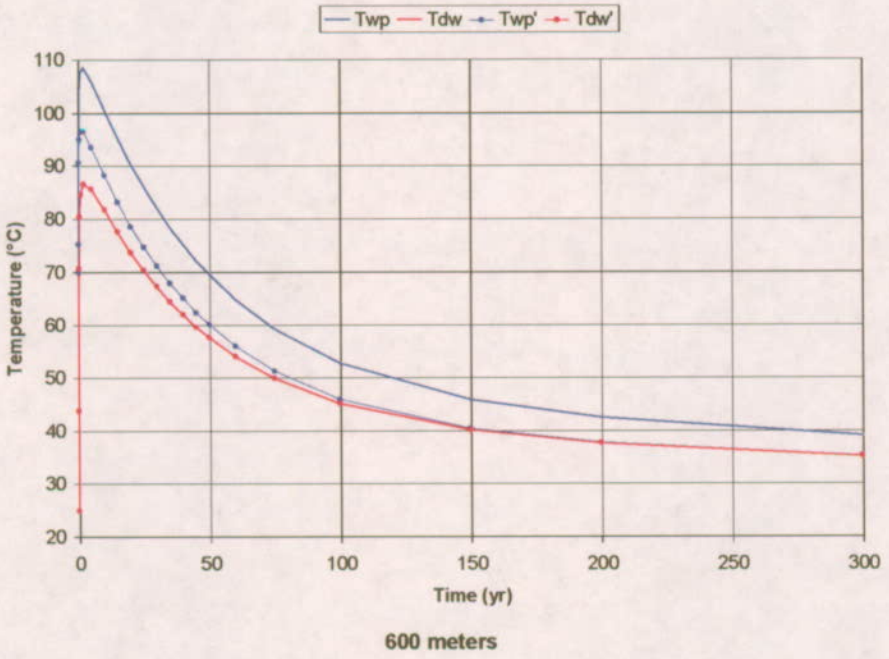

Figure 6-23. Application of the Wall Heat Fraction as a Function of Time and Drift Length to Reduce the Waste Package Heat Decay, Adjusted Waste Package Temperature Calculated from Equation 6-35 and Applied at the Waste Package Surface with Temperature Results Shown for the Drift Entrance and Exit (DTN: MO0210MWDVEN30.005)

7. MODEL VALIDATION

This section presents the results of model validation exercises. The EBS Technical Work Plan determined the level of validation to be low for the Ventilation Model based on the following:

1. It is not extrapolated over large distances, spaces, or time frames
2. It has nominal uncertainties in pertinent input parameters such as surface emissivities, convection heat and mass transfer coefficients, and rock mass thermal conductivity.
3. It is not used to demonstrate compliance or licensing positions
4. It's output will not have significant impacts on TSPA dose calculations results

The approach for validating the conceptual model for preclosure ventilation involves an inspection of the processes 1 through 4 as outlined in Section 6.1.1 in terms of their applicability to adequately simulate the heat transfer in and around a ventilated emplacement drift. These processes and the methods to validate them are outlined in Table 7-1.

Table 7-1. Validation Methods

Conceptual Model Process	Validation Method	Pertinent Input Parameter	Criteria used to Determine Validation	Section
Thermal radiation heat transfer between the surfaces of the waste package and the drift wall using the Stefan-Boltzmann Law	Corroboration with published literature	Surface Emissivity	Engineering Judgement	7.1.1
Convection heat transfer to the ventilation airstream off the waste package and drift wall surfaces by use of convection heat transfer coefficients	Corroboration of post-test analyses with acquired testing results from the quarter-scale ventilation tests conducted at the Atlas Facility	Heat Transfer Coefficient	Match the model results to the test data within ± 5°C using a reasonable range of heat transfer coefficients	7.1.2
Conduction dominated heat transfer within the rock mass surrounding the emplacement drift using Fourier's Law	Corroboration with published results from the Drift Scale Heater Test	Rock Thermal Conductivity	Engineering Judgement	7.1.3

If these processes can be validated for a range of pertinent input parameters (i.e. surface emissivities, convection coefficients, and host rock thermal conductivities), then any numerical application of the conceptual model that uses the input parameters appropriately need only satisfy the conservation of energy and mass to be of use.

7.1 VALIDATION OF THE HEAT TRANSFER PROCESSES OF THE VENTILATION CONCEPTUAL MODEL

The following sections provide the validation exercises for the heat transfer processes outlined above in Table 7-1.

7.1.1 Validation of the Radiation Heat Transfer Model

The use of the Stefan-Boltzmann Law to calculate the radiative heat transfer between two surfaces is an accepted approach within the scientific and engineering community. The valid use of the Stefan-Boltzmann Law to calculate the radiative heat transfer between the surface of an eccentrically located waste package and the drift wall requires the following:

1. An assumption that the in-drift air does not participate in the radiation heat transfer by absorbing significant amounts of energy that would have been otherwise transferred to the drift wall
2. Appropriate values for the emissivities of the waste package and drift wall surfaces

7.1.1.1 Thermal Radiation to a Participating Gas

For enclosures such as an emplacement drift, a medium such as air that separates the radiating surfaces is said to be nonparticipating if it neither absorbs nor scatters the radiation, and it emits no radiation itself. Incropera and DeWitt (Incropera and DeWitt 1996) state that:

> The foregoing conditions and the related equations [summarized in Section 6.1.2 Of this Model Report] may often be used to obtain reliable first estimates and, in most cases, highly accurate results for radiation heat transfer in an enclosure...For *nonpolar* gases, such as O_2 or N_2, such neglect [of participating gaseous radiation] is justified, since the gases do not emit radiation and are essentially transparent to the incident thermal radiation. However, the same may not be said for polar molecules, such as CO_2, H_2O (vapor), NH_3, and hydrocarbon gases, which emit and absorb over a wide temperature range.

The design of the preclosure ventilation system draws air from the outside environment to the intake shafts and then to the emplacement drifts. The initial composition of the ventilation airstream will resemble that of the outside air, or approximately 78% N_2 and 22% O_2 with some small fraction of water vapor. The composition of the ventilation airstream may change as it proceeds through the emplacement drift and acquires additional water vapor and CO_2 from the host rock. However, the numerical application of the Alternative Conceptual Model using MULTIFLUX-Full presented herein, shows that the ventilation airstream does not acquire enough water vapor to make any significant impact on the thermal radiation heat transfer.

7.1.1.2 Validation Criteria Met for the Radiation Heat Transfer Model

Engineering judgement dictates the use of the Stefan-Boltzmann Law to model radiation heat transfer within waste emplacement drifts. This is corroborated by its use in the engineering

community outside of the Yucca Mountain Project. Further bounding calculations, and where available analysis of exhaust air from the ESF, may be needed to further validate the argument that the in-drift air does not offer any significant participation in the radiation heat transfer between the waste package and drift wall during the ventilation period. However, for the level of confidence required for the Ventilation Model, this validation criteria is met.

7.1.2 Validation of the Convection Heat Transfer Model

The validation of the convection heat transfer model used in the Ventilation Conceptual Model hinges upon the appropriate use of convective heat transfer coefficients. Phases 1 and 2 of the one-quarter scale ventilation tests performed at the North Las Vegas Atlas Facility during 2001 and 2002 provide valuable data for determining a range of valid convection heat transfer coefficients. A detailed description of the ventilation tests is provided in the *Development Plan for EBS Ventilation Test* (CRWMS M&O 2000g) and an interoffice correspondence *Guidance for the Ventilation Test* (Kramer 2001). The primary difference between phases 1 and 2 is that the ventilation air in Phase 2 was conditioned to better control its inlet temperature and relative humidity. The Phase 1 test brought in ambient air from outside the test train that exhibited diurnal temperature changes of around 4 °C. The same ventilation air flow rates and linear heat loads were used for both phases. Considering these aspects, and that the ANSYS methodology for simulating ventilation does not account for the relative humidity of the in-drift air, the Phase 1 test data is sufficient to provide the level of validation required for the ANSYS model. Therefore, the use of the ventilation test data for post-test ANSYS modeling and validation for this revision of the Ventilation Model Report is confined to the Phase 1 cases. It is not anticipated that post-test modeling of the Phase 2 ventilation test cases will provide any higher level of confidence in the validation process. Table 7-2 lists the Phase 1 ventilation tests and cases for which ANSYS post-test modeling was performed.

Table 7-2. Ventilation Phase 1 Test Matrix

Test No.	Case No.	Nominal Flow (m^3/s)	Nominal Power (kW/m)
1	4	1	0.18
2	5	0.5	0.18
3	1	1	0.36
4	5	2	0.36
5	3	0.5	0.36

7.1.2.1 Post-Test ANSYS Model

Figure 7-1 shows the saddle-like temperature trends for the waste package of Test 1, Case 4 of Ventilation Test Phase 1. The same trend is observed in all the other cases. The temperature peaks that occur around Station 3 are due to heat losses at the inlet and outlet of the test train. However, the ANSYS methodology outlined in Section 6.2.1 is not capable of modeling the profile of axial temperature exhibited by the test data. An underlying assumption of the ANSYS methodology is that temperatures of the in-drift components, drift wall, and ventilation air are always increasing as the calculation proceeds down the length of the drift. This limitation forced the development of a two-dimensional ANSYS-based ventilation model. In other words, only a

two-dimensional cross-section at Station 3 was modeled using ANSYS rather than the ANSYS/Excel methodology described in Section 6.2.1 for a pseudo-three-dimensional analysis from Station 1 to Station 5.

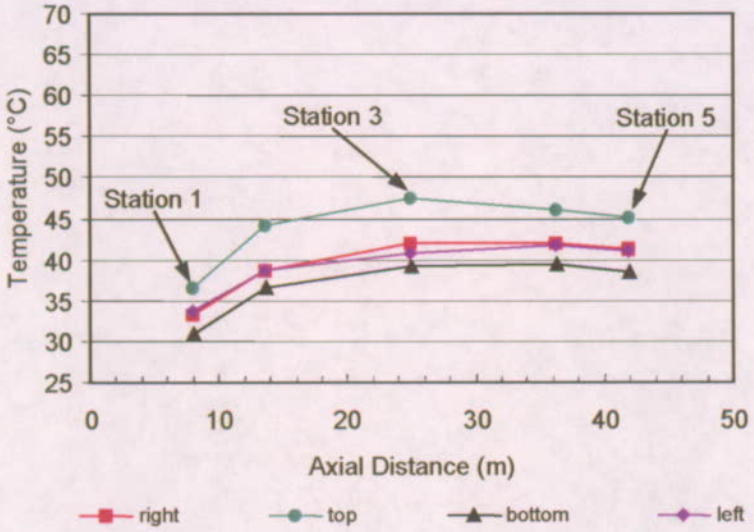

Figure 7-1. Ventilation Phase 1, Test 1, Case 4 Waste Package Temperatures Versus Axial Distance Down the Test Train for Data Recorded 10/15/00

7.1.2.2 Mesh

Figure 7-2 shows a detailed drawing through a cross-section of the test train. It also includes the relative locations of the instrumentation. Figure 7-3 shows the discretization of the test domain or the computational mesh used for the ANSYS post-test modeling. The meshes for the post and pre-test modeling are the same with the exception that additional groupings of elements have been created for the application of post-test boundary conditions. The pallet that supports the simulated waste package is not continuous in the test configuration. Rather, it supports the ends of the package. The contribution of heat transfer via conduction from the package through the pallet, and into the invert is considered to be negligible in comparison to the amount of heat transferred by radiation. For this reason, the pallet was not modeled.

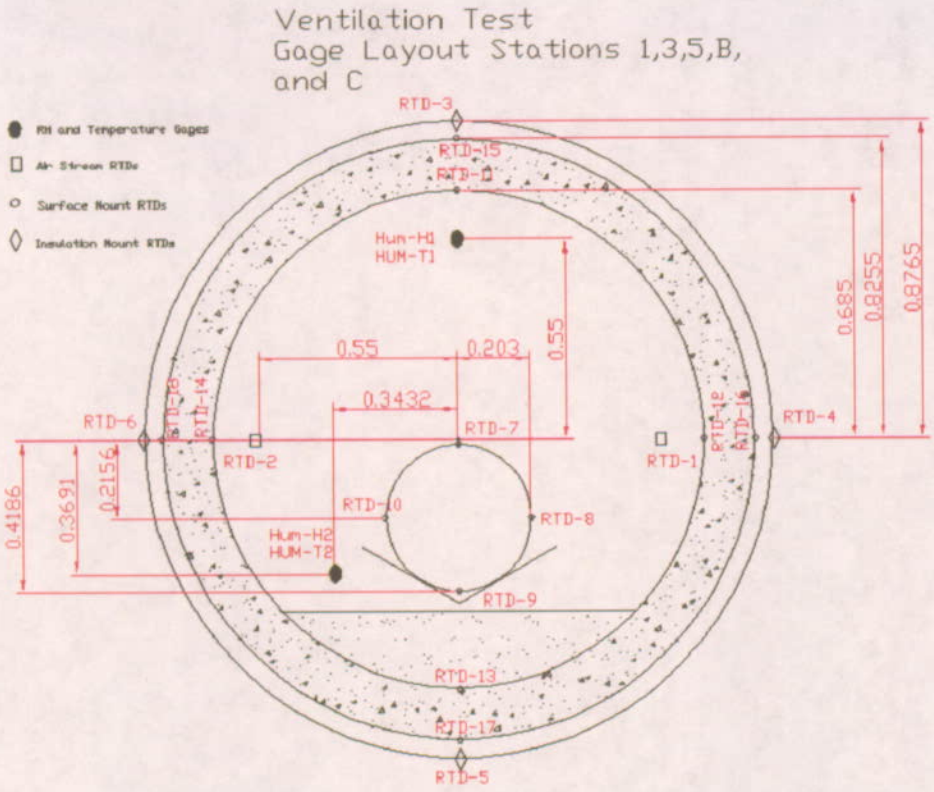

Figure 7-2. Cross-sectional View of the Ventilation Test Train

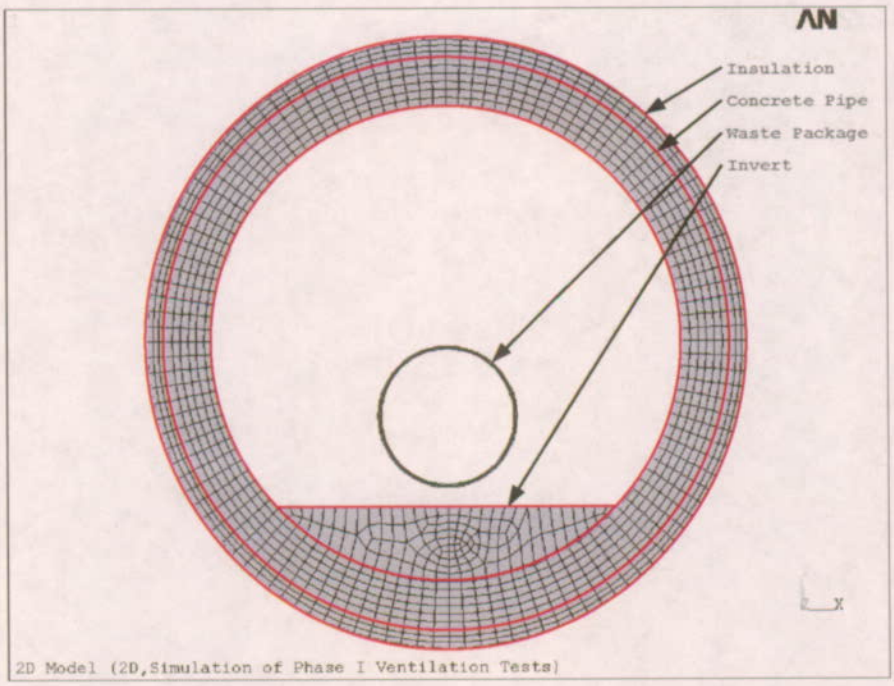

Figure 7-3. ANSYS Mesh

7.1.2.3 Inputs

Table 7-3 summarizes the material and thermal properties used in the ANSYS post-test modeling (Section 4.2).

Table 7-3. Material and Thermal Properties for the Ventilation Test Components

Parameter	Simulated Waste Package	Concrete Pipe	Insulation	Invert
Density (kg/m^3)	7840	2280	12	2530
Thermal Conductivity (W/m·K)	38.37	2.75	0.04	0.14
Specific Heat (J/kg·K)	410.98	1016.16	700	919
Emissivity	0.8	0.93	0.96	0.93

7.1.2.4 Boundary Conditions

The recorded temperatures on the outer insulation at Station 3 of the test train were used as the outer boundary conditions for the ANSYS post-test models. Each test case had a different set of recorded temperatures over its life span. Due the difficulty in maintaining constant ambient conditions in the high-bay of the facility, a data fit for each case was performed on the outer insulation temperature histories to aid in the implementation of this boundary condition. Figure 7-4 shows the outer insulation temperature histories and the data fits for the cases modeled.

The ANSYS methodology requires that an inlet ventilation air stream temperature be specified. Therefore, the temperatures of the ventilation air stream recorded at Station 3 were used as input to the ANSYS post-test models. Each test case had a different set of air stream temperature histories. Again, a data fit for each case was performed on the recorded temperature data to simplify its implementation into the models. Figure 7-5 shows the ventilation air stream temperature histories and the data fits for the cases modeled.

The simulated waste packages were hollow rolled steel tubes, with heater rods suspended concentrically inside. Due to the nature of the experimental set-up, natural convection cells developed within the placid annulus of the waste packages. This caused a non-uniform heat flux, and hence temperature distribution, around the circumference of the waste package. No temperature measurements were recorded inside the waste package (i.e. the annulus air or the rod-heater). Rather than model the complexity of the natural convection inside of the waste package, the ANSYS model supplied a heat flux at the waste package wall. The heat flux was partitioned around the waste package circumference using the recorded steady-state temperature distributions as a basis. Table 7-4 summarizes the distributions for the test cases listed in Table 7-2. The validity of this partitioning methodology is confirmed by the consistency of the calculated distributions from case to case.

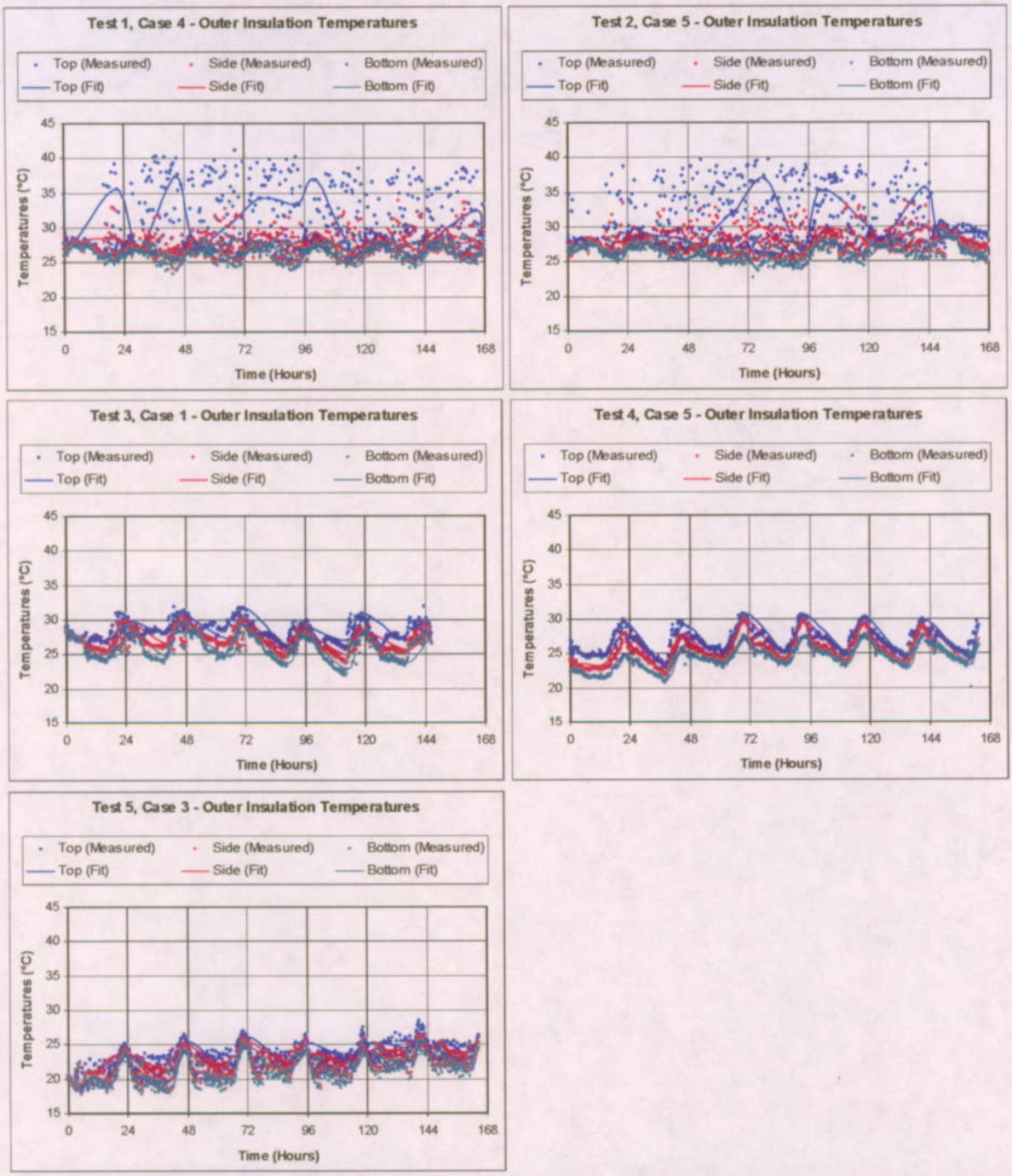

Figure 7-4. Outer Insulation Boundary Temperatures for the ANSYS Post-Test Ventilation Model (DTN MO0209MWDANS30.017)

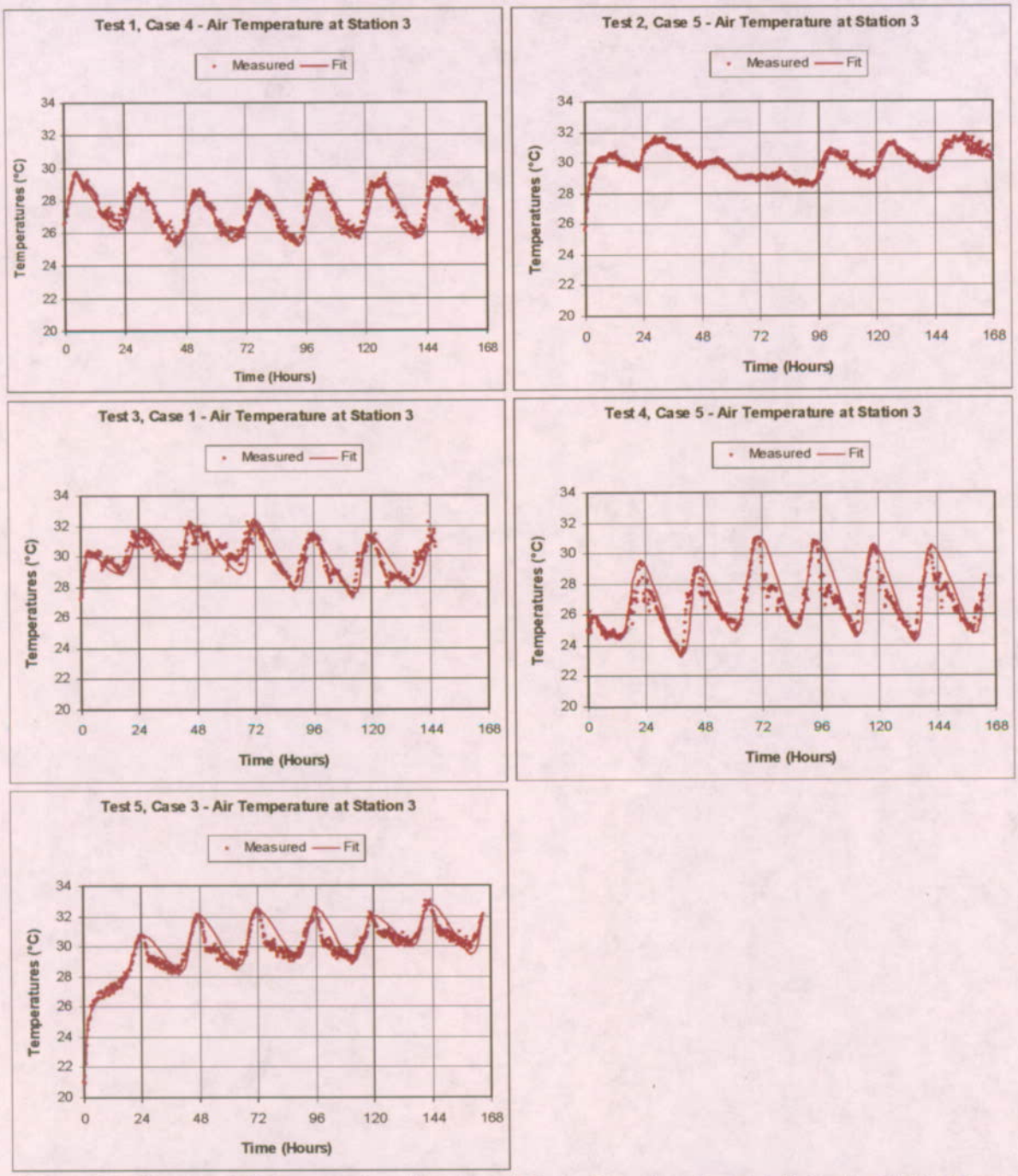

Figure 7-5. Measured Air Temperature Histories at Station 3 used as the Inlet Air for the ANSYS Post-Test Ventilation Model (DTN MO0209MWDANS30.017)

Table 7-4. Distribution of Total Power to the Top, Sides, and Bottom Quarters of the Waste Package Based on Temperature Measurements

Test No.	Case No.	Nominal Power (kW/m)	WP Top Quarter	WP Side Quarter	WP Bottom Quarter
1	4	0.18	32%	24%	20%
2	5	0.18	32%	24%	20%
3	1	0.36	32%	24%	20%
4	5	0.36	32%	24%	20%
5	3	0.36	31%	24%	21%

7.1.2.5 Correlating the Model Results to the Test Data Using Heat Transfer Coefficients

Having determined appropriate distributions of power around the circumference of the waste package, ANSYS models were run iteratively using different values for the heat transfer coefficients until the model results reasonably matched the test data.

7.1.2.6 Results

Table 7-5 shows the heat transfer coefficient values which resulted in reasonable comparisons to the measured temperature data. The temperature results from the ANSYS models are compared to the recorded test data in Figures 7-6 through 7-10. Table 7-6 compares the average heat transfer coefficient calculated for each test case from Table 7-5 to heat transfer coefficients calculated using the Dittus-Boelter correlation.

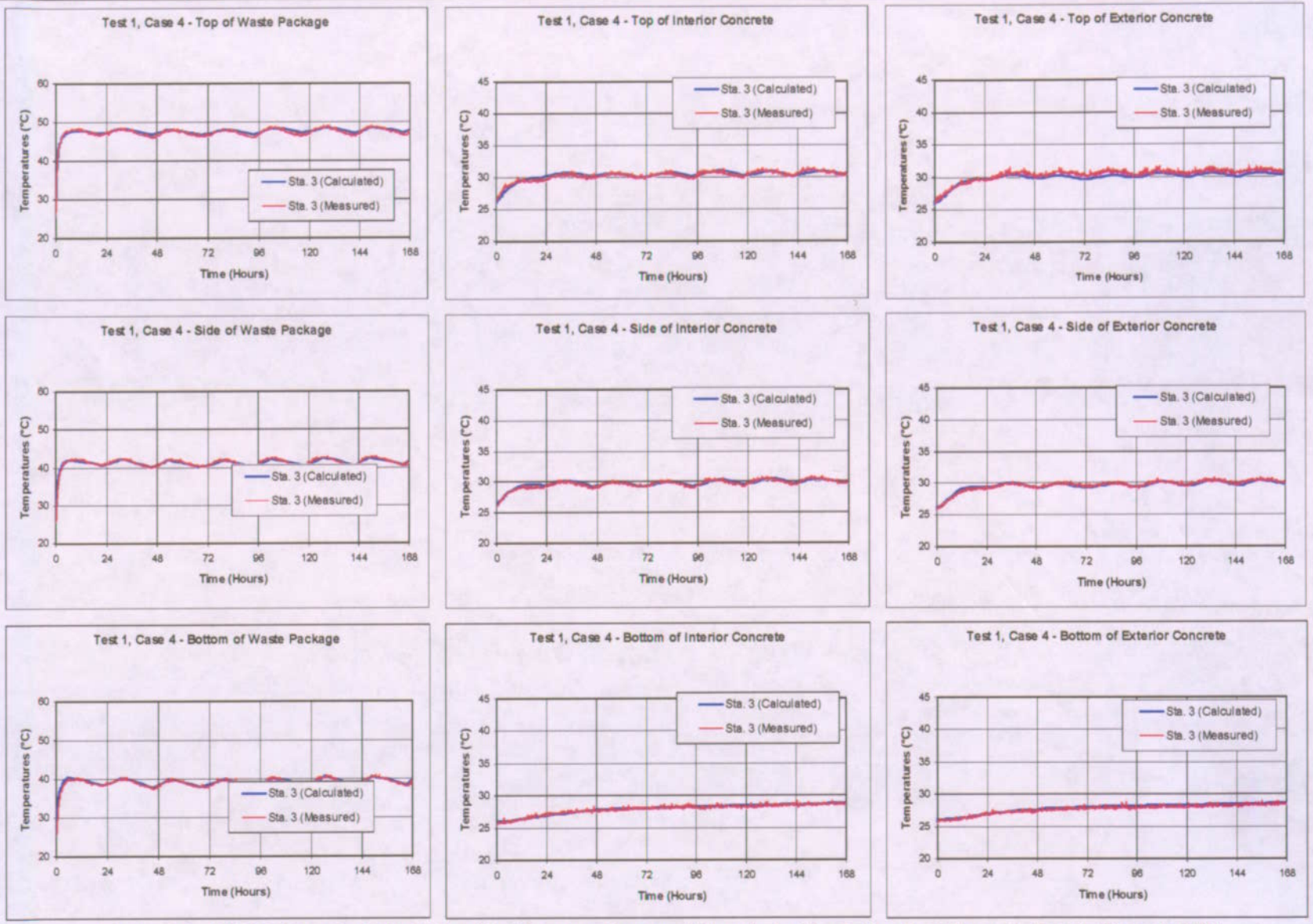

Figure 7-6. ANSYS Post-Test Ventilation Model versus Measured Results for Ventilation Test Phase 1, Test 1, Case 4 (DTN MO0209MWDANS30.017)

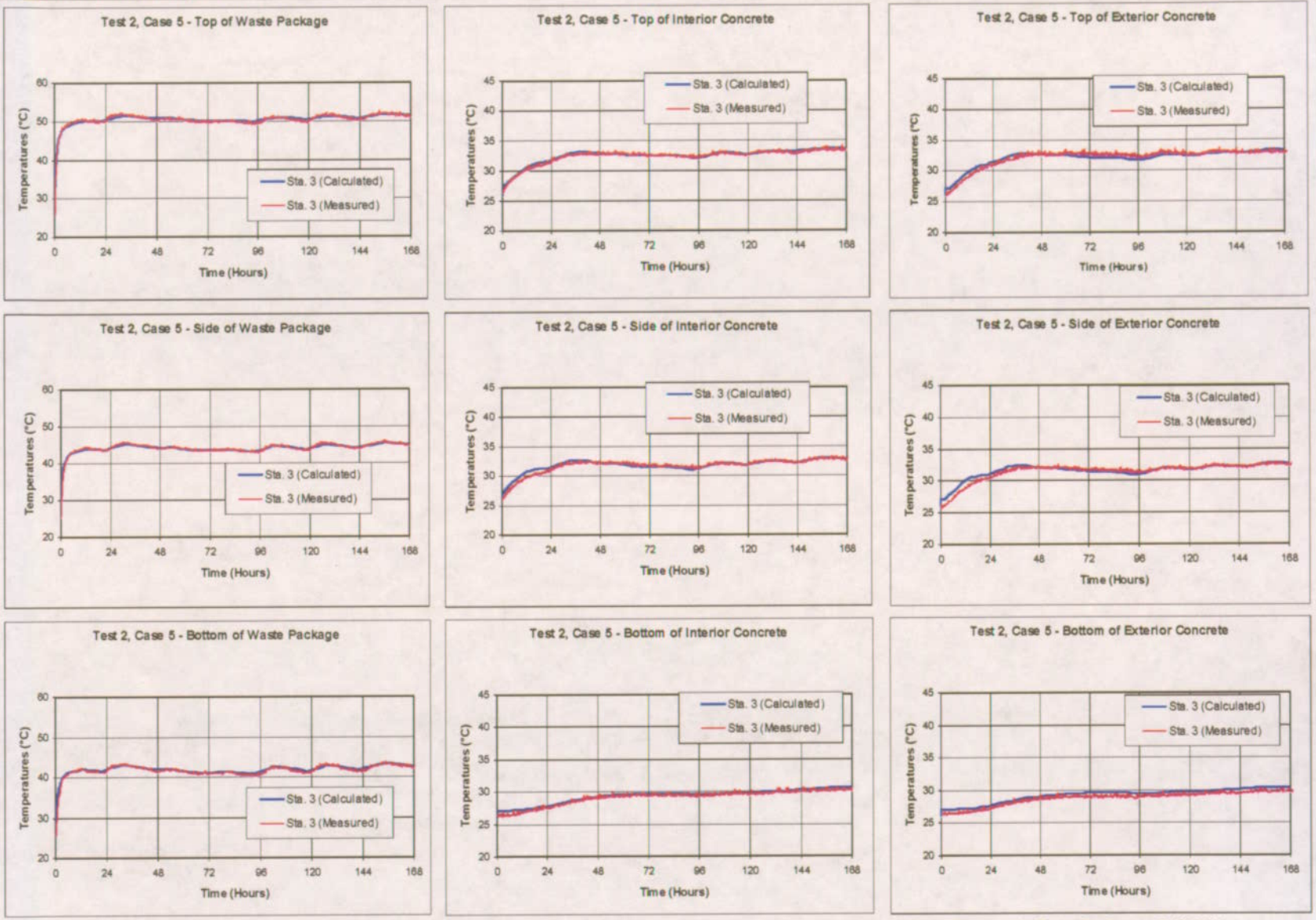

Figure 7-7. ANSYS Post-Test Ventilation Model versus Measured Results for Ventilation Test Phase 1, Test 2, Case 5 (DTN MO0209MWDANS30.017)

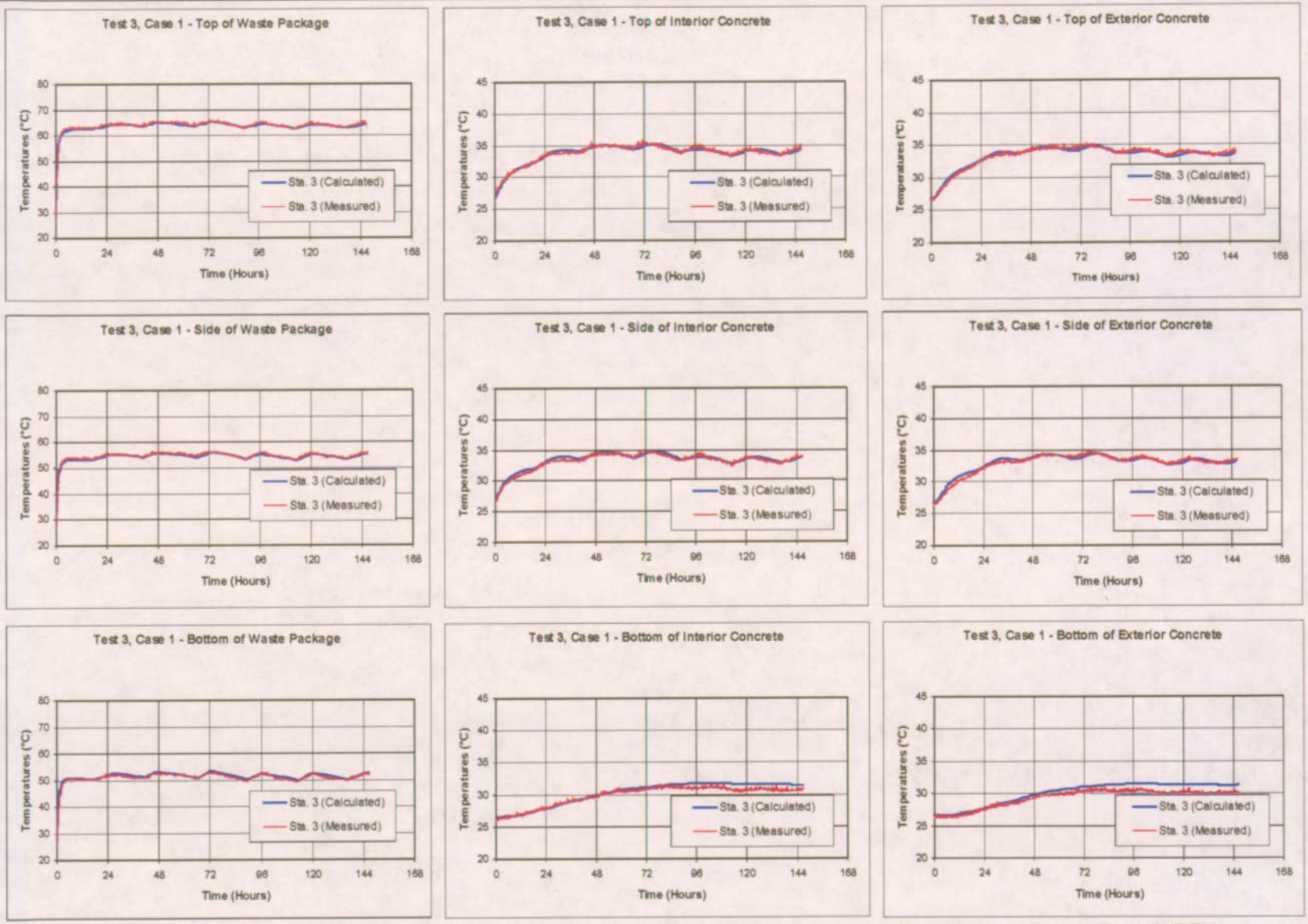

Figure 7-8. ANSYS Post-Test Ventilation Model versus Measured Results for Ventilation Test Phase 1, Test 3, Case 1 (DTN MO0209MWDANS30.017)

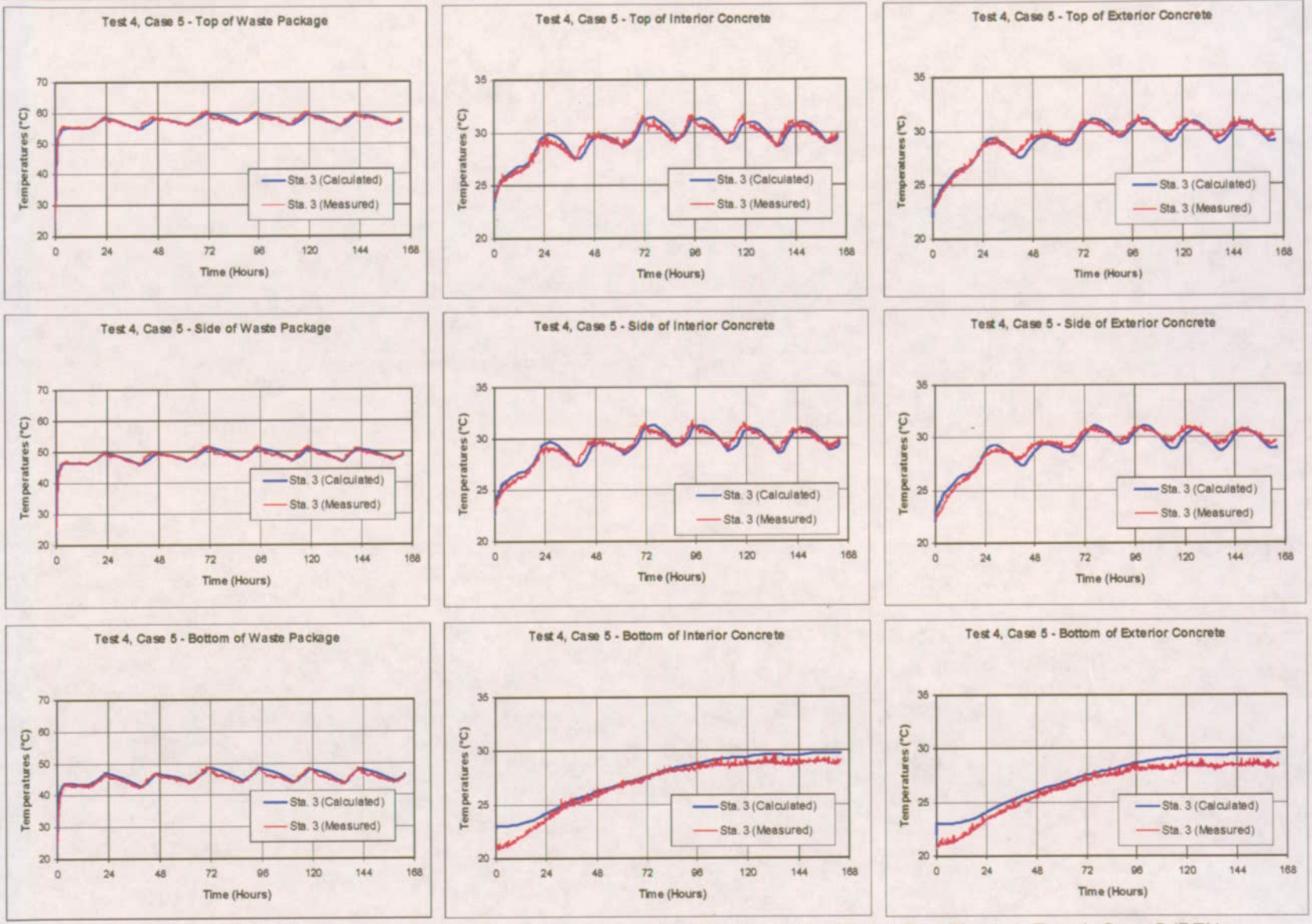

Figure 7-9. ANSYS Post-Test Ventilation Model versus Measured Results for Ventilation Test Phase 1, Test 4, Case 5 (DTN MO0209MWDANS30.017)

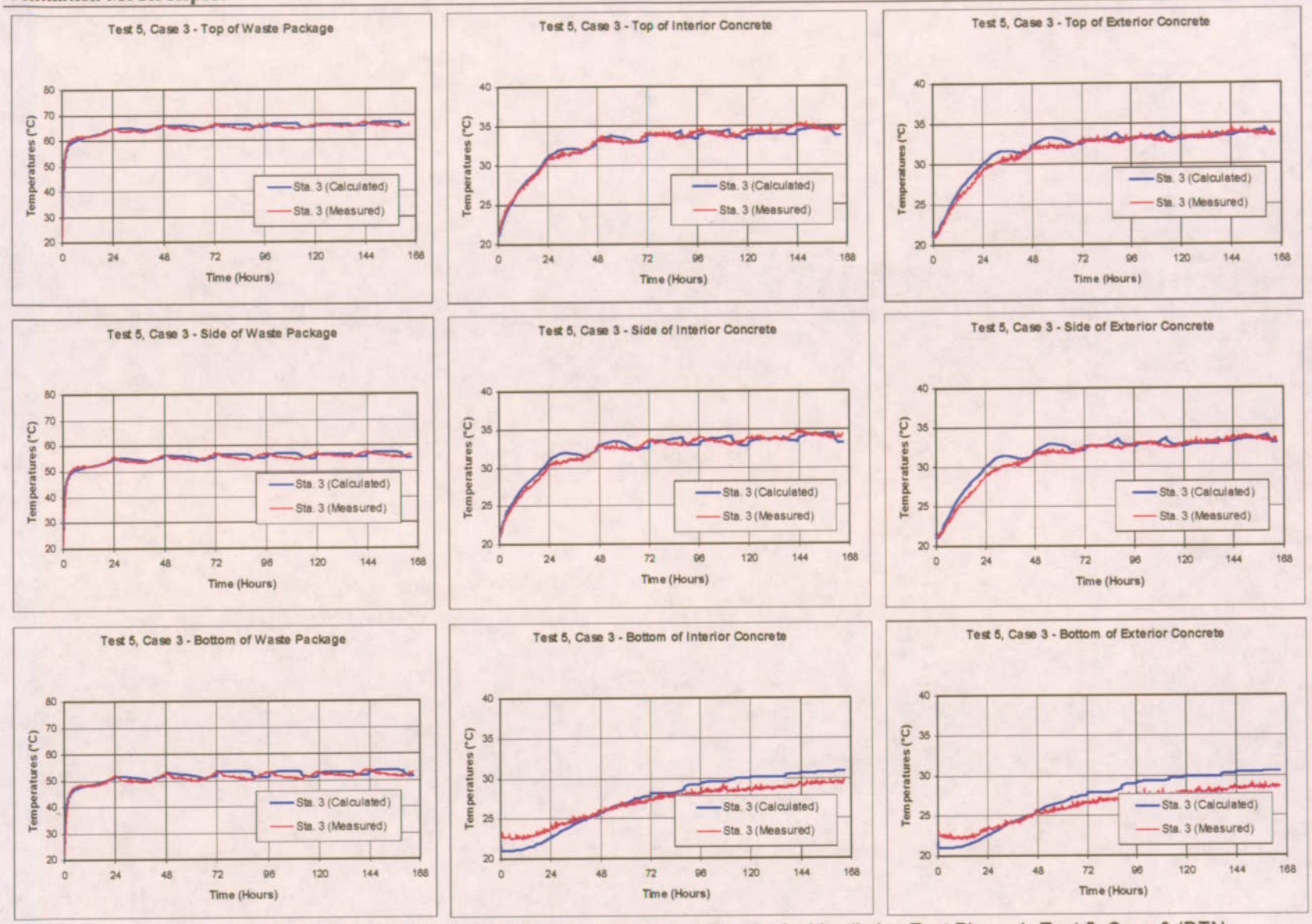

Figure 7-10. ANSYS Post-Test Ventilation Model versus Measured Results for Ventilation Test Phase 1, Test 5, Case 3 (DTN MO0209MWDANS30.017)

Table 7-5. Developed Heat Transfer Coefficients from the ANSYS Post-Test Modeling of Phase 1 of the Ventilation Test

		Heat Transfer Coefficient ($W/m^2 \cdot K$)					
Test No.	Case No.	WP Top Quarter	WP Side Quarter	WP Bottom Quarter	Upper Concrete	Lower Concrete	Invert
1	4	0.5	7.5	7.0	5.0	9.0	9.0
2	5	0.0	7.0	7.0	5.0	15.0	9.0
3	1	2.0	8.0	8.0	7.0	11.0	6.0
4	5	3.5	9.5	10.5	13.0	15.0	2.0
5	3	1.0	7.5	8.5	9.5	16	5.0

Table 7-6. Comparison of Heat Transfer Coefficients using Data-Fitting and the Dittus-Boelter Correlation

			Heat Transfer Coefficient ($W/m^2 \cdot K$)	
Test No.	Case No.	Flow Rate (m^3/s)	ANSYS Fitted Average	Dittus-Boelter
1	4	1.0	6.3	2.7
2	5	0.5	7.2	1.5
3	1	1.0	7.0	2.7
4	5	2	8.9	4.6
5	3	0.5	7.9	1.5

The average of the heat transfer coefficients range from approximately two to five times larger than heat transfer coefficients calculated using the Dittus-Boelter correlation. Two reasons would tend to account for the differences. First, the Dittus-Boelter equation is a forced convection correlation. Analyses of the ventilation test data indicate a mixed (i.e. natural and forced) convection regime inside the concrete pipe annuls. Second, the Dittus-Boelter correlation for calculating a forced convection heat transfer coefficient was developed for hollow tube geometries. The correlation can be extended to a cylinder within a tube (i.e. waste package inside a drift) by using the hydraulic diameter instead of the geometric diameter. However, a cylinder within a tube, eccentrically located, is a very different geometry which would tend to invalidate the Dittus-Boelter correlation within the range of air flow velocities being considered herein. Add an invert, and the geometry of the problem lies even farther beyond the range of the Dittus-Boelter correlation. The values presented in Table 7-6 for the ANSYS fitted heat transfer coefficients argue that both natural and forced convection are important heat removal mechanisms for the experimental set-up of the Ventilation Test. Although scaling the quarter scale test results to a full scale drift is beyond the scope of this model report, it stands to reason that a convection coefficient correlation which considers both natural and forced convection is more appropriate for use than the simple Dittus-Boelter equation (for the current drift design, heat load range, and ventilation flow rate).

Table 7-7 summarizes the ventilation heat removal rates for the 5 cases as modeled by ANSYS.

Table 7-7. Heat Removal Ratios for the ANSYS Post-Test Ventilation Models

Test No.	Case No.	Heat Removal Ratio
1	4	0.87
2	5	0.83
3	1	0.78
4	5	0.93
5	3	0.81

7.1.2.7 Validation Criteria Met for the Convection Heat Transfer Model

The ANSYS numerical model matched the Phase I Ventilation Test results within the validation criteria of ± 5°C using a reasonable range of heat transfer coefficients. The range of heat transfer coefficients required to match the test results indicates a mixed convection regime inside the test train. The Dittus-Boelter correlation for calculating forced convection heat transfer coefficients is therefore, at best, only a conservative approach. The impact of using such a correlation, as was done for the ventilation models presented in this model report, is a lower or more conservative rate of heat removal by ventilation. A more realistic correlation would be one that accounts for both natural and forced convection to remove heat from the drift. Even so, the use of heat transfer coefficients calculated using only a forced convection correlation would produce reasonable results. Therefore, the validation criteria for the convection heat transfer model is considered to be met with respect to the level of confidence required in the model. Additional sensitivity runs using a range of heat transfer coefficients may be required to determine the effects on the heat removal rates and peak postclosure temperatures.

7.1.3 Validation of the Host Rock Conduction Heat Transfer Model

It is assumed that conduction heat transfer dominates other heat transfer mechanisms (i.e. convection in fractures and lithophysae, and latent heat) in the host rock. This assumption is a conclusion reached by the Multiscale Thermohydrologic Model (BSC 2001) and is supported by preliminary and unpublished numerical modeling of the Drift Scale Test and earlier work documented by Sass (Sass et al. 1988). Additional effort may be needed to confirm this assumption. However, for the level of confidence required for the Ventilation Model, the assumption that conduction dominates the heat transfer in the host rock does not compromise the validity of the conceptual model.

7.2 VALIDATION OF THE MASS TRANSFER PROCESS OF THE VENTILATION ALTERNATIVE CONCEPTUAL MODEL

The following section provides a validation argument for the mass transfer process of the ventilation alternative conceptual model.

7.2.1 Validation of the Mass Transfer Process

As stated earlier is Section 6.4, a heat transfer analog is used to calculate the mass transfer coefficient at the drift wall. The mass transfer coefficient is calculated by taking the product of the heat transfer coefficient and the Lewis Number (Danko et al. 1988). This is common and

well documented approach in the literature for calculating the mass transfer, and in the absence of actual field or lab data, is considered sufficient for the level of validation required in the Technical Work Plan that governs this model report.

In addition, a bounding analytical calculation was performed which demonstrates the insignificance of the mass transfer processes on the heat transfer. Analytical equations for steady state unsaturated flow in porous media to a specified moisture potential boundary condition at the drift wall were developed with the help of *Soil Physics* (Jury et al. 1991) and *Contaminant Hydrogeology* (Fetter 1993). Using an assumption of 30% relative humidity in the drift, the moisture potential at the drift wall was calculated to be -1.691×10^{6} cm (Attachment XI). The moisture potential in the surrounding host rock at some distance from the drift wall was calculated using the mean of 377 measurements, from several boreholes, of matrix saturation in the tsw35 geologic unit. Based on the mean and the mean plus one standard deviation of the measurements, bounding steady state moisture fluxes to the drift wall from the surrounding host rock were calculated to be 0.484 mm/yr and 2.259 mm/yr respectively. Assuming that all the moisture which fluxes to the drift wall over the entire length of the emplacement drift is evaporated at an assumed constant temperature, the total latent heat contribution to the in-drift air over the 300-year preclosure period can be calculated. The latent heat contribution was then divided by the total heat output by the waste packages over the same 300-year period and 600 meter long drift. The results are presented in Table 7-8.

Table 7-8. Latent Heat Contribution Expressed as a Percentage of the Total Waste Package Heat Over 300 Years and 600 Meters of Drift

Model	Latent Heat Contribution
Analytical model with a moisture flux = 0.484 mm/yr [1]	0.15%
Analytical model with a moisture flux = 2.259 mm/yr [2]	0.70%
MULTIFLUX-Full (mass transfer coefficient = 0.0012 kg/s)	2.28%

By comparison, Table 7-8 also shows latent heat contribution calculated by the MULTIFLUX-Full model (DTN: MO0209MWDMUL30.002) to be 5.32×10^{13} J (using a temperature dependent function for the latent heat of vaporization), or 2.28% of the total waste package heat output. Both the MULTIFLUX-Full model and the analytical calculation indicate that:

- The contribution of heat by vaporization of moisture is rate limited by the hydrogeologic properties of the host rock
- The contribution of heat by vaporization of moisture is a very small percentage of the total heat input

These conclusions confirm the results of the MULTIFLUX-Full model that moisture has little impact on the total heat transfer process and the ability of ventilation air to remove heat from the emplacement drift.

8. CONCLUSIONS

This model report presents a conceptual model for the thermal energy processes in ventilated emplacement drifts. As described in Section 6.1, these processes include:

1. Thermal radiation between the waste package and drift wall.
2. Thermal convection from the waste package to the ventilation air stream.
3. Thermal convection from the drift wall to the ventilation air stream.
4. Thermal conduction in the surrounding host rock.

An alternative conceptual model is also presented which includes, in addition to the thermal processes described above, the following mass transfer processes:

5. Phase change of near-field host rock pore water.
6. Movement of mobilized water vapor and liquid water in the rock and into the ventilation air stream.

The implementation of the conceptual model using the ANSYS and MULTIFLUX codes produced similar results in terms of temperatures and ventilation heat removal ratios. Both codes confirm that ventilation is a viable option for not only delaying the onset of peak waste package and drift wall temperatures, but also reducing their respective magnitudes. In addition, the numerical implementation of the alternative conceptual model and an analytical bounding calculation showed that water and water vapor mass transport is limited by the properties of the rock, and had little effect on the ability of ventilation to remove heat generated by the waste packages. Therefore, the mass transfer processes and their associated effects on the overall heat transfer need not be included at this time in the conceptual model for ventilation of waste emplacement drifts.

8.1 SUMMARY ACCOMPLISHMENT OF THE VENTILATION MODEL PURPOSES

The purposes of the Ventilation Model Report were numerated in Section 1. A brief summary of their accomplishment is outlined below:

1. The heat transfer mechanisms, which describe the conceptual model for preclosure ventilation of emplacement drifts, were successfully validated in Section 7. Additionally, the numerical application of these processes using ANSYS and MULTIFLUX were verified by comparing the results of each model, along with comparisons from other submodels.
2. With respect to KTI agreement RDTME 3.14, a comparison between the two ANSYS ventilation models in Section 6.2.3.1 showed the adequacy of the coarse discretization of the drift along its axis. Also with respect to KTI agreement RDTME 3.14, the applicability of the wall heat fraction to initialize postclosure thermal models was shown in Section 6.6.
3. KTI agreement TEF 2.07 is satisfied by providing the results of post-test ANSYS modeling of the Atlas Facility Ventilation Test. This effort also served to validate the use

of heat transfer coefficients to adequately model convection heat transfer inside the drift (see Section 7.1.2).

4. KTI agreements RDTME 3.01 and 3.14 are fully satisfied by providing the source documentation referred to in the KTI Letter Report (Williams 2002). The results of a numerical application of the alternative conceptual model using MULTIFLUX-Full, which simulates the coupled processes of heat and mass transfer in and around waste emplacement drifts during periods of forced ventilation, are included (see Section 6.3 and 6.4).

8.2 MODEL OUTPUTS

The primary purpose of the Ventilation Model Report is to present and validate the heat transfer processes which comprise the conceptual model for ventilating waste emplacement drifts. The Ventilation Model Report does not attempt to predict repository performance during the preclosure period. Therefore, all inputs and subsequent outputs are used solely for validation and verification purposes. Future analyses will exercise the ventilation conceptual model against a range of pertinent input parameters such as, but not limited to, surface emissivity, convection heat transfer coefficient, and host rock thermal conductivity. From these analyses will stem the ranges of applicability of the ventilation model to predict repository performance, as well an identification of the model uncertainties.

The DTNs of the developed data from this report are MO0210MWDTVE30.018, MO0210MWDTEM30.019, MO0209MWDANS30.017, MO0209MWDMUL30.002, MO0209MWDMOD30.003, and MO0210MWDVEN30.005.

9. INPUTS AND REFERENCES

9.1 DOCUMENTS CITED

BSC (Bechtel SAIC Company) 2001. *Multiscale Thermohydrologic Model.* ANL-EBS-MD-000049 REV 00 ICN 02. Las Vegas, Nevada: Bechtel SAIC Company. ACC: MOL.20020123.0279.

BSC (Bechtel SAIC Company) 2002. *Technical Work Plan for Engineered Barrier System Department Modeling and Testing FY 02 Work Activities.* TWP-MGR-MD-000015 REV 02. Las Vegas, Nevada: Bechtel SAIC Company. ACC: MOL.20021014.0209.

Carslaw, H.S. and Jaeger, J.C. 1959. *Conduction of Heat in Solids.* 2nd Edition. Oxford, Great Britain: Oxford University Press. TIC: 206085.

CertainTeed. 1996. Submittal Sheet, Standard Fiber Glass Duct Wrap. Valley Forge, Pennsylvania: CertainTeed Corporation. TIC: 249257.

CRWMS M&O 1997. *Overall Development and Emplacement Ventilation Systems.* BCA000000-01717-0200-00015 REV 00. Las Vegas, Nevada: CRWMS M&O. ACC: MOL.19980123.0661.

CRWMS M&O 1998a. *Repository Subsurface Waste Emplacement and Thermal Management Strategy.* B00000000-01717-0200-00173 REV 00. Las Vegas, Nevada: CRWMS M&O. ACC: MOL.19980918.0084.

CRWMS M&O 1998b. *Multiple WP Emplacement Thermal Response - Suite 1.* BBA000000-01717-0210-00001 REV 00. Las Vegas, Nevada: CRWMS M&O. ACC: MOL.19980807.0311.

CRWMS M&O 1999a. *Classification of the MGR Subsurface Ventilation System.* ANL-SVS-SE-000001 REV 00. Las Vegas, Nevada: CRWMS M&O. ACC: MOL.19990928.0219.

CRWMS M&O 1999b. *Thermal Modeling Parameters by Stratigraphic Unit.* Input Transmittal SSR-NEP-99261.T. Las Vegas, Nevada: CRWMS M&O. ACC: MOL.19990910.0090; MOL.19990920.0109.

CRWMS M&O 1999c. *Thermal Calculation of the Waste Package with Backfill.* BB0000000-01717-0210-00001 Rev 00. Las Vegas, Nevada: CRWMS M&O. ACC: MOL.19981214.0073.

CRWMS M&O 1999d. *Enhanced Design Alternative (EDA) II Repository Estimated Waste Package Types and Quantities.* Input Transmittal EBS-SR-99325.T. Las Vegas, Nevada: CRWMS M&O. ACC: MOL.19991103.0236.

CRWMS M&O 2000a. *Subsurface Facility System Description Document.* SDD-SFS-SE-000001 REV 01. Las Vegas, Nevada: CRWMS M&O. ACC: MOL.20000807.0078.

CRWMS M&O 2000b. *Emplacement Drift System Description Document.* SDD-EDS-SE-000001 REV 01. Las Vegas, Nevada: CRWMS M&O. ACC: MOL.20000803.0348.

CRWMS M&O 2000c. *Conceptual Arrangement Simulated Emplacement Ventilation Test.* [Las Vegas, Nevada: CRWMS M&O]. ACC: MOL.20001219.0107.

CRWMS M&O 2000d. *Thermal and Physical Properties of Granular Materials.* Input Transmittal 00148.T. Las Vegas, Nevada: CRWMS M&O. ACC: MOL.20000320.0003.

CRWMS M&O 2000e. *Subsurface Ventilation System Description Document.* SDD-SVS-SE-000001 REV 01. Las Vegas, Nevada: CRWMS M&O. ACC: MOL.20000803.0356.

CRWMS M&O 2000f. *NUFT 3.0S Users Manual.* 10088-UM-3.0s-00, Rev. 00. Las Vegas, Nevada: CRWMS M&O. ACC: MOL.20000920.0092.

CRWMS M&O 2000g. *Development Plan for Ventilation Test.* TWP-EBS-MD-000001 REV 00. Las Vegas, Nevada: CRWMS M&O. Submit to RPC.

Danko, George;Mousset-Jones, Pierre;McPherson, Malcolm J 1988. "Heat, Mass, and Impulse Transport Analogies for Underground Airways." *Proceedings, 4th International Mine Ventilation Congress, Brisbane, Queensland Australia, 1988.* Gillies, A.D.S. 237-248. Queensland, Australia: University of Queensland, Brisbane. TIC: 253200.

Daugherty, R.L. and Franzini, J.B., eds. 1965. *Fluid Mechanics with Engineering Applications.* 6th Edition. New York, New York: McGraw-Hill Book Company. TIC: 217647.

Fetter, C.W. 1993. *Contaminant Hydrogeology.* Upper Saddle River, New Jersey: Prentice Hall. TIC: 240691.

Flint, L.E. 1998. *Characterization of Hydrogeologic Units Using Matrix Properties, Yucca Mountain, Nevada.* Water-Resources Investigations Report 97-4243. Denver, Colorado: U.S. Geological Survey. ACC: MOL.19980429.0512.

Hartman, H.L. 1982. *Mine Ventilation and Air Conditioning.* Mutmansky, J.M. and Wang, Y.J., eds. 2nd Edition. New York, New York: John Wiley & Sons. TIC: 210152.

Holman, J.P. 1997. *Heat Transfer.* 8th Edition. New York, New York: McGraw-Hill. TIC: 239954.

Incropera, F.P. and DeWitt, D.P. 1996. *Fundamentals of Heat and Mass Transfer.* 4th Edition. New York, New York: John Wiley & Sons. TIC: 243950.

Jury, W.A.; Gardner, W.R.; and Gardner, W.H. 1991. *Soil Physics.* 5th Edition. New York, New York: John Wiley & Sons. TIC: 241000.

Kramer, N.E. 2001. "Guidance for the Ventilation Test Rev 02." Interoffice correspondence from N.E. Kramer to Distribution, February 5, 2001, LV.SSPTS.NEK.02/01-022, with enclosures. ACC: MOL.20010313.0630.

Nitao, J.J. 1998. *Reference Manual for the NUFT Flow and Transport Code, Version 2.0.* UCRL-MA-130651. Livermore, California: Lawrence Livermore National Laboratory. ACC: MOL.19980810.0391.

Nitao, J.J. 2000. *Documentation of the Thermal Energy Balance Equation used in the USNT Module of the NUFT Flow and Transport Code.* UCRL-MA-139836. Livermore, CA: Lawrence Livermore National Laboratory. ACC: MOL.20020711.0161.

Reamer, C.W. and Williams, D.R. 2001a. Summary Highlights of NRC/DOE Technical Exchange and Management Meeting on Repository Design and Thermal-Mechanical Effects. Meeting held February 6-8, 2001, Las Vegas, Nevada. Washington, D.C.: U.S. Nuclear Regulatory Commission. ACC: MOL.20010307.0511; through; MOL.20010307.0521.

Reamer, C.W. and Williams, D.R. 2001b. Summary Highlights of NRC/DOE Technical Exchange and Management Meeting on Thermal Effects on Flow. Meeting held January 8-9, 2001, Pleasanton, California. [Washington, D.C.]: U.S. Nuclear Regulatory Commission. ACC: MOL.20010202.0095; through; MOL.20010202.0108.

Sass, J.H.; Lachenbruch, A.H.; Dudley, W.W., Jr.; Priest, S.S.; and Munroe, R.J. 1988. *Temperature, Thermal Conductivity, and Heat Flow Near Yucca Mountain, Nevada: Some Tectonic and Hydrologic Implications.* Open-File Report 87-649. [Denver, Colorado]: U.S. Geological Survey. TIC: 203195.

Stroe, D.E. 2001. "PO#: A18763CM0A, Transmittal of Test Results." Letter from D.E. Stroe (Anter Laboratories) to M. Knudsen (CRWMS M&O), January 31, 2001, PR20939-51554c, with attachment. ACC: MOL.20010220.0057.

Williams, N.H. 2002. "Contract No. DE-AC08-01RW12101 – Key Technical Issues (KTI) RDTME 3.01, RDTME 3.14, and TEF 2.07 Deliverables to the U.S. Nuclear Regulatory Commision (NRC) – April 2002." Letter from N.H. Williams (BSC) to S. Brocoum (DOE/YMSCO), April 8, 2002, LTS:mm – 0325021948, with enclosures. ACC: MOL.20020409.0153.

9.2 CODES, STANDARDS, REGULATIONS, AND PROCEDURES

AP-3.15Q, Rev. 3, ICN 3. *Managing Technical Product Inputs.* Washington, D.C.: U.S. Department of Energy, Office of Civilian Radioactive Waste Management. ACC: MOL.20020830.0001.

AP-SI.1Q, Rev. 3, ICN 4. *Software Management.* Washington, D.C.: U.S. Department of Energy, Office of Civilian Radioactive Waste Management. ACC: MOL.20020520.0283.

AP-SIII.10Q, Rev. 0, ICN 2. *Models.* Washington, D.C.: U.S. Department of Energy, Office of Civilian Radioactive Waste Management. ACC: MOL.20020506.0911.

AP-SV.1Q, Rev. 0, ICN 2. *Control of the Electronic Management of Information.* Washington, D.C.: U.S. Department of Energy, Office of Civilian Radioactive Waste Management. ACC: MOL.20000831.0065.

DOE (U.S. Department of Energy) 2000. *Quality Assurance Requirements and Description.* DOE/RW-0333P, Rev. 10. Washington, D.C.: U.S. Department of Energy, Office of Civilian Radioactive Waste Management. ACC: MOL.20000427.0422.

9.3 SOURCE DATA, LISTED BY DATA TRACKING NUMBER

GS000308311221.005. Net Infiltration Modeling Results for 3 Climate Scenarios for FY99. Submittal date: 03/01/2000.

GS000508312231.006. Physical Properties and Water Content from Borehole USW NRG-6, 3/19/94 to 3/27/95. Submittal date: 05/23/00.

GS950408312231.004. Physical Properties and Water Potentials of Core from Borehole USW SD-9. Submittal date: 03/01/1995.

GS950408312231.005. Physical Properties and Water Potentials of Core from Borehole USW UZ-14. Submittal date: 03/09/1995.

GS951108312231.009. Physical Properties, Water Content, and Water Potential for Borehole USW SD-7. Submittal date: 09/26/1995.

GS951108312231.010. Physical Properties and Water Content for Borehole USW NRG-7/7A. Submittal date: 09/26/1995.

GS951108312231.011. Physical Properties, Water Content, and Water Potential for Borehole USW UZ-7A. Submittal date: 09/26/1995.

LB0110ECRBH2OP.001. Water Potential Data From Three Locations in the ECRB. Submittal date: 11/12/2001.

LB990861233129.001. Drift Scale Calibrated 1-D Property Set, FY99. Submittal date: 08/06/1999.

SN0003T0571897.013. Thermal Modeling Parameters by Stratigraphic Unit. Submittal date: 03/29/2000.

SN0107F3409100.004. Preclosure Ventilation Test: 1/4-Scale, Including Data from Cases 1 through 6 (with Results from 10/5/2000 through 12/22/2000) Final Data Revised July 2001. Submittal date: 07/25/2001.

9.4 SOFTWARE CODES

BSC 2001. *MULTIFLUX.* v2.2 (10/29/01). 10485-202 (10/29/01)-00.

BSC 2002. *Software Code: ANSYS.* V5.6.2. HP-UX 11.00. 10364-5.6.2-01.

LLNL (Lawrence Livermore National Laboratory) 12/20/01. *NUFT V3.0s.* Sun. 10088-3.0s-01.

LLNL (Lawrence Livermore National Laboratory) 2000. *Software routine: RADPRO V3.22.* V3.22. Sun Ultra10. 10204-3.22-00.

9.5 OUTPUT DATA, LISTED BY DATA TRACKING NUMBER

MO0210MWDTVE30.018. Temperatures and Ventilation Efficiencies Calculated by ANSYS with Fine Drift Segments Ventilation Model Report. Sun, Y. Las Vegas, Nevada.

MO0210MWDTEM30.019. Temperatures and Ventilation Efficiencies Calculated by ANSYS with Coarse Drift Segments for Ventilation Model Report. Sun, Y. Las Vegas, Nevada.

MO0209MWDANS30.017. Revised ANSYS Calculations in Support of Ventilation Model Validiation Based on Measurements from Phase I Ventilation Tests. Sun, Y. Las Vegas, Nevada.

MO0209MWDMUL30.002. MULTIFLUX-Con and MULTIFLUX-Full Calculations in Support of the Ventilation Model Report. Chipman, V. Las Vegas, Nevada.

MO0209MWDMOD30.003. Model Verification Exercises in Support of the Ventilation Model Report. Chipman, V. Las Vegas, Nevada.

MO0210MWDVEN30.005. Application of Pre-Closure Ventilation Effects on Thermal Calculation Supporting Ventilation Model Report, ANL-EBS-MD-000030 REV01. Leem, J. Las Vegas, Nevada.

10. ATTACHMENTS

ATTACHMENT I	DECAY HEAT USING MS EXCEL FOR MULTIFLUX CALCULATIONS
ATTACHMENT II	DECAY HEAT USING MS EXCEL FOR ANSYS CALCULATIONS
ATTACHMENT III	DITTUS-BOELTER MS EXCEL CALCULATIONS FOR CONVECTIVE HEAT TRASNFER COEFFICIENTS
ATTACHMENT IV	ANSYS VENTILATION CALCULATIONAL METHOD
ATTACHMENT V	ANSYS-Coarse VENTILATION INPUT AND OUTPUT FILES
ATTACHMENT VI	ANSYS-Refined VENTILATION INPUT AND OUTPUT FILES
ATTACHMENT VII	MULTIFLUX-Con INPUT AND OUTPUT FILES
ATTACHMENT VIII	MULTIFLUX-Full INPUT AND OUTPUT FILES
ATTACHMENT IX	SUBMODEL VERIFICATION INPUT AND OUTPUT FILES
ATTACHMENT X	VENTILATIN PHASE 1 POST-TEST ANSYS INPUT AND OUTPUT FILES
ATTACHMENT XI	ANALYTICAL SOLUTION USNG MATHCAD FOR THE CONTRIBUTION OF LATENT HEAT TO THE IN-DRIFT AIR OF A VENTILATED EMPLACEMENT DRIFT USING A SOLUTION FOR STEADY STATE UNSATURATED FLOW TO MOISTURE POTENTIAL BOUNDARY AT THE DRIFT WALL
ATTACHMENT XII	SELECT FULL-SIZE FIGURES FROM SECTION 6

ATTACHMENT I

DECAY HEAT USING MS EXCEL FOR MULTIFLUX CALCULATIONS

REFERENCES:

Ref. 1: CRWMS M&O 1999c. Enhanced Design Alternative (EDA) II Repository Estimated Waste Package Types and Quantities. Input Tracking No.: EBS-SR-99325.T. Las Vegas, Nevada: CRWMS M&O. ACC: MOL.19991103.0236.

Ref. 2: DTN: SNT05071897001.004 (files: "avgdhlw.txt" & "nrctor4pck.txt")

EXTRAPOLATION FOR 21-PWR AND 44BWR HEAT AT 0 YR

The heat generation rates at 0 yr for 21-WPR and 44-BWR are not available in Ref.1. They are estimated by extrapolation from years 0.01 and 0.02, which are the closest data points for this purpose.

21 PWR EXTRAPOLATION

Time (yr)	Heat (KW)	
0.01	11.3337	<-- Ref.1
0.02	11.3299	<-- Ref.1
0	11.3375	**<-- Extrapolation**

44-BWR EXTRAPOLATION

Time (yr)	Heat (KW)	
0.01	7.1346	<-- Ref.1
0.02	7.1324	<-- Ref.1
0	7.1368	**<- Extrapolation**

24-BWR Thick

Time (yr)	Heat (KW)	
0.01	0.491	<-- Ref.1
0.02	0.491	<-- Ref.1
0	0.4910	**<-- Extrapolation**

21 PWR (Control Rods)

Time (yr)	Heat (KW)	
0.01	2.3709	<-- Ref.1
0.02	2.3705	<-- Ref.1
0	2.3713	**<-- Extrapolation**

12-PWR Long

Time (yr)	Heat (KW)	
0.01	9.5402	<-- Ref.1
0.02	9.5374	<-- Ref.1
0	9.5430	**<- Extrapolation**

INTERPOLATION FOR 21-PWR, 44-BWR, DHLW,AND DSNF HEAT AT 2 MONTH

The heat rates at 2 month (or 0.167 yr) for 21-WPR, 44-BWR DHLW, and DSNF are not available in Ref.1 or Ref.2. They are estimated by interpolation from the values for 0.15 and 0.20 yrs, which are the closest data points for that time.

21-PWR INTERPOLATION

Time (years)	Heat (KW)	
0.15	11.2829	<-- Ref.1
0.2	11.2648	<-- Ref.1
0.167	11.2767	**<-- Interpolation**

44-BWR INTERPOLATION

Time (years)	Heat (KW)	
0.15	7.1016	<-- Ref.1
0.2	7.0897	<-- Ref.1
0.167	7.0976	**<- Interpolation**

24-BWR Thick

Time (years)	Heat (KW)	
0.15	0.4898	<-- Ref.1
0.2	0.4896	<-- Ref.1
0.167	0.4897	**<-- Interpolation**

DHLW INTERPOLATION

Time (years)	Heat (W)	
0.15	780.5932082	<-- Ref.2
0.2	771.0441027	<-- Ref.2
0.167	777.3465	**<-- Interpolation**

DSNF INTERPOLATION

Time (years)	Heat (W)	
0.15	196.7114993	<-- Ref.2
0.2	196.5837976	<-- Ref.2
0.167	196.6681	**<-- Interpolation**

21 PWR (Control Rods)

Time (years)	Heat (KW)	
0.15	2.3646	<-- Ref.1
0.2	2.3625	<-- Ref.1
0.167	2.3639	**<-- Interpolation**

12-PWR Long

Time (years)	Heat (KW)	
0.15	9.5003	<-- Ref.1
0.2	9.4862	<-- Ref.1
0.167	9.4955	**<-- Interpolation**

Table I-1

Column A	Column B	Column C
Time	21-PWR	44-BWR
(Years)	(W/Pack)	(W/Pack)
0	11337.5	7136.8
0.167	11276.746	7097.554
0.5	11160.2	7021.5
1	10995.4	6914.6
2	10689	6722.3
5	9965.3	6268.2
10	8995.6	5653.6
15	8188.7	5146.7
20	7513.8	4710.2
25	6911.5	4309.8
30	6379.2	3970.1
35	5916.5	3666.1
40	5498.4	3391.5
45	5119.2	3149.1
50	4791.2	2932.6
60	4222.9	2562.1
75	3565.4	2136.6
100	2831.4	1668.5
150	2079	1197.7
200	1729.1	987.8
300	1365.4	788.9

Table I-2

Column D	Column E	Column F
Time	DHLW Asmbly	DSNF Asmbly
(Years)	(W/assembly)	(W/assembly)
0	811.6231253	198.25
0.167	777.3465123	196.6680807
0.5	721.6470237	195.8189723
1	661.5685975	194.549539
2	591.1933186	192.030456
5	511.5961623	184.631475
10	450.3094257	172.8274
15	401.8174876	161.682775
20	359.1687797	151.1976
25	321.3375262	141.371875
30	287.7308117	132.2056
35	257.9145003	123.698775
40	231.3900497	115.8514
45	207.8284042	108.663475
50	186.8603203	102.135
60	151.7067808	91.0564
75	112.1839205	79.384375
100	70.3630508	73.12
150	33.08532855	61.22295286
200	20.11824406	55.13696022
300	12.07181088	47.57232809

Decay Heat for Base Case (Average 1.5477 kW/m)

Table I-3 Base 21-PWR

Column G	Column H	Column I	Column J	Column K
Time	21-PWR	AVERAGE	Avg for Half WP	NORMALIZED
	(From Table I-1)	(for two adjacent timesteps)	0.5*(Column I)	(21-PWR)
(Years)	(W/Pack)	(W/Pack)	(W/Half-WP)	(% of initial step)
0	11337.5			
0.167	11276.746	11307.123	5653.5615	1
0.5	11160.2	11218.473	5609.2365	0.992159809
1	10995.4	11077.8	5538.9	0.979718714
2	10689	10842.2	5421.1	0.95888229
5	9965.3	10327.15	5163.575	0.913331358
10	8995.6	9480.45	4740.225	0.838449356
15	8188.7	8592.15	4296.075	0.759888258
20	7513.8	7851.25	3925.625	0.69436319
25	6911.5	7212.65	3606.325	0.637885517
30	6379.2	6645.35	3322.675	0.587713603
35	5916.5	6147.85	3073.925	0.543714789
40	5498.4	5707.45	2853.725	0.50476589
45	5119.2	5308.8	2654.4	0.469509353
50	4791.2	4955.2	2477.6	0.43823703
60	4222.9	4507.05	2253.525	0.398602721
75	3565.4	3894.15	1947.075	0.344397952
100	2831.4	3198.4	1599.2	0.282865942
150	2079	2455.2	1227.6	0.217137463
200	1729.1	1904.05	952.025	0.168393852
300	1365.4	1547.25	773.625	0.136838522

Table I-4 Base 44-BWR

	Column P	Column Q	Column R	Column S
Time	44-BWR	AVERAGE	AVG for Half WP	NORMALIZED
	(From Table I-1)	(for two adjacent timesteps)	0.5*(Column I)	(44-BWR)
(Years)	(W/Pack)	(W/Pack)	(W/Half-WP)	(% of initial step)
0	7136.8			
0.167	7097.554	7117.177	3558.5885	1
0.5	7021.5	7059.527	3529.7635	0.991899878
1	6914.6	6968.05	3484.025	0.979046889
2	6722.3	6818.45	3409.225	0.958027319
5	6268.2	6495.25	3247.625	0.912616055
10	5653.6	5960.9	2980.45	0.83753713
15	5146.7	5400.15	2700.075	0.758748869
20	4710.2	4928.45	2464.225	0.692472591
25	4309.8	4510	2255	0.633678213
30	3970.1	4139.95	2069.975	0.581684283
35	3666.1	3818.1	1909.05	0.536462701
40	3391.5	3528.8	1764.4	0.495814562
45	3149.1	3270.3	1635.15	0.459493982
50	2932.6	3040.85	1520.425	0.427255076
60	2562.1	2747.35	1373.675	0.386016815
75	2136.6	2349.35	1174.675	0.330095767
100	1668.5	1902.55	951.275	0.267318067
150	1197.7	1433.1	716.55	0.201357926
200	987.8	1092.75	546.375	0.153536999
300	788.9	888.35	444.175	0.124817747

Table I-5 Base DHLW

	Column L	Column M1	Column M	Column N	Column O
Time	DHLW Asmbly	5-DHLW WP	AVERAGE	Avg for Half WP	NORMALIZED
	(From Table I-2)	5*(Column L)	(for two adjacent timesteps)	0.5*(Column M)	(DHLW)
(Years)	(W/assembly)	(W/Pack)	(W/Pack)	(W/Half-WP)	(% of initial step)
0	811.6231253	4058.115627			
0.167	777.3465123	3886.732562	3972.424094	1986.212047	1
0.5	721.6470237	3608.235119	3747.48384	1873.74192	0.943374562
1	661.5685975	3307.842988	3458.039053	1729.019527	0.870511046
2	591.1933186	2955.966593	3131.90479	1565.952395	0.788411488
5	511.5961623	2557.980812	2756.973702	1378.486851	0.694028039
10	450.3094257	2251.547129	2404.76397	1202.381985	0.60536436
15	401.8174876	2009.087438	2130.317283	1065.158642	0.536276398
20	359.1687797	1795.843899	1902.465668	951.2328341	0.478918067
25	321.3375262	1606.687631	1701.265765	850.6328824	0.428268917
30	287.7308117	1438.654059	1522.670845	761.3354224	0.383310243
35	257.9145003	1289.572502	1364.11328	682.05664	0.343395682
40	231.3900497	1156.950249	1223.261375	611.6306875	0.307938263
45	207.8284042	1039.142021	1098.046135	549.0230674	0.276417147
50	186.8603203	934.3016015	986.7218113	493.3609056	0.248392867
60	151.7067808	758.533904	846.4177528	423.2088764	0.213073361
75	112.1839205	560.9196025	659.7267533	329.8633766	0.166076617
100	70.3630508	351.815254	456.3674283	228.1837141	0.114883864
150	33.08532855	165.4266428	258.6209484	129.3104742	0.065104063
200	20.11824406	100.5912203	133.0089315	66.50446576	0.033483064
300	12.07181088	60.3590544	80.47513735	40.23756868	0.020258446

Table I-6 Base DSNF

	Column T	Column U	Column V	Column W	Column X
Time	DSNF Asmbly	4-DSNF WP	AVERAGE	Avg for Half WP	NORMALIZED
	(From Table I-2)	4*(Column T)	(for two adjacent timesteps)	0.5*(Column V)	(DSNF)
(Year)	(W/Asmbly)	(W/Pack)	(W/Pack)	(W/Half-WP)	(% of initial step)
0	198.25	793			
0.167	196.6680807	786.6723228	789.8361614	394.9180807	1
0.5	195.8189723	783.2758892	784.974106	392.487053	0.993844223
1	194.549539	778.198156	780.7370226	390.3685113	0.988479714
2	192.030456	768.121824	773.15999	386.579995	0.978886544
5	184.631475	738.5259	753.323862	376.661931	0.953772312
10	172.8274	691.3096	714.91775	357.458875	0.905146896
15	161.682775	646.7311	669.02035	334.510175	0.84703687
20	151.1976	604.7904	625.76075	312.880375	0.792266524
25	141.371875	565.4875	585.13895	292.569475	0.740835858
30	132.2056	528.8224	547.15495	273.577475	0.692744871
35	123.698775	494.7951	511.80875	255.904375	0.647993565
40	115.8514	463.4056	479.10035	239.550175	0.606581939
45	108.663475	434.6539	449.02975	224.514875	0.568509992
50	102.135	408.54	421.59695	210.798475	0.533777726
60	91.0564	364.2256	386.3828	193.1914	0.489193606
75	79.384375	317.5375	340.88155	170.440775	0.43158514
100	73.12	292.48	305.00875	152.504375	0.386167113
150	61.22295286	244.8918114	268.6859057	134.3429529	0.340179291
200	55.13696022	220.5478409	232.7198262	116.3599131	0.294643165
300	47.57232809	190.2893124	205.4185766	102.7092883	0.260077452

Table I-7 Calculate kW per WP Based on Average Heat Load of 1.5477 kW/m

Average Heat Load: **1.5477** kW/m (see Attachment II, page II-2)

In the table below, the WP heat outputs are "assigned" based on the length of drift occupied by WP and the gap.

		1/2 21-PWR + 1/2 Gap	1/2 44-BWR + 1/2 Gap	1/2 5-DHLW WP + 1/2 Gap	1/2 4-DSNF WP + 1/2 Gap
		WP Length (m)[1]			
		5.305	5.275	3.73	5.57
Time (years)[2]	Decay[2]	(kW)	(kW)	(kW)	(kW)
0	100.00%	4.1826593	4.1594438	2.9638455	4.3877295
0.167	99.46%	4.1601365	4.1370460	2.9478858	4.3641024
0.5	98.43%	4.1167893	4.0939394	2.9171698	4.3186300
1	96.96%	4.0555921	4.0330819	2.8738053	4.2544324
2	94.27%	3.9429308	3.9210459	2.7939731	4.1362474
5	87.90%	3.6764690	3.6560631	2.6051575	3.8567215
10	79.33%	3.3179767	3.2995606	2.3511287	3.4806527
15	72.21%	3.0202669	3.0035031	2.1401706	3.1683465
20	66.21%	2.7693584	2.7539873	1.9623761	2.9051364
25	60.81%	2.5434933	2.5293758	1.8023273	2.6681974
30	56.09%	2.3462216	2.3331991	1.6625400	2.4612537
35	51.96%	2.1732562	2.1611938	1.5399762	2.2798081
40	48.22%	2.0170404	2.0058450	1.4292812	2.1159333
45	44.86%	1.8763752	1.8659605	1.3296054	1.9683714
50	41.93%	1.7536924	1.7439587	1.2426719	1.8396736
60	36.86%	1.5418631	1.5333051	1.0925691	1.6174586
75	31.02%	1.2973071	1.2901065	0.9192759	1.3609124
100	24.51%	1.0252286	1.0195382	0.7264802	1.0754942
150	17.89%	0.7482097	0.7440569	0.5301838	0.7848935
200	14.84%	0.6208852	0.6174391	0.4399612	0.6513264
300	11.76%	0.4918624	0.4891324	0.3485353	0.5159778

notes:
1. From Section 5.1
2. Attachmant II, pg. II-3

Summary of Initial Heat Output for 1/2 WP + 1/2 Gap (average of the first two time steps)

1/2 21-PWR + 1/2 Gap	1/2 44-BWR + 1/2 Gap	1/2 5-DHLW WP + 1/2 Gap	1/2 4-DSNF WP + 1/2 Gap
4171.398	4148.245	2955.866	4375.916
Watts	Watts	Watts	Watts

Table I-8 Calculate Total kW of 8 WPs in the Selected Drift Segment

	21-PWR	44-BWR	5-DHLW WP	4-DSNF WP			
Time	3 packs[1]	2 packs[1]	1.5 packs[1]	0.5 packs[1]	Total	Total Average Between Time Steps	NORMALIZED
(Years)	Total kW	Total kW	Total kW	Total kW	(kW per 8 WPs and Gaps)	(kW per 8 WPs and Gaps)	(% of initial step)
0	25.095956	16.637775	8.891537	4.387730	55.012997	na	na
0.167	24.960819	16.548184	8.843657	4.364102	54.716762	54.864879	100%
0.5	24.700736	16.375757	8.751509	4.318630	54.146633	54.431697	99.2105%
1	24.333553	16.132328	8.621416	4.254432	53.341729	53.744181	97.9573%
2	23.657585	15.684183	8.381919	4.136247	51.859935	52.600832	95.8734%
5	22.058814	14.624252	7.815473	3.856721	48.355261	50.107598	91.3291%
10	19.907860	13.198242	7.053386	3.480653	43.640141	45.997701	83.8382%
15	18.121601	12.014012	6.420512	3.168347	39.724472	41.682307	75.9727%
20	16.616150	11.015949	5.887128	2.905136	36.424364	38.074418	69.3967%
25	15.260960	10.117503	5.406982	2.668197	33.453642	34.939003	63.6819%
30	14.077330	9.332796	4.987620	2.461254	30.859000	32.156321	58.6100%
35	13.039537	8.644775	4.619929	2.279808	28.584049	29.721524	54.1722%
40	12.102243	8.023380	4.287844	2.115933	26.529400	27.556724	50.2265%
45	11.258251	7.463842	3.988816	1.968371	24.679281	25.604340	46.6680%
50	10.522154	6.975835	3.728016	1.839674	23.065678	23.872479	43.5114%
60	9.251179	6.133221	3.277707	1.617459	20.279565	21.672622	39.5018%
75	7.783843	5.160426	2.757828	1.360912	17.063009	18.671287	34.0314%
100	6.151372	4.078153	2.179441	1.075494	13.484459	15.273734	27.8388%
150	4.489258	2.976227	1.590551	0.784893	9.840931	11.662695	21.2571%
200	3.725311	2.469756	1.319884	0.651326	8.166278	9.003604	16.4105%
300	2.951174	1.956529	1.045606	0.515978	6.469288	7.317783	13.3378%

notes: 1. From Section 5.1

Total Segment Length = 35.545 m

Backcheck = 1.5477 kW/m **TRUE**

ATTACHMENT II

DECAY HEAT USING MS EXCEL FOR ANSYS CALCULATIONS

(1) Estimate of Linear Heat Load Along Emplacement Drift

Waste Package Type		Number of WPs	Fraction of Total	Length (m)	Heat Output Rate (KW) per package	Drift Length Required (meters)	Total Heat Output (kW)	Linear Heat Load (kW/m)
		Sec. 4.1.14		Sec. 4.1.14	See Attchm't I	see Note 1		
21-PWR	Absorber	4279	0.429	5.305	11.3375	23128.00	48513.16	2.10
21-PWR	Control Rods	87	0.009	5.305	2.3713	470.24	206.30	0.44
12-PWR	Long	158	0.016	5.791	9.5430	930.78	1507.79	1.62
44-BWR	Absorber	2889	0.29	5.275	7.1368	15528.38	20618.22	1.33
24-BWR	Thick Plates	6	0.001	5.245	0.4910	32.07	2.95	0.09
5-DHLW		1249	0.125	3.73	4.0580	4783.67	5068.44	1.06
5-DHLW	Long	414	0.042	5.357	5.8280	2259.20	2412.79	1.07
Naval	Combined	285	0.029	5.888	7.1368	1706.58	2033.99	1.19
DOE/Other		598	0.06	5.57	0.7930	3390.66	474.21	0.14
Total		9965	1			52229.56	80837.86	
Average				5.141				1.5477

Note 1: Total drift length required for a given type of WPs is determined using:
Total drift length = (Number of WPs)*(WP length + 0.1 m), where 0.1 m is the gap between WPs (see Section 4.1.4).

(2) Thermal Decay for CSNF

Time (years)	21-PWR Absorber Plates kW (Sec 5.1)	21-PWR Control Rods kW (Sec 5.1)	12-PWR Long kW (Sec 5.1)	44-BWR Absorber Plates kW (Sec 5.1)	24-BWR Thick Absorber Plates kW (Sec 5.1)	Total Heat of All CSNF WP (kW)	Percentage Decay of All CSNF WP (%)
0	11.3375	2.3713	9.5430	7.1368	0.4910	70848.42	100.00%
0.01	11.3337	2.3709	9.5402	7.1346	0.4910	70825.33	99.97%
0.167	**11.2767**	**2.3639**	**9.4955**	**7.0976**	**0.4897**	70466.92	**99.46%**
0.5	**11.1602**	**2.3495**	**9.4034**	**7.0215**	**0.4870**	69732.68	**98.43%**
1	10.9954	2.3285	9.2722	6.9146	0.4829	68696.08	96.96%
2	**10.6890**	**2.2974**	**9.0259**	**6.7223**	**0.4721**	66787.75	**94.27%**
5	9.9653	2.1785	8.4286	6.2682	0.4445	62274.26	87.90%
10	8.9956	2.0095	7.5901	5.6536	0.4030	56201.90	79.33%
15	8.1887	1.8547	6.8815	5.1467	0.3689	51159.11	72.21%
20	7.5138	1.7241	6.3149	4.7102	0.3341	46909.07	66.21%
25	6.9115	1.6038	5.8009	4.3098	0.3065	43083.23	60.81%
30	6.3792	1.4942	5.3407	3.9701	0.2806	39741.73	56.09%
35	5.9165	1.3980	4.9411	3.6661	0.2578	36811.93	51.96%
40	5.4984	1.3106	4.5868	3.3915	0.2369	34165.86	48.22%
45	5.1192	1.2333	4.2517	3.1491	0.2182	31783.18	44.86%
50	4.7912	1.1649	3.9792	2.9326	0.2033	29705.11	41.93%
60	4.2229	1.0443	3.5026	2.5621	0.1754	26117.01	36.86%
75	3.5654	0.9070	2.9482	2.1366	0.1445	21974.58	31.02%
100	2.8314	0.7545	2.3024	1.6685	0.1111	17365.94	24.51%
150	2.0790	0.5983	1.6766	1.1977	0.0799	12673.63	17.89%
200	1.7291	0.5244	1.3818	0.9878	0.0684	10516.93	14.84%
300	1.3654	0.4452	1.0804	0.7889	0.0583	8331.46	11.76%

Note 3: Values for 0.167 year are base on linear interpolation (see Attachment I, pg.2).

(3) Decay of Linear and Volumetric Heat Load

Time (years)	Total Heat of All CSNF WP (kW)	Percentage Decay of All CSNF WP (%)	All WP Linear Heat Load (kW/m)	Volumetric Heat Rate (J/yr m^3)
	(page II-3)	(page II-3)	(page II-2)	(See Note 4)
0	70848.4208	100.00%	1.5477	2.54E+10
0.01	70825.3276	99.97%	1.5472	2.54E+10
0.167	70466.9161	99.46%	1.5394	2.53E+10
0.5	69732.6750	98.43%	1.5233	2.50E+10
1	68696.0805	96.96%	1.5007	2.47E+10
2	66787.7543	94.27%	1.4590	2.40E+10
5	62274.2638	87.90%	1.3604	2.23E+10
10	56201.9031	79.33%	1.2277	2.02E+10
15	51159.1129	72.21%	1.1176	1.84E+10
20	46909.0735	66.21%	1.0247	1.68E+10
25	43083.2325	60.81%	0.9412	1.55E+10
30	39741.7253	56.09%	0.8682	1.43E+10
35	36811.9330	51.96%	0.8042	1.32E+10
40	34165.8551	48.22%	0.7464	1.23E+10
45	31783.1816	44.86%	0.6943	1.14E+10
50	29705.1059	41.93%	0.6489	1.07E+10
60	26117.0133	36.86%	0.5705	9.37E+09
75	21974.5756	31.02%	0.4800	7.89E+09
100	17365.9444	24.51%	0.3794	6.23E+09
150	12673.6306	17.89%	0.2769	4.55E+09
200	10516.9307	14.84%	0.2297	3.77E+09
300	8331.4641	11.76%	0.1820	2.99E+09

Note 4: Based on Linear heat load values. For example, in year 0.01,
1.5477(kW/m)*[1000(J/s)/kW]*[365.25*24*60*60(s/yr)]/[(Pi/4)*(1.564 m)^2]
= 2.54E+10 (J/yr-m^3)
Where 1.564 m is the WP diameter (Section 5.1) used in the calculation.

ATTACHMENT III

DITTUS-BOELTER MS EXCEL CALCULATIONS FOR CONVECTIVE HEAT TRANSFER COEFFICIENTS

Calculating Convective Heat Transfer Coefficients for ANSYS and MULTIFLUX Ventilation Models Using the Dittus-Boelter Correlation

Input Parameter	Value	Source
Constant (pi), dimensionless	3.141592654	Universal Constant
Emplacement Drift Diameter (D), m	5.5	(Sec. 4.1.11)
Waste Package Diameter (d), m	1.564	(Sec. 5.2)
Wetted Perimeter (P), m	22.2	P=Pi*(D+d)
Cross Section Area (A), m^2	21.84	A=pi/4*(D^2-d^2)
HydraulicDiameter (Dh), m	3.936	Dh=4A/P=D-d
Air Density (rho), kg/m^3	1.0561	(Sec. 4.1.12)
Air Thermal Conductivity (k), W/m-K	0.0261	(Sec. 4.1.12)
Air Specific Heat (Cp), J/kg-K	1005.7	(Sec. 4.1.12)
Air Dynamic Viscosity (mu), kg/m-s	1.8371E-05	(Sec. 4.1.12)
Air Prandtl Number (Pr), dimensionless	0.7079	(Sec. 4.1.12)
Air Flow Rate (Q), m^3/s per drift	**15**	(Sec. 5.7)
Air Flow Velocity (v), m/s	0.69	v=Q/A
Reynolds Number (Re), dimensionless	155425.74	Re=rho*v*Dh/mu
Nusselt Number (Nu), dimensionless	285.06	Nu=0.023*Re^0.8*Pr^0.4
Conv. Heat Transfer Coef. (h), W/m^2-K	**1.89**	h=k*Nu/Dh
	or h = 5.96E+07	**J/(yr-m^2-K)**

Calculating Convective Heat Transfer Coefficients for Ventilation Test Phase 1 Using the Dittus-Boelter Correlation

Input Parameter	Value	Source
Constant (pi), dimensionless	3.141592654	Universal Constant
Emplacement Drift Diameter (D), m	1.3716	(Section 4.2.2)
Waste Package Diameter (d), m	0.4064	(Section 4.2.1)
Wetted Perimeter (P), m	5.6	P=Pi*(D+d)
Cross Section Area (A), m^2	1.35	A=pi/4*(D^2-d^2)
HydraulicDiameter (Dh), m	0.9652	Dh=4A/P=D-d
Air Density (rho), kg/m^3	1.0561	(Sec. 4.1.12)
Air Thermal Conductivity (k), W/m-K	0.0261	(Sec. 4.1.12)
Air Specific Heat (Cp), J/kg-K	1005.7	(Sec. 4.1.12)
Air Dynamic Viscosity (mu), kg/m-s	1.8371E-05	(Sec. 4.1.12)
Air Prandtl Number (Pr), dimensionless	0.7079	(Sec. 4.1.12)

Test 2 - Case 5, Test 5 - Case 3

Air Flow Rate (Q), m^3/s per drift	**0.5**	(Sec. 4.2.4)
Air Flow Velocity (v), m/s	0.37	v=Q/A
Reynolds Number (Re), dimensionless	20583.57	Re=rho*v*Dh/mu
Nusselt Number (Nu), dimensionless	56.56	Nu=0.023*Re^0.8*Pr^0.4
Conv. Heat Transfer Coef. (h), W/m^2-K	**1.53**	h=k*Nu/Dh

Test 1 - Case 4, Test 3 - Case 1

Air Flow Rate (Q), m^3/s per drift	**1**	(Sec. 4.2.4)
Air Flow Velocity (v), m/s	0.74	v=Q/A
Reynolds Number (Re), dimensionless	41167.13	Re=rho*v*Dh/mu
Nusselt Number (Nu), dimensionless	98.48	Nu=0.023*Re^0.8*Pr^0.4
Conv. Heat Transfer Coef. (h), W/m^2-K	**2.66**	h=k*Nu/Dh

Test 4 - Case 5

Air Flow Rate (Q), m^3/s per drift	**2**	(Sec. 4.2.4)
Air Flow Velocity (v), m/s	1.48	v=Q/A
Reynolds Number (Re), dimensionless	82334.26	Re=rho*v*Dh/mu
Nusselt Number (Nu), dimensionless	171.47	Nu=0.023*Re^0.8*Pr^0.4
Conv. Heat Transfer Coef. (h), W/m^2-K	**4.64**	h=k*Nu/Dh

ATTACHMENT IV

ANSYS VENTILATION CALCULATIONAL METHOD

Calculation of Instantaneous Ventilation Efficiency

The results of Steps 1 through 18 yield the ventilation efficiency as a function of both time and axial position from the drift entrance.

1. Run 2D ANSYS at 0-meters (drift entrance) with $T_{air(Drift\_Entrance)}$ = 25°C which yields $T_{WP(Drift\_Entrance)}$ and $T_{DW(Drift\_Entrance)}$ for t = {0 0.01 0.167 0.5 1 2 5 10 15 20 25 30 35 40 45 50 60 75 100 150 200 300} years.

2. For t = 0 years, calculate total heat input for Segment_1:

$$q_{in(Segment\_1)} = q_{WP} L_{Segment\_1}$$

3. For t = 0 years, calculate total heat output to the air for Segment_1:

$$q_{out(Segment\_1)} = q_{WP-air} + q_{DW-air}$$

where

$$q_{WP-air} = hA_{WP}\left(T_{WP(Drift\_Entrance)} - T_{air(Drift\_Entrance)}\right)$$

and

$$q_{DW-air} = hA_{DW}\left(T_{DW(Drift\_Entrance)} - T_{air(Drift\_Entrance)}\right)$$

4. For t = 0 years, calculate the efficiency for Segment_1:

$$\eta = \frac{q_{out(Segment\_1)}}{q_{in(Segment\_1)}}$$

5. For t = 0 years, calculate the segment exit air temperature for Segment_1:

$$T_{air(Segment\_1\_Exit)} = T_{air(Drift\_Entrance)} + \frac{q_{out(Segment\_1)}}{\rho_{air} c_p Q_{airflow}}$$

6. Increment to the next time step and repeat Steps 2-5 for t = 0.01, 0.167, 0.5...300 years.

7. Run 2D ANSYS at the beginning Segment_2 with $T_{air(Segment\_1\_Exit)}$ as calculated from Step 5 for each time step which yields $T_{WP(Segment\_2\_Entrance)}$ and $T_{DW(Segment\_2\_Entrance)}$ for t = {0 0.01 0.167 0.5 1 2 5 10 15 20 25 30 35 40 45 50 60 75 100 150 200 300} years.

8. Repeat Steps 2 through 6 for t = 0, 0.01, 0.167, 0.5...300 years.

9. Repeat steps 2 through 8, incrementing the Segment number until the drift exit is reached.

Calculation of Integrated Ventilation Efficiency

The results of Steps 19 through 23 yield a single value of efficiency over the entire drift length and ventilation duration (300 years).

19. Using the results of Steps 1 through 9 (specifically Step 3 for each time step), calculate the sum of the heat output to the air from the waste package and from the drift wall over the entire length of the drift for t = 0, 0.01, 0.167, 0.5...300 years.

20. Calculate the sum of the heat input from the waste package for t = 0, 0.01, 0.167, 0.5...300 years.

21. Integrate the sum of the heat output to the air (Step 19) from t = 0 to t = 300 years.

22. Integrate the sum of the heat input from the waste package (Step 20) from t = 0 to t = 300 years.

23. Calculate the "overall" efficiency by dividing the result of Step 21 by Step 22.

ATTACHMENT V

ANSYS-Coarse VENTILATION INPUT AND OUTPUT FILES

See the attached CD-ROM

Compressed Excel files with its name and size are listed as follows:

```
08/25/02  01:55p               170,175 amr15cs.zip
```

amr15cs.zip: Results for an initial linear heat load of 1.55 kW/m, air flow rate of 15 m^3/s, and intake air temperature of 25°C. The file contains air, emplacement drift, and waste package temperatures, and ventilation efficiencies. Compressed Microsoft Excel 97 file.

Grouped and compressed files of ANSYS runs are listed as follows:

```
08/26/02  09:30a               486,659 amr.tar.Z
08/25/02  03:44p           168,286,715 amr-10cs.tar.Z
08/25/02  03:50p           168,313,862 amr-15cs.tar.Z
08/25/02  03:52p           168,644,409 amr-5cs.tar.Z
```

amr.tar.Z: Grouped and compressed file that contains material properties, model configurations, mesh sizes, and etc. of ANSYS runs for all cases analyzed. ANSYS text and binary files.

amr15cs.tar.Z: Grouped and compressed file that contains input and output files of ANSYS runs for an initial linear heat load of 1.55 kW/m, air flow rate of 15 m^3/s, and intake air temperature of 25°C. The file contains boundary conditions, loads, and emplacement drift and waste package temperatures. ANSYS text and binary files.

ATTACHMENT VI

ANSYS-Refined VENTILATION INPUT AND OUTPUT FILES

See the attached CD-ROM.

Compressed Excel file with its name and size is listed as follows:

```
08/25/02  01:54p               529,446 amr15fs.zip
```

amr15fs.zip: Results for an initial linear heat load of 1.55 kW/m, air flow rate of 15 m^3/s, and intake air temperature of 25°C. The file contains air, emplacement drift, and waste package temperatures, and ventilation efficiencies. Compressed Microsoft Excel 97 file.

Grouped and compressed file of ANSYS runs is listed as follows:

```
08/25/02  02:25p           703,669,190 amr15fs.tar.Z
```

amr15fs.tar.Z: Grouped and compressed file that contains input and output files of ANSYS runs for an initial linear heat load of 1.55 kW/m, air flow rate of 15 m^3/s, and intake air temperature of 25°C. The file contains material properties and calculation configurations, and emplacement drift and waste package temperatures. ANSYS text and binary files.

ATTACHMENT VII

MULTIFLUX-Con INPUT AND OUTPUT FILES

See the attached CD-ROM.

Grouped and compressed file of MULTIFLUX run is listed as follows:

-rw-r--r-- 1 leemj user 4557571 Dec 17 17:12 MF-con_mfv20-102901.tar.Z

MF-con_mfv20-102901.tar.Z:	The MULTIFLUX input and output text files for the ventilation model with no saturation and infiltration (MF-Con).

ATTACHMENT VIII

MULTIFLUX-Full INPUT AND OUTPUT FILES

See the attached CD-ROM.

Grouped and compressed file of MULTIFLUX run is listed as follows:

-rw-r--r-- 1 hyang user 4517735 Dec 17 17:21 MF-full_mfv20-102901.tar.Z

-rw-r--r-- 1 leemj user 4557571 Jan 02 08:46 MF-full_saturation.tar.gz

MF-full_mfv20-102901.tar.Z:	The MULTIFLUX input and output text files for the full heat and moisture ventilation model (MF-Full).
MF-full_saturation.tar.gz:	The MULTIFLUX input and output text files for the full heat and moisture ventilation model (MF-Full) with details of rock saturation and dryout.

ATTACHMENT IX

SUBMODEL VERIFICATION INPUT AND OUTPUT FILES

See the attached CD-ROM.

Grouped and compressed file of MULTIFLUX run is listed as follows:

```
09/09/2002  11:15:43 AM             1,363,745 model_verification.zip
```

model_verification.zip: Input and output files for the model verification exercises.

ATTACHMENT X

VENTILATION PHASE 1 POST-TEST ANSYS INPUT AND OUTPUT FILES

See the attached CD-ROM.

Compressed Excel file with its name and size is listed as follows:

```
08/25/02  01:48p             2,100,387 vtia.zip
08/25/02  01:50p             5,033,296 vtib.zip
08/25/02  01:51p             3,527,662 vtic.zip
08/25/02  01:52p             3,246,544 vtid.zip
08/25/02  01:52p             3,324,959 vtie.zip
```

vtia.zip: Results for Test #1 (a linear heat load of 0.18 kW/m and an air flow rate of 1.0 m^3/s). The file contains concrete pipe, waste package, and insulation temperatures, and ventilation efficiencies. Compressed Microsoft Excel 97 file.

vtib.zip: Results for Test #2 (a linear heat load of 0.18 kW/m and an air flow rate of 0.5 m^3/s). The file contains concrete pipe, waste package, and insulation temperatures, and ventilation efficiencies. Compressed Microsoft Excel 97 file.

vtic.zip: Results for Test #3 (a linear heat load of 0.36 kW/m and an air flow rate of 1.0 m^3/s). The file contains concrete pipe, waste package, and insulation temperatures, and ventilation efficiencies. Compressed Microsoft Excel 97 file.

vtid.zip: Results for Test #4 (a linear heat load of 0.36 kW/m and an air flow rate of 2.0 m^3/s). The file contains concrete pipe, waste package, and insulation temperatures, and ventilation efficiencies. Compressed Microsoft Excel 97 file.

vtie.zip: Results for Test #5 (a linear heat load of 0.36 kW/m and an air flow rate of 0.5 m^3/s). The file contains concrete pipe, waste package, and insulation temperatures, and ventilation efficiencies. Compressed Microsoft Excel 97 file.

Grouped and compressed file of ANSYS runs is listed as follows:

```
08/25/02  03:41p           126,456,851 vti.tar.Z
```

vti.tar.Z: Grouped and compressed file that contains input and output files of ANSYS runs for all cases analyzed. The file contains material properties, model configurations, boundary and initial conditions, heat loads, and concrete pipe, waste package, and insulation temperatures. ANSYS text and binary files.

ATTACHMENT XI

ANALYTICAL SOLUTION USING MATHCAD FOR THE CONTRIBUTION OF LATENT HEAT TO THE IN-DRIFT AIR OF A VENTILATED EMPLACEMENT DRIFT USING A SOLUTION FOR STEADY STATE UNSATURATED FLOW TO MOISTURE POTENTIAL BOUNDARY AT THE DRIFT WALL

Steady State Solution Summary Unsaturated Flow to a Drift Subject to a Moisture Potential Boundary Condition at the Drift Surface

Electronic files with their name and size are listed as follows:

```
Steady State Unsaturated Flow Solution Rev01 mcad7.mcd
10/07/02    01:18p      240,912

Steady State Unsaturated Flow.xls
10/07/02    01:19p      125,440

Output.prn
10/07/02    01:36p      360
```

Develop a steady solution for radial unsaturated flow to the specified moisture potential conditions. Neglect the gravity component of flow, and consider the Van Genuchten constitutive relationships. *Soil Physics* (Jury et al. 1991, Section 3.4) develops the solution for radial flow under unsaturated conditions. In the case of steady state flow under saturated conditions, the water conservation equation for a cylindrical coordinate geometry is given by:

$$\frac{1}{r}\cdot\frac{d}{dr}(r\cdot J_r)=0 \qquad \text{Eq. XI-1}$$

where

r	=	Radial Coordinate
J_r	=	Darcy Flux in the Radial Direction

Equation XI-1 can be integrated once to produce the result:

$$r\cdot J_r=\phi=Cons\tan t=Q/(2\cdot\pi\cdot z_0) \qquad \text{Eq. XI-2}$$

where

Q	=	Flow rate per Unit Length along the Tunnel
z_0	=	Length Along the Tunnel

The radial flux under Darcy's Law is given by:

$$J_r=-K_s\cdot\frac{dp}{dr} \qquad \text{Eq. XI-3}$$

where

K_S	=	Saturated Hydraulic Conductivity
p	=	Pressure or Pressure Head Depending on convention adopted for Darcy's

Law

Writing Darcy's Law for radial flow to the tunnel surface:

$$-K_s \cdot \frac{dp}{dr} = \frac{Q}{2\pi \cdot z_0 \cdot r}$$

Eq. XI-4

This equation can be integrated after placing all factors explicitly for r on the same side of the equation:

$$dp = \frac{-Q}{2\pi \cdot K_s} \cdot \frac{dr}{r}$$

Eq. XI-5

Since $p(R_1) = p_1$ and $p(R_2) = p_2$ are specified at the boundary then:

$$\int_{p_1}^{p_2} dp = \frac{Q}{2 \cdot \pi \cdot K_s \cdot z_0} \int_{R_1}^{R_2} \frac{dr}{r}$$

Eq. XI-6

from which we calculate:

$$Q = \frac{K_s \cdot 2\pi \cdot (p_1 - p_2)}{\ln(\frac{R_2}{R_1})}$$

Eq. XI-7

This expression agrees with the formulation presented in *Soil Physics* (Jury et al., 1991, p. 113 Equation 3.92).

Now consider the unsaturated flow case. The pressure gradient becomes a moisture potential gradient. For unsaturated flow, the unsaturated hydraulic conductivity is a strong nonlinear function of the moisture potential ψ. The boundary conditions for flow are represented in Figure XI-1.

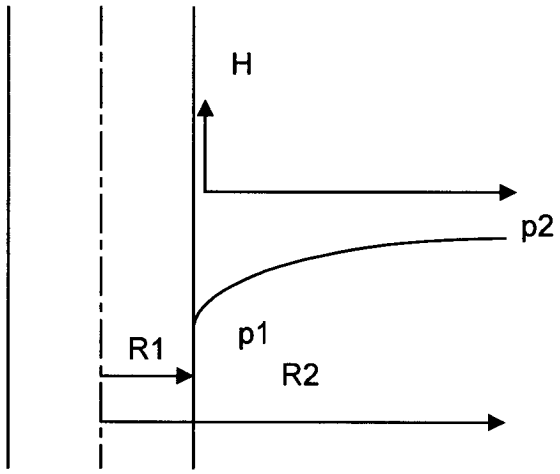

Figure XI-1. Geometry for Unsaturated Flow Calculation

Neglecting the elevation head:

$$H_1 = \frac{p_1}{\psi_w} + 0 = -\psi_1$$

$$H_2 = \frac{p_2}{\gamma_w} + 0 = -\psi_2$$

Eq. XI-8

where

H_1	=	Total Potential at the Drift Surface R1
H_2	=	Total Potential at the Outer Boundary R2
ψ_1	=	Moisture Potential at Radius R1 Set by the RH in the Drift
ψ_2	=	Moisture Potential at Radius R2 Set by Undisturbed State of Capillary Equilibrium
γ_w	=	Unit Weight of Water

Writing Darcy's Law for unsaturated radial flow:

$$-K(\psi)\cdot\frac{dH}{dr} = \frac{Q}{2\pi\cdot z_0\cdot r}$$

Eq. XI-9

Noting that if we neglect the elevation head:

$$H \approx \psi$$

$$-K(\psi)\cdot\frac{dH}{dr}=\frac{Q}{2\pi\cdot z_0\cdot r}$$

Eq. XI-10

The convention is adopted that moisture potential is in units of head (Jury et al., 1991, p. 51). Now the Van Genuchten constitutive relation can be invoked. From *Contaminant Hydrogeology* (Fetter 1993, p. 182), the constitutive relation is:

$$K(\psi)=\frac{K_s\cdot\left\{1-(\alpha\psi)^{n-1}\cdot\left[1+(\alpha\psi)^n\right]^{-m}\right\}^2}{\left[1+(\alpha\psi)^n\right]^{\frac{m}{2}}}$$

Eq. XI-11

where

n	=	1/(1-m)
α	=	Van Genuchten Parameter
m	=	Van Genuchten Parameter

Substituting in the constitutive relation into Darcy's Law:

$$\frac{K_s\cdot\left\{1-(\alpha\psi)^{n-1}\cdot\left[1+(\alpha\psi)^n\right]^{-m}\right\}^2}{\left[1+(\alpha\psi)^n\right]^{\frac{m}{2}}}\cdot\frac{d\psi}{dr}=\frac{Q}{2\pi\cdot z_0\cdot r}$$

Eq. XI-13

Equation XI-12 can be integrated in the same manner:

$$\int_{\psi_1}^{\psi_2}\frac{K_s\cdot\left\{1-(\alpha\psi)^{n-1}\cdot\left[1+(\alpha\psi)^n\right]^{-m}\right\}^2}{\left[1+(\alpha\psi)^n\right]^{\frac{m}{2}}}\cdot d\psi=\frac{Q}{2\pi\cdot z_0}\cdot\int_{R_1}^{R_2}\frac{dr}{r}=\frac{Q}{2\pi\cdot z_0}\cdot\ln\left(\frac{R_2}{R_1}\right)$$

Eq. XI-14

Note that the sign convention in the constitutive law is positive while in Darcy's Law it is negative. Note that ψ_1 and ψ_2 are expressed in units of head consistent with sign convention presented by *Soil Physics* (Jury et al., 1991 p. 151). Substituting in the definition of hydraulic conductivity (Fetter 1993, p. 181):

$$K_s=\frac{\rho\cdot g\cdot k}{\mu}$$

Eq. XI-14

$$Q = \frac{-2\pi \frac{\rho \cdot g \cdot k}{\mu} \int_{\psi_1}^{\psi_2} \frac{\left\{1-(\alpha\psi)^{n-1}\cdot\left[1+(\alpha\psi)^n\right]^{-m}\right\}^2}{\left[1+(\alpha\psi)^n\right]^{\frac{m}{2}}} \cdot d\psi}{\ln\left(\frac{R_2}{R_1}\right)}$$

Eq. XI-15

Now consider the boundary conditions, and the geometry for the problem. Assume that the RH is 30 percent (Section 5.10) in the ventilated drift and use the Kelvin Equation to calculate moisture potential (Jury et al., 1991, p. 60):

$$RH = \exp\left(\frac{M_w \cdot \psi_1}{\rho_w \cdot R \cdot T}\right)$$

Eq. XI-16

Input properties for analysis. The properties for water are obtained from *Fundamentals of Heat and Mass Transfer* (Incropera and DeWitt 1996, p. 846):

Density of water

$$\rho_w := 1000 \cdot \frac{kg}{m^3}$$

$$\rho_w = 1.000 \frac{gm}{cm^3}$$

Molecular weight of water

$$M := 18 \cdot \frac{gm}{mole}$$

The universal gas constant is given by is obtained from *Fundamentals of Heat and Mass Transfer* (Incropera and DeWitt 1996, Backcover):

Gas Constant

$$R := 8.314510 \cdot \frac{joule}{moleK}$$

Nominal temperature

$$T := (273.16 + 25) \cdot K$$

Substituting into Equation XI-16:

$$\psi(RH,T) := \frac{\rho_w \cdot R \cdot T}{M} \cdot \ln\left(\frac{RH}{100}\right)$$

$$\psi(30,T) = -1.658 \times 10^{8}\,kgm^{-1}s^{-2}$$

The moisture potential is expressed in bars. Calculate the moisture potential in units of head:

$$\psi_1 := \frac{\psi(30,T)}{\rho_w \cdot g}$$

$$\psi_1 = -1.691 \times 10^{6}\,cm$$

Input the properties for the tuff surrounding the tunnel (DTN: LB990861233129.001):

Properties :=

	Unit	k_m (m^2)	ϕ_m	α_m (1/Pa)	m_m	S_{lrm}	S_{lsm}	ϕ_f	α_f (1/Pa)	m_f	S_{lrf}	S_{lsf}	γ
0	TSw34	4.07E-18	0.110	3.86E-6	0.291	0.19	1.00	2.76E-13	1.0E-2	5.16E-4	0.608	0.01	1.00
1	TSw35	3.04E-17	0.131	6.44E-6	0.236	0.12	1.00	1.29E-12	1.1E-2	7.39E-4	0.611	0.01	1.00
2	TSw36	5.71E-18	0.112	3.55E-6	0.380	0.18	1.00	9.91E-13	1.5E-2	7.84E-4	0.610	0.01	1.00
		0	1	2	3	4	5	6	7	8	9	10	11

From *Fundamentals of Heat and Mass Transfer* (Incropera and DeWitt 1996, p. 846)

Viscosity of Water at 300 K:

$$\mu_w := 8.55 \cdot 10^{-4} \cdot \frac{N \cdot s}{m^2}$$

Consider the matrix of the TSw35 unit. Convert the air-entry parameter (cm^{-1}):

$$k := Properties_{1,2} = 3.040 \times 10^{-17}\ m^2$$

$$\alpha := Properties_{1,4} = \rho_w \cdot g = 6.315 \times 10^{-4}\ cm^{-1}$$

$$m' := Properties_{1,3} = 0.236$$

$$\theta_r = Properties_{1,1} \cdot Properties_{1,4} = 0.016$$

$$\theta_s = \text{Properties}_{1,1} \cdot \text{Properties}_{1,5} = 0.131$$

$$n := \frac{1}{1 - m'}$$

$$n = 1.309$$

$$z_0 := 1 \cdot mm$$

$$z_0 = 1.000 \times 10^{-3} m$$

The moisture potential in the surrounding formation at a radius $r = R_2$ is calculated in the following manner. The matrix saturation is estimated based upon measurements on core samples. The retention relationship (Fetter, 1993, p. 172, Equation 4.9) is used to calculate the moisture potential.

Characterization of Hydrogeologic Units Using Matrix Properties (Flint 1998, p. 17) described the test method (ASTM R97-47 1977) for matrix properties. After initial sample weighing, core samples were saturated with CO_2 after evacuation of air under a vacuum to enable the saturation of small internal pores. The samples were then submersed in distilled, de-aired water. Samples were removed, dried with a damp towel, and weighed to determine the saturated weight. The sample was suspended in a beaker of water in a wire basket to determine volume displacement, dried for 48 hours in a relative humidity oven at 60 °C and 65 percent relative humidity, and reweighed. The samples were then dried at 105 °C for at least 48 hours to obtain a standard dry weight. Test determinations were made for matrix porosity (fM), bulk density (r), and grain density (rG) for both RH and oven dry weights. The table below presents the source for the matrix saturation for 377 measurements from several boreholes. The saturation can be determined from the initial weighing and the properties.

Borehole	DTN Core Data
USW SD-7	GS951108312231.009
USW UZ-7A	GS951108312231.011
USW NRG-7/7A	GS951108312231.010
USW NRG-6	GS000508312231.006
USW SD-9	GS950408312231.004
USW UZ-14	GS950408312231.005

The average saturation from these 377 measurements is 0.76 (Steady State Unsaturated Flow.xls, Worksheet: Matrix Saturation).

Calculate the average volumetric moisture content:

$$\theta := 0.76 \cdot \theta_s$$

$$\theta = 0.100$$

The retention relationship (Fetter, 1993, p. 172, Equation 4.9) is used to calculate the moisture potential:

$$\theta = \theta_r + \frac{\theta_s - \theta_r}{\left[1 + (\alpha \cdot \psi)^n\right]^m}$$

Eq. XI-17

$$n = \frac{1}{1 - m}$$

Eq. XI-18

Solve for m:

$$m' := \frac{-(-n + 1)}{n}$$

$$m' = 0.236$$

Solve for moisture potential in terms of volumetric moisture content:

$$\psi := \frac{\left[-1 + \left[\frac{-(-\theta_s + \theta_r)}{(\theta - \theta_r)}\right]^{\left(\frac{1}{m'}\right)}\right]^{\left(\frac{1}{n}\right)}}{\alpha}$$

Eq. XI-19

$$\psi = 3.529 \times 10^3 \text{ cm}$$

The calculated value is 3530 cm.

$$\psi_2 := \psi$$

Input the geometry of the drift. Assume a radius of influence of 6 m. Note that subsequently this value is varied to assess the sensitivity to the radius of influence:

$$R_1 := 2.75 \cdot m$$

$$R_2 := 6 \cdot m$$

$$k = 3.040 \times 10^{-17} m^2$$

$$\psi_1 = -1.691 \times 10^{4} m$$

$$\psi_2 = 35.292 m$$

Calculate the steady state flux rate at the wall (Equation XI-15):

$$Q := -2 \cdot \pi \cdot z_0 \cdot \frac{\rho_w \cdot g \cdot k}{\mu_w} \cdot \frac{\int_{|\psi_1|}^{|\psi_2|} \frac{\left[1 - (\alpha \cdot \psi)^{n-1} \cdot \left[1 + (\alpha \cdot \psi)^n\right]^{-m'}\right]^2}{\left[1 + (\alpha \cdot \psi)^n\right]^{\frac{m'}{2}}} d\psi}{\ln\left(\frac{R_2}{R_1}\right)}$$

$$z_0 = 1.000 \times 10^{-3} m$$

$$R_1 = 2.750 m$$

$$Q = 2.653 \times 10^{-13} m^3 s^{-1}$$

$$z_0 = 0.100 cm$$

$$R_2 = 6.000 m$$

$$k = 3.040 \times 10^{-13} cm^2$$

$$Flux := \frac{Q}{2 \cdot \pi \cdot R_1 \cdot z_0}$$

$$\text{Flux} = 0.484 \frac{\text{mm}}{\text{yr}}$$

$$\text{Flux} \cdot \pi \cdot 5.5 \cdot \text{m} \cdot 600 \cdot \text{m} = 1.327 \times 10^3 \frac{\text{gal}}{\text{yr}}$$

Calculate the latent heat transfer by multiplying by the latent heat of vaporization. From *Fundamentals of Heat and Mass Transfer* (Incropera and DeWitt 1996, p. 846):

$$2.334 \cdot 10^3 \cdot \frac{\text{J}}{\text{kg}} \cdot 1000 \cdot 1000 \frac{\text{kg}}{\text{m}^3} \cdot (\text{Flux} \cdot \pi \cdot 5.5 \cdot \text{m} \cdot 600 \cdot \text{m}) = 371.475\,\text{W}$$

Note that the factor of 1000 is for kJ in the reference.

Calculate the total energy for 300 years:

$$2.334 \cdot 10^3 \cdot \frac{\text{J}}{\text{kg}} \cdot 1000 \cdot 1000 \cdot \frac{\text{kg}}{\text{m}^3} \cdot (\text{Flux} \cdot \pi \cdot 5.5 \cdot \text{m} \cdot 600 \cdot \text{m}) \cdot 300 \cdot \text{yr} = 3.517 \times 10^{12}\,\text{J}$$

Compare this calculation with the average line loading used in the ventilation analysis. The heat load is calculated out to three hundred years, and the average value for the line loading is determined during this period (Attachment II).

Initial Heat Load	1.5477	kW/m					
Time (yr)	Decay (%	Heat Load	Area				
0	100.00%	1.5477	0		Average	0.412514	
0.01	99.97%	1.547196	0.015474				
0.167	99.46%	1.539366	0.25777				
0.5	98.43%	1.523326	0.767708				
1	96.96%	1.500682	1.52371				
2	94.27%	1.458994	3.003548				
5	87.90%	1.360396	7.232632				
10	79.33%	1.227743	13.70298				
15	72.21%	1.117583	19.56629				
20	66.21%	1.024739	24.9221				
25	60.81%	0.941163	29.83686				
30	56.09%	0.868167	34.36018				
35	51.96%	0.804165	38.54101				
40	48.22%	0.746361	42.41733				
45	44.86%	0.694311	46.01901				
50	41.93%	0.648915	49.37707				
60	36.86%	0.570532	55.47431				
75	31.02%	0.48004	63.35359				
100	24.51%	0.379363	74.09613				
150	17.89%	0.276858	90.50166				
200	14.84%	0.229745	103.1667				
300	11.76%	0.182003	123.7541				

$$123 \cdot 1000 \cdot \frac{W}{m} \cdot yr \cdot 600 \cdot m = 2.329 \times 10^{15} J$$

$$\frac{3.517 \cdot 10^{12} J}{2.329\,10^{15} J} = 0.151\,\%$$

The latent heat transfer is approximately 0.151% and is a small percentage of the waste package heat loading. Repeat the calculation for a higher farfield saturation. Consider a saturation of the mean (0.76) plus one standard deviation (0.15).

$$0.76 + 0.15 = 0.910$$

$$\theta := 0.91 \cdot \theta_s$$

Substituting into Equation XI-19:

$$\psi := \frac{\left[-1 + \left[\frac{-\left(-\theta_s + \theta_r\right)}{\left(\theta - \theta_r\right)}\right]^{\left(\frac{1}{m'}\right)}\right]^{\left(\frac{1}{n}\right)}}{\alpha}$$

$$\psi = 1.044 \times 10^{3}\,\text{cm}$$

The calculated value is 1040 cm.

$$\psi_2 := \psi$$

Calculate the steady state flux rate at the wall (Equation XI-15):

$$Q := -2\cdot\pi\cdot z_0 \cdot \frac{\rho_w \cdot g \cdot k}{\mu_w} \cdot \frac{\int_{|\psi_1|}^{|\psi_2|} \frac{\left[1 - (\alpha\cdot\psi)^{n-1}\cdot\left[1 + (\alpha\cdot\psi)^{n}\right]^{-m'}\right]^{2}}{\left[1 + (\alpha\cdot\psi)^{n}\right]^{\frac{m'}{2}}} d\psi}{\ln\left(\frac{R_2}{R_1}\right)}$$

$$z_0 = 1.000 \times 10^{-3}\,\text{m}$$

$$R_1 = 2.750\,\text{m}$$

$$Q = 1.237 \times 10^{-12}\,\text{m}^3\,\text{s}^{-1}$$

$$z_0 = 0.100\,\text{cm}$$

$$R_2 = 6.000\,\text{m}$$

$$k = 3.040 \times 10^{-13}\,\text{cm}^2$$

$$\text{Flux} := \frac{Q}{2\cdot\pi\cdot R_1\cdot z_0}$$

$$\text{Flux} = 2.259\frac{\text{mm}}{\text{yr}}$$

$$\text{Flux}\cdot\pi\cdot 5.5\cdot\text{m}\cdot 600\cdot\text{m} = 6.186\times 10^{3}\frac{\text{gal}}{\text{yr}}$$

Calculate the latent heat transfer by multiplying by the latent heat of vaporization. From *Fundamentals of Heat and Mass Transfer* (Incropera and DeWitt 1996, p. 846):

$$2.334\cdot 10^{3}\cdot\frac{\text{J}}{\text{kg}}\cdot 1000\cdot 1000\frac{\text{kg}}{\text{m}^{3}}\cdot\left(\text{Flux}\cdot\pi\cdot 5.5\cdot\text{m}\cdot 600\cdot\text{m}\right) = 1.732\times 10^{3}\,\text{W}$$

Calculate the total energy for 300 years:

$$2.334\cdot 10^{3}\cdot\frac{\text{J}}{\text{kg}}\cdot 1000\cdot 1000\cdot\frac{\text{kg}}{\text{m}^{3}}\cdot\left(\text{Flux}\cdot\pi\cdot 5.5\cdot\text{m}\cdot 600\cdot\text{m}\right)\cdot 300\cdot\text{yr} = 1.640\times 10^{13}\,\text{J}$$

$$\frac{1.64\cdot\left(10^{13}\cdot\text{J}\right)}{2.329\,10^{15}\,\text{J}} = 0.704\,\%$$

The latent heat transfer is approximately 0.704% and is a small percentage of the waste package heat loading.

The calculation of the farfield moisture potential from the saturation on core measurements, and the Van Genuchten retention relationship may be compared with measurements made in the ECRB.

Water-potential measurements along three horizontal boreholes in the ECRB Cross Drift are summarized in *In Situ Field Testing of Processes AMR* (BSC 2001, Section 6.10.2.2). The water potential as a function of depth and time are presented in DTN: LB0110ECRBH2OP.001. Low water potentials close to the drift increase rapidly over a distance of several meters, and remain close to saturation values along the deeper profile. As discussed subsequently, these qualitative observations are in agreement with the calculation of the moisture potential profile presented subsequently.

Among the monitored boreholes, the borehole located at CD 15+00 in the Tptpll unit has the lowest water potential (driest condition) close to the driftwall. The borehole at CD 20+00 also shows lower water potentials up to a distance of about 1.5 m from the borehole collar. The borehole located furthest into the ECRB Cross Drift at CD 25+00 did not show large drops in saturated potential closer to the collar, nor did the borehole show any increases in water

potentials following the installation of the bulkhead doors. The following table summarizes the measurements at ECRB Station 15+00 on 07/29/2000.

DEPTH (m)	WATER POTENTIAL (m)
0.62	-258.8
1.12	-90.7
1.62	-10.4
2.12	-24.23
2.62	-36.78
3.12	-4.62
3.62	3.51
4.12	-12.49
4.62	-13.52
5.12	-7.62
5.62	-9.99

The calculation of farfield moisture potential from the average and high saturation values on core samples, and the Van Genuchten relationship (-1000 to -3500 cm) presented above are in approximate agreement with water potential measurements made at Station 15+00 at depths of 2 to 5 meters in the ECRB drift.

Repeat the calculation for different radii of influence. Consider a radius of influence of 4.75 m (Flow path length of 2 m) and the farfield moisture potential of 3529 cm.

$$\psi_1 = -1.691 \times 10^6 \text{cm}$$

$$\psi_2 := 3529 \cdot \text{cm}$$

$$R_2 := 4.75 \cdot \text{m}$$

Restate the flow rate equation (Equation XI-15):

$$Q := -2 \cdot \pi \cdot z_0 \cdot \frac{\rho_w \cdot g \cdot k}{\mu_w} \cdot \frac{\int_{|\psi_1|}^{|\psi_2|} \frac{\left[1 - (\alpha \cdot \psi)^{n-1} \cdot \left[1 + (\alpha \cdot \psi)^n\right]^{-m'}\right]^2}{\left[1 + (\alpha \cdot \psi)^n\right]^{\frac{m'}{2}}} d\psi}{\ln\left(\frac{R_2}{R_1}\right)}$$

$$z_0 = 1.000 \times 10^{-3}\,\text{m}$$

$$R_1 = 2.750\,\text{m}$$

$$Q = 3.787 \times 10^{-13}\,\text{m}^3\,\text{s}^{-1}$$

$$z_0 = 0.100\,\text{cm}$$

$$R_2 = 4.750\,\text{m}$$

$$k = 3.040 \times 10^{-13}\,\text{cm}^2$$

$$\text{Flux} := \frac{Q}{2 \cdot \pi \cdot R_1 \cdot z_0}$$

$$\text{Flux} = 0.692\,\frac{\text{mm}}{\text{yr}}$$

$$\text{Flux} \cdot \pi \cdot 5.5 \cdot \text{m} \cdot 600 \cdot \text{m} = 1.894 \times 10^3\,\frac{\text{gal}}{\text{yr}}$$

Calculate the latent heat transfer by multiplying by the latent heat of vaporization. From *Fundamentals of Heat and Mass Transfer* (Incropera and DeWitt 1996, p. 846):

$$2.334 \cdot 10^3 \cdot \frac{\text{J}}{\text{kg}} \cdot 1000 \cdot 1000\,\frac{\text{kg}}{\text{m}^3} \cdot (\text{Flux} \cdot \pi \cdot 5.5 \cdot \text{m} \cdot 600 \cdot \text{m}) = 530.311\,\text{W}$$

Calculate the total energy for 300 years:

$$2.334 \cdot 10^3 \cdot \frac{\text{J}}{\text{kg}} \cdot 1000 \cdot 1000 \cdot \frac{\text{kg}}{\text{m}^3} \cdot (\text{Flux} \cdot \pi \cdot 5.5 \cdot \text{m} \cdot 600 \cdot \text{m}) \cdot 300 \cdot \text{yr} = 5.020 \times 10^{12}\,\text{J}$$

$$\frac{5.021 \cdot (10^{12} \cdot \text{J})}{2.329\,10^{15}\,\text{J}} = 0.216\%$$

The percentage is less than one percent for a radius of influence extending 4.75 m out. The following table presents a summary of the percentages for various radii of influence.

4.75m	0.216%

6.00m	0.151%
10.00m	0.091%
20.00m	0.059%

$$\psi_2 = 35.290\,\text{m}$$

$$\psi_2 := 3529 \cdot \text{cm}$$

$$R_2 := 6 \cdot \text{m}$$

Solve for the base case flow. Construct the moisture potential profile surrounding the drift. Restate the flow equation (Equation XI-15):

$$Q = 3.787 \times 10^{-13}\,\text{m}^3\,\text{s}^{-1}$$

$$Q := -2 \cdot \pi \cdot z_0 \cdot \frac{\rho_w \cdot g \cdot k}{\mu_w} \cdot \frac{\int_{|\psi_1|}^{|\psi_2|} \frac{\left[1 - (\alpha \cdot \psi)^{n-1} \cdot \left[1 + (\alpha \cdot \psi)^n\right]^{-m'}\right]^2}{\left[1 + (\alpha \cdot \psi)^n\right]^{\frac{m'}{2}}}\, d\psi}{\ln\left(\frac{R_2}{R_1}\right)}$$

$$Q = 2.653 \times 10^{-13}\,\text{m}^3\,\text{s}^{-1}$$

In order to solve for the moisture profile, we solve the transcendental equation presented below, and then solve for ψ as a function of r for a given flow rate.

Define a transcendental equation based upon Equation XI-15:

$$\psi_1 = -1.691 \times 10^6\,\text{cm}$$

$$F(\psi, r) := \frac{-1.0\rho_w \cdot g \cdot k}{\mu_w} \cdot \int_{|\psi_1|}^{\psi} \frac{\left[1 - (\alpha \cdot \psi)^{n-1} \cdot \left[1 + (\alpha \cdot \psi)^n\right]^{-m'}\right]^2}{\left[1 + (\alpha \cdot \psi)^n\right]^{\frac{m'}{2}}}\, d\psi - \frac{Q}{2 \cdot \pi \cdot z_0} \cdot \ln\left(\frac{r}{R_1}\right)$$

Once ψ is determined for each value of r, then the volumetric moisture content can be determined for each value ψ from the basic Van Genuchten retention relationship. The Van Genuchten retention relationship is given by (Fetter 1993, p. 172, Equation 17):

$$\theta(\psi) := \theta_r + \frac{(\theta_s - \theta_r)}{\left[1 + (\alpha \cdot |\psi|)^n\right]^{m'}}$$

$$\theta_r = 0.016$$

$$\theta_s = 0.131$$

$$\frac{\rho_w \cdot g}{\mu_w} \cdot k = 3.487 \times 10^{-8} \frac{cm}{s}$$

Plot the retention relationship, and the hydraulic conductivity relationship for the TSw35 unit.

$$\psi := 100 \cdot cm, 110 \cdot cm .. 100000 \cdot cm$$

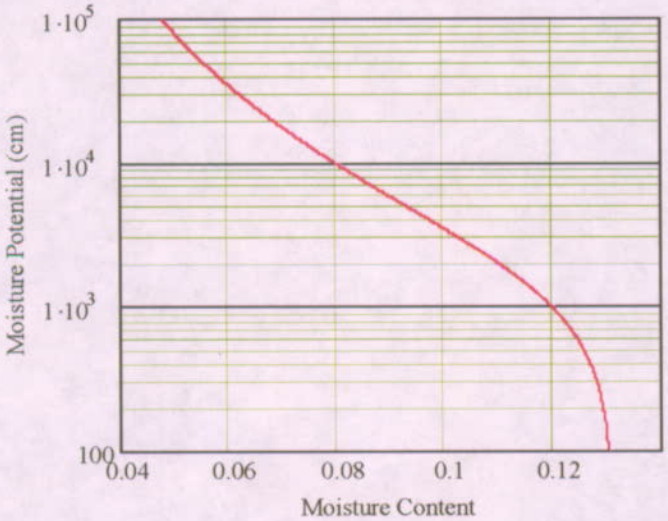

Figure XI-2. Moisture Potential Relationship for TSw35

Define the unsaturated hydraulic conductivity relationship from Equation XI-11:

$$K_r(\psi) := \frac{\rho_w \cdot g}{\mu_w} \cdot k \cdot \frac{\left[1 - (\alpha \cdot \psi)^{n-1} \cdot \left[1 + (\alpha \cdot \psi)^n\right]^{-m'}\right]^2}{\left[1 + (\alpha \cdot \psi)^n\right]^{\frac{m'}{2}}}$$

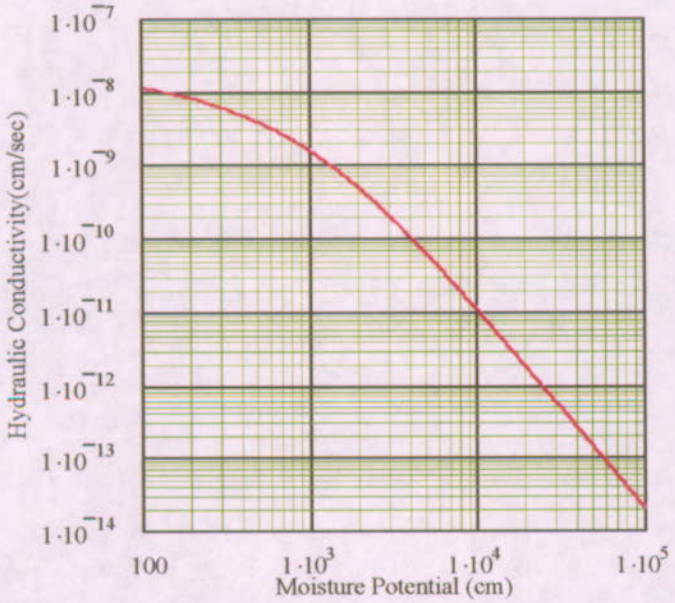

Figure XI-3. Unsaturated Hydraulic Conductivity Relationship

Develop the profile for the moisture content in the following manner:

1. Select the radius.

2. Plot the transcendental equation as a function of ψ, and estimate the root.

$$r := 5.50 \cdot m$$

$$\psi := 1000 \cdot cm, 2000 \cdot cm .. 500000 \cdot cm$$

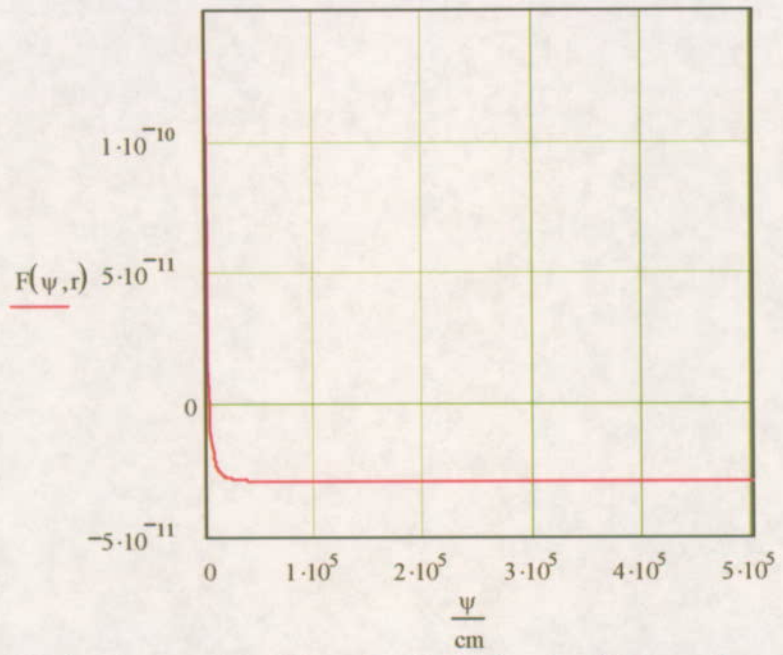

Figure XI-4. Transcendental Equation Extracting the Moisture Potential

3. Estimate the root from the plot. Use the estimated root with the root function. Make multiple substitutions to reduce the error.

$$\psi := 3818 \cdot cm$$

$$r = 5.500\,m$$

$$\psi_{ans} := root(F(\psi, r), \psi)$$

$$\psi_{ans} = 3.818 \times 10^{3}\,cm$$

$$F(\psi_{ans}, r) = 6.825 \times 10^{-19}\,m^{2}s^{-1}$$

4. Check the answer by substituting into Equation XI-15.

$$Q := -2\cdot\pi\cdot z_0\cdot\frac{\rho_w\cdot g\cdot k}{\mu_w}\cdot\frac{\int_{|\psi_1|}^{\psi_{ans}}\frac{\left[1-(\alpha\cdot\psi)^{n-1}\cdot\left[1+(\alpha\cdot\psi)^n\right]^{-m'}\right]^2}{\left[1+(\alpha\cdot\psi)^n\right]^{\frac{m'}{2}}}\,d\psi}{\ln\left(\frac{r}{R_1}\right)}$$

$$Q = 2.653\times 10^{-13}\,m^3\,s^{-1}$$

$$z_0 = 1.000\times 10^{-3}\,m$$

5. Calculate the moisture content based upon the retention relationship.

$$r = 5.500\,m$$

$$\theta(\psi_{ans}) = 0.0980$$

6. Place the data into a matrix and export to EXCEL.

$$A := \begin{pmatrix} 2.76 & .049 \\ 2.78 & 0.057 \\ 2.80 & .060 \\ 2.82 & .063 \\ 2.84 & .065 \\ 2.86 & .067 \\ 2.90 & .070 \\ 2.94 & .072 \\ 2.98 & .073 \\ 3.02 & .075 \end{pmatrix}$$

$$B := \begin{pmatrix} 3.25 & .081 \\ 3.50 & .085 \\ 3.75 & .088 \\ 4.0 & .090 \\ 4.25 & .092 \\ 4.50 & .094 \\ 4.75 & .095 \\ 5.0 & .096 \\ 5.25 & .097 \\ 5.5 & .098 \end{pmatrix}$$

$$\theta(3529 \cdot cm) = 0.100$$

$$C := stack(A, B)$$

Plot the moisture content profile.

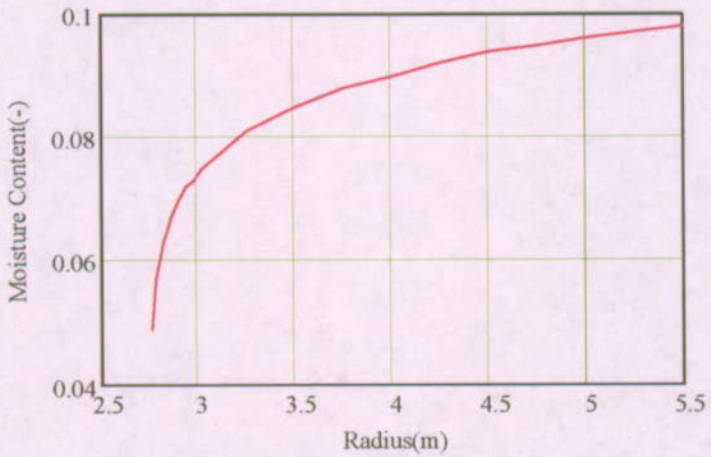

Figure XI-5. Steady State Moisture Content Profile

Conclusions: Under the assumptions made for the analysis, the latent heat associated with evaporation of porewater is small for a range of farfield moisture potentials, and radii of influence.

ATTACHMENT XII

SELECT FULL-SIZE FIGURES FROM SECTIONS 6

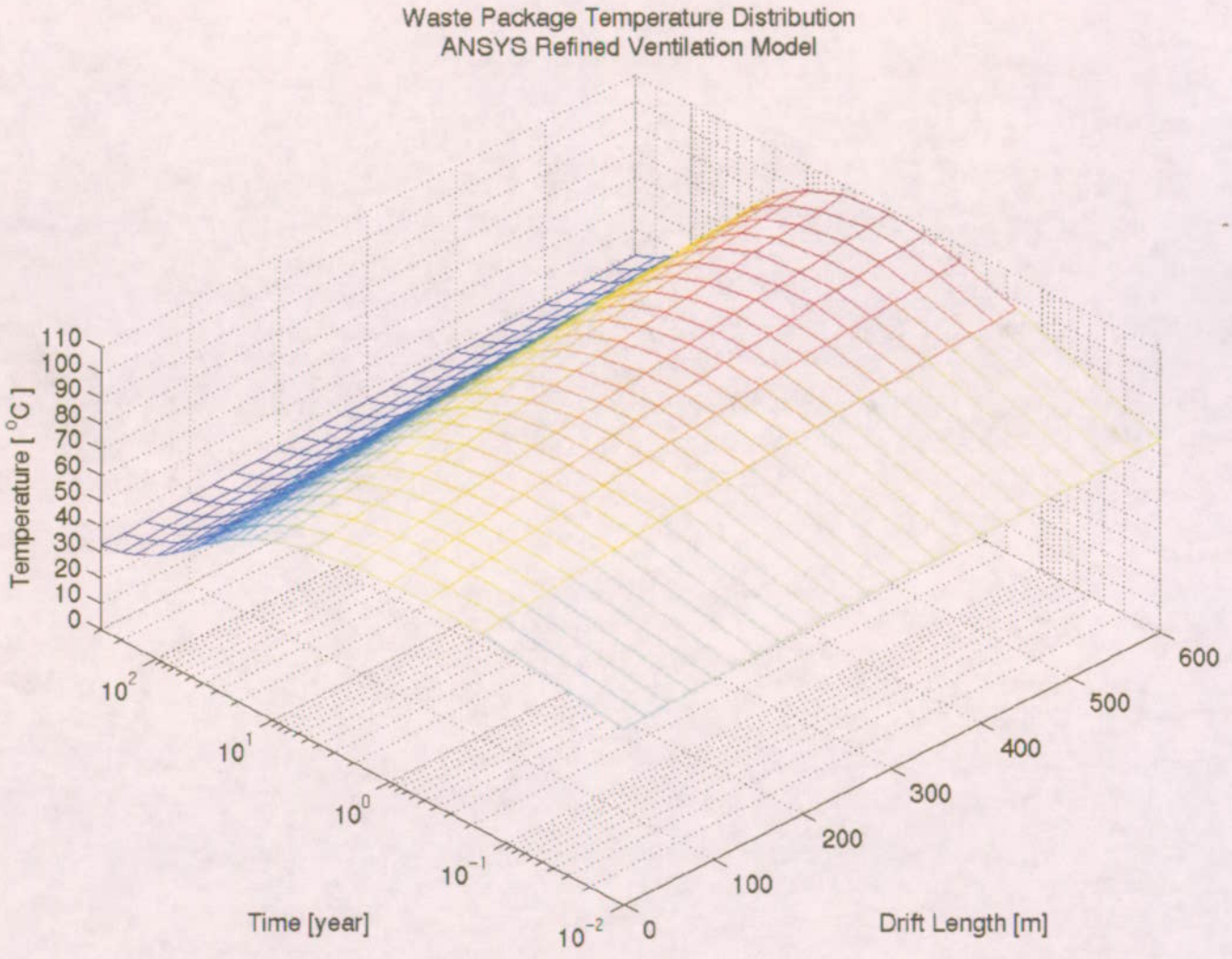

Figure XII-1 (Figure 6-7). Waste Package Temperature as a Function of Time and Drift Length for the ANSYS-Refined Ventilation Numerical Models (DTN MO0210MWDTVE30.018)

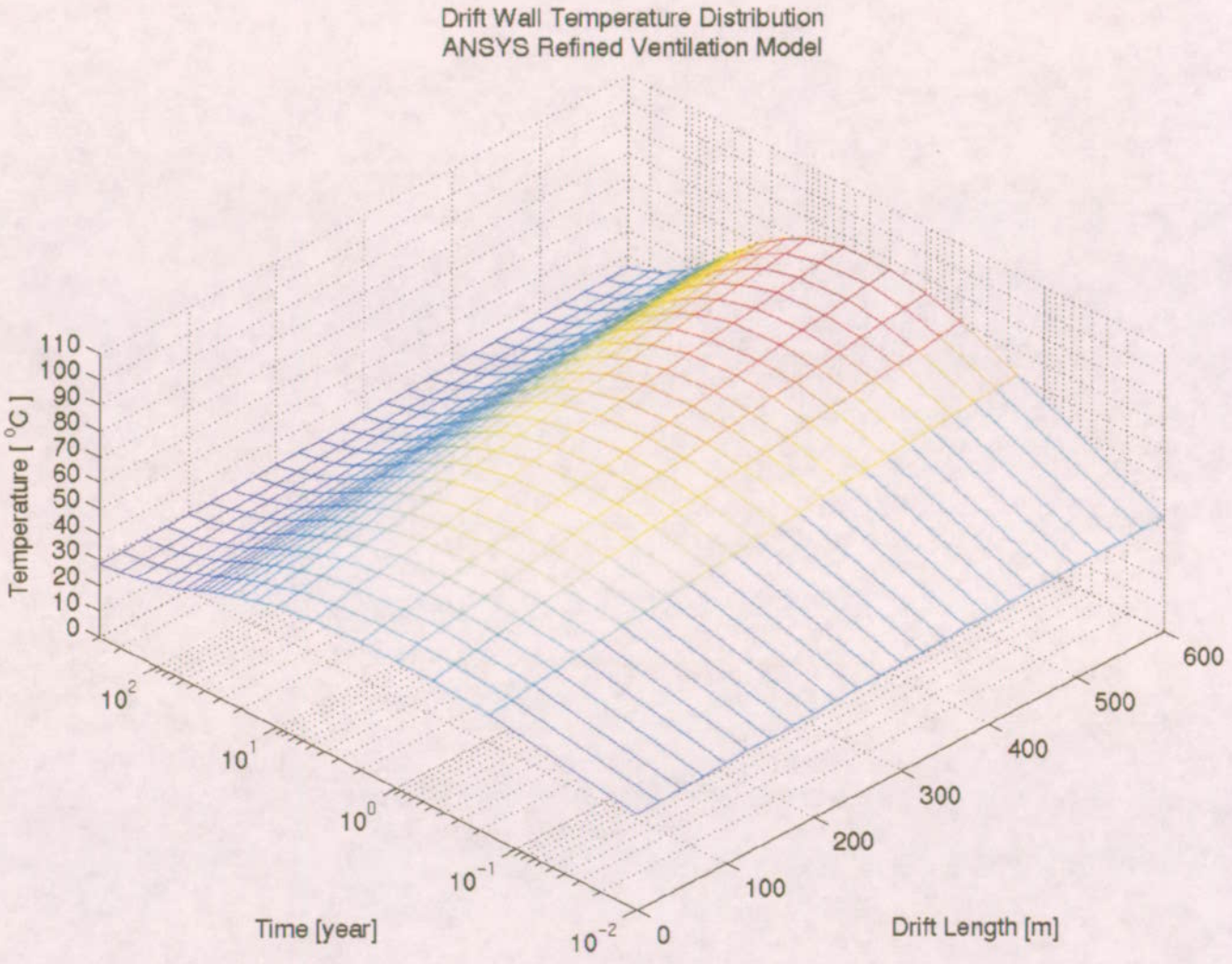

Figure XII-2 (Figure 6-7). Drift Wall Temperature as a Function of Time and Drift Length for the ANSYS-Refined Ventilation Numerical Models (DTN MO0210MWDTVE30.018)

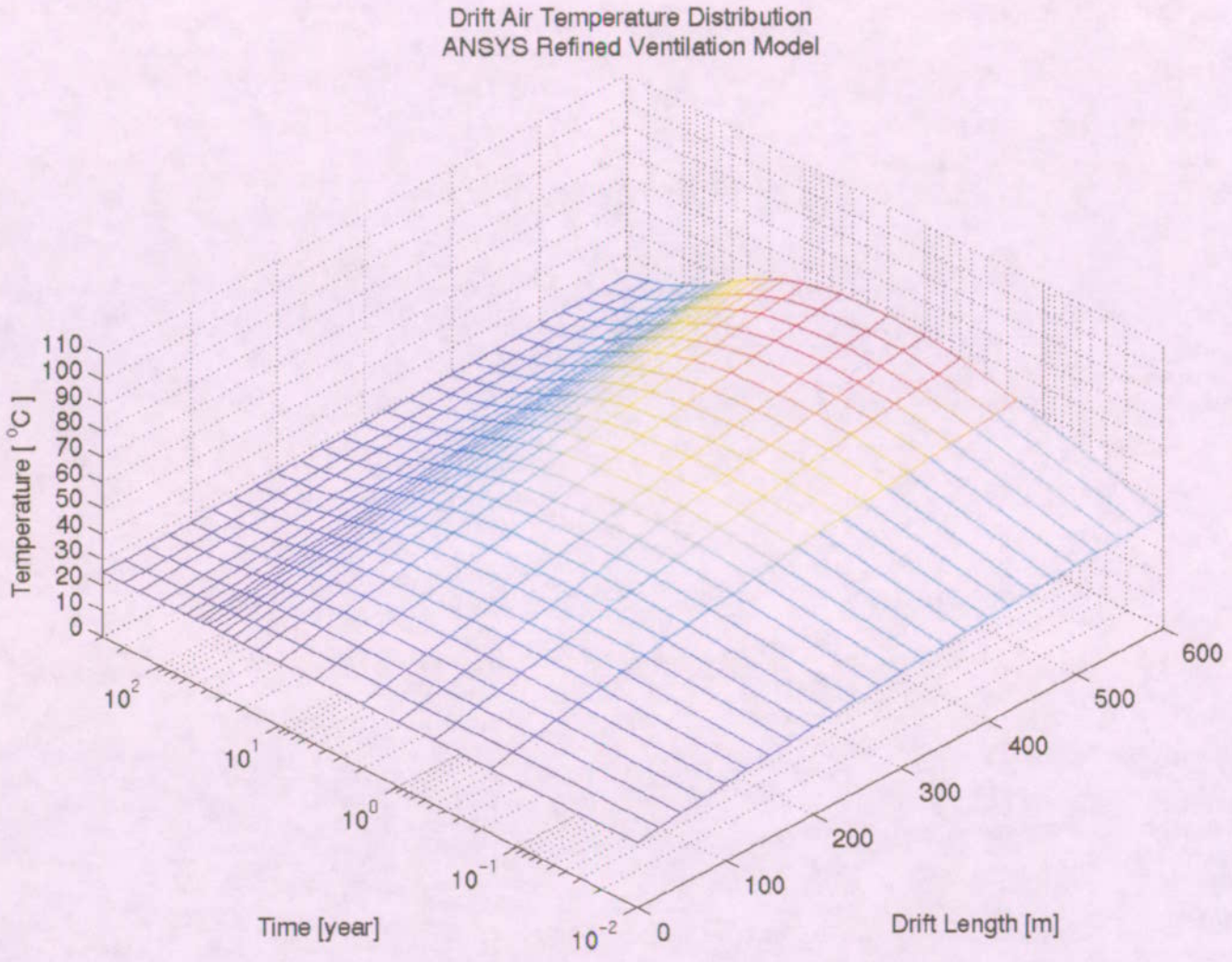

Figure XII-3 (Figure 6-7). Drift Air Temperature as a Function of Time and Drift Length for the ANSYS-Refined Ventilation Numerical Models (DTN MO0210MWDTVE30.018)

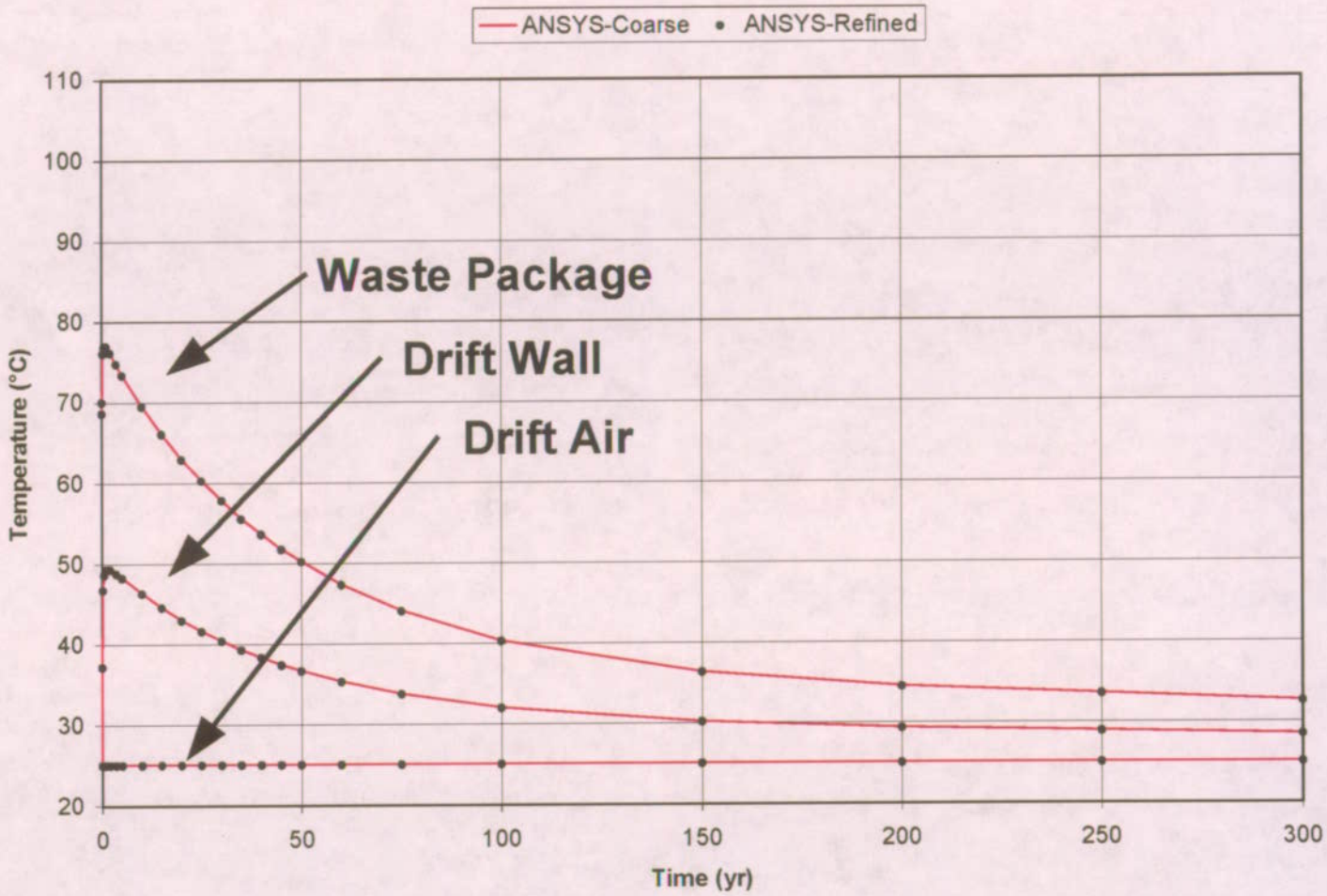

Figure XII-4 (Figure 6-8). Plots of Waste Package, Drift Wall, and Drift Air Temperatures as a Function of Time at 0 Meters from the Drift Entrance for the ANSYS-Coarse and ANSYS-Refined Ventilation Numerical Models (DTNs MO0210MWDTVE30.018 and MO0210MWDTEM30.019)

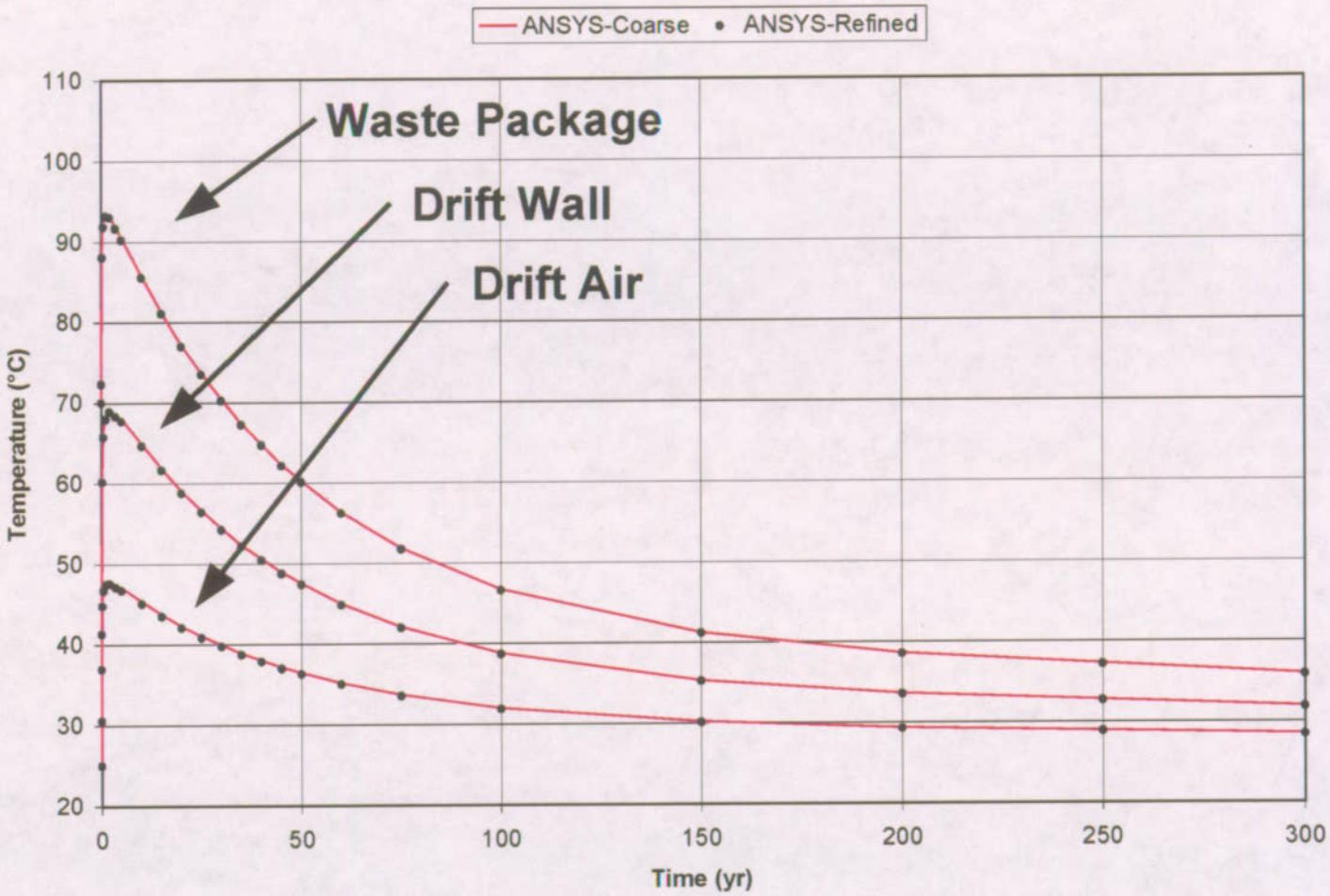

Figure XII-5 (Figure 6-8). Plots of Waste Package, Drift Wall, and Drift Air Temperatures as a Function of Time at 300 Meters from the Drift Entrance for the ANSYS-Coarse and ANSYS-Refined Ventilation Numerical Models (DTNs MO0210MWDTVE30.018 and MO0210MWDTEM30.019)

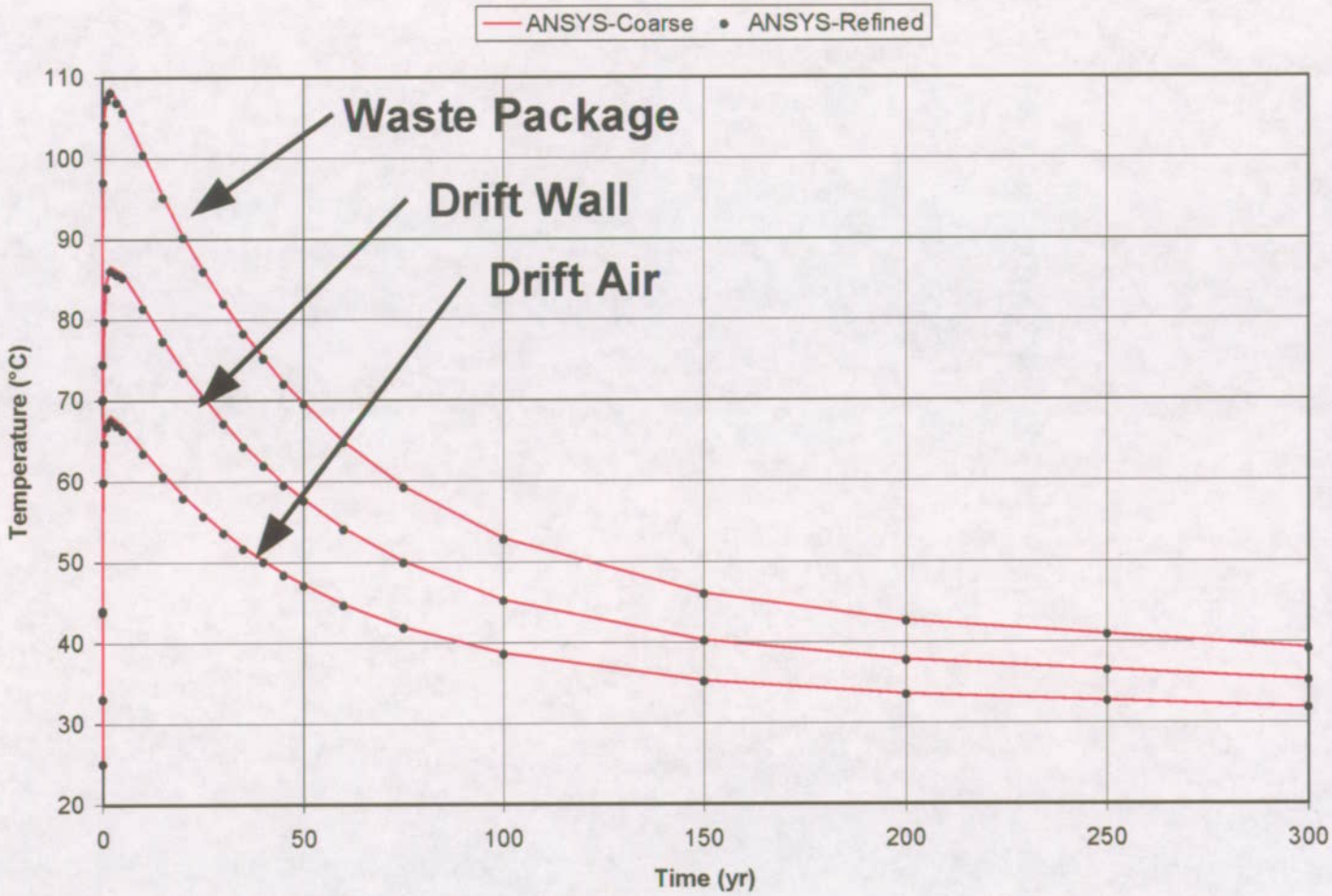

Figure XII-6 (Figure 6-8). Plots of Waste Package, Drift Wall, and Drift Air Temperatures as a Function of Time at 600 Meters from the Drift Entrance for the ANSYS-Coarse and ANSYS-Refined Ventilation Numerical Models (DTNs MO0210MWDTVE30.018 and MO0210MWDTEM30.019)

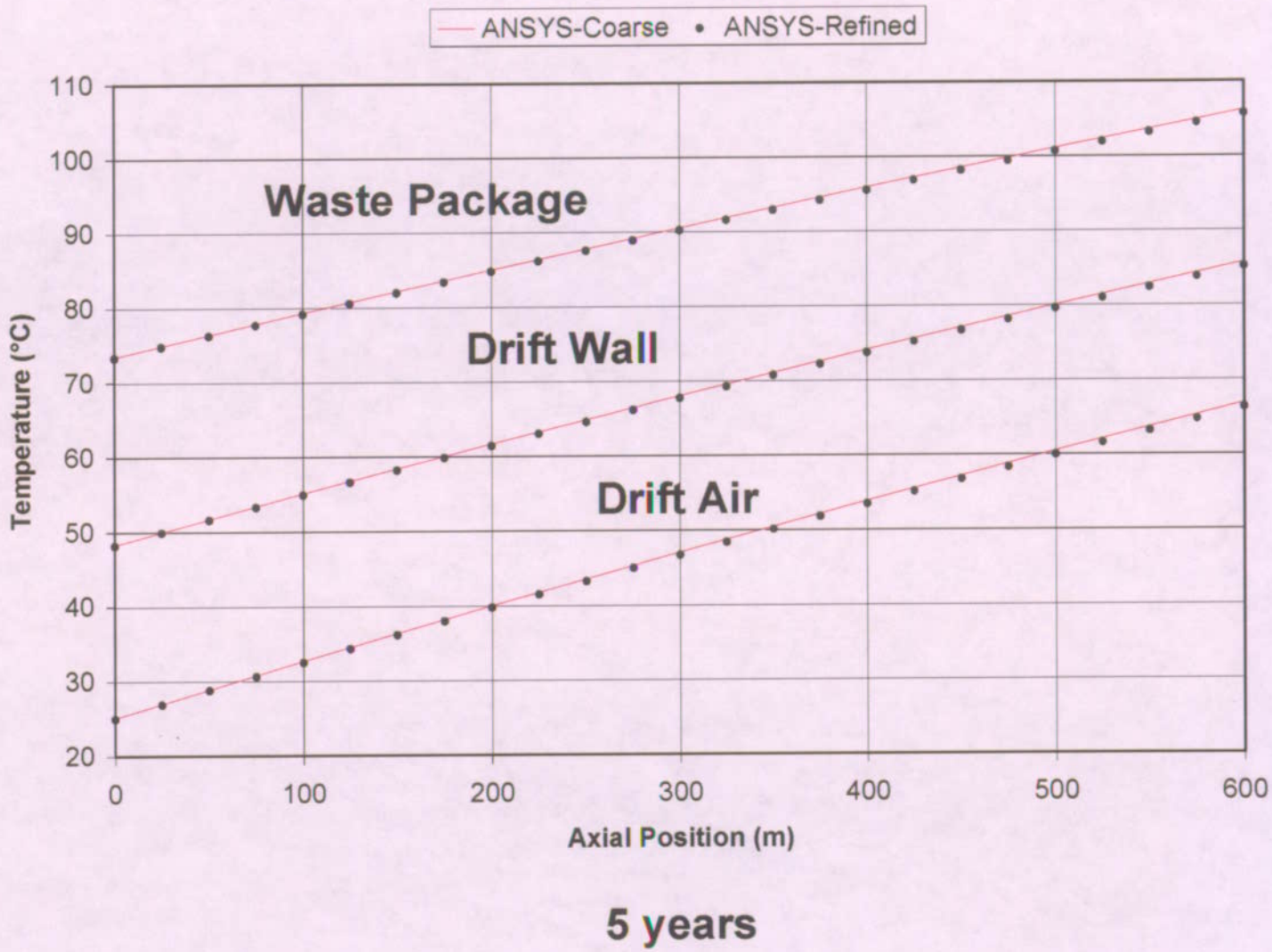

Figure XII-7 (Figure 6-9). Plots of Waste Package, Drift Wall, and Drift Air Temperatures as a Function of Drift Length at 5 Years from the Time of Waste Emplacement for the ANSYS-Coarse and ANSYS-Refined Ventilation Numerical Models (DTNs MO0210MWDTVE30.018 and MO0210MWDTEM30.019)

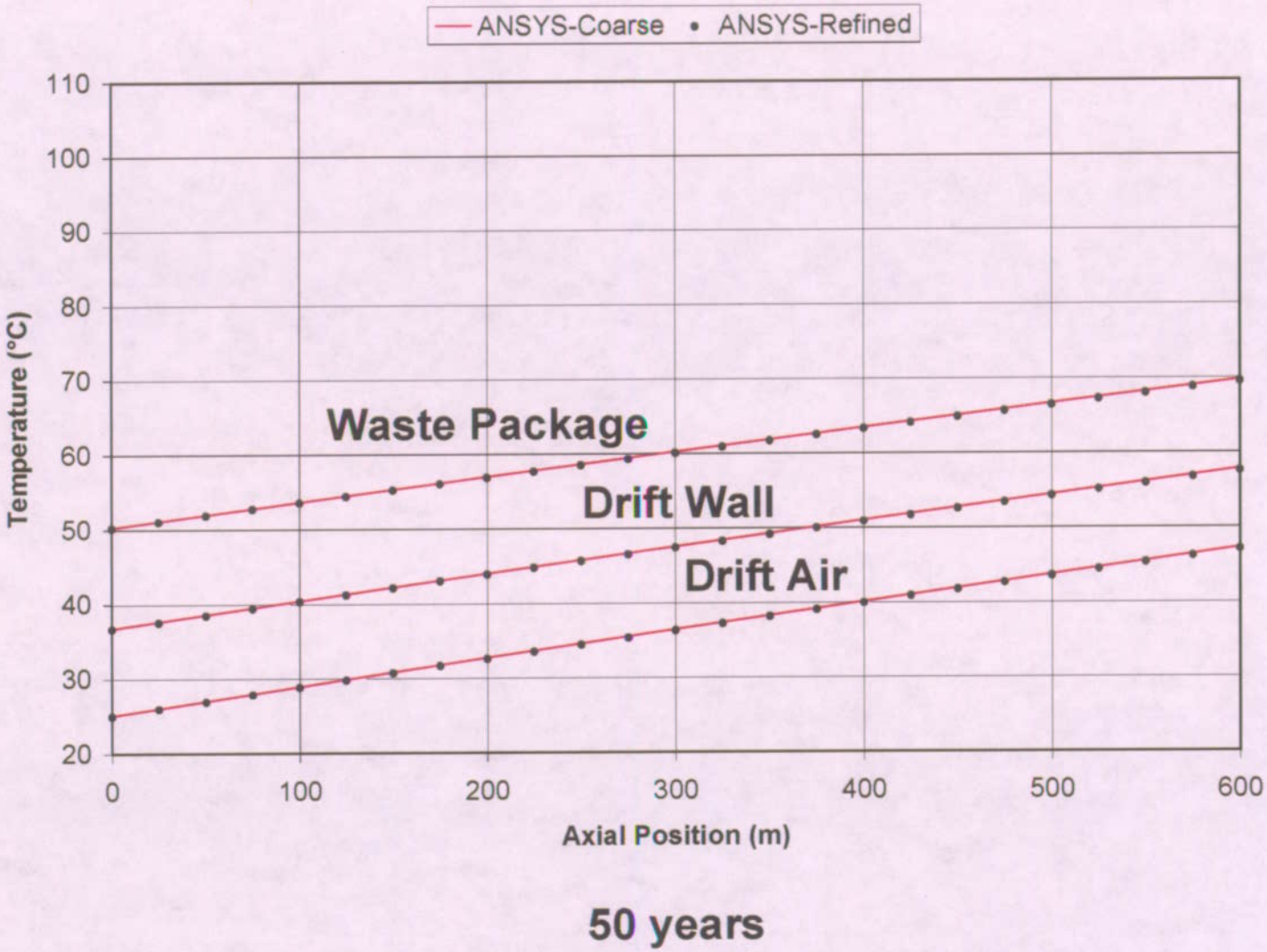

Figure XII-8 (Figure 6-9). Plots of Waste Package, Drift Wall, and Drift Air Temperatures as a Function of Drift Length at 50 Years from the Time of Waste Emplacement for the ANSYS-Coarse and ANSYS-Refined Ventilation Numerical Models (DTNs MO0210MWDTVE30.018 and MO0210MWDTEM30.019)

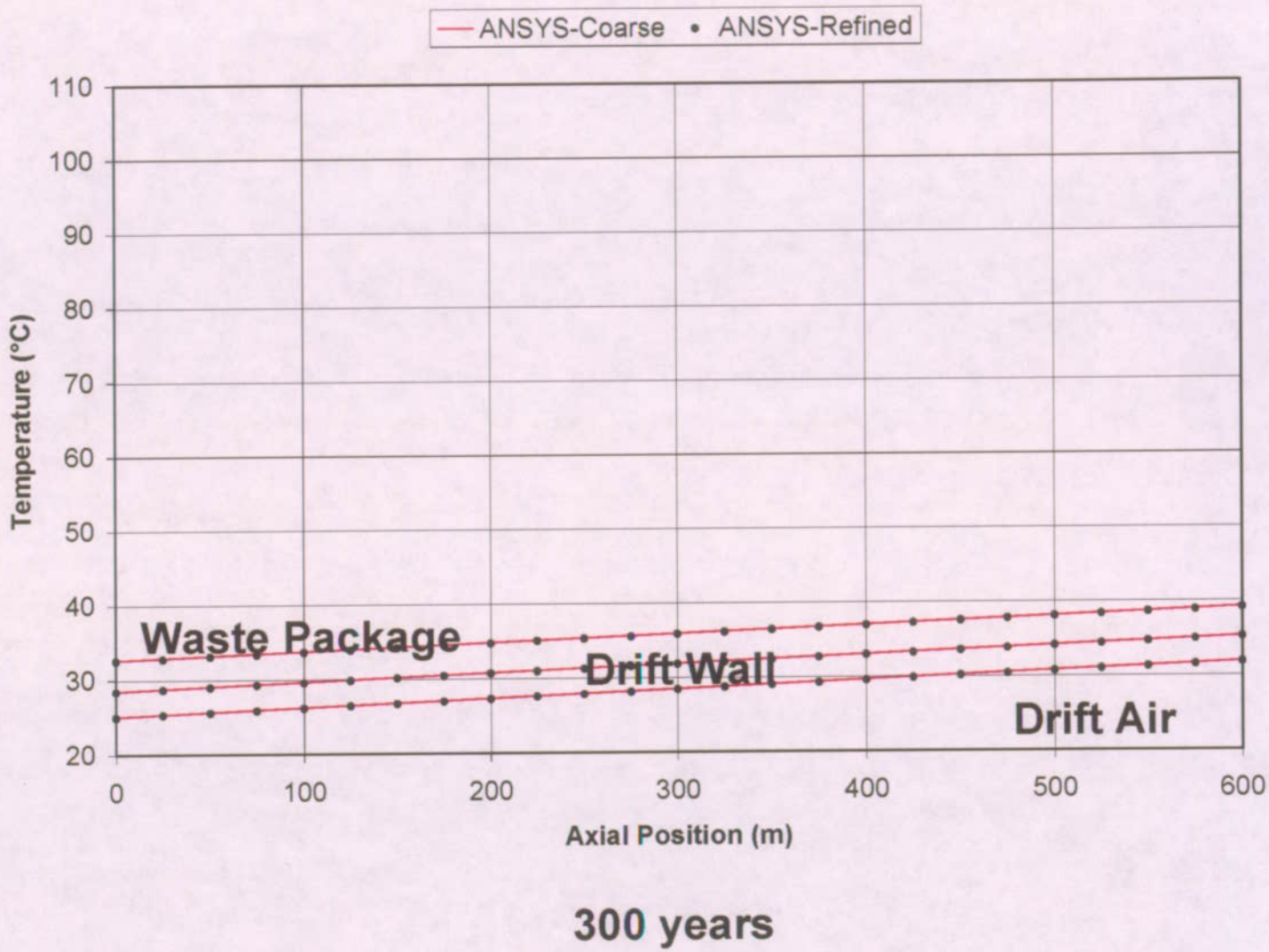

Figure XII-9 (Figure 6-9). Plots of Waste Package, Drift Wall, and Drift Air Temperatures as a Function of Drift Length at 300 Years from the Time of Waste Emplacement for the ANSYS-Coarse and ANSYS-Refined Ventilation Numerical Models (DTNs MO0210MWDTVE30.018 and MO0210MWDTEM30.019)

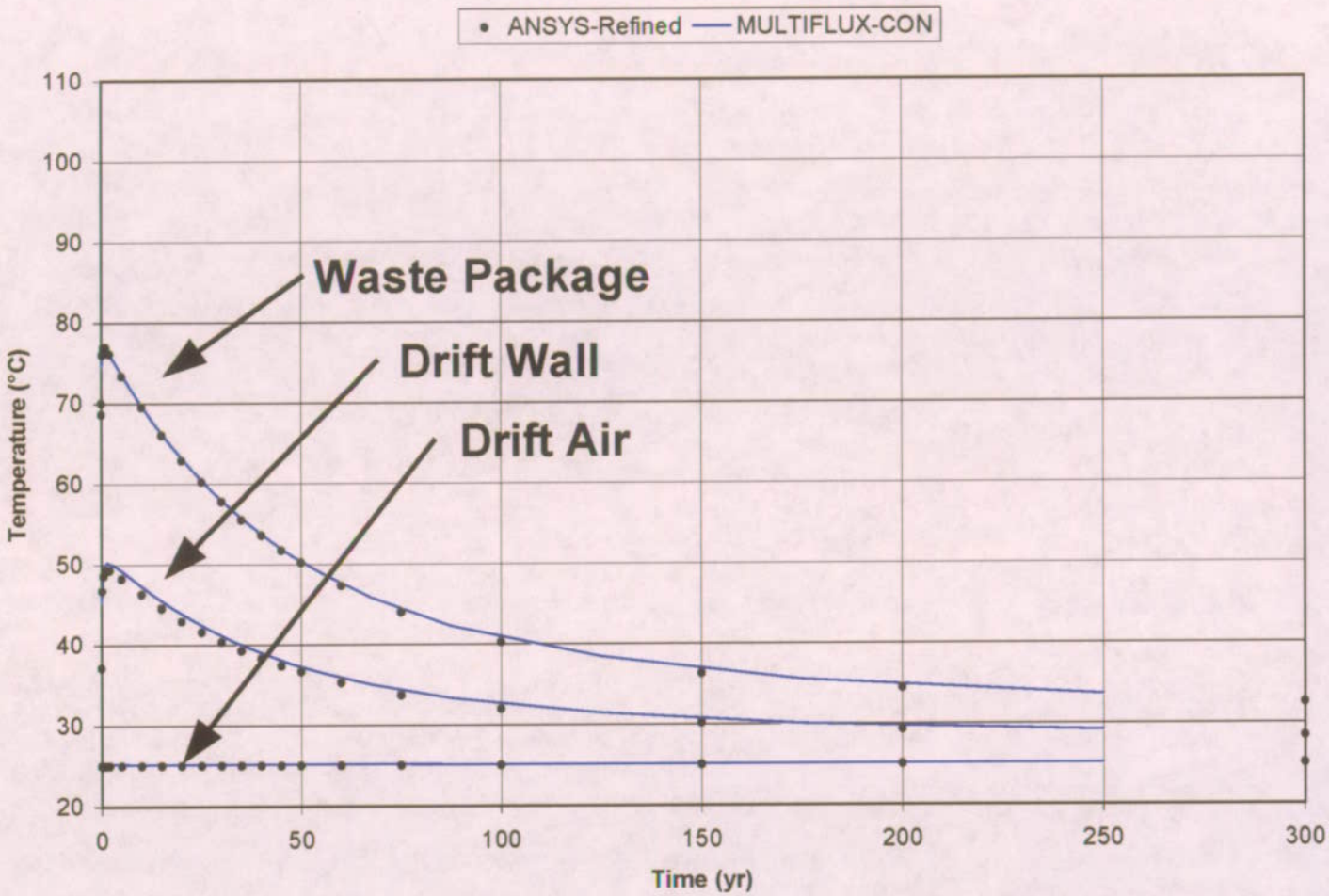

0 meters

Figure XII-10 (Figure 6-11). Plots of Waste Package, Drift Wall, and Drift Air Temperatures as a Function of Time at 0 meters from the Drift Entrance for the ANSYS-Refined and MULTIFLUX-Con Ventilation Numerical Models (DTNs MO0210MWDTVE30.018 and MO0209MWDMUL30.002)

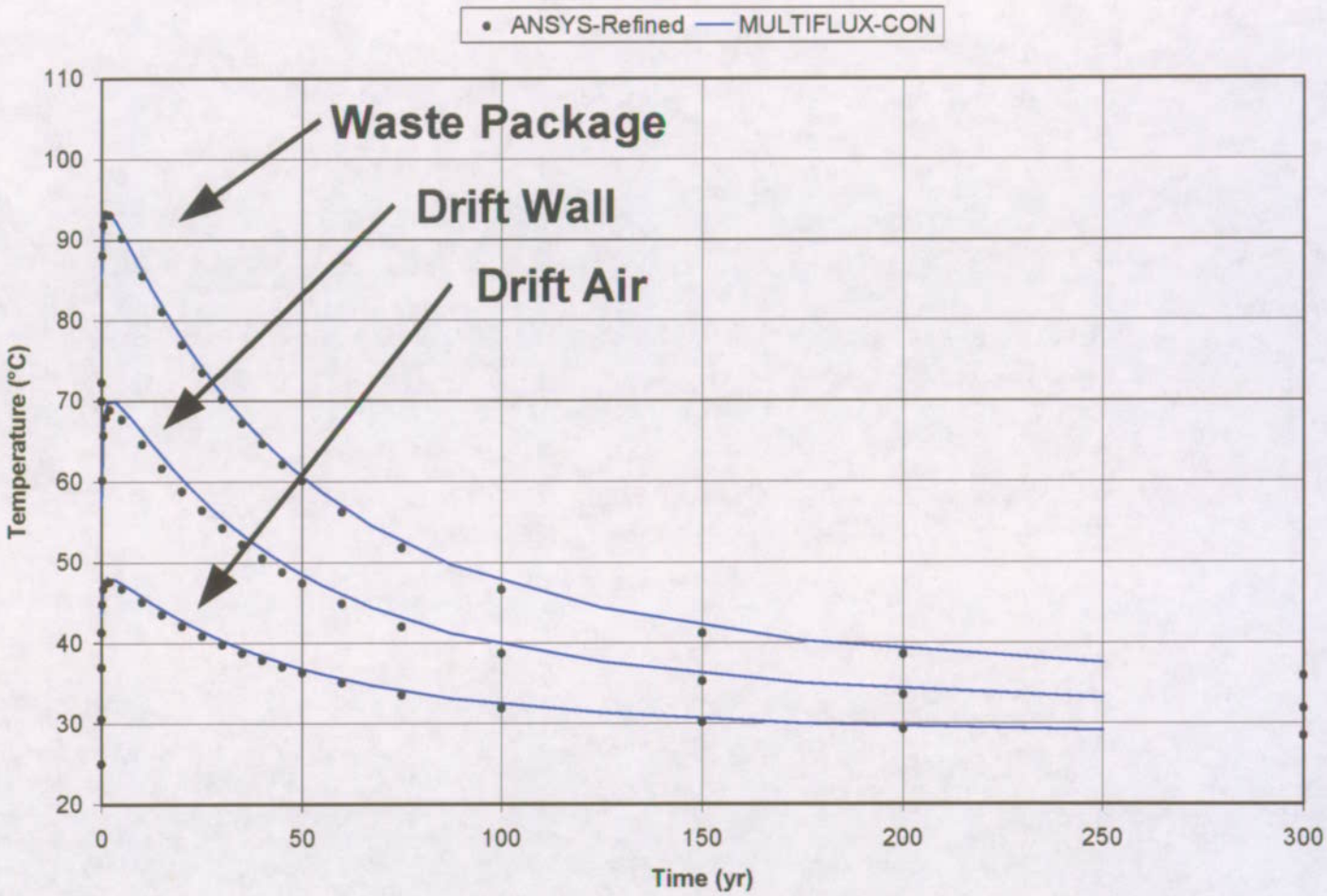

Figure XII-10 (Figure 6-11). Plots of Waste Package, Drift Wall, and Drift Air Temperatures as a Function of Time at 300 meters from the Drift Entrance for the ANSYS-Refined and MULTIFLUX-Con Ventilation Numerical Models (DTNs MO0210MWDTVE30.018 and MO0209MWDMUL30.002)

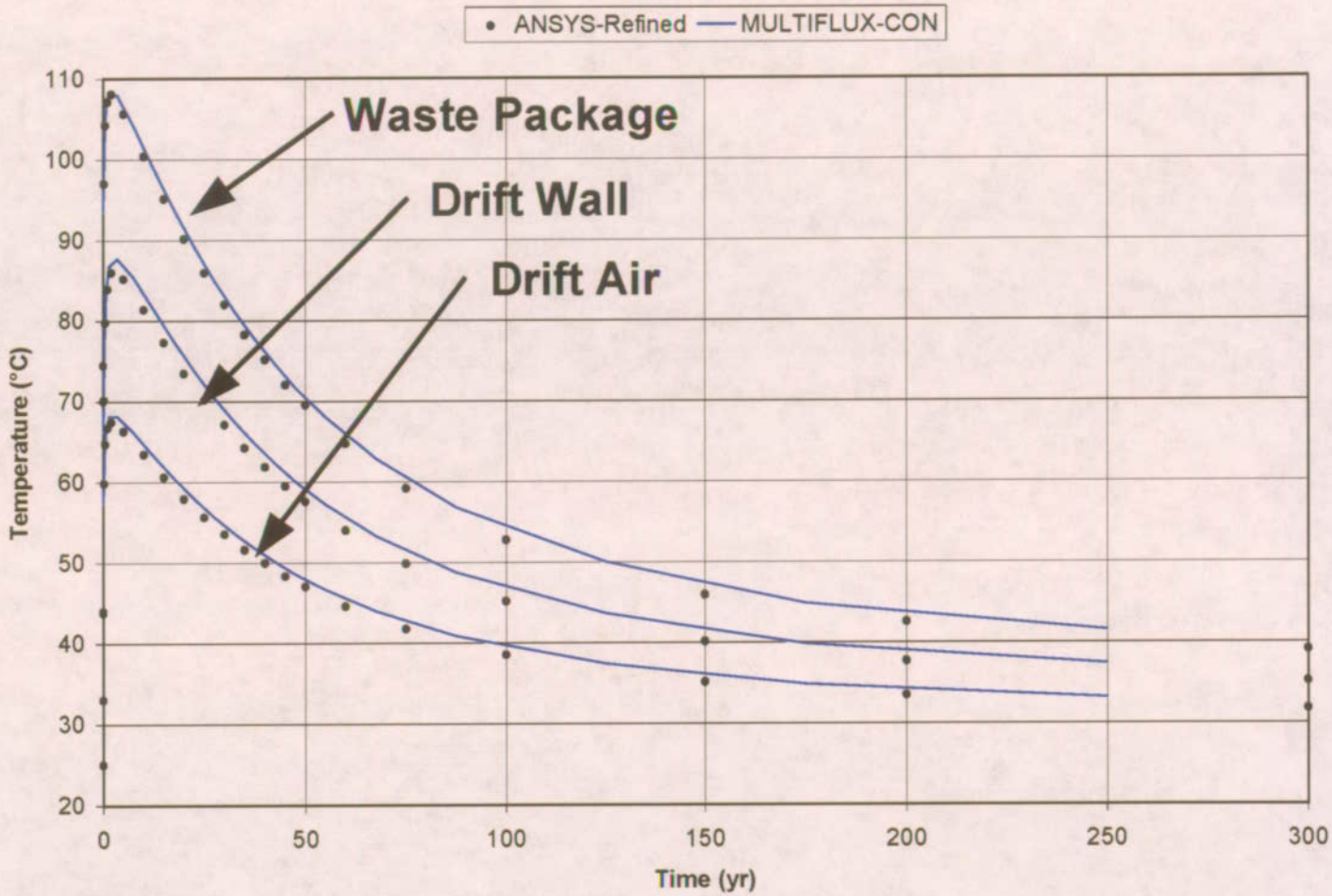

Figure XII-10 (Figure 6-11). Plots of Waste Package, Drift Wall, and Drift Air Temperatures as a Function of Time at 600 meters from the Drift Entrance for the ANSYS-Refined and MULTIFLUX-Con Ventilation Numerical Models (DTNs MO0210MWDTVE30.018 and MO0209MWDMUL30.002)

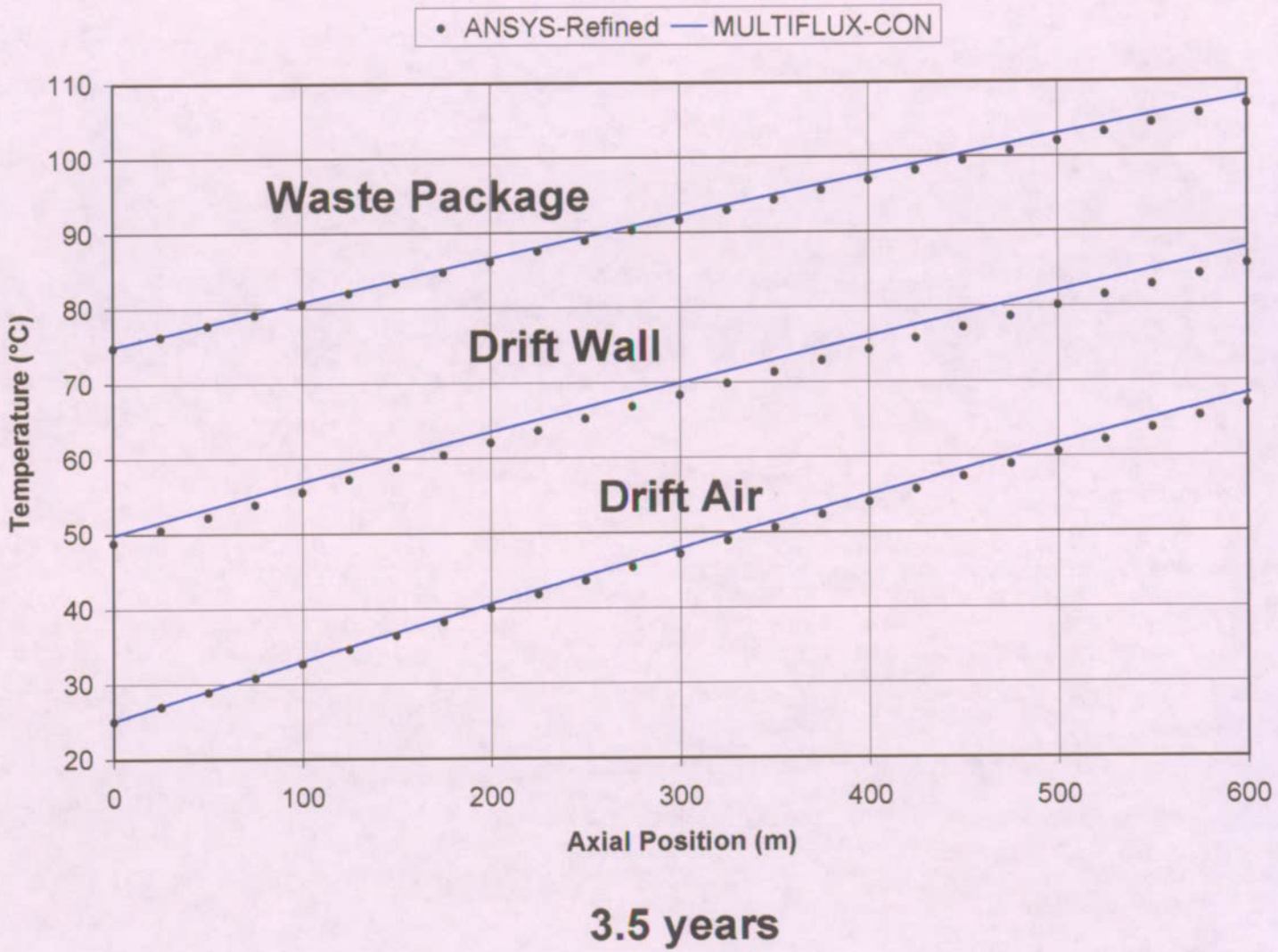

Figure XII-11 (Figure 6-12). Plots of Waste Package, Drift Wall, and Drift Air Temperatures as a Function of Drift Length at 3.5 Years from the Time of Waste Emplacement for the ANSYS-Refined and MULTIFLUX-Con Ventilation Numerical Models (DTNs MO0210MWDTVE30.018 and MO0209MWDMUL30.002)

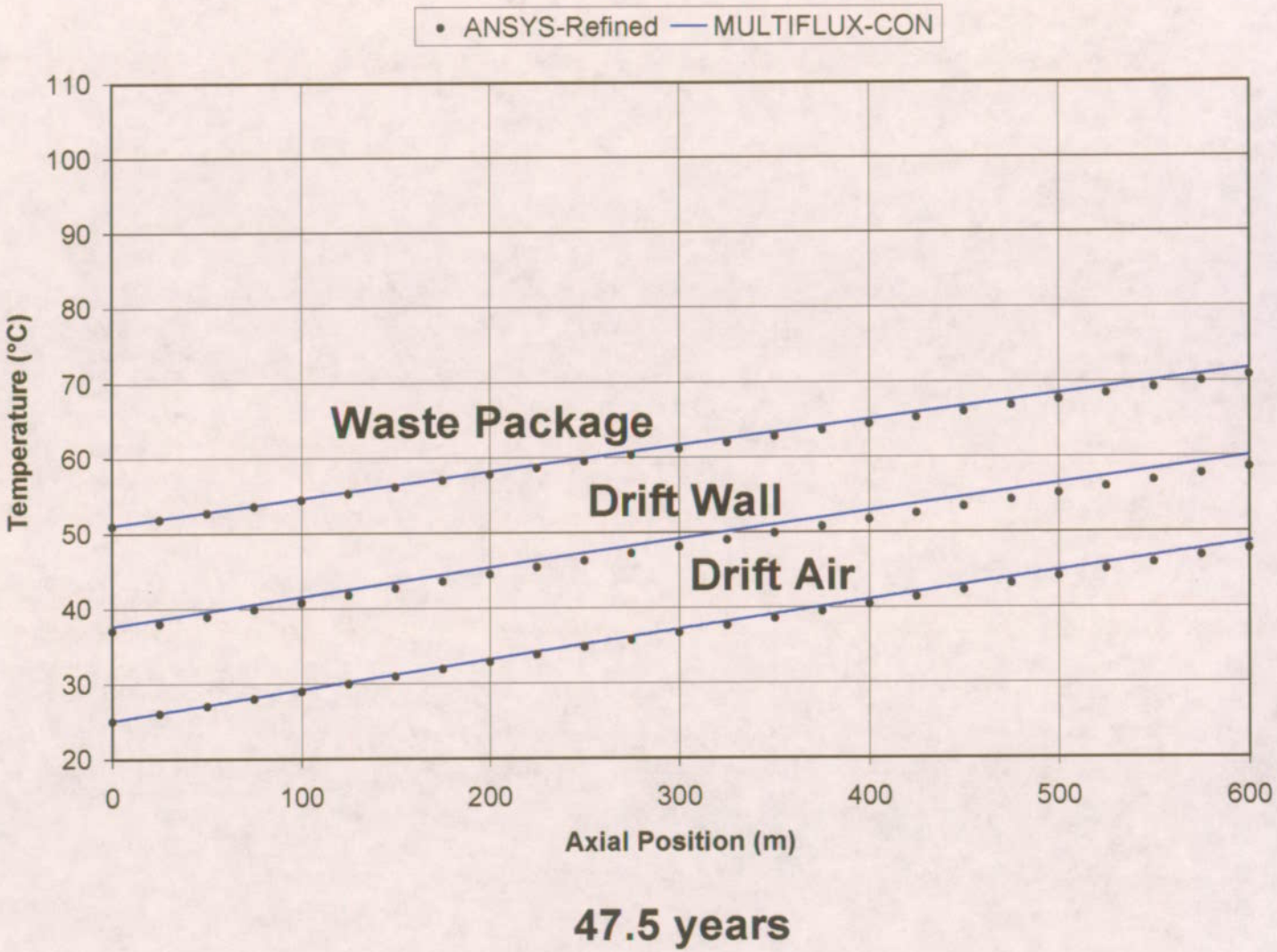

Figure XII-11 (Figure 6-12). Plots of Waste Package, Drift Wall, and Drift Air Temperatures as a Function of Drift Length at 47.5 Years from the Time of Waste Emplacement for the ANSYS-Refined and MULTIFLUX-Con Ventilation Numerical Models (DTNs MO0210MWDTVE30.018 and MO0209MWDMUL30.002)

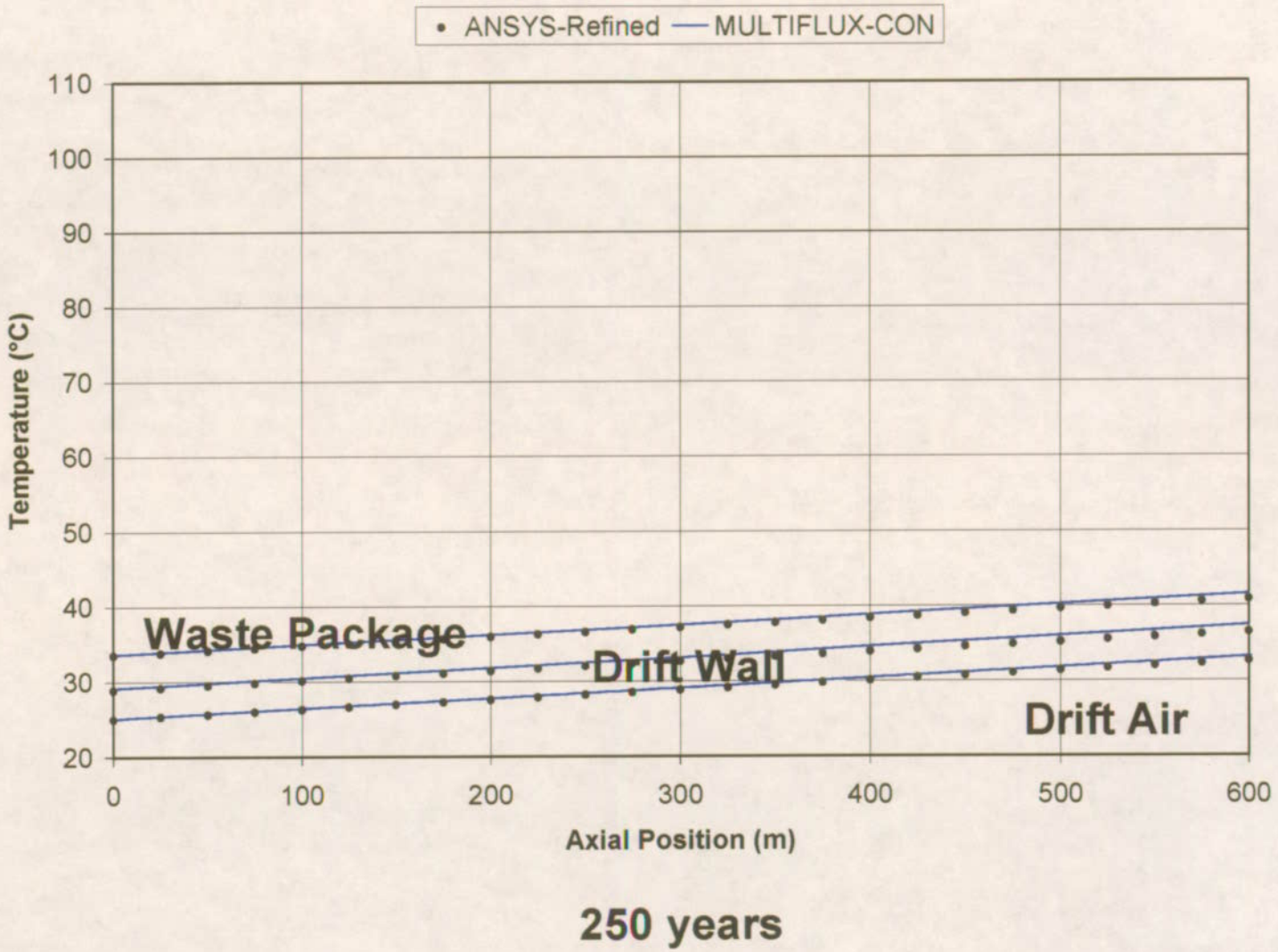

Figure XII-11 (Figure 6-12). Plots of Waste Package, Drift Wall, and Drift Air Temperatures as a Function of Drift Length at 250 Years from the Time of Waste Emplacement for the ANSYS-Refined and MULTIFLUX-Con Ventilation Numerical Models (DTNs MO0210MWDTVE30.018 and MO0209MWDMUL30.002)

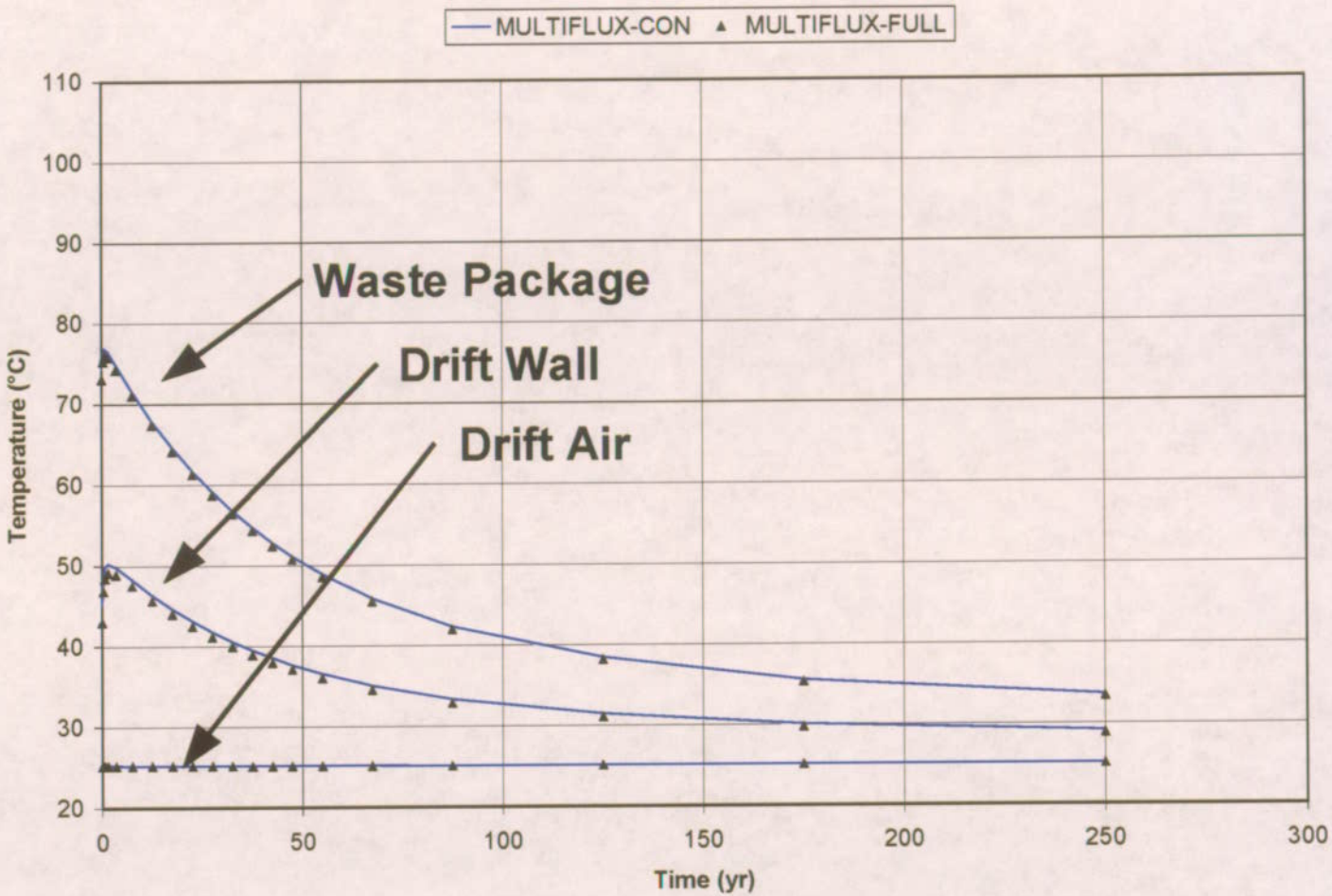

0 meters

Figure XII-12 (Figure 6-14). Plots of Waste Package, Drift Wall, and Drift Air Temperatures as a Function of Time at 0 Meters from the Drift Entrance for the MULTIFLUX-Con and MULTIFLUX-Full Ventilation Numerical Models (DTN MO0209MWDMUL30.002)

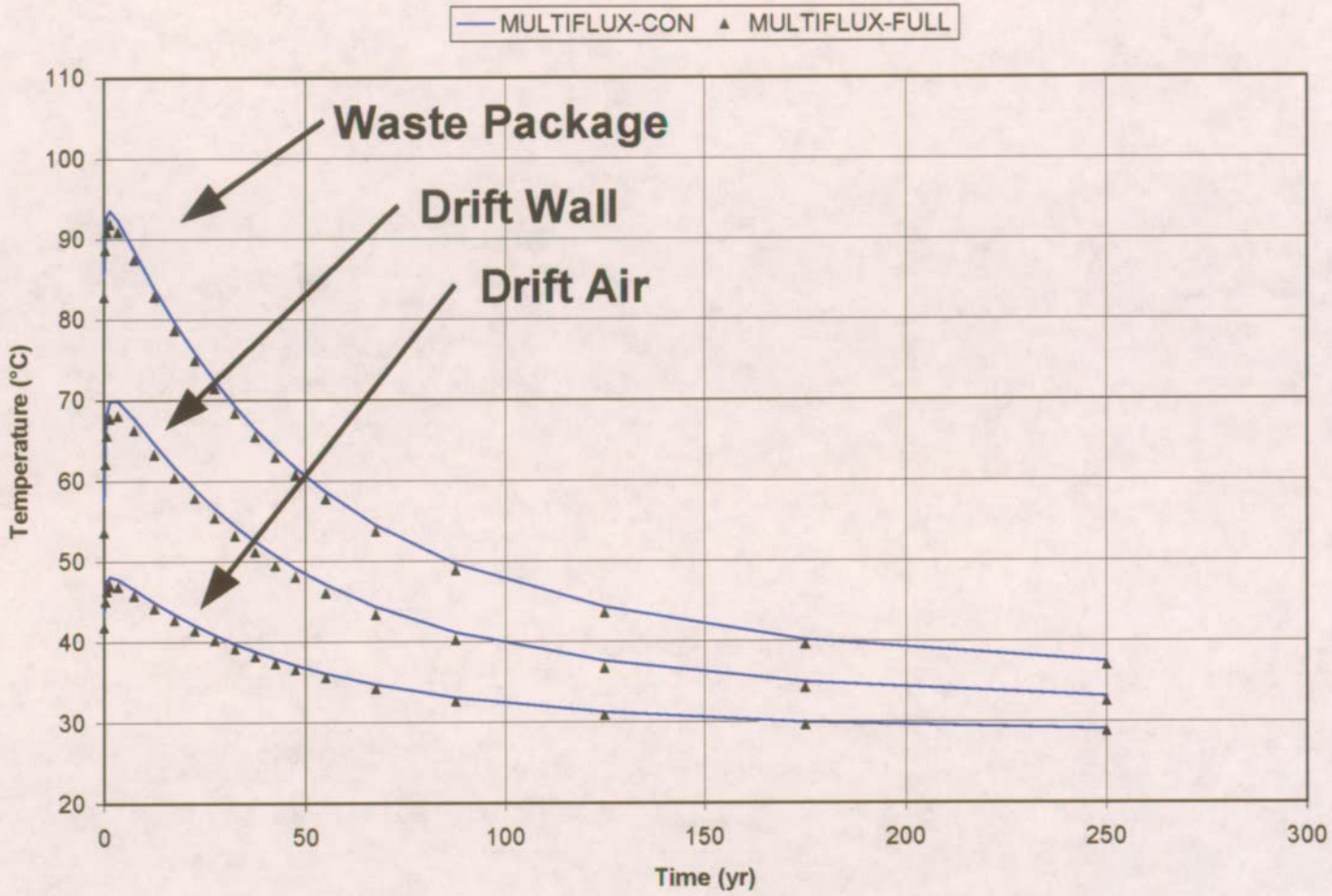

Figure XII-12 (Figure 6-14). Plots of Waste Package, Drift Wall, and Drift Air Temperatures as a Function of Time at 300 Meters from the Drift Entrance for the MULTIFLUX-Con and MULTIFLUX-Full Ventilation Numerical Models (DTN MO0209MWDMUL30.002)

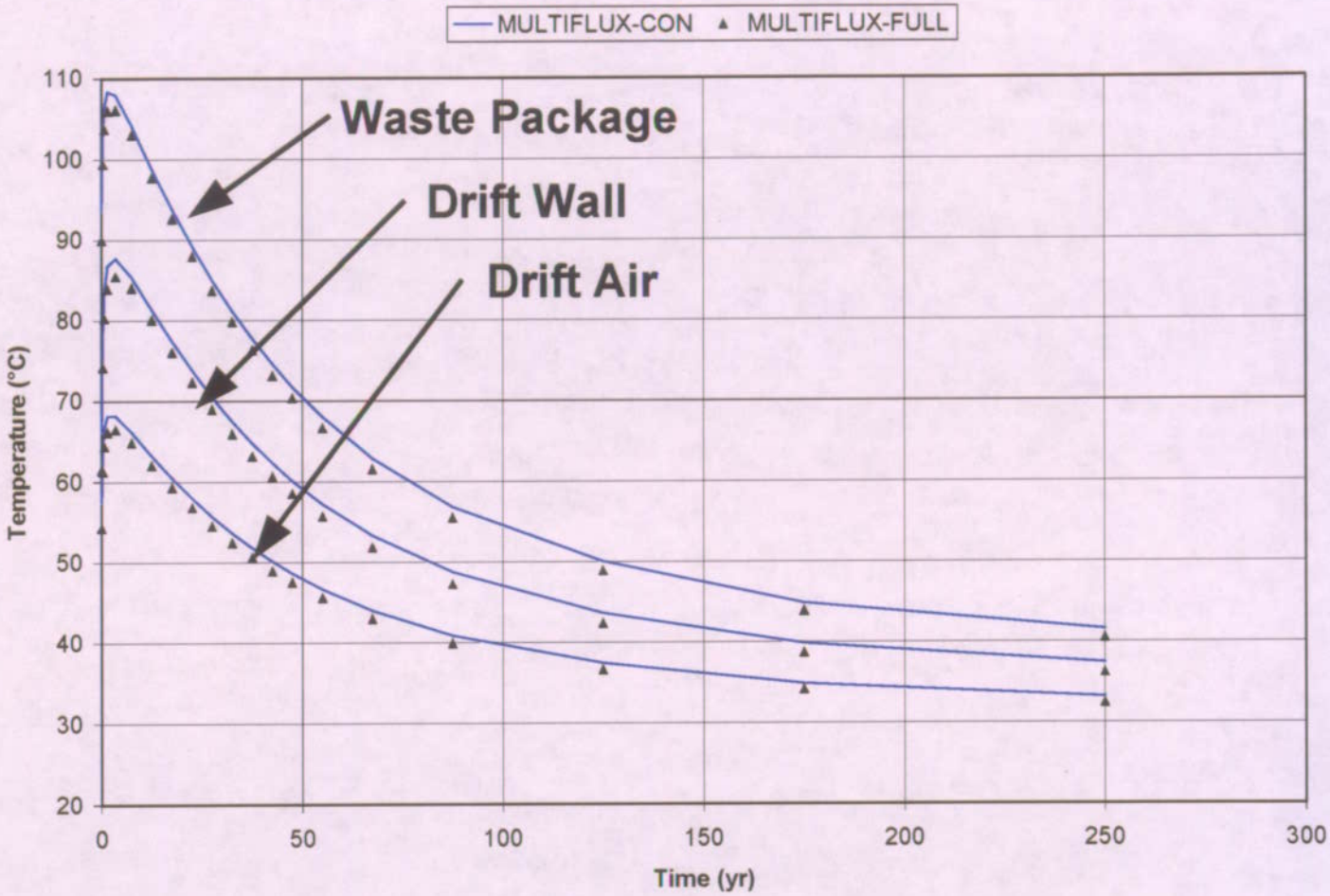

Figure XII-12 (Figure 6-14). Plots of Waste Package, Drift Wall, and Drift Air Temperatures as a Function of Time at 600 Meters from the Drift Entrance for the MULTIFLUX-Con and MULTIFLUX-Full Ventilation Numerical Models (DTN MO0209MWDMUL30.002)

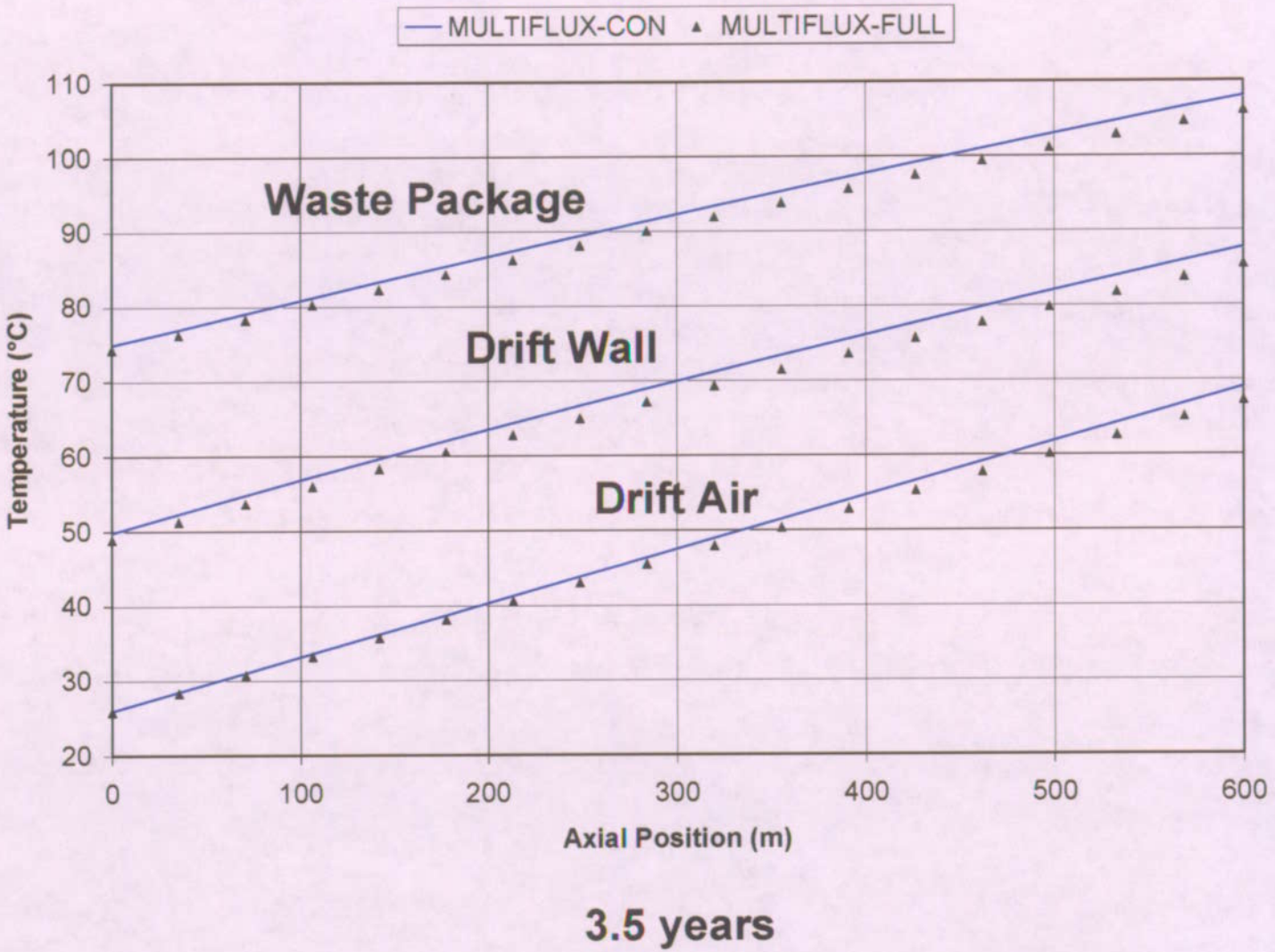

Figure XII-13 (Figure 6-15). Plots of Waste Package, Drift Wall, and Drift Air Temperatures as a Function of Drift Length at 3.5 Years from the Time of Waste Emplacement for the MULTIFLUX-Con and MULTIFLUX-Full Ventilation Numerical Models (DTN MO0209MWDMUL30.002)

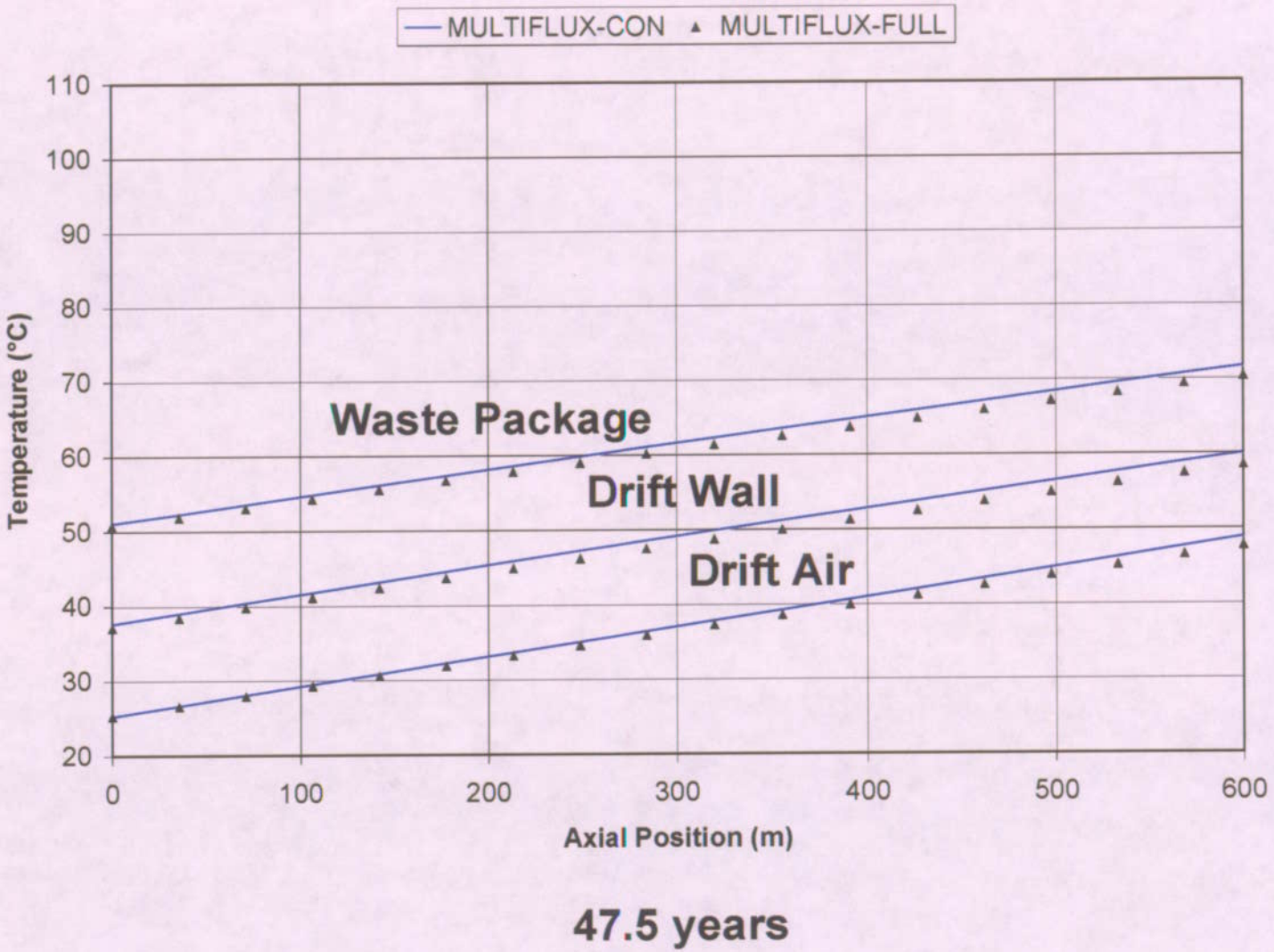

Figure XII-13 (Figure 6-15). Plots of Waste Package, Drift Wall, and Drift Air Temperatures as a Function of Drift Length at 47.5 Years from the Time of Waste Emplacement for the MULTIFLUX-Con and MULTIFLUX-Full Ventilation Numerical Models (DTN MO0209MWDMUL30.002)

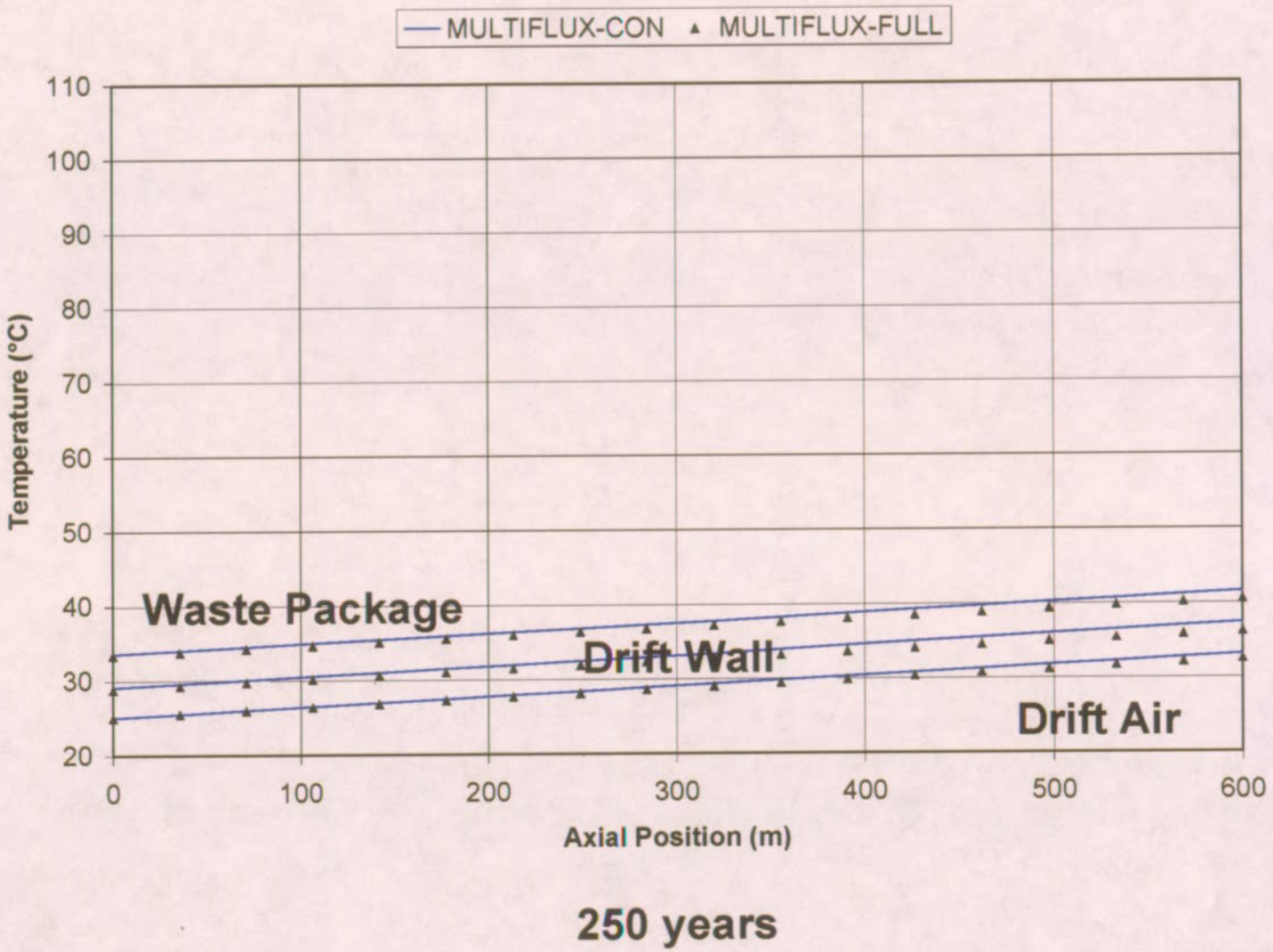

Figure XII-13 (Figure 6-15). Plots of Waste Package, Drift Wall, and Drift Air Temperatures as a Function of Drift Length at 250 Years from the Time of Waste Emplacement for the MULTIFLUX-Con and MULTIFLUX-Full Ventilation Numerical Models (DTN MO0209MWDMUL30.002)